

# Friction Spot Joining of Metal-Composite Hybrid Structures

Vom Promotionsausschuss der  
Technischen Universität Hamburg-Harburg  
zur Erlangung des akademischen Grades  
Doktor-Ingenieur (Dr.-Ing.)  
genehmigte Dissertation

von

Seyed Mohammad Goushegir

aus

Tehran

2015

**Gutachter:**

Prof. Dr.-Ing. Sergio de Traglia Amancio Filho

Prof. Dr.-Ing. Prof. h.c. Stefan Böhm

**Vorsitzender des Prüfungsausschusses:**

Prof. Dr.-Ing. Bodo Fiedler

**Tag der mündlichen Prüfung:**

22. September 2015

---

## Acknowledgements

During my PhD work, I have received continuous support and encouragement from many people. I would like to express my gratitude to the following people who supported this work:

- first and foremost, my deepest appreciation to my PhD advisor Prof. Dr.-Ing. Sergio Amancio for his unconditional support, discussions, encouragement and friendship
  - Prof. Dr.-Ing. Stefan Böhm for being the second reviewer of this work, for his time and contribution
  - Prof. Dr.-Ing. Norbert Huber for giving me the opportunity to work at Helmholtz-Zentrum Geesthacht and for his recommendations
  - Dr. Jorge F. dos Santos for his unconditional support, recommendations and friendship
  - Dr. Nico Scharnagl for his contribution in XPS analysis and fruitful discussions
  - Prof. Dr. Erica Lilleodden for her contribution in nanoindentation experiments and fruitful discussions
  - Mr. Fernando Fernandez and Mr. Marcos Miyazaki from Embraer Co. for their support with aluminum surface preparation and bonding
  - all my friends, colleagues and students of the Young Investigator Group for their incredible support, encouragement, discussions, patience and friendship. My sincere and especial thanks to Andre Abibe, Lucian Blaga, Natalia Manente and Matheus Pavarini
  - all members of the department of solid state joining processes (WMP) for their friendship and professional support. I wish to express my especial thanks to Dagmar Koschek for all her support
  - Stephanie Koch for her administrative support within the institute
  - colleagues from WMF, particularly Jürgen Knaack and Kay Erdmann, for their support with mechanical testing
  - all my family and friends for their support and encouragement
  - my parents and my sister for their continuous support, patience and love throughout my whole life. I have no words to thank you for all you have done for me
  - my son Liam for bringing more love to our life, giving me more motivation and strength to accomplish this work
  - my lovely wife Hamideh for her uninterrupted support, understanding, patience and exceptional encouragement. I love you!
-



---

## Abstract

In recent decades, environmental concerns, economic factors and limited resources have encouraged the production of high-performance, reliable finished products. Along with a demand for rapid transportation, these issues have directed the transport industries to develop lightweight but strong vehicles, aiming to reduce fuel consumption and CO<sub>2</sub> emissions. The need for high-performance products has been the driving force behind scientists and engineers in developing advanced materials and processes. The employment of various materials with distinct physicochemical properties in the automotive and aerospace industries has also opened a new field of research into the joining of dissimilar materials. Several alternative methods have recently developed for joining metal-polymer multi-material structures. Friction spot joining (FSpJ) is one of these newly developed technologies.

Prior to this work, only very limited information was available on the microstructure, bonding mechanisms and quasi-static mechanical performance of FSpJ joints. Moreover, there was no information on the durability and fatigue behavior of FSp joints available in the literature; two essential factors for the industrial transfer of this new joining technology. That is why this PhD work was devised to further develop and understand the fundamentals of the advanced FSpJ process. Case-study joints were produced using aircraft grade lightweight aluminum alloy AA2024-T3 and carbon-fiber reinforced poly(phenylene sulfide) (CF-PPS). The process temperature was measured through thermography and thermometry that showed an average peak temperature of approximately 437°C for the optimized set of joining parameters. The process-related physicochemical changes in the composite were studied through thermal analysis methods (DSC and TGA) that suggested no extensive thermal degradation occurred during the process. Microstructure of the aluminum and composite in the joining area was changed as a result of the thermo-mechanical effect of the process. Microstructural changes caused an alteration to the local mechanical properties as confirmed by microhardness and nanohardness measurements. Moreover, microstructural analysis of the composite part revealed the formation of a small number of volumetric defects such as pores and fiber-matrix debonding.

In addition to a fundamental understanding of the FSpJ process, the influence of various aluminum surface pre-treatments on the bonding mechanisms and mechanical performance of single lap shear (SLS) joints was studied. Mechanical, chemical and electrochemical pre-treatments were applied to the aluminum surface prior to the joining process. All surface pre-treatments increased the joint strength to some extent, compared with specimens without surface pre-treatments. In addition, some surface pre-treatments (chemical and electrochemical) led to the formation of strong chemical bonding between the aluminum and composite, which was confirmed by X-ray photoelectron spectroscopy (XPS). Moreover, the morphology and chemical composition of the aluminum after surface pre-treatments were analyzed in detail to study the correlation between bonding mechanisms and the mechanical performance of the joints.

The durability of the joints was also investigated under accelerated aging conditions using selected aluminum surface pre-treatments. Most of the SLS joints showed only a small reduction of approximately 10% of their initial quasi-static strength, indicating a high durability performance of friction spot joints. Only one surface pre-treatment (phosphoric acid anodizing - PAA) led to a reduction of approximately 40% in the aged joints. This was attributed to the very fine microporous oxide structure of the PAA pre-treated aluminum surface, allowing the diffusion of moisture in the bonding area.

The fatigue life of the SLS FSp joints with selected aluminum surface pre-treatments was also analyzed. Three statistical models (exponential, power law, and wear-out) were selected to fit the experimental fatigue data. All the models fitted well and illustrated similar behavior within the experimental range. The residual quasi-static strength of joints after surviving one million cycles of fatigue was evaluated and this revealed no damage accumulation in the joints at the examined load level. Therefore, this work succeeds in further developing and describing the fundamentals of the advanced FSpJ process.

---

## Zusammenfassung

In den letzten Jahrzehnten haben Wirtschaftswachstum, Klimaveränderungen, und begrenzte Ressourcen die Produktion von hochleistungsfähigen und zuverlässigen End-Produkten gefördert. Neben der Nachfrage nach schnellerem Transport haben die oben genannten Bedingungen die Industrie dazu bewegt, leichte und zugleich starke Fahrzeuge mit dem Ziel zu entwickeln, den Kraftstoffverbrauch und die CO<sub>2</sub>-Emissionen zu verringern. Angetrieben durch den Bedarf an leistungsfähigen Produkten, sind Wissenschaftler und Ingenieure kontinuierlich dabei, neue Werkstoffe und Prozesse zu entwickeln. Allerdings hat die Verwendung von verschiedenen Werkstoffen mit unterschiedlichen physikalisch-chemischen Eigenschaften in großen Bauteilen (z.B. in Kraftfahrzeugen und Flugzeugen) ein neues - im Bereich der Verbindung artfremder Materialkombinationen - Forschungsgebiet geschaffen. Mehrere alternative Fügeverfahren wurden bereits für Metall-Polymer-Multimaterial-Strukturen entwickelt. Reibpunktfügen (auf Englisch: Friction Spot Joining - FSpJ) ist eine von diesen neu entwickelten Technologien.

Vor dieser vorliegenden Arbeit waren nur sehr begrenzte Informationen über Mikrostruktur, Haftmechanismen und quasi-statische mechanische Belastung von FSpJ-Verbindungen vorhanden. Darüber hinaus gab es keine Informationen bezüglich Dauerhaftigkeit und Ermüdungsverhalten von FSpJ. Die aktuelle Doktorarbeit setzt sich das tiefere Verstehen der Grundlagen und die Weiterentwicklung des FSpJ-Verfahrens zum Ziel. Die Fallstudie der Arbeit befasst sich mit dem Fügen von Aluminiumlegierung AA2024-T3 und kohlenstofffaserverstärkten Polyphenylensulfid (CF-PPS), die als Flugzeugbauwerkstoffe in der Industrie dienen. Die Prozesstemperatur wurde durch Thermografie und Thermometrie gemessen. Die Temperatur für die optimale Verbindung lag bei etwa 437°C. Die prozessbedingten physikalisch-chemischen Veränderungen im CF-PPS wurden durch thermische Analysen ermittelt und deuteten darauf hin, dass während des Prozesses keine umfangreiche thermische Degradation auftrat. Die Mikrostruktur des Aluminiums und CF-PPS im Fügebereich hat sich durch thermomechanische Wirkung des Verfahrens verändert. Die Änderungen der Mikrostruktur des Gefüges verursachten eine Veränderung der lokalen mechanischen Eigenschaften. Außerdem wurden die Veränderungen der Eigenschaften durch Mikro- und Nanohärtemessungen bestätigt. Die Mikrostrukturanalyse des Verbundwerkstoffes zeigte die Bildung einiger volumetrischer Defekte an, wie zum Beispiel Poren und Faser-Matrix Debonding.

Zusätzlich wurde auch der Einfluss von verschiedenen Aluminiumoberflächenvorbehandlungen auf die Haftmechanismen und auf das mechanische Verhalten von Scherzugproben untersucht. Die Oberfläche des Aluminiums wurde mechanisch, chemisch und elektrochemisch vorbehandelt. Alle Oberflächenvorbehandlungen erhöhten die Zugscherfestigkeit in einem gewissen Grad im Vergleich zu den Proben ohne Vorbehandlung. Darüber hinaus führten bestimmte Oberflächenvorbehandlungen - chemische und elektrochemische - zur Bildung einer starken chemischen Bindung zwischen dem Aluminium und CF-PPS. Diese wurde durch Röntgen-Photoelektronenspektroskopie (XPS) bestätigt. Zusätzlich wurden die Topographie und die chemische Zusammensetzung der Aluminiumoberfläche nach den Vorbehandlungen detailliert analysiert, um den Zusammenhang zwischen den Haftmechanismen und der mechanischen Festigkeit der Verbindungen zu untersuchen.

Außerdem wurde die Dauerhaftigkeit der Verbindung unter beschleunigten Alterungsbedingungen - mit Verwendung ausgewählter Aluminiumoberflächenvorbehandlungen - untersucht. Die meisten Scherzugproben zeigten nur eine kleine Verringerung von etwa 10% ihrer ursprünglichen statischen Festigkeit; das zeigt eine hohe Dauerhaftigkeit der Reibpunktfügetechnologie (FSpJ). Nur eine einzige Oberflächenvorbehandlung - eloxieren in Phosphorsäure-Lösung (PAA) - führte zu einer Verringerung von etwa 40% der Festigkeit der Verbindung. Dies kann darauf zurückgeführt werden, dass die sehr feine mikroporöse Struktur der mit PAA Oxid vorbehandelten Aluminiumoberfläche die Diffusion der Feuchtigkeit zum Fügebereich begünstigt.

Die Ermüdungslebensdauer der Scherzugproben wurde für ausgewählte Aluminiumoberflächenvorbehandlungen ebenfalls analysiert. Drei statistische Modelle - exponentiell, Power-Law und Wear-Out - wurden ausgewählt, um die experimentellen Ermüdungsdaten zu untersuchen. Alle Modelle passen gut und zeigten ein ähnliches Verhalten zu dem experimentellen Bereich. Die Restfestigkeit der Verbindungen, die eine Million Zyklen ohne Versagen standhielten, zeigten keine Schadensakkumulation in der Verbindung bei dem untersuchten Lastniveau. Fazit: die Arbeit hat erfolgreich das FSpJ-Verfahren weiterentwickelt und dessen Grundlagen beschrieben.

---

# List of Abbreviations

ANOVA	Analysis of Variance
AP	Acid Pickling
AR	As-received
AZ	Adhesion Zone
BM	Base Material
BSZ	Broken Stir Zone
CAA	Chromic Acid Anodizing
CC	Conversion Coating
CF-PPS	Carbon-Fiber-Reinforced Poly(Phenylene Sulfide)
CFRP	Carbon-Fiber-Reinforced Polymer
CP	Clamping Pressure
CR	Cooling Rate
CSM	Continuous Stiffness Measurement
CT	Cross-Tensile
DF	Degree of Freedom
DoE	Design of Experiments
DRX	Dynamic Recrystallization
DSC	Differential Scanning Calorimetry
DTG	Derivative Thermogravimetry
EDS	Energy Dispersive Spectroscopy
ESS	Equivalent Static Strength
FSpJ	Friction Spot Joining
FSpW	Friction Spot Welding
FSW	Friction Stir Welding
FWHH	Full-Width at Half-Height
GFRP	Glass-Fiber-Reinforced Polymer
GPB	Guinier-Preston-Bagaryatsky
HCF	High Cycle Fatigue
HFZ	Hexafluorozirconate
HHI	High Heat Input

---

HR	Heating Rate
ICJ	Injection Clinching Joining
IR	Infrared
JP	Joining Pressure
JT	Joining Time
LCF	Low Cycle Fatigue
LHI	Low Heat Input
LOM	Light Optical Microscopy
LSCM	Laser Scanning Confocal Microscopy
MG	Mechanical Grinding
MHAZ	Metal Heat Affected Zone
MLE	Maximum-Likelihood Estimation
MSZ	Metal Stir Zone
MTMAZ	Metal Thermo-Mechanically Affected Zone
OFAT	One-Factor-at-a-Time
PA	Polyamide
PAA	Phosphoric Acid Anodizing
PAA-P	Phosphoric Acid Anodizing + Primer
PD	Plunge Depth
PDZ	Plastically Deformed Zone
PHAZ	Polymer Heat Affected Zone
PS	Pass Energy
RS	Rotational Speed
SAA	Sulfuric Acid Anodizing
SB	Sandblasting
SEM	Scanning Electron Microscopy
SLS	Single Lap Shear
TC	Thermocouple
TEM	Transmission Electron Microscopy
TG	Thermogravimetry
TGA	Thermogravimetric Analysis
TZ	Transition Zone
ULSF	Ultimate Lap Shear Force
XPS	X-ray Photoelectron Spectroscopy

---

# List of Symbols

a, b, c, d, A, C, S'	Fatigue Models Parameters
d	Depth
F	Applied cyclic force
F <sub>e</sub>	Equivalent Static Force
F <sub>max</sub>	Maximum Applied Cyclic Force
F <sub>p</sub>	Critical Linearity Index
F <sub>r</sub>	Fatigue Residual Strength
H <sub>cr</sub>	Kruskal-Wallis Critical Value
H <sub>kw</sub>	Kruskal-Wallis Statistical Index
h <sub>max</sub>	Maximum indentation depth
N	Fatigue Life (number of cycles)
P <sub>max</sub>	Maximum indentation load
R	Fatigue Stress ratio
R(N)	Reliability Value
R <sub>a</sub>	Arithmetic mean value
R <sub>z</sub>	Maximum peak-to-valley distance
S	Stiffness
T	Temperature
t	Time
T <sub>g</sub>	Glass transition temperature
w	Width
X <sub>c</sub>	Crystallinity fraction
α	Weibull Shape Parameter
α <sub>f</sub>	Maximum Weibull Shape Parameter
β	Weibull Scale Parameter
ΔH <sup>o</sup> <sub>m</sub>	Enthalpy of melting for 100% crystallinity
ΔH <sub>c</sub>	Enthalpy of crystallization
ΔH <sub>m</sub>	Enthalpy of melting

---

# Contents

<b>Chapter 1. Introduction .....</b>	<b>1</b>
<b>Chapter 2. Motivation and Objectives.....</b>	<b>5</b>
<b>Chapter 3. Literature Review.....</b>	<b>6</b>
3.1 Metal-polymer joining techniques.....	6
3.1.1 Adhesive bonding.....	6
3.1.2 Mechanical fastening.....	9
3.1.2.1 FricRiveting.....	9
3.1.2.2 Injection Clinching Joining .....	10
3.1.3 Welding-based technologies.....	12
3.1.3.1 Induction welding.....	12
3.1.3.2 Ultrasonic welding.....	12
3.1.3.3 Laser welding .....	13
3.2 Mechanisms of adhesion at the metal-polymer interface .....	14
3.2.1 Mechanical interlocking .....	14
3.2.2 Adsorption theory.....	15
3.3 Influence of metal surface pre-treatments on the adhesion mechanisms.....	16
3.3.1 Mechanical pre-treatments .....	16
3.3.2 Chemical pre-treatments.....	17
3.3.3 Electrochemical pre-treatments .....	18
3.3.4 Primers.....	19
3.4 Durability of metal-polymer joints .....	19
3.5 Fatigue behavior of metal-polymer joints .....	21
3.6 Materials used in this work.....	22
3.6.1 AA2024-T3.....	22
3.6.2 CF-PPS composite laminate .....	23
<b>Chapter 4. Friction Spot Joining (FSpJ) Technique .....</b>	<b>26</b>
4.1 Principles of the process.....	26
4.2 Process parameters .....	31
4.3 Defects in FSpJ.....	33
4.4 Advantages, limitations, and potential applications .....	35
<b>Chapter 5. Experimental Approach.....</b>	<b>38</b>

---

<b>Chapter 6. Materials, Equipment, and Methods.....</b>	<b>40</b>
6.1 Base materials.....	40
6.1.1 AA2024-T3 rolled sheets.....	40
6.1.2 CF-PPS .....	41
6.2 FSpJ equipment .....	42
6.3 Methods .....	43
6.3.1 Joining procedure.....	43
6.3.2 Temperature measurement.....	43
6.3.3 Microstructural analysis.....	44
6.3.4 Chemical composition .....	45
6.3.4.1 Energy dispersive X-ray spectroscopy (EDS) .....	45
6.3.4.2 X-ray photoelectron spectroscopy (XPS) .....	45
6.3.5 Thermal analysis (DSC and TGA).....	46
6.3.6 Local mechanical properties .....	47
6.3.6.1 Microhardness.....	47
6.3.6.2 Nanoindentation.....	47
6.3.7 Global mechanical properties .....	48
6.3.7.1 Single lap shear (SLS) testing.....	48
6.3.7.2 Cross-tensile (CT) testing .....	48
6.3.7.3 Fatigue experiments.....	49
6.3.8 Aluminum surface pre-treatments .....	50
6.3.9 Durability of the joints (accelerated aging) .....	52
<b>Chapter 7. Development of the FSpJ Process.....</b>	<b>54</b>
7.1 Process optimization for detailed joint characterization.....	54
7.2 Temperature development .....	55
7.3 Process-related physicochemical changes in the CF-PPS .....	58
7.4 Microstructural zones .....	63
7.5 Local mechanical properties .....	66
7.5.1 AA2024-T3.....	66
7.5.2 CF-PPS .....	67
7.6 Bonding zones, failure, and fracture analysis .....	70
7.6.1 Bonding zones .....	70
7.6.2 Failure analysis .....	72
7.6.3 Fracture analysis .....	75

---

---

<b>Chapter 8. Influence of the Aluminum Surface Pre-treatments on the FSp Joints.....</b>	<b>82</b>
8.1 Aluminum surface analysis .....	82
8.1.1 Wettability .....	82
8.1.2 Surface topography and morphology .....	84
8.1.3 Surface chemical composition.....	88
8.2 Mechanical performance of the joints .....	92
8.3 Failure and fracture surface analysis .....	94
8.4 Interfacial bonding mechanisms .....	97
8.5 Comparison between the mechanical performance of FSp and state-of-the-art adhesively bonded joints .....	99
<b>Chapter 9. Durability of FSp Joints .....</b>	<b>102</b>
9.1 Surface features and chemical composition .....	102
9.2 Mechanical performance of the SLS joints .....	107
9.3 Failure and fracture surface analysis .....	109
<b>Chapter 10. Fatigue Behavior of the FSp Joints .....</b>	<b>113</b>
10.1 Fatigue life analysis of the FSp joints .....	113
10.1.1 Application of the models.....	113
10.1.2 Residual strength .....	117
10.2 Fatigue failure behavior.....	117
<b>Chapter 11. Summary of the Results and Conclusions .....</b>	<b>120</b>
<b>Chapter 12. Recommendations for Future Work.....</b>	<b>123</b>
<b>Appendices .....</b>	<b>X</b>

---

# Chapter 1. Introduction

The requirements of modern society have changed over the centuries and particularly in the last few decades. Reliable and safe structures with high performance, new energy sources, and environmentally friendly, sustainable products and processes are some of the demands in this new era. In addition, as a result of globalization rapid transportation has become a major requirement with the need for travel and the export of goods and services around the world. Revolutionary transportation concepts such as frictionless vehicles, flying cars, superfast trains and supersonic aircraft have been designed or their development proposed for future generations. Furthermore, environmental protection is now a major concern. Reduction in emissions of greenhouse gases (such as carbon dioxide), particularly from vehicles by weight saving and leaner fuel consumption, helps circumvent negative environmental impacts. Such requirements and concerns have motivated scientists and engineers in scientific communities and industrial sectors to design lightweight yet mechanically strong and reliable structures. Lightweight structures are nowadays increasingly in demand for a wide range of engineering applications, such as the transport industry [1-3], wind power [4] and bridge construction [5]. Especially in the transport industry, where energy efficiency is required, the use of high-performance polymers and their respective composites, such as carbon-fiber and glass-fiber reinforced polymers (CFRP and GFRP), has been emerging in the design of hybrid, multi-material structures. This is primarily due to their inherent capacity to reduce the weight of an engineering structure, such as an aircraft or car. In addition to the lightweight character of composites, they possess outstanding corrosion resistance, environmental stability, high strength and high fatigue performance, making them attractive for a variety of industries [6, 7]. In addition, advanced lightweight metals such as aluminum, titanium and magnesium alloys are being further developed to reduce the weight of a structure while maintaining high mechanical performance. The development and employment of different materials with a diverse range of properties helps designers to select the right combination of materials to fulfill the required properties of the desired structure [6]. New generation aircraft, e.g. Boeing 787 Dreamliner and Airbus A350 XWB, are examples of large multi-material structures. In both aircraft, approximately 50 wt% composites are mixed with 50 wt% lightweight metal alloys such as aluminum [8, 9] - as illustrated in Figure 1.1 for the Airbus A350 XWB.

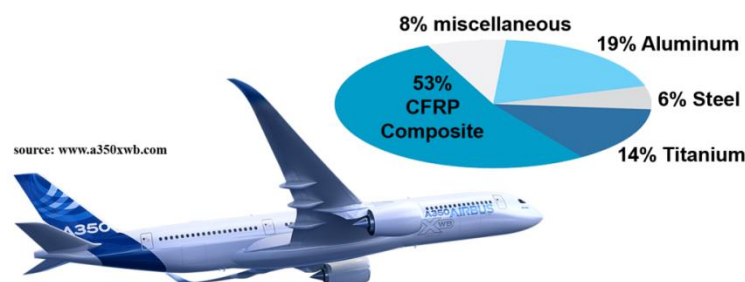


**Figure 1.1 Materials breakdown in Airbus A350XWB. Adapted from [8] with permission.**

In addition to the aircraft industry, automotive manufacturers intend to use more polymers and composites in the bodies of their cars [10-14]. Recently it was stated that by 2030 in the USA polymers and composites will be the primary materials used by the automotive industry to fulfill its demands [12]. Thus more material mixing is expected in automobiles in the near future. The

---

Mercedes-Benz F125 research vehicle [15] is an example of a new concept under development for the year 2025 and beyond. As illustrated in Figure 1.2 the car will consist of metal-polymer hybrid structures to reach its goal of emission-free mobility.

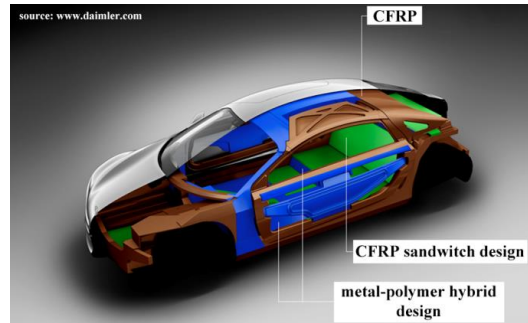


**Figure 1.2 Mercedes-Benz F125 research vehicle concept. Adapted from [15] with permission.**

Despite the benefits of using different lightweight materials in a structure, the joining of dissimilar materials such as metal alloys and composites presents a great challenge due to their distinct physicochemical properties [2]. Amancio and dos Santos [16] have categorized various joining technologies for metal-polymer hybrid structures, these range from more conventional adhesive bonding and mechanical fastening to new welding-based technologies. Nevertheless, traditional bonding and mechanical fastening exhibit technological and environmental limitations. For instance, the curing time of an adhesive for structural adhesive bonding is a major shortcoming. In addition, bonding of thermoplastic composites requires special pre-treatments to increase the intrinsic adhesion between the composite and the adhesive to improve the wettability and surface tension of the thermoplastics [17]. Problems in the mechanical fastening of metal-composite joints have also been reported for the Airbus A380 [6]. During the development phase of the A380 wing, composite ribs were joined to the metal skin by bolting on aluminum brackets. During the operation, some cracks appeared in the brackets, which could have led to failure of the entire component. Such technical limitations have motivated recent investigations into alternative and advanced joining technologies suitable for hybrid structures, to overcome or reduce the drawbacks of traditional techniques.

Friction spot joining (FSpJ) is an alternative joining technology for producing metal-composite joints, patented by and developed at Helmholtz-Zentrum Geesthacht, Germany [18]. As the name implies, FSpJ belongs to friction-based joining and welding technologies. The new technology was developed as a variant of the Friction Spot Welding (FSpW) of metals [19]. This PhD study was devised to evaluate and understand the fundamental scientific and technological aspects of the FSpJ process. For this purpose, a materials science approach was selected to address the relationship between the FSpJ process, the microstructure and mechanical properties of the joints, from micro-scale characterizations to the overall performance of the joints.

This thesis is structured with the following chapters:

Following this introduction as Chapter 1, Chapter 2 describes the motivation for and primary objectives of this work.

Chapter 3 reviews the state-of-the-art literature on the joining technologies available for metal-polymer hybrid structures. Further, it briefly introduces general aspects of the metal-polymer

---

interface, the influence of metal surface pre-treatments on the mechanical performance of metal-polymer joints, the effects of accelerated aging on the behavior of the joints and metal-polymer fatigue. A brief description on the basic characteristics of the materials used in this work rounds off this chapter.

Chapter 4 describes the main principles of the FSpJ process. The primary process parameters are introduced and their functions in the process are explained. Further, the typical microstructure of the FSp joint and any defects commonly observed in the joint are reviewed. In addition, a short summary of the advantages, limitations and potential applications of the process is given. This chapter is based partly on the results obtained in this PhD work as well as previous publications about the process.

Chapter 5 explains the experimental approach and different phases carried out in this work. A flowchart is used to illustrate the steps of the project.

Chapter 6 deals with the materials, equipments and methods used throughout this work to analyze different aspects of the joints such as their microstructure, local and global mechanical properties, physicochemical properties and failure analysis.

The results and discussion part is divided into five chapters. Chapter 7 presents the main results obtained in this study to further develop the FSpJ process. A brief description on optimization of the process is given at the beginning of the chapter. Further, the temperature history during the FSpJ process is explained with the aim of describing the process-related physicochemical changes in the composite and the formation of different microstructural zones, both in the metal and composite. The local mechanical properties of the metal and composite are explored using microhardness and nanoindentation. In addition, this chapter presents a simplified model to describe the bonding zones observed in FSpJ. Finally, failure analysis and fractography of the joints by scanning electron microscopy (SEM) are elaborated.

Chapter 8 is devoted to the influence of metal surface pre-treatment on behavior of the FSp joint. Various lab scale and industrially used metal surface pre-treatments that are available were applied. The effects of surface pre-treatments on metal wettability, surface topography and surface chemistry prior to the joining process are explained. Furthermore, a study of the fracture surfaces of the joints by visual observation, SEM and energy dispersive spectroscopy (EDS) on SEM is shown. In addition, the analysis of the metal-polymer interface through X-ray photoelectron spectroscopy (XPS) is presented to explain the nature of the bonding formation during the FSpJ process.

Chapter 9 describes the influence of an accelerated aging environment on the surface features and chemical composition of the joining parts, outside and inside the bonding area. In addition, the mechanical performance of single lap shear (SLS) joints after accelerated aging for the selected surface pre-treatments is explained. This chapter also gives an explanation about the analysis of the fracture surface of the joints.

Chapter 10 presents the results obtained on fatigue performance of the selected surface pre-treated specimens. The resultant fatigue S-N curves are explained, based on three selected fitting procedures. The fitting procedures are also briefly discussed in Appendix A.11. Moreover, the residual strength of the joints after surviving one million fatigue cycles is presented. Finally, the failure behavior of the joints and typical fracture surface features are described.

---

Chapter 11 summarizes the results obtained in this PhD study about different aspects of the FSpJ process, and finally Chapter 12 offers recommendations for future scientific and technological work.

---

## Chapter 2. Motivation and Objectives

The ever-increasing demand for lightweight metal-polymer multi-material structures, particularly in the transport industries, and the limitations of traditional joining techniques are driving forces behind the development of alternative metal-polymer joining technologies. FSpJ is a new, alternative and innovative metal-polymer joining process that was developed at Helmholtz-Zentrum Geesthacht [18] prior to this PhD project.

The feasibility of the process was investigated in preliminary works. It has been shown that the process can successfully join magnesium alloy AZ31 [20] and aluminum alloy AA6181-T4 [21] to GFRP and CFRP composites. In these works, the main characteristics of the process, its bonding mechanisms, joint microstructure, and the mechanical properties of SLS geometry were preliminary investigated and addressed. However, no detailed investigation into the metal-polymer bonding mechanisms and interface, process-related physicochemical changes on the polymer or composite, or any failure and fracture analysis were carried out. Furthermore, no previous studies investigated the influence of surface pre-treatments on the mechanical performance of the joints, the behavior of the FSp joint under harsh environmental conditions or the fatigue performance of the joints, and so there remained a knowledge gap. Therefore, this PhD work was carried out with the aim of fulfilling the above mentioned gaps in our scientific knowledge.

Based on the knowledge gaps identified, the case-study material combination of aluminum alloy AA2024-T3 and carbon-fiber reinforced poly(phenylene sulfide) (CF-PPS) was selected to permit a fundamental understanding of the FSpJ process. The following objectives were defined in this work:

- a) Establish the relationship between process parameters (heat input), microstructure and mechanical properties of the joint.
- b) Investigate the bonding, failure and fracture mechanisms of single lap shear joints.
- c) Understand the influence of selected metal surface pre-treatments and accelerated environmental aging on interfacial bonding mechanisms and the mechanical performance of overlap joints.
- d) Determine the influence of cyclic loading on the fatigue performance of the FSp joints.

---

# Chapter 3. Literature Review

## 3.1 Metal-polymer joining techniques

The joining of dissimilar metal-polymer or composite hybrid structures dates back to the last century. Over time and due to increased industrial demand to use metal-polymer hybrid structures, various joining techniques have been developed. Figure 3.1 illustrates the categories of technologies that are suitable for dissimilar metal-polymer joining. According to the classification by Amancio and dos Santos [16], the individual joining techniques are adhesive bonding, mechanical fastening, and welding-based technologies. Combinations of one or more of these individual techniques are known as hybrid joining technologies.

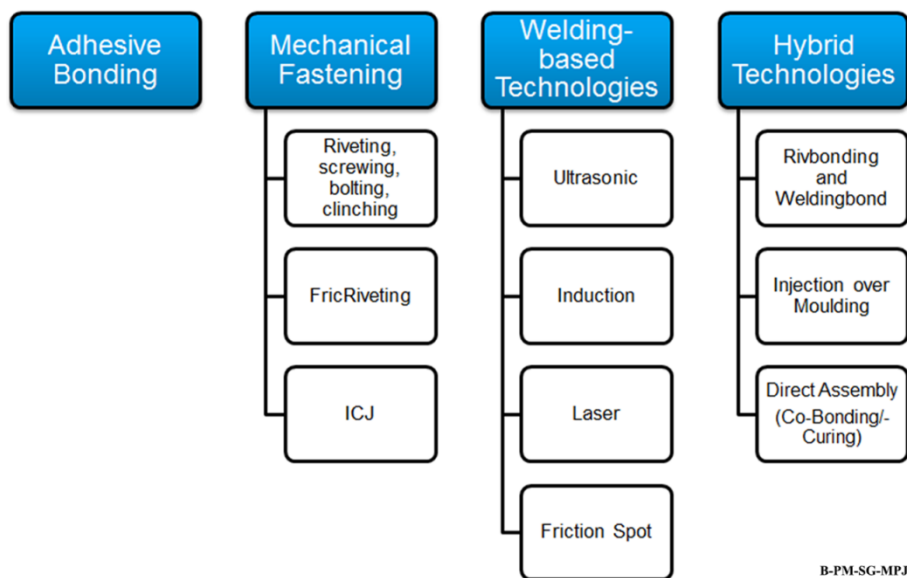


Figure 3.1 Joining techniques for metal-polymer multi-materials [16].

In the following sections, the main features of each individual joining technique are briefly overviewed.

### 3.1.1 Adhesive bonding

Adhesive bonding is a traditional, consolidated joining technology, not only used in structural applications, but also as sealants or as a means of bonding surface coatings [22]. Aircraft fuselage and wing structures [23, 24], as well as automotive body and interior parts [23] are examples of structural applications of adhesive bonding.

With adhesive bonding, two major elements exist: first the joining parts known as adherends, and second the adhesive. The process of adhesive bonding is divided into the following steps: The process usually begins with surface preparation of the adherends. The surface of the adherends should be completely clean and free of contaminants to maximize the adhesion between the adhesive and adherends. Surface treatment is an important step in adhesive bonding to obtain a clean, contamination-free surface so that the adhesive can spread over and wet the adherends.

---

Moreover, surface treatment changes the topography and/or chemical state of the surface of adherends for an improved adhesion. Usually, without any surface treatment the mechanical performance of adhesively bonded joints is limited. Various surface treatments prior to bonding are available, depending on the material of the adherend. A brief review of surface treatments for aluminum alloys will be given later in this chapter. After surface preparation of the adherends, the adhesive is applied to the surfaces of joining parts. The joining parts are then brought together and firmly clamped. The final step is curing of the adhesive, which may be performed at room or elevated temperatures, depending on the nature of the adhesive. During the curing phase, the adhesive undergoes a hardening process that leads to the joining of the parts. The curing phase at elevated temperatures can take several minutes to hours, whereas at room temperature several days may be required to achieve an acceptable adhesive strength [25].

In adhesive bonding theory, two main terms are used to explain bonding mechanisms; adhesion and cohesion. Adhesion refers to the attractive forces between the adhesive and each adherend, whereas cohesion explains the internal forces between the adhesive's molecules producing the internal strength of the adhesive. Derived from these definitions, the two primary failure types of an adhesively bonded structure are "adhesive failure" and "cohesive failure". Adhesive failure takes place when cracks propagate at the interface between the adhesive and one of the adherends. However, when cracks propagate inside the adhesive, as a result of strong bonding between the adhesive and adherends, the failure is known as cohesive. Figure 3.2 (a) illustrates the adhesive bonding in an SLS joint geometry as an example of a metal and a composite. Adhesive and cohesive failure types are also schematically presented in Figure 3.2 (b) and (c). In addition to adhesive and cohesive failures, a mixed mode failure has been reported in adhesively bonded metal-composite hybrid joints [26]. As illustrated in Figure 3.2 (d), in the mixed mode failure type, adhesive remains attached to both adherends. This means that the crack path changes from one interface to another within the adhesive. Furthermore, there are other types of failures classified in the ASTM D5573 standard for adhesive bonding of fiber-reinforced plastic joints [27] that might also occur in metal-composite hybrid joints. One category is fiber-tear failure, as illustrated in Figure 3.2 (e). In this case, failure occurs in the composite part where a part of the composite remains attached to the other fracture surface. If the failure happens near the interface, the failure type is known as light fiber-tear failure. Finally, the failure may occur in one of the adherends outside the bonding area known as a stock-break failure. This type of failure is depicted in Figure 3.2 (f).

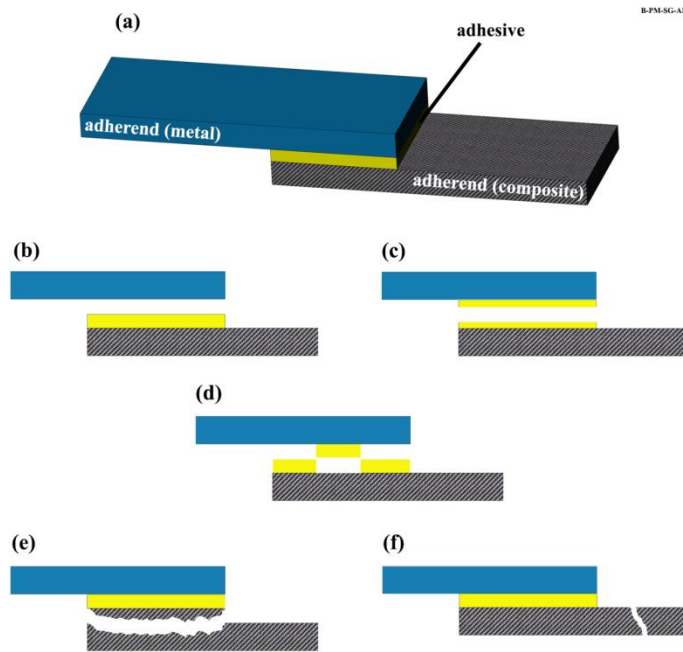


**Figure 3.2 Schematic illustration of (a) adhesive bonding of a metal-composite SLS joint, (b) adhesive, (c) cohesive, (d) mixed mode, (e) fiber-tear, and (f) stock-break failure types.**

SLS joint geometry is widely used to assess the mechanical performance of an adhesively bonded joint. In such joint geometry the adhesive transfers the load between the adherends by shear. Classic theoretical models were developed to analyze the stress distribution in adhesively bonded SLS joints. The earliest studies were performed by Volkersen [28] and Goland and Reissner [29]. It was illustrated through these studies that the shear stress distribution is not uniform throughout the overlap area. The shear stresses generated are minimum in the center of the overlap and increase at its edges. Furthermore, out-of-plane forces (the so called peel forces) are also generated as a result of the secondary bending effect in SLS joints [30]. Due to the generation of such stresses, further types of joint geometries were developed and investigated to reduce the undesired stresses [31].

Surface treatment prior to bonding is an important step to achieve strong joints. This is due to the fact that the surface of adherends should be activated to form strong bonds with the adhesive. Also, as mentioned earlier, the substrate surfaces should be clean and free of contamination to maximize adhesion. This is particularly important when bonding thermoplastic composites, for instance in metal-composite structures. Special treatments are required to increase the intrinsic adhesion between the composite and the adhesive that improve the wettability and surface tension of thermoplastics [17].

Some of the main advantages of adhesive bonding are [32-34]: no drilling is required, which reduces the stress concentration, very thin sheets (less than 500  $\mu\text{m}$ ) can be bonded, a more homogeneous stress distribution in the bonding area, weight saving, smooth surface finish, and the possibility of joining dissimilar materials. However, there are also some disadvantages related to this technique such as [32-34]: limited elevated temperature applications due to the loss of properties of the adhesive, durability of the bonded joints is an issue especially when suitable surface treatments are not applied, requiring extensive surface treatments prior to bonding, long curing times, limited suitable non-destructive testing methods, prediction of bond failure is problematic and disassembling the joints is difficult.

---

### 3.1.2 Mechanical fastening

Mechanical fastening is another traditional joining technique that is widely used in industrial applications such as aeronautics and automotive [35]. Mechanical fastening is considered a sub-category of mechanical joining methods, along with mechanical attachment [36]. In the design of mechanical fastening the strength of the structure is achieved completely by mechanical forces, in contrast with adhesive bonding where primarily chemical forces are responsible for the integrity of a bonded structure [36]. Mechanically fastened joints are designed primarily to sustain shear loading [36]. Similar to metallic structures, for composites joined by mechanical fastening four failure modes are observed [37]: net-tension, shear-out, cleavage-tension, and bearing.

There are many advantages that make mechanical fastening methods favored techniques to join structures. These include [34, 36]: easy disassembly of the joining parts, which is useful for replacing damaged parts, the capability of joining dissimilar materials where special and time-consuming preparation of the joining parts is unnecessary, joint inspection is easy and there is high engineering confidence in the design due to failure predictability. However, there are certain shortcomings related to this joining technique such as [34, 36]: high stress concentration at the fastening points, non-continuous joint that allows diffusion of moisture, fluids, etc., intensive labor involved and weight penalty. Besides these common disadvantages, when polymers or composites are joined further limitations arise. The major concern is the notch sensitivity of the composites that may lead to crack initiation during drilling of the hole. Crack initiation in this stage may cause premature failure of the joint.

Various types of mechanical fastening methods have been proposed such as [36, 38]: bolting, blind-riveting, press-in fastening, self-tapping screwing, clinching, and staking. Besides traditional mechanical fastening techniques mentioned above, there are newly developed processes suitable for metal-polymer or composite hybrid structures [38]. Friction riveting (FricRiveting) and Injection Clinching Joining (ICJ) are among them, which will now be discussed briefly.

#### 3.1.2.1 *FricRiveting*

FricRiveting is a new, innovative joining technology, patented by [39] and developed [40] at Helmholtz-Zentrum Geesthacht, that is suitable for metal-polymer or composite hybrid structures. Basically in this process a metallic rivet is used to join one or more polymeric plates. The principles of the technique are as follows [40, 41]: In a simple configuration, a rotating cylindrical rivet is inserted into a polymeric part. During penetration of the rotating metallic rivet, frictional heat is generated due to the high rotational speed of the rivet as well as applied axial force. Due to the low thermal conductivity of the polymer, the local temperature at the tip of the rivet increases. Two phenomena occur at this stage as a result of the high temperature generated; a volume of the polymer around the rivets tip is molten, and the tip of the rivet is plasticized. At this stage the rotational speed of the rivet is decreased and the axial pressure (forging pressure) is increased, this leads to deformation of the plasticized rivet tip. The deformed tip of the rivet increases in diameter yielding a parabolic shape. Finally the joint is consolidated under pressure. Figure 3.3 illustrates the main process steps in a simple configuration. The main bonding mechanism that holds the parts together is mechanical anchoring of the deformed rivet within the polymer part [40, 41]. However, adhesive forces at the metal-polymer interface may also coexist [42].

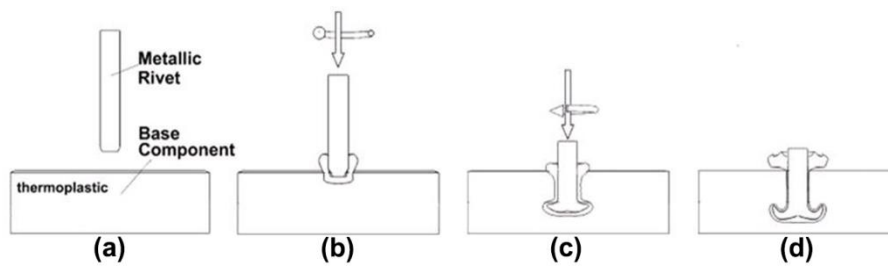


**Figure 3.3 Schematic illustration of the FricRiveting process; (a) positioning of the joining parts, (b) rivet approaching the polymer part, (c) forging of rivet into the polymer, and (d) joint consolidation. Adapted from [41].**

Several studies [41, 43-45] have been conducted to demonstrate the feasibility of the process on a wide range of materials. In addition to the feasibility of the process, the microstructure, thermal, and mechanical properties of the joints were studied. For more information refer to the above mentioned works.

FricRiveting offers various advantages over other mechanically fastened joining methods that include [38, 40]: very short joining cycles in the range of few seconds, no pre-hole drilling is required, capability of joining a wide range of materials, no need for surface preparation or cleaning, single side accessibility, high mechanical performance. However, like any other process, FricRiveting has some limitations, such as difficult disassembly and, similar to traditional mechanical fastening, the joints are discontinuous [38, 40]. Furthermore, the process cannot directly be used to join metal-composite hybrid structures and it is more suitable for polymer-polymer or composite-composite joints. In the case of metal-composite joints, pre-drilling of the metallic part is required, which makes the process time-consuming and expensive. Moreover, the addition of rivets increases the weight of the structure, which is not always desired.

Although FricRiveting was originally developed to join thermoplastic composites, its capability of joining metals (for instance Ti) with a thermoset composite was recently demonstrated [46]. Along with the advantages that FricRiveting offers, its ability to join thermoset composites makes this technique a very suitable, alternative technology for joining advanced metal-polymer hybrid structures.

### **3.1.2.2 Injection Clinching Joining**

ICJ is another mechanical joining technique patented by [47] and developed [48-50] at Helmholtz-Zentrum Geesthacht. This technique is an advanced form of staking that is suitable for joining dissimilar materials [47]. As explained by Abibe *et al.* [48, 49] the principles of ICJ are based on staking, mechanical fastening and injection molding. The basic principles of ICJ can be described as follows [38, 48, 49]: overlap joints are produced between a thermoplastic part with an integrated stud and a joining partner with a through cavity. The joining partner can be a thermoset polymer, a metal alloy or any other material that can withstand the heating produced at the joining area. The parts are assembled together prior to the joining process such that the stud of the thermoplastic part fits into the cavity of the joining partner. An energy source and axial force are used to heat up and deform the stud into a rivet shape, creating mechanical anchoring between the joining parts.

In the first variant of ICJ developed an electric source was used to heat the thermoplastic stud [49]. However, the time required for the process was long, in ranges of several minutes. To shorten the joining cycle a new variant was developed and patented [51] making use of frictional heat to plasticize and deform the stud. In friction-based ICJ (F-ICJ) the joining cycle reduced to between 3 and 20 seconds, nevertheless achieving good mechanical performance [52].

Figure 3.4 illustrates the main process steps of the electric-based ICJ (E-ICJ) and F-ICJ techniques. As explained above, an energy source is required to heat up and plasticize the thermoplastic stud. In case of E-ICJ, a hot case is used for this purpose, as shown in Figure 3.4 (a). A punch-piston is also employed to deform the plasticized stud into the form of a rivet. In F-ICJ (Figure 3.4 (b)) plasticization and deformation of the stud occurs simultaneously with a one part, non-consumable tool. The tool rotating at high angular velocities approaches the polymer stud. As a result of friction between the rotating tool and the stud, frictional heat is generated that melts the top layers of the stud. The tool then stops rotating while axial pressure is applied that spreads the molten/plasticized polymer stud into the metal's cavity. Finally, the tool is retracted and the joint consolidates.

Besides the advantages of F-ICJ, such as reduced joining cycles, the process presents some limitations. Similar to FricRiveting and other mechanical fastening approaches, pre-drilling of the metal sheet is required, which increases the production time and cost. In addition, stress concentration around the stud during mechanical loading may lead to pre-mature failure of the joints. Furthermore, with the current knowledge of the process, ICJ is not a suitable technology for joining laminated composites.

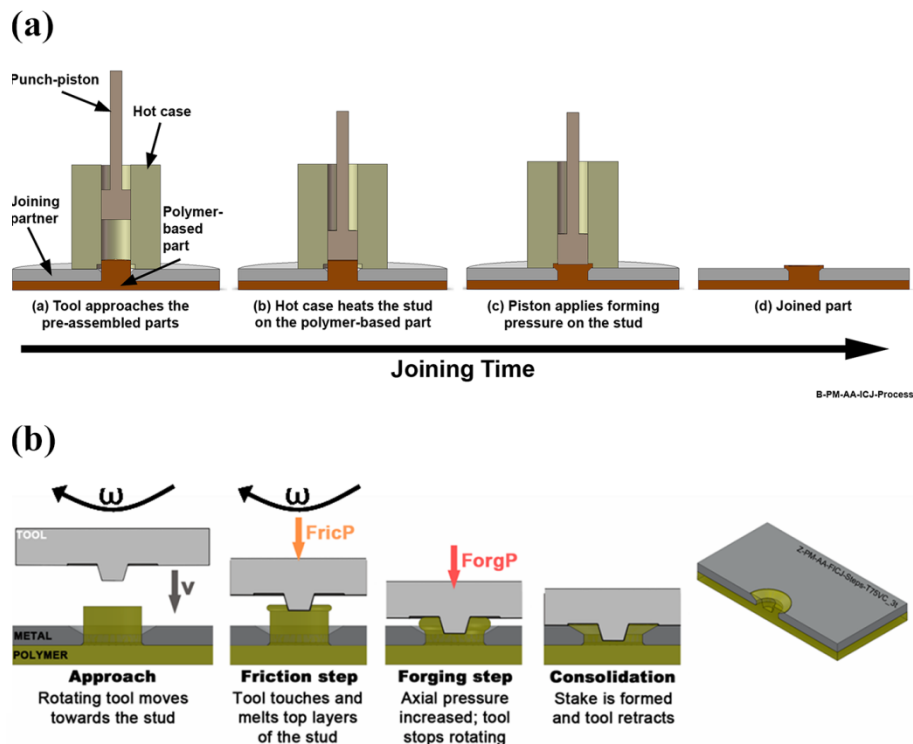


Figure 3.4 Process steps of (a) E-ICJ (adapted from [48]) and (b) F-ICJ (adapted from [52]).

---

### 3.1.3 Welding-based technologies

The welding-based joining techniques for metal-polymer joints reviewed here are relatively new techniques that have been developed in the last 10 years. Induction welding, ultrasonic welding and laser welding are briefly discussed here, whereas FSpJ will be thoroughly explained in Chapter 4. The principles of all welding-based techniques are based on the melting of a thermoplastic part that forms a joint with a metal partner after consolidation. Basically, mechanical interlocking and adhesion forces are responsible for holding the joint's parts together.

#### 3.1.3.1 Induction welding

Although, induction welding was one of the first techniques developed for joining metal-polymer structures among the joining methods mentioned, there is very little information in the literature [53, 54]. For induction welding a magnetic inductor is used as the main energy source to heat up the joining parts. The process steps can be explained as follows [53, 54]: the joining parts are placed in the overlap configuration. In the first step (heating), the metal close to the inductor is heated by generation of electrical eddy currents. Such currents induce heat by resistance and a magnetic field. The heat is then conducted to the polymer/composite, leading to melting of the polymer. The joining parts are then transferred to the consolidation station in step 2. Finally, in step 3, the joint cools down and consolidates under application of joining pressure. The process steps are illustrated in Figure 3.5. A temperature drop of approximately 50°C was identified in the transport step for the selected AlMg3 / CF-PA66 joint [53]. Therefore, the temperature during heating step must be sufficiently higher than the polymer melting temperature (close to its degradation temperature) to assure its melted state continues until the beginning of step 3.

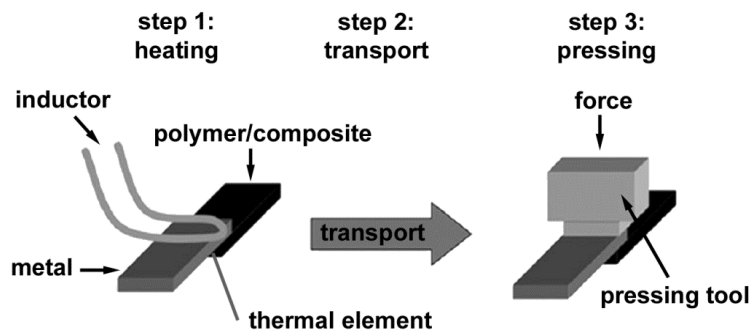


**Figure 3.5 Schematic illustration of the induction welding process steps. Adapted from [53].**

In a modified configuration, the heating and pressing steps are integrated together [53]. By eliminating the transport step, deconsolidation of the composite part (as a result of excess heating) is reduced. However, a shortcoming of the process is the long joining time, which is approximately two minutes.

#### 3.1.3.2 Ultrasonic welding

Ultrasonic welding is another welding-based technology to produce metal-polymer hybrid joints. With this technique, ultrasonic metal welding equipment is used to join the parts, as illustrated in Figure 3.6. The process steps are as follows [55-57]: the main voltage (50 Hz) is converted to a

high frequency output (20 kHz) by an ultrasonic generator. This electrical oscillation is converted into mechanical oscillation by a piezoelectric converter in the welding tool (known as a sonotrode). Similar to the ultrasonic welding of metals, the sonotrode oscillates parallel to the joining parts. The joining parts are positioned in an overlap configuration and clamped to an anvil below the sonotrode. The oscillating sonotrode is brought into contact with the metal part and the oscillation leads to the transversal movement of the metal piece. The relative movement of the metal against the stationary polymer causes friction between the two parts. As a result, frictional heat is generated at the interface between the metal and polymer [57]. Finally, the sonotrode is removed and the joint consolidates.

The bonding mechanisms in ultrasonic welded metal-composite joints consist of mechanical interlocking between metal and load bearing fibers, as well as intermolecular forces (adhesion) between the joining parts [55, 57].

Although, ultrasonic welding has many advantages, it appears metal sheet thickness is limited in this technology. No ultrasonic welding of metal-composite structures with a metal thickness of more than 1 mm has been reported.

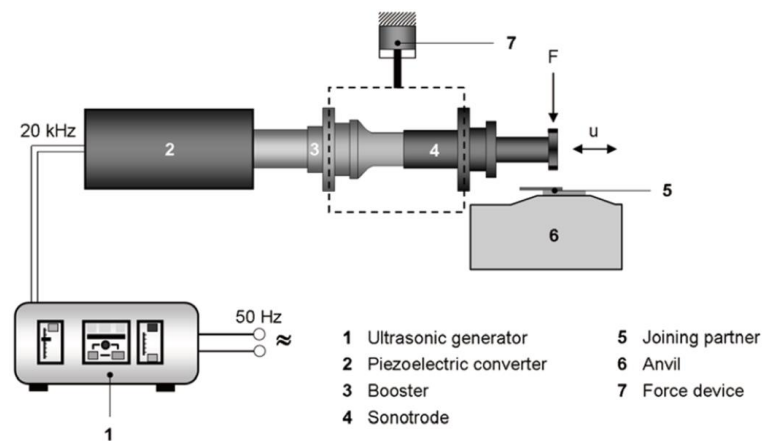


Figure 3.6 Schematic illustration of the ultrasonic welding equipment. Adapted from [58].

### 3.1.3.3 Laser welding

Laser welding, as the name implies, makes use of a laser as the energy source. Various types of laser source can be employed, such as the fiber-coupled diode laser [59]. One of two overlap configurations is selected prior to the joining process, dependent on laser transparency of the polymer part [59]. When the polymer is laser-transparent, the laser is transmitted through the polymer to heat the metal part. An increase in metal temperature at the interface with the polymer leads to melting of a volume of the polymer. However, when the polymer has a low transmission coefficient, the metal part is directly irradiated instead, which absorbs the laser energy and generates heat at the surface. The heat is conducted to the polymer part and the polymer melts at the interface with the metal. Similar to other welding-based techniques, the molten polymer then consolidates, leading to the generation of adhesion forces that hold the joint's parts together. In addition to the adhesion forces, micro-mechanical interlocking may act as further bonding mechanism, if there are irregularities on the metal surface in contact with polymer [59].

---

With laser welding of metal-polymer joints, controlling the process parameters, particularly laser power, is crucial to avoid polymer degradation. The generation of pores and bubbles has been reported in the polymer or composite part [60-62]. Two mechanisms were proposed to explain the appearance of such defects [62]. Firstly that the pores are generated as a result of non-homogeneous solidification of the molten polymer [62]. Secondly that the pores are formed as a result of thermal degradation of the polymer part, as reported for steel-polyamide 6 joints [60, 62], and steel-polyethylene terephthalate joints [61]. In particular thermal degradation of the polymer part should be avoided as much as possible, because degradation diminishes the local mechanical performance of the polymer and hence the strength of the joint.

## **3.2 Mechanisms of adhesion at the metal-polymer interface**

Similar to adhesive bonding, in all welding-based techniques the interaction between metal and polymer at the interface is of utmost importance, because it directly influences the strength of the joint. While the polymer is molten its molecules have more freedom to move, interact, and generate bonds with the metal during the consolidation phase. As melting and re-consolidation of the polymer are important to achieve a strong bond, most efforts have been focused on joining thermoplastics with metals. This type of interaction strongly depends on the chemical state and topography of the metal surface. Such interaction leads to adhesion between metal and polymer, which is responsible for the strength of the joint. Various adhesion mechanisms and models have been proposed. Among them mechanical interlocking and adsorption theory are briefly discussed in this section as they are more relevant to discussions in this thesis. For further information on other types of mechanisms such as diffusion, electrostatic bonding and weak boundary theory, refer to [63]. Although all these theories have been proposed through extensive research carried out into adhesive bonding in recent decades, they can also be used to explain the adhesion mechanisms in the case of welding-based techniques, in which category FSpJ also belongs.

### **3.2.1 Mechanical interlocking**

Mechanical interlocking was one of the first mechanisms proposed to explain the adhesion of metal-polymer or adhesive. This mechanism relies on penetration of a molten polymer into the asperities and irregularities of a metal surface. Mechanical interlocking, or keying, is deemed entirely responsible for joint strength [63-66]. It is well-known from adhesive bonding theories that, in addition to the shape and angle of surface asperities, the wettability of the surface plays an important role in the strength of the joints [63, 67, 68].

As proposed by van der Leeden and Frens [68], three types of surface irregularities can be identified, as illustrated in Figure 3.7. The authors proposed that crevices of type “b” create mechanical interlocking, contributing to the joint strength. The effectiveness of mechanical keying of irregularities of type “a” and “c” depends strongly on the load direction [63]. These types of features may also increase the joint strength under shear loading, but they do not seem to be as effective under tensile loading.

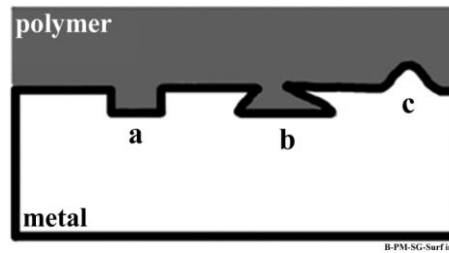


**Figure 3.7 Schematic illustration of various types of metal surface irregularities in contact with a molten polymer. Adapted from [68].**

Moreover, the molten polymer must completely fill the pores and irregularities on the surface of the metal to achieve acceptable joint strength and durability [69]. Two criteria are important in controlling of pore filling. The first is the shape of the pores as discussed by Packham [70]. It was explained that cylindrical pores (type “a” in the figure above) are more easily filled by polymer compared to ink-bottle pores (type “b” in figure above). The second concerns the rheological properties of the molten polymer (or adhesive), as pointed out by Maeva *et al.* [67]. Sufficiently low viscosity and enough time support better pore filling.

It should be noted that mechanical interlocking does not explain the forces at the molecular level, it is just a technical method to increase the strength of the joint [63].

### **3.2.2 Adsorption theory**

In contrast to mechanical interlocking, adsorption theory describes the interaction and forces between molecules and atoms at the interface, also known as adhesion forces [63, 65, 71]. Adhesion forces are generally divided into physical forces (physisorption) and chemical forces (chemisorption) [63]. Physical forces are referred to as secondary, weak bonding as a result of Van der Waals forces and hydrogen bonds, whereas chemical forces correspond to primary, strong chemical bonds related to covalent, ionic, and metallic bonds [63, 65, 67].

One important criterion for physical and chemical bonds is the effective wetting of the metal surface by molten polymer [63, 67]. This is required to achieve intimate contact between metal and molten polymer and thus promote physical and chemical bonding. Figure 3.8 illustrates the wetting behavior of a molten polymer in contact with a metal surface. Thorough wetting leads to more contact between the polymer and metal and hence promotes adhesion forces. However, poor wetting, as illustrated in Figure 3.8 (b), results in a reduction in contact area, which leads to less adhesion forces and lower joint strength. Surface contamination and very large irregularities are among the parameters that reduce the wettability.

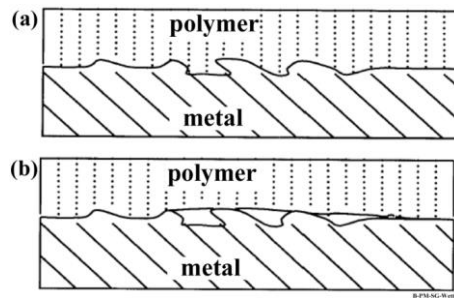


**Figure 3.8 Wetting of a metal surface by the molten polymer; (a) efficient wetting, and (b) poor wetting. Adapted from [63].**

### **3.3 Influence of metal surface pre-treatments on the adhesion mechanisms**

It is well understood from the principles of adhesive bonding that the surface energy of the substrate should be higher or equal to the adhesive to achieve a complete wetting, good adhesion, and therefore increased mechanical performance [32, 72, 73]. One of the methods frequently used to increase the surface energy of the metal is surface pre-treatment [32, 74].

It has been reported [75] that a proper surface pre-treatment should result in a clean surface, without any contamination, increased wettability, adequate surface roughness, mechanical stability and hydrolytic stability.

In the case of aluminum, various pre-treatments were investigated, these range from mechanical pre-treatments, chemical pre-treatments and conversion coatings, to electrochemical pre-treatments [76]. Primers may also be applied after electrochemical pre-treatment, prior to adhesive bonding or joining processes. However, the application of primers is not classified as a pre-treatment process. In addition to the cleaning effect of the mentioned pre-treatments, surface topography and chemical state are also modified, thereby enhancing the adhesion mechanisms. Critchlow and Brewis [76] reviewed more than 40 aluminum surface pre-treatments prior to adhesive bonding. Moreover, extensive studies have been conducted to analyze the influence of different aluminum surface pre-treatments on the topography, chemical composition and strength of joints. In this part, some of the relevant aluminum pre-treatments are reviewed. For further information on this topic, refer to the extensive review by Critchlow and Brewis [76].

#### **3.3.1 Mechanical pre-treatments**

One of the most used mechanical pre-treatments is sandblasting (SB) or grit-blasting using alumina or silica particles. SB aims to generate a macroscopically rough surface, promoting mechanical interlocking as the primary bonding mechanism between metal and polymer [63, 76, 77]. It was stated that SB can also remove loose surface contaminations, increase the effective surface area, improve wettability, and may also alter the physicochemical state of the aluminum surface [77].

Water contact angle measurement can be used to quantify the wetting of a solid surface. In addition to the cleanness of the surface, the spreading of a water droplet is another aspect influencing the contact angle obtained. However, spreading of the water and the resultant contact angle remain

---

controversial topics among researchers, as briefly overviewed by Harris and Beevers [77]. Several studies [78, 79] claim that the presence of peaks and asperities on the surface of a rough solid limits spreading of the water droplet, leading to a low value for contact angle and thus reduced measured wettability. By contrast, the increased effective surface area associated with generated surface roughness was used as an argument for improved wettability [80, 81]. The results of contact angle measurement should therefore be interpreted carefully.

Despite the controversy about wetting interpretation of SB treated surfaces, in most of the reported cases the joint strength was increased, due to the increase in mechanical interlocking [53, 82-84]. Other types of mechanical pre-treatments include [76]: mechanical abrasion or grinding, and machining.

### **3.3.2 Chemical pre-treatments**

Chemical pre-treatments for aluminum prior to adhesive bonding or joining have been investigated frequently. Such pre-treatments usually provide an initial strength and durability superior to those from mechanical, but inferior to electrochemical pre-treatments [75, 76]. Chemical pre-treatments can generally be divided into two categories of acid etching (also known as acid pickling) and conversion coating. A number of different acid etching processes for aluminum alloys have been investigated, ranging from a concentrated solution such as nitric acid [82] and chromic acid to dichromate-sulfuric acid etching [76]. The latter is known as Forest Products Laboratory (FPL), which is the preferred chemical etching in the US aircraft industry [76].

The functions of chemical etching can be summarized as follows [75]: They are effective in cleaning the aluminum surface from adhered contaminations. They also eliminate the weak natural aluminum oxide layer, but at the same time a new, thin oxide layer is generated on the surface of aluminum. This newly developed oxide layer is supposed to be more stable in humid and corrosive environments [75]. In addition, depending on the etching process, the morphology of the surface may alter and a highly micro-rough surface can be obtained. The generation of a microporous oxide layer increases the mechanical interlocking and thus the initial strength of the joint. An increase in initial quasi-static strength (prior to aging) of more than 40% was reported for induction welded [53] and ultrasonic welded [82] aluminum-CFRP joints.

As well as chemical etching, conversion coating (CC) is a further class of chemical pre-treatments. CC as its name implies, deposits a layer on the surface of the aluminum with a thickness in the range of a few nanometers to approximately one micrometer [75]. One of the main functions of CC is to generate a layer that is chemically active by the presence of various chemical elements and compounds, which can produce strong chemical bonds with a molten polymer or adhesive [85, 86]. Moreover, depending on the CC solution and treatment procedure, the coated layer may act as a passive layer that inhibits hydration and corrosion of the aluminum surface [75, 85, 86].

Different types of CC solution have been investigated, such as a chromate conversion coating [87-89], Ti-Zr based coatings [90, 91], and a Zr-F coating [92]. As mentioned above, the layer formed by all of these CC treatments significantly enhances the corrosion resistance of aluminum, for examples see [87, 90, 93]. The initial quasi-static strength of the bonded joints through application of CC pre-treatments was reported to be similar or even superior to that of chemically-etched bonded joints [75].

---

### 3.3.3 Electrochemical pre-treatments

Electrochemical pre-treatments have been extensively studied as a way to convert the aluminum surface to aluminum oxide. The most common electrochemical pre-treatments for aluminum are [75]: chromic acid anodizing (CAA), phosphoric acid anodizing (PAA), and sulfuric acid anodizing (SAA). All anodizing processes are multi-step procedures to achieve the desired properties of the pre-treatment. CAA and PAA are the most often used pre-treatments in the aerospace industry [31].

In general CAA and PAA pre-treatments lead to the formation of a highly microporous aluminum oxide layer with specific characteristics. The formation mechanisms of the anodized oxide layer are beyond the scope of this work, however information may be obtained from [75, 94-96]. Figure 3.9 illustrates the oxide layer formed on the aluminum surface after anodizing pre-treatment. The generated oxide forms a barrier layer on top of the aluminum base material to protect it against corrosion or humid environments. The thickness of this layer depends on the applied voltage, time, and its relative resistivity [97]. Moreover, the oxide at the top of the barrier layer consists of a large number of microscopic open porosities [75, 94]. Investigation of the oxide layer shows a homogeneous cell structure arranged in a closely packed hexagonal structure with open porosities in the center of the cells [75, 94]. Such a highly microporous structure increases micro-mechanical interlocking at the interface between the aluminum oxide and the molten polymer or adhesive, thereby enhancing joint initial strength [96]. It was reported that CAA produces a thicker oxide layer than PAA, which could be beneficial against corrosion [75]. However, other studies, for instance [98], showed the effectiveness of PAA pre-treatment in decelerating hydration of the aluminum in a humid environment, leading to excellent durability.

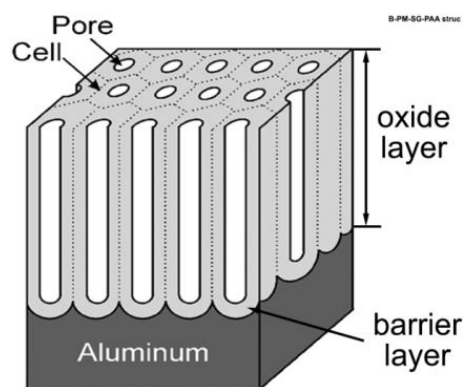


**Figure 3.9 Schematic illustration of the oxide layer structure on aluminum after anodizing pre-treatment. Adapted from [95].**

A highly porous oxide structure was also reported for SAA pre-treated aluminum, while the influence of different anodizing parameters on the oxide morphology was also reviewed [95]. It was also pointed out that the oxide layer formed after SAA pre-treatment is very thick, particularly if a DC voltage is used for anodizing, thus protecting the aluminum against corrosion [99]. However, it was shown that the aluminum surface after SAA pre-treatments contains up to 15 wt% aluminum sulfate [99, 100]. Aluminum sulfate is very susceptible to water absorption and this may lead to a large amount of water absorption if the aluminum is exposed to a humid environment [99, 100]. Such hydrated oxide may be detrimental to the joint strength, particularly in adhesive bonding. Release of water during curing was also reported to form blisters, leading to a reduction in joint strength [99, 101].

---

Among the aluminum surface pre-treatments mentioned above, PAA and CAA are the preferred techniques in the aircraft industry, whereas SAA and CC are more common in the automotive industry. However, according to the European Union regulations [90, 102], the use of hexavalent chromium is strictly limited to less than 2 g for each car produced. The regulations are still not very strict for aircraft production, but it is anticipated that similar limitations in the use of hazardous chromium compounds will eventually be applied in the aerospace industry. For this reason the use of non-chromate surface pre-treatments has been the focus of recent researches.

### **3.3.4 Primers**

Primers are organic liquids that along with other types of adhesion promoters enhance adhesion mechanisms and are used for both metallic and non-metallic substrates [103]. Some of the main functions of primers are as follows [103]: adjusting the surface energy of the aluminum and enhancing wettability, inhibiting corrosion of the surface, eliminating surface contaminations by dissolving organic compounds, and promoting chemical bonding with other polymers or adhesives. In particular, when a primer is used on a metal surface, corrosion inhibitors such as strontium chromate or other inorganic chromate salts may be added. Due to these characteristics, primers are widely used in the transport industries, particularly for promoting adhesion and eliminating corrosion problems [104]. The primers used in the aerospace and automotive industries for metals are usually epoxy based, due to their good chemical and corrosion resistance [103]. The primer is usually applied to the surface prior to bonding and is partially cured. A full cure of the primer is achieved along with curing of the adhesive [103].

## **3.4 Durability of metal-polymer joints**

In addition to initial strength, the durability of a joint, which is its ability to retain initial strength under harsh environments for long time, is particularly important, because engineering structures such as an airplane or car are constantly exposed to the environment. In order to select and use a specific joining method, its long-term behavior must be understood. Due to time limitations, the aging of a joint is usually analyzed over a shorter time, but under an extremely harsh environment (high relative humidity and high temperature). This is known as accelerated aging.

It is of utmost importance to understand the degradation mechanisms under accelerated aging conditions, to be able to design a durable joint. Three types of mechanisms may cause degradation of a joint (particularly adhesively bonded ones) in a humid environment.

The first mechanism is degradation of the metal-polymer interface [105-107]. If the metal-polymer bonding contains weak boundaries, where no intimate contact exists as a result of poor surface wetting, moisture may diffuse at the interface. Moisture can degrade the adhesion forces such as hydrogen bonds [105], leading to a reduction of joint strength and durability.

The second mechanism to consider is the influence of moisture on the polymer (or adhesive) [108, 109]. It has been suggested that humidity may degrade the properties of the polymer through plasticization [108-110] or the generation of swelling stresses [108, 109]. Thus a weakening of the polymer is another reason for reduced durability of a joint.

---

The third mechanism suggests degradation of the metallic part, in this case aluminum [96, 111]. It is well known that aluminum oxide is prone to hydration in a humid atmosphere [96, 98]. Aluminum hydroxide forms a weak layer that may be easily detached from the underlying aluminum oxide. Aluminum oxide converts to the crystalline aluminum hydroxide (AlOOH) known as boehmite [75, 96]. Upon further hydration AlOOH transforms to  $\text{Al}(\text{OH})_3$  known as bayerite [75, 96]. Accordingly, hydration of the aluminum surface also degrades the joint durability.

Sealants and paints may be used as a solution against the first two mechanisms of durability degradation. However, to reduce the hydration of the aluminum surface, various surface pre-treatments may be useful. Among the surface pre-treatments explained in the previous section, electrochemical pre-treatments showed the highest durability, followed by chemical and mechanical pre-treatments [76, 112]. The durability of SB joints was reported to be better or inferior to chemically pre-treated bonded joints in different studies reviewed in [76]. This might be attributed to the extent of the macroporosity generated on the aluminum surface and the wettability of the surface. Proper wettability is necessary for obtaining a durable joint when mechanical pre-treatment is employed. Electrochemical pre-treatments showed excellent durability as a result of generation of a thick oxide layer, forming a barrier against humidity and corrosive environments.

Among the electrochemical pre-treatments, it is reported [111] that PAA offers the best durability. Davis *et al.* [98] explained for the first time the mechanisms of hydration inhibition by PAA pre-treatment. They pointed out that a very thin layer of  $\text{AlPO}_4$  is formed on top of the aluminum oxide. This layer absorbs water from humidity to form  $\text{AlPO}_4 \cdot \text{H}_2\text{O}$ , which inhibits further hydration of the underlying aluminum oxide. Nevertheless, if the aluminum is exposed to a humid atmosphere sufficiently long, the  $\text{AlPO}_4 \cdot \text{H}_2\text{O}$  layer starts to dissolve. This leaves the underlying oxide layer exposed to moisture and it begins to degrade.

In addition to the above-mentioned effects, when a metal-polymer joint is exposed to a corrosive environment, two major corrosion mechanisms may occur: galvanic corrosion and corrosion under rust (or corrosion creep). Galvanic corrosion is especially important when a CFRP is used. If the metal part, such as aluminum, is in direct contact with carbon fibers it potentially leads to galvanic corrosion [113]. By using a transition layer, such as glass [113] or titanium [114], between the joining parts the contact between metal part and carbon fibers and hence the galvanic corrosion may be inhibited. The second type of corrosion is the so-called corrosion creep that is particularly an issue in adhesive bonding [115]. It happens when a corrosive medium infiltrates at the interface between the adhesive layer and the metal part. In this type of corrosion mechanism, the metal part below the adhesive layer starts to corrode and failure takes place in the base material rather than at the bondline. Usually different types of surface pre-treatments are required to inhibit the corrosion mechanisms and failure of the joint [115]. Because corrosion was not in the scope of this work, in-depth literature review on the corrosion mechanisms is not given here.

To further protect the aluminum against hydration and corrosion, a suitable primer layer may be used. Bland *et al.* [112] used an epoxy-based primer containing strontium and chromium particles on a PAA pre-treated aluminum alloy prior to adhesive bonding. Their findings suggest that the primed joint had better durability compared to PAA pre-treatment alone.

It is clear from the explanations above that a proper surface pre-treatment not only enhances the adhesion mechanisms and therefore initial joint strength but also durability of the joint.

---

No information could be found in the literature regarding the influence of surface pre-treatments on the accelerated aging behavior of welding-based joining techniques.

### 3.5 Fatigue behavior of metal-polymer joints

Engineering structures such as an aircraft or a car are not only subjected to humid environments, but also to cyclic loading. So understanding the fatigue behavior of a structure (including a joint) is fundamental for the reliable design of applications. There are primarily two approaches to analyze the fatigue life of a joint (particularly adhesively bonded joints) [116]: firstly, by stress-life (or S-N curve) analysis, and secondly, by analysis of fatigue crack growth. Most of the literature about adhesive bonding has focused on the crack growth approach. However, due to its relevance to this work, the stress-life analysis approach is briefly discussed in this section.

In order to analyze and predict the fatigue strength (or life) of a material (or joint) various models have been proposed. One of the very first models developed to fit the S-N curve of metallic structures was introduced by Basquin [117]. This was essentially a power law model (in the form of  $\sigma = bN^a$ , where  $\sigma$  is the fatigue strength,  $N$  is the respective fatigue life, and  $a$  and  $b$  are model parameters) that is used for fatigue data obtained under uniaxial loading conditions [118]. However, it was stated that this model could fit the data for high cycle fatigue (HCF), but does not properly fit when a low number of cycles is the case [119]. Therefore, the model was improved by the addition of new parameters to better control the shape of the S-N curve in both the low and high cycle fatigue regions [120]. As a first attempt, the Basquin model was used to analyze the fatigue life behavior of composites. However, due to the more complex damage mechanisms of composites under fatigue loading, modified models were derived, for example in [121].

Another issue with the fatigue analysis of composite materials was the high standard deviation associated with fatigue life [118, 120]. New models were therefore proposed, that considered the probabilistic nature of fatigue life of composite materials [122-124]. Of particular importance are the differences between assumptions in each model. In a model established by ASTM [122] it is assumed that fatigue life follows a normal distribution at each stress level, whereas in the other models [123, 124] a Weibull distribution is assumed. Three relevant statistical models for this work are briefly explained in Appendix A.11.

Apart from the different models used to obtain a reliable S-N curve for fatigue life analysis of a material or joint, various aspects such as joint design and joining partners may influence the fatigue strength of a joint [116]. Surface pre-treatments are also among the influential parameters affecting fatigue behavior. Several studies have shown that chemical pre-treatments can improve the fatigue life of adhesively bonded metal-metal [125] and metal-polymer [116, 126] joints. Improved adhesion at the interface was reported [116, 126] to positively influence not only the quasi-static strength of the joints, but also their fatigue life. Furthermore, Bland *et al.* [112] investigated the influence of pre-treatments on the wet fatigue behavior of adhesively bonded aluminum joints. Although in wet conditions (a harsher environment), their findings pointed out that PAA pre-treatment with a subsequent primer application had the best fatigue performance followed by stand-alone PAA pre-treatment and SB.

At the time of writing this thesis, the only published data regarding the fatigue behavior of welding-based joining techniques is reported by Balle *et al.* [127] for the ultrasonic welding of aluminum

---

alloy 5754 and carbon-fiber reinforced polyamide (CF-PA66). The aluminum alloy was acid pickled prior to welding. The S-N curve of the joint was presented, although the employed stress ratio ( $R = \text{minimum cyclic stress} / \text{maximum cyclic stress}$ ) was not accurately given. The authors used a power law model to fit the fatigue data and concluded that the fatigue limit was approximately 35% of the respective quasi-static strength for the selected pre-treatment.

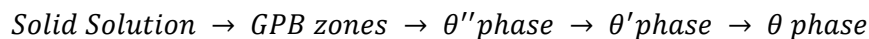
## 3.6 Materials used in this work

### 3.6.1 AA2024-T3

AA2024 is a heat-treatable aluminum alloy from the 2xxx series. The alloy has found application primarily in the aerospace sector, particularly for the fuselage skin of aircraft [128-130]. Cu and Mg are the main alloying elements in AA2024, which increase the mechanical properties of the alloy, especially its strength and toughness [131, 132]. However, the addition of Cu adversely influences the corrosion resistance of AA2024 [132]. Reduced corrosion resistance of AA2024 is mainly due to the formation of Cu-rich secondary strengthening particles, which are precipitated in the grain boundaries [133]. The presence of adjacent regions that are Cu-rich (at grain boundaries) and Cu-depleted (inside the grains) leads to intergranular corrosion in AA2024 [133-135]. Pitting corrosion is another common mechanism occurring in AA2024, which has also been attributed to the presence of Cu-rich secondary particles [133, 136, 137].

AA2024 is an alloy suited to precipitation hardening, whereby formation and precipitation of secondary particles by the aging process provide high mechanical performance to the alloy [131, 138]. For Al-Cu-Mg alloys, two precipitation sequences are generally proposed depending on the Cu to Mg atomic ratio [138, 139]. In the case of a high Cu/Mg ratio, the following sequence was suggested [140, 141]:

The first phase formed from solid solution produces the so called GPB (Guinier-Preston-Bagaryatsky) zones, which are precipitated homogeneously as a coherent phase with the aluminum matrix. As aging proceeds, the GPB zones dissolve to form a semi-coherent  $\theta''$  phase. After further aging, a  $\theta'$  phase starts to nucleate with a platelet shape. Finally, a  $\theta$  phase with the composition  $\text{Al}_2\text{Cu}$ , an incoherent phase with the aluminum matrix, is formed. The sequence of precipitation is summarized as follows:



In 2xxx series alloys with a low Cu/Mg ratio the sequence of precipitation is slightly different [140, 142, 143]. The first phase precipitated from solid solution is the GPB in the same way mentioned above. However, the following phases are named as  $S''$  and  $S'$ . These are metastable phases that are coherent and semi-coherent respectively with the aluminum matrix. The final phase precipitated in the aging sequence is the equilibrium S phase with the composition  $\text{Al}_2\text{CuMg}$ . The precipitation sequence is summarized as follows:

---

*Solid Solution* → *GPB zones* → *S'' phase* → *S' phase* → *S phase*

For AA2024, the formation of S phase ( $\text{Al}_2\text{CuMg}$ ) predominates over the  $\theta$  phase ( $\text{Al}_2\text{Cu}$ ) as reported frequently [144, 145].

Generally, it is accepted that the welding of 2xxx series aluminum alloys is limited in conventional fusion welding processes [146, 147]. Solidification cracking and porosities are among the problems associated with fusion welding of aluminum 2xxx series [148, 149]. Solid-state welding processes, such as friction stir welding (FSW) [150, 151] and FSpW [152] have been successfully used to weld 2xxx series, avoiding the problems associated with the solidification of fusion welding processes.

### 3.6.2 CF-PPS composite laminate

CF-PPS is a high-performance semi-crystalline engineering thermoplastic composite [153-155] with applications mainly in primary and secondary aircraft structures, such as the Airbus A380 wing panels of the pylon forward and the Fokker 50 undercarriage door [155]. The PPS matrix of the composite was discovered by Friedel and Crafts in 1888 [156, 157]. The primary structure of PPS consists of aromatic rings linked to divalent sulfur atoms [153, 156, 158] as illustrated in Figure 3.10. PPS offers a great combination of properties such as good mechanical properties, thermal stability, low moisture absorption and excellent chemical resistance [153, 156, 158, 159].

Since its discovery in 1888, various routes were proposed to synthesize and produce PPS. The most recent process, which allowed the commercialization of PPS production, was patented by the Phillips Petroleum Co. in 1967 [160]. Basically, the process involves polymerization of p-dichlorobenzene and the reaction with sodium sulfide at an elevated temperature and applied pressure [153, 158]. This synthesis route enables linear PPS to be processed [153, 158]. As a result of its market attraction, many companies started to produce neat PPS resin, mainly in the USA, Japan, Germany, and South Korea [158].

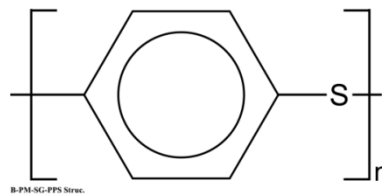


**Figure 3.10 Schematic illustration of the PPS main structure.**

When quenched from the molten state, PPS has an entirely amorphous structure. However, for engineering applications, it is usually cooled slowly to achieve a partial crystalline structure along with an amorphous part [153]. Crystallinity can be further improved by isothermal annealing PPS at temperatures above its glass transition temperature [153]. The crystal structure of PPS has spherulite morphology as shown in Figure 3.11. The spherulites consist of a lamellae structure that is arranged in a spherical shape, growing from a nucleation site in the center [161]. As crystallization time progresses, spherulites start to grow, forming planar boundaries upon contacting each other [161].

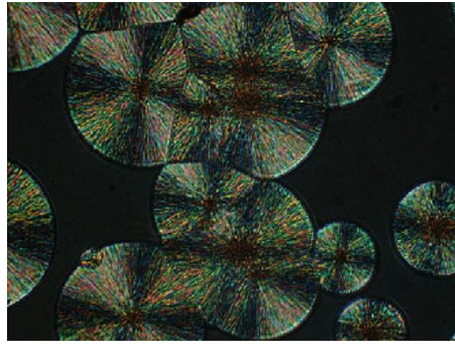


**Figure 3.11 Spherulitic crystal structure of PPS. Adapted from [162].**

It is reported [153, 158, 159] that the glass transition temperature of the amorphous phase of PPS is 85-95°C. In addition, the crystalline fraction of PPS undergoes melting in a temperature range of 280-295°C, depending on the size of the crystals [153, 159, 163, 164]. The morphological aspects and kinetics of crystallization in PPS have been studied extensively. It was shown that PPS has a cold crystallization temperature (crystallization during the heating process) of 120-126.5°C [153, 165, 166]. If PPS is isothermally annealed in this temperature range, the highest crystallinity may be obtained when enough time is given. Furthermore, it was pointed out that carbon fibers (in a PPS matrix composite) [153] with some degree of cross-linking [167] may act as nucleation sites facilitating crystallization of PPS. In another study, Nohara *et al.* [164] illustrated that although the melting temperature of PPS is approximately 285°C, remnant crystals persist up to 340°C. Therefore, a higher temperature than 340°C should be used to completely melt the crystalline structure of PPS. The authors mentioned that the presence of such remnant crystals in a PPS melt can act as nucleation sites during the cooling phase. For more information on the crystallization behavior of the PPS refer to the excellent and extensive review by Spruiell and Janke [153].

In addition to its crystallization, thermal degradation of PPS by thermogravimetric analysis (TGA) has been the focus of several researches. The onset of decomposition temperature for PPS is frequently reported above 500°C, for example in [168]. However, Day and Budgell [169] showed that the thermal degradation of PPS is very sensitive to the heating rate. They concluded that the onset of thermal degradation shifts from 380°C to approximately 490°C when the heating rate changes from 1°C/min to 5°C/min. Therefore, a rapid heating rate delays the thermal degradation of PPS. The kinetics of thermal degradation and weight loss of PPS was also studied [169-171] and showed single stage degradation with a maximum degradation rate above 500°C. By using various analytical techniques, it was shown [170] that the degradation of linear PPS occurs in one stage pyrolysis, consisting of depolymerization, main chain random scission, and carbonization.

Cross-linking is another degradation phenomenon reported for PPS occurring after main chain scission [169]. Cross-linking or branching of molecular chains may increase the molecular weight of PPS and in turn impairs the molecular motion [172]. It was shown that cross-linking leads to a reduction of the melting temperature of thermoplastics such as PPS [173].

CF-PPS possesses very high mechanical performance, making it suitable for engineering structures. However, like any other fiber-reinforced composite, its mechanical properties depend very much on the volume fraction of fibers, the sequence of fiber plies, the orientation of fibers, and the degree of crystallinity of PPS [113]. Deporter and Baird [174] showed that the flexural strength of unidirectional CF-PPS increased with an increase in the degree of crystallinity. Furthermore,

---

temperature has a remarkable influence on the mechanical properties of PPS as pointed out by Vieille *et al.* [175]. The authors investigated various mechanical properties of quasi-isotropic and angle-ply CF-PPS at elevated temperatures. Their findings showed that the tensile strength of the quasi-isotropic samples decreased by approximately 7% when the temperature increased from room temperature to 120°. However, this decrease was 31% in the case of angle-ply specimens. The reduction in mechanical properties was attributed to degradation of the fiber-matrix interfacial bonding. Comparing the fiber stacking and orientation, a higher reduction of tensile strength in the ply-angle samples was related to the matrix-dominated properties of this configuration. Since the properties are more matrix-dependent, reduction of the PPS matrix properties at high temperature influences the composite as well. However, for the quasi-isotropic specimens the properties are fiber-dependent, thus less sensitivity to the temperature increase was observed.

---

# Chapter 4. Friction Spot Joining (FSpJ) Technique

## 4.1 Principles of the process

In the FSpJ process, a non-consumable tool consisting of three parts is used to generate frictional heat. The tool includes a clamping ring, sleeve and pin, which are mounted coaxially and can be moved independently of each other (Figure 4.1). The clamping ring is the external component of the tool that is used to hold the parts to be joined together during the process against a backing bar. The pin and sleeve can move vertically and rotate independently. They produce the required heat as a result of the friction between these parts and the metal.

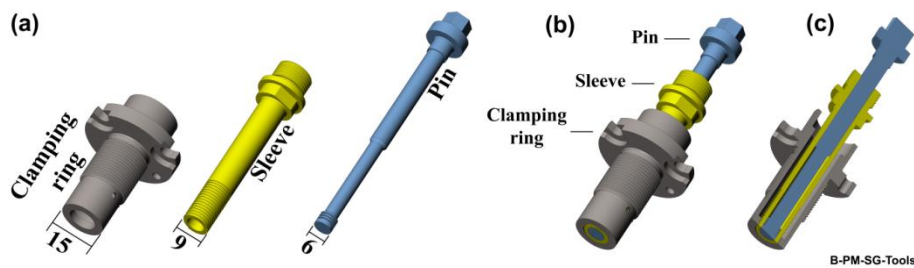


**Figure 4.1** Illustration of the FSpJ tool; (a) consisting of three parts (dimensions in mm), (b) tool parts coaxially mounted together, and (c) cross-section of the tool in the middle plane.

Before the process starts, the sheets to be joined are held together in an overlapping configuration on a sample holder, using a clamping device. The parts are kept clamped during the whole process to avoid any separation of the sheets during the cooling phase. This is due to the large differences in coefficients of thermal expansion and shrinkage behavior of metal and polymer. Next, the tool approaches the top sheet (in this case a metal alloy) and the joining parts are fixed by the clamping ring against a backing bar, through the application of the joining pressure. Figure 4.2 illustrates the configuration of the joining parts before the process starts.

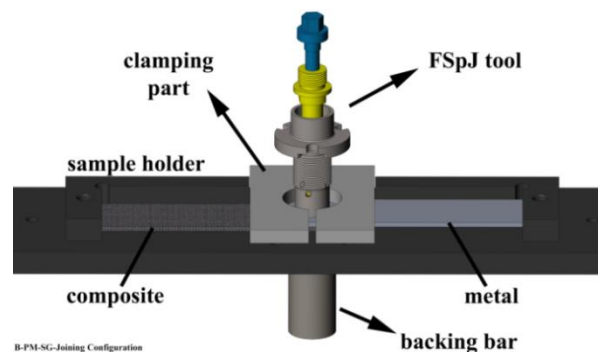


**Figure 4.2** Configuration of the joining parts and the FSpJ tool before the process starts.

The FSpJ process can be divided into three main steps [20]. There are two possible variants for the FSpJ technique: “Pin Plunge” and “Sleeve Plunge” [20]. In the *sleeve plunge variant*, the first step of the process starts when the rotating sleeve plunges into the metallic sheet at a pre-defined

position and the pin retracts upwards. Due to the friction between the rotating sleeve and the metal, the temperature rises locally in a volume around the tool but below the melting point of the metal, this causes local softening and plasticizing of the metal alloy. The plasticized metal alloy flows into the reservoir left behind by retraction of the pin (Figure 4.3-1). As a second step, the pin is pushed against the softened metal to refill the key-hole left in the metallic sheet that was created by the plunging sleeve (Figure 4.3-2). Finally, the tool is retracted and the joint consolidates under cooling and pressure (Figure 4.3-3). Note that the tool only plunges into the metal part to a shallow depth that does not reach the composite interface, to avoid any damage to the load-bearing network of fibers. Figure 4.4 depicts the top view of a sound metal-composite FSp joint.

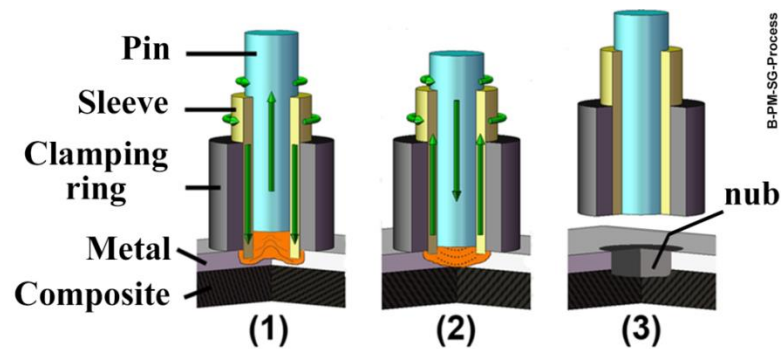


**Figure 4.3** Schematic representation of the FSpJ process steps; (1) the sleeve plunging plasticizes the metal, (2) spot refilling, and (3) joint consolidation. Adapted from [20].

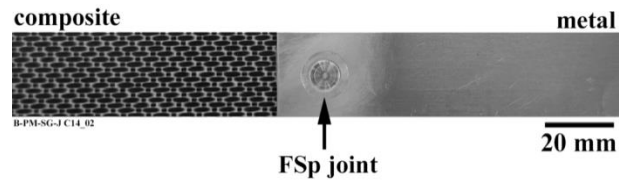


**Figure 4.4** Top view of a sound metal-composite FSp joint.

In the *pin plunge variant*, the pin penetrates into the metal piece while the sleeve is retracted [20]. The other process steps are equivalent to the sleeve plunge variant. As the area of the sleeve is larger than the area of the pin, it can be assumed that in the sleeve plunge variant the bonding area is bigger, resulting from a higher heat input, and hence better mechanical performance will be achieved. The difference between the mechanical performances of the FSp joints based on the two variants is illustrated in Appendix A.1. Due to its superior static mechanical performance, the *sleeve plunge variant* is used throughout this dissertation.

An example of the course of the process is shown graphically in Figure 4.5. The graph plots the motion of the tool (sleeve and pin), by rotational speed and position over time [176]. As shown in the figure, in the first phase, both the sleeve and pin approach the metal surface (position: 0 mm) while their rotational speed (black line) increases to the predefined speed. In the second phase, the sleeve (blue line) plunges into the metal while the pin (red line) retracts upward. The third phase starts with the downward movement of the pin which pushes the plasticized metal back to its original position (position: 0 mm) while the sleeve retracts away from the metal. Both the second and third phases together are considered the joining time during which the rotational speed of the

tool is kept constant. Finally in the fourth phase, the tool (both sleeve and pin) is retracted upward from the surface of the metal, the rotational speed of the tool decreases and the joint consolidates.

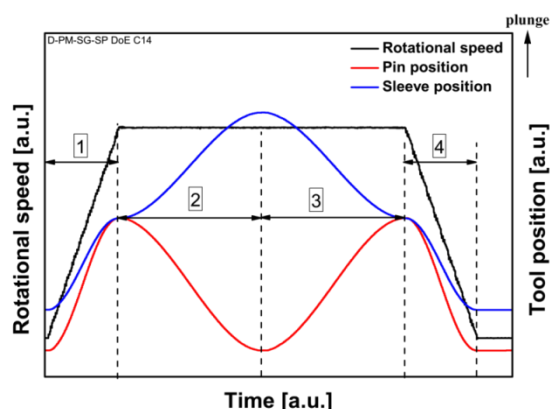


**Figure 4.5** Example of a variation-monitoring diagram showing the FSpJ process phases in the sleeve plunge variant.

The spot formed in an FSp joint consists of three concentric rings. Figure 4.6 illustrates a detailed view of the rings that are related to impressions of the FSpJ tool's parts that are left behind on the metal in the spot area. Figure 4.6 (a) illustrates the top view of the spot area, whereas Figure 4.6 (b) shows its 3D view. The outer ring corresponds to the impression left by the clamping ring, the middle ring is associated with the sleeve, and the inner ring appears as a result of the pin's impression. However, it is not always possible to distinguish the pin and sleeve impressions and one ring is likely observed as a result of materials mixing below the sleeve and the pin as showed in [20].

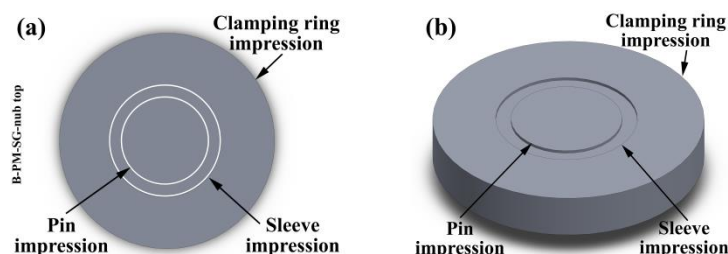


**Figure 4.6** Schematic illustration of the spot area showing the impression of the tool parts on the top surface of the metal; (a) top view and (b) 3D view.

During the joining process, high temperatures around the tool increase the local formability of the metal. For this reason the plasticized metal is deformed by the plunging motion of the sleeve and the pin and it creates a geometrical undercut in the form of a “nub” [20]. As a result of the axial force exerted by the tool, the nub is slightly inserted into the composite and this increases mechanical interlocking between the joining parts. Figure 4.7 shows the cross-section of an FSp joint in the middle of the spot, where the nub is indicated by a black rectangle. A reservoir is created in the center of the nub where the composite is entrapped and accommodated inside. The nub reservoir is also indicated in a 3D graphical view of the spot area in Figure 4.8 (without the composite partner to aid visualization).

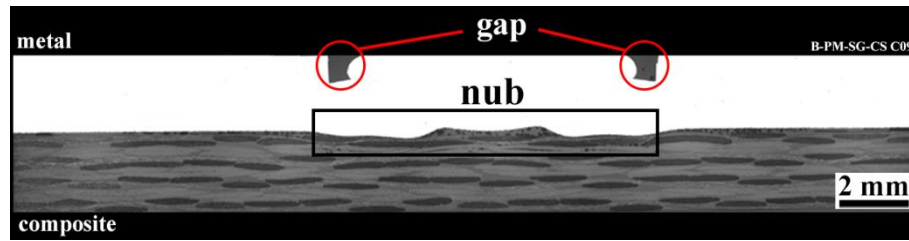


**Figure 4.7** Example of a cross-section of an FSp joint in the middle of the spot. The rectangle indicates the nub, and the red circles show the gap formation below the plunging sleeve. (rotational speed: 2900 rpm, plunge depth: 0.8 mm, joining time: 4 s, joining pressure: 0.3 MPa).

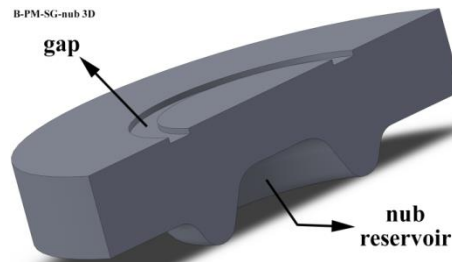


**Figure 4.8** Schematic illustration of the cross-section of the middle of the spot area. A nub reservoir is formed that accommodates the molten polymer. The composite partner is omitted for better visualization.

The shape of the nub depends not only on local formability of the metal at high temperature, but also on the properties of the composite beneath the metal. Generally, the nub is not so pronounced in the case of a continuous fiber-reinforced composite due to high stiffness of the network of fibers. In addition to stiffness of the fiber network, a large volume fraction of continuous fibers in the composite makes it difficult for the metal to displace the fiber bundles and penetrate the composite. In contrast, using an un-reinforced polymer or a composite reinforced with short fibers and lower local stiffness leads to a more noticeable nub. Figure 4.9 shows a cross-section of two FSp joints, comparing the shape of the nub when using (a) continuous fiber-reinforced composite and (b) short fiber-reinforced composite. In both cases the joining parameters, the metal alloy and the matrix of the composites are the same; the only difference is the use of continuous and short fibers. It is clear from these cross-sections that using a less stiff short fiber-reinforced composite leads to a larger nub. This observation was also reported by Amancio *et al.* [20] for FSpJ of magnesium alloy with continuous and short carbon-fiber reinforced composite.

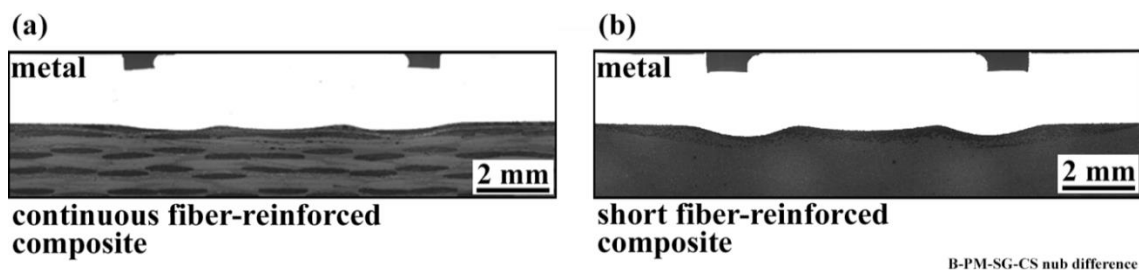


**Figure 4.9** Comparison of the nub shape in case of (a) a continuous fiber-reinforced composite, and (b) a short fiber-reinforced composite. (rotational speed: 1900 rpm, plunge depth: 0.5 mm, joining time: 4 s, joining pressure: 0.2 MPa).

Another feature that can be observed in an FSp joint is the formation of a gap below the sleeve (between the pin and the sleeve impressions), as can be seen in Figure 4.7 and Figure 4.8. The gap is formed on the surface of the metal below the plunging sleeve, because a portion of the metal mass is displaced into the composite at the interface in the nub region. The mass displacement occurs because of the increased local formability of the metal, induced by the high temperature and axial force applied by the tool. This means there is insufficient material to refill the gap completely that is created below the plunging sleeve. It should be noted, however, that the extent of the gap depends very much on the shape of the nub. If the nub is not inserted deeply into the composite, more material is available to refill the gap. Figure 4.10 shows the cross-section of two joints, (a) where the gap is pronounced as a result of large metal mass displacement into the composite, and (b) where there is almost no gap present on the surface of the metal, because less metal is displaced into the composite and the key-hole is completely filled. Red dashed lines in the figure illustrate the mid-plane before joining, *i.e.*, the original level of the metal at the interface with the composite (and outside the nub region). All the white parts under the lines show displaced metal into the composite. Further, the two small bumps (indicated by arrows) in Figure 4.10 (b) that formed at the sides of the nub help the key-hole filling. Usually large tool plunge depth leads to the displacement of more metal mass and hence formation of the gap on the top surface of the metal. In Figure 4.10 (a) a plunge depth of 0.8 mm was used in comparison with Figure 4.10 (b) where the plunge depth was 0.5 mm.

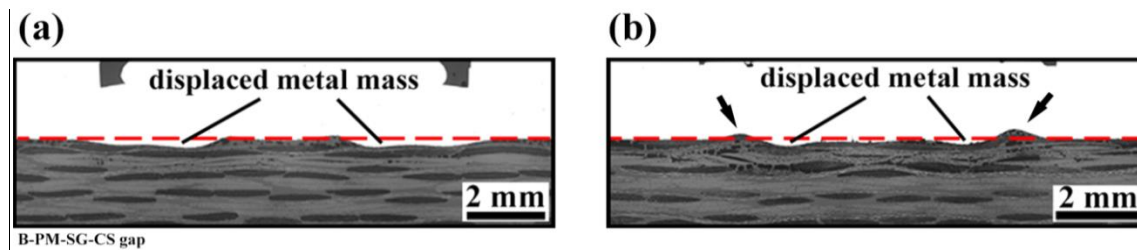


**Figure 4.10 Comparison of the gap formed on the surface of the metal with a plunge depth of (a) 0.8 mm, and (b) 0.5 mm. Other joining parameters were rotational speed: 2900 rpm, joining time: 4 s, and joining pressure: 0.3 MPa. The dashed lines display the mid-plane between metal and composite before the joining process. The arrows in (b) indicate the two bumps helping the keyhole filling.**

In the course of the joining process, the frictional heat generated is transferred from the metal alloy to the composite interface via conduction. Resulting from the very low thermal conductivity of the composite, this heat is accumulated at the interface and leads to a local increase of the temperature. Since the temperature exceeds the melting or glass transition temperature of the composite's matrix, a thin layer of the molten or softened polymer forms in the spot area. A part of the molten layer is squeezed out and flows laterally throughout the overlap region as a result of the axial pressure exerted by the tool. The molten layer is then consolidated under pressure, whereby it induces adhesion forces between the metal and the composite. The total bonding area in the FSpJ corresponds to the outer periphery of the consolidated molten layer, as shown in Figure 4.11. Figure 4.11 (a) depicts the presence of adhesion forces between metal and composite inside the bonding area. A fracture surface of the joint after lap shear testing is also illustrated in Figure 4.11 (b) where the total bonding area is indicated by the dashed circle on the metal part.

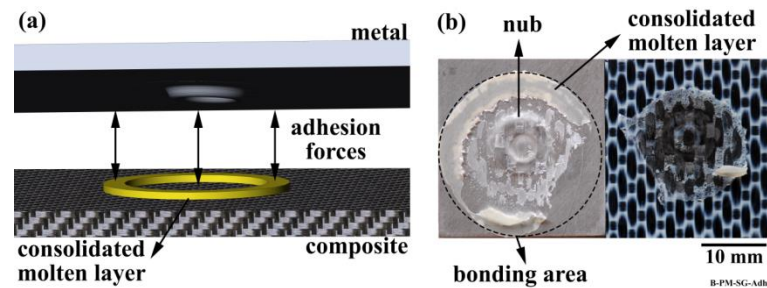


**Figure 4.11 (a) Illustration of the adhesion forces as one of the primary bonding mechanisms in FSpJ, and (b) an example of the fracture surface of an FSp joint tested by lap shear.**

“Mechanical interlocking” and “adhesion forces” are the primary bonding mechanisms in the friction spot joints. Both these bonding mechanisms can be further subdivided. Mechanical interlocking occurs on both the macro and micro levels. Macro-mechanical interlocking is a result of polymer entrapment in the formed nub. Micro-mechanical interlocking may also occur. Surface pre-treatments have been used frequently to increase the surface roughness and to generate pores, crevices, and asperities. Penetration of the molten polymer into such micro-scale metal irregularities leads to the micro-mechanical interlocking phenomenon. Furthermore, with FSpJ some of the fibers in the composite are entrapped by the metal, particularly in and around the nub region where the metal is plasticized and slightly deformed. Fiber entrapment is also classified under the micro-mechanical interlocking category. These aspects of mechanical interlocking in FSpJ will be further discussed in Chapter 7 and Chapter 8. Adhesion forces can also be divided into physical and chemical as discussed in Section 3.2.2. Physical adsorption and bonding (as a result of weak Van der Waals forces) are believed to be present in FSpJ where the molten polymer is in intimate contact with the metal. In addition, strong chemical adsorption and bonding may occur between the molten polymer and the joining parts if the surface of the metal and/or composite is activated by suitable surface pre-treatments. The presence of chemical bonding in FSpJ will be discussed in detail in Chapter 8.

It is also worth mentioning that there are three main differences between FSpJ and FSpW. Firstly, unlike the FSpW of metals and thermoplastics, with FSpJ the tool only plunges to a shallow depth in the metallic part and does not reach the composite. The reason for this is to avoid excessive degradation of the matrix of composite and damage to its network of load bearing fibers. Secondly, with FSpJ the adhesion forces from creation of a molten layer act as one of the main bonding mechanisms. However, atomic diffusion (in metal spot welds) and molecular interdiffusion (in thermoplastic spot welds) are the main mechanisms leading to weld formation. Furthermore, in FSpJ material mixing does not happen due to the huge physicochemical differences of metal and polymer parts, which usually lead to sharp interfaces [84].

## 4.2 Process parameters

Similar to the FSpW of metals [177, 178], there are four primary process parameters in FSpJ [20, 21, 84]: rotational speed (RS) of the plunging sleeve, sleeve plunge depth (PD) into the metal alloy, joining time (JT), and joining pressure (JP). Further important process parameters are: clamping pressure (CP) when the joining parts are clamped to avoid separation in the cooling phase, and cooling rate (CR) at the end of the joining process. The process parameters affect the bonding mechanisms, microstructure, and therefore the mechanical performance of the joints. RS controls

---

the heat input and temperature evolution during the joining cycle. Due to the temperature changes, the local microstructure of the metal part is influenced by the process. Furthermore, the amount of molten polymer generated is directly related to the heat input and hence the RS of the sleeve. In addition, the viscosity of the molten polymer, its rheological behavior as well as the formation and extent of defects in the composite are all temperature-dependent phenomena that are influenced indirectly by RS. JT, which includes sleeve plunging time and retraction time, governs the joining speed. It also contributes to the amount of the heat input into the process and the extent of temperature development around the tool. Similar to RS, the above mentioned temperature-dependent phenomena are also affected by JT. Another important function of RS and JT is to indirectly control the shape of the metallic nub, since the generation of more frictional heat increases the local formability of the metal. PD of the sleeve has a forging function and is mainly responsible for the shape and inserted depth of the nub into the composite. Higher PD usually leads to a deeper indentation of the deformed metal into the composite, thus better macro-mechanical interlocking between the parts, as we reported recently in our manuscript [21]. JP is a parameter with the main function of controlling the flow of the molten polymer. An exerted axial force on the spot area as a result of the applied joining pressure influences the lateral flow of molten polymer. The combination of heat input and JP influences the flow and the bonding area as explained in [176]. In addition, an intimate contact between the molten polymer and the metal at the interface depends on the applied JP. This is especially important when the surface of the metal is rough, for instance resulting from surface pre-treatment. Complete filling of asperities in the metal surface by the molten polymer by applied JP leads to an increase in micro-mechanical interlocking and hence mechanical performance of the joints.

CP is required during and after the joining cycle to avoid separation of the joining parts. However, a very high CP may hinder lateral flow of the molten polymer and thus decrease the total bonding area. CR is another parameter that influences the joint's characteristics. The cooling phase starts after retraction of the tool by blowing pressurized air onto the joining area. CR can influence the crystalline state of the molten polymer in cases of semi-crystalline thermoplastics. A very high CR may reduce the crystallinity of the molten polymer or even turn it into an amorphous state, so affecting the local mechanical properties of this layer. Generated volumetric defects may be also influenced by the CR, since a lower CR gives more time for the entrapped air to escape the molten layer leading to a reduction of defects. Table 4.1 summarizes FSpJ joining parameters and their respective functions.

---

**Table 4.1 Controllable FSpJ process parameters and their respective functions.**

Joining parameter	Symbol	Function
Rotational speed	RS	Influences heat input and temperature evolution, shape of the nub, microstructural changes in metal and composite, formation of defects.
Plunge depth	PD	Controls shape of the nub and its inserted depth into the composite.
Joining time	JT	Controls the joining speed, extent of temperature development around the tool.
Joining Pressure	JP	Governs the type of molten polymer flow.
Clamping pressure	CP	Controls a firm contact between the joining parts and hinders their separation during the cooling phase.
Cooling rate	CR	Influences crystallinity of semi-crystalline composites as well as the formation of volumetric defects.

### 4.3 Defects in FSpJ

In welding-based joining techniques, where high temperatures and melting of the thermoplastic matrix are involved, defects may be introduced into the joining area. In FSpJ, two main types of defect could be detected [20, 21, 84, 179].

The first type of defect is related to a de-consolidation phenomenon, which is also reported in the literature as a major defect occurring in the welding of thermoplastics. In FSpJ, two types of de-consolidation may occur: firstly, generation of voids and porosity in the consolidated molten layer, especially adjacent to the interface with the metal (Figure 4.12 (a)); and secondly, fiber-matrix debonding (Figure 4.12 (b)). Voids are thought to be formed as a result of air entrapment in the molten polymer during consolidation. Since the temperature during the joining cycle is relatively high, the viscosity of the molten polymer reduces and air can become entrapped in the molten layer. During the consolidation phase, when the cooling rate is extremely fast this entrapped air cannot escape from the molten layer and this leaves voids of air pockets after consolidation. To reduce the amount of de-consolidation voids, sufficient pressure should be applied during the joining process [180], otherwise the coalescence and growth of volumetric voids can occur. In addition to air entrapment, examples of other phenomena that may cause volumetric flaws in a joint are polymer thermal degradation and the evolution of structural or absorbed water [181]. The formation of voids as a result of thermal degradation and decomposition is especially reported in the laser-based joining of thermoplastics and metal-polymer systems [61, 62, 182-184] as a result of the very high concentration of temperature. The second type of de-consolidation defect, fiber-matrix debonding, occurs because the coefficient of thermal expansion and the shrinkage behavior of the fibers and thermoplastic matrix are immense. In addition, the squeeze flow of the low viscosity molten polymer leads to a mass displacement from the central region of the spot joint that may further the generation of voids as well as the debonding phenomenon. Another reason for de-consolidation defects may be thermoplastic degradation. As the process temperature is high, a part of the thermoplastic matrix can undergo thermal degradation. However, thermal degradation is unlikely to happen due to the very short joining cycle.

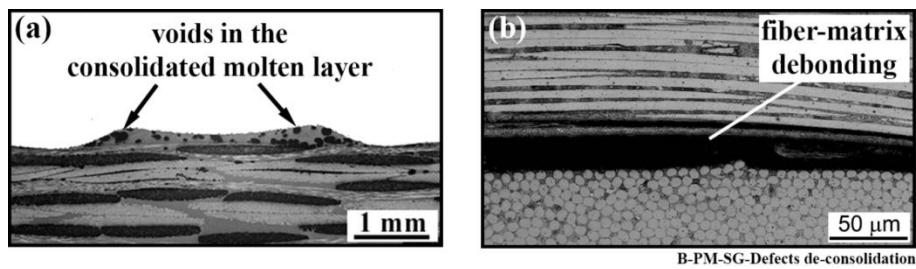


**Figure 4.12 De-consolidation defects in the composite with FSpJ, showing (a) voids in the consolidated molten layer, and (b) fiber-matrix debonding.**

In addition to the above mentioned causes that lead to the generation of de-consolidation defects, there are other phenomena that should be considered as well. In the production of fiber-reinforced composite laminates a relatively high consolidation pressure is used to process the laminate and pack the fiber bundles. Such pressure generates elastic energy in the fiber bundles [185]. During the joining process, as the viscosity of the polymer matrix decreases, the stored elastic energy is released; thereby potentially inducing de-consolidation and void growth. Furthermore, generation of inhomogeneous thermal stresses is an important phenomenon that leads to defect formation, especially in semi-crystalline thermoplastic composites [186]. The cooling rate has an opposite effect on the generation of residual thermal stresses in crystalline and amorphous phases [187]. This leads to different shrinkage behaviors of the two phases, which in turn may facilitate defect generation.

The second type of defect we reported for FSpJ [21, 188] is known as a broken stir zone (BSZ). A part of the metal below the tool in the center of the spot joint breaks off and becomes detached. The broken metal remains attached to the retracted pin and is removed from the joining area as can be seen in Figure 4.13. As the broken part is removed from the stir zone in the metal, this defect is termed a broken stir zone.

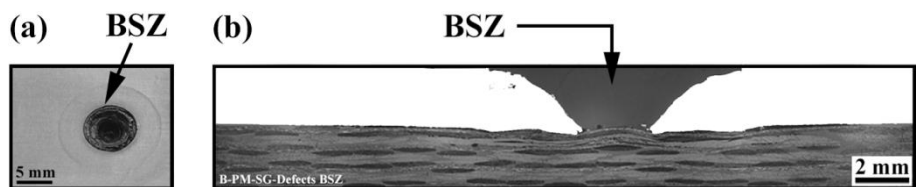


**Figure 4.13 Illustration of a broken stir zone (BSZ) that occurs in the metal part; (a) top view of the metal part, and (b) cross-section of the joint in (a) at the center of the spot. (rotational speed: 2900 rpm, plunge depth: 0.8 mm, joining time: 8 s, joining pressure: 0.3 MPa).**

The causes of a BSZ are explained [21, 188] as due to excessive formability of the metal and tool plunge depth, as can be seen illustratively in Figure 4.14. Excessive heat input increases the local formability of the metal under the sleeve and the pin. In addition, the local strength of the metal is reduced, due to the high temperature around the tool [21, 176]. It is known that the strength and toughness of metals (such as aluminum) are reduced by increasing the temperature [189, 190]. When the sleeve plunges excessively into the metal piece, the thickness of the metal below the sleeve is reduced enormously, as indicated in Figure 4.14 (a). This combination of high temperature and low thickness reduces the local strength of the softened metal. As well the local stiffness of the composite below the tool is reduced as a result of the formation of molten polymer and so it cannot support the plasticized metal to bear the applied pressure of the plunging sleeve. Therefore, the load

imposed by the plunging sleeve exceeds the local strength of the metal, leading to an initiation of cracks, as indicated in Figure 4.14 (b). Crack initiation is considered to be related to: (1) the reduction of the metal's local strength, (2) reduction of the metal's thickness under the sleeve, (3) reduced local stiffness of the composite, and (4) stress concentration at the interface of metal and molten polymer below the sleeve. The cracks that are initiated start to propagate in the direction of the tool at the interface between the plasticized and un-plasticized metal as the pin pushes the displaced softened metal downwards to the original metal surface as shown in Figure 4.14 (c). Eventually, a piece of metal is removed and remains attached to the tool after retraction (Figure 4.14 (d)). The composite under the BSZ is thereby exposed to environmental conditions, which may further deteriorate the mechanical properties of the joint.

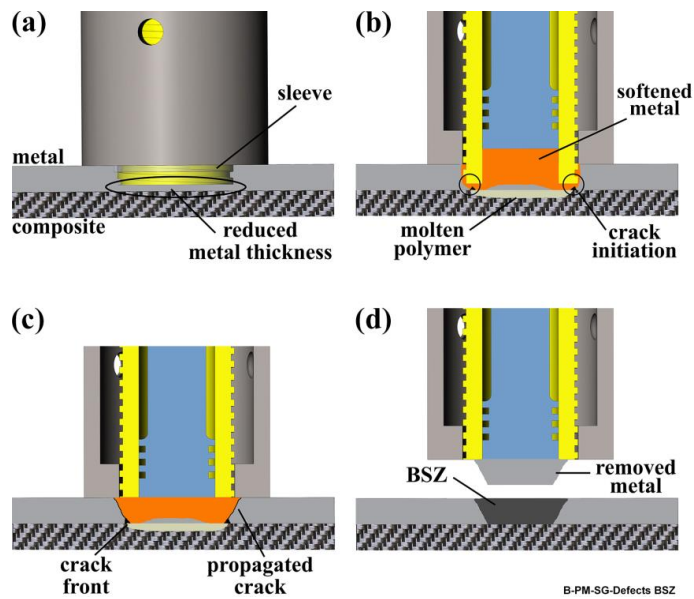


**Figure 4.14 Mechanism of the BSZ formation; (a) excessive sleeve plunge, (b) initiation of micro-cracks in the metal, (c) propagation of the crack, and (d) formation of the BSZ.**

#### 4.4 Advantages, limitations, and potential applications

The main advantages of FSpJ are listed below:

- a) **Short joining cycles:** the joining time in FSpJ varies between 2 s to 8 s depending on the metal alloy and the polymer or composite in use [20], which is much faster than state-of-the-art adhesive bonding.
- b) **Weight saving:** because in FSpJ no obligatory use of additional material (such as fillers or rivets) is necessary to that of the joining parts, no additional weight is added to the structure.
- c) **No drilling:** unlike traditional mechanical fastening techniques, there is no need to pre-drill a hole with FSpJ. This is especially important in cases of continuous fiber-reinforced composites, because these materials are highly susceptible to cracking as a result of drilling, which deteriorates their local mechanical strength leading to premature failure of the joint.
- d) **Environmentally sound:** the process is green, environmentally friendly, because there are no emissions generated during or after the joining cycle [20].

- 
- e) Reparability: since thermoplastics (as one of the joining parts) can withstand being re-melted and solidified several times, the joints may be repaired on the same spot (a preliminary result is given in Appendix A.2).
  - f) Recyclability: the joints can be recycled by separating the joining parts. The joint can be heated above the melting temperature of the thermoplastic, to separate the metal from the composite.
  - g) Joining over sealant: in real life applications, joints are normally sealed against corrosion and environmental effects. If joining can be performed over a pre-applied sealant (e.g. by the addition of a film interlayer as we have shown in [188]), the time and required effort for post application of sealant is reduced.
  - h) Low cost machinery: the equipment required for production use of FSpJ is the same as the available FSpW machine and no further alteration or adaptation is required [20].

Besides the main advantages that FSpJ offers, there are several limitations of the process as follows:

- a) Joint geometry: only overlap configuration joints can be produced with FSpJ [20].
- b) Disassembling: since the joining parts are physically and chemically bonded, there is no possibility of disassembling and reassembling the joints.
- c) Low torsion and peeling strength: similar to adhesive bonding, FSp joints are mainly capable of bearing a shear loading, but the torsion and peeling strengths of the joints are relatively low.
- d) Thickness of metal sheet: due to local mechanical deformation of the metal (nub area) and the possibility of defective joint formation (BSZ as explained in Section 4.3), thin metallic sheets (less than one millimeter for engineering aluminum alloys) cannot be FSp joined with present knowledge.

Weight saving is a major issue in transportation vehicles so there is an increasing tendency to use the benefits of thermoplastic composites and lightweight metal alloys in engineering structures. For this reason, FSpJ may be seen as a potential technology for transportation, particularly in the aerospace and automotive industries, for joining metal-composite hybrid structures.

Figure 4.15 illustrates an example of a potential metal-composite hybrid fuselage in an aircraft where the parts could be joined by advanced friction-based joining technologies. Figure 4.15 (a) shows the inside overview of a presumptive overlapped metal-composite skin structure stiffened by both metallic and composite stringers. The outside view of the hybrid skin can be seen in Figure 4.15 (b) where FSpJ could be used to join the two overlapped parts of the skin. Furthermore, the metallic stringers, which are used as stiffeners for the skin, are the other potential areas for FSpJ use. Mechanical fastening is the dominant method in joining skin-stringer parts [191, 192], which indeed increases the weight of the structure by the use of rivets. As can be seen from Figure 4.15 (c) some of these fasteners may be replaced by FSpJ. A combination of FSpJ and mechanical fastening can give the required mechanical strength, leading to a reliable structure and at the same time saving weight in the whole structure tremendously. The risk of the crack initiation may also be reduced as a result of less drilling required on the composite, further leading to a safer structure and increasing the flexibility of designing new generation aircrafts.

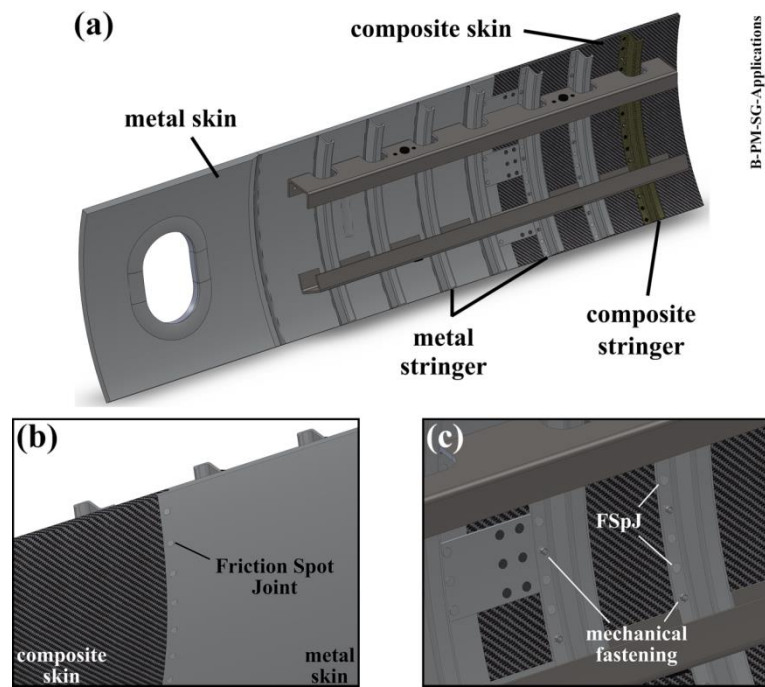


**Figure 4.15** Schematic illustration of potential FSpJ applications; (a) in the aircraft structure, to join (b) a metal skin to a composite skin, and (c) a metal stringer to the composite skin.

---

## Chapter 5. Experimental Approach

The experimental approach of this PhD can be divided into six main phases. In the first phase of the project, the feasibility of FSpJ for the selected joining parts, AA2024-T3 and CF-PPS, was evaluated. Further, a window of variation ranges of process parameters, RS, PD, JT, and JP, was established, based on the mechanical performance of the SLS joints. A one-factor-at-a-time (OFAT) approach was chosen to study the influence of individual process parameters on the SLS strength of the joints and to reduce the range of variation for each parameter. The results of this phase are not included in the thesis.

After defining the range of process parameters, the FSpJ process was optimized for the selected joining parts in the second phase of the work. For process optimization, statistical analysis based on the full-factorial design of experiments (DoE) and analysis of variance (ANOVA) were employed. The influence of individual process parameters and their interactions on the bonding area and the SLS strength of the joints were studied. An optimized set of parameters was obtained through this study, to increase the mechanical performance of the SLS joints. The optimized joining condition was used from phase four to phase seven of this work. The results of this optimization process are briefly presented in Section 7.1. However, that was not the focus of this thesis. For further information and discussion refer to [176].

In the third phase of the work, a detailed analysis of the joints was carried out. This involved a thorough investigation into the bonding mechanisms, understanding the process-related physicochemical changes in the composite, analysis of the joint microstructure, investigation of local and global mechanical properties, and analysis of joint failure and fracture. A wide range of analytical techniques were used to investigate the above mentioned aspects of FSpJ. These included light optical microscopy (LOM), SEM, thermal analysis (differential scanning calorimetry - DSC and TGA), microhardness, and nanoindentation. Two joining conditions were selected for comparison purposes in this phase, which are mentioned later in the Results and Discussion Chapters.

In the fourth phase of the project, the influence of a wide range of aluminum surface pre-treatments on the surface features of the aluminum, interfacial bonding mechanisms, mechanical performance of the joints, and the failure mechanisms was investigated. Mainly SEM, EDS, XPS and mechanical testing were used for this purpose, to evaluate the influence of aluminum surface pre-treatments. Based on the results obtained in this work, four aluminum surface pre-treatments were selected for the fifth and sixth phases.

In the fifth phase of the work, the durability behavior of the FSp joints under a harsh environment, known as accelerated aging, was studied. Four surface pre-treatments were selected from the previous phase. The effects of the accelerated aging condition on the surface features, mechanical performance of the SLS joints, and failure and fracture surfaces were investigated using SEM, EDS, and XPS.

In the sixth phase, the behavior of the FSp joint under cyclic loading was studied. In this phase also four aluminum surface pre-treatments from phase four were used to perform the fatigue experiments. A fatigue life analysis (S-N curve) of the joints was carried out considering three

different fitting procedures to propose the best fitting model for the obtained experimental data. The failure mechanisms of the joints under cyclic loading were briefly investigated in this phase using SEM.

Based on the results and knowledge obtained from the various phases of this work, FSpJ can be proposed as an alternative metal-polymer joining technology. Figure 5.1 illustrates the experimental approach of this PhD.

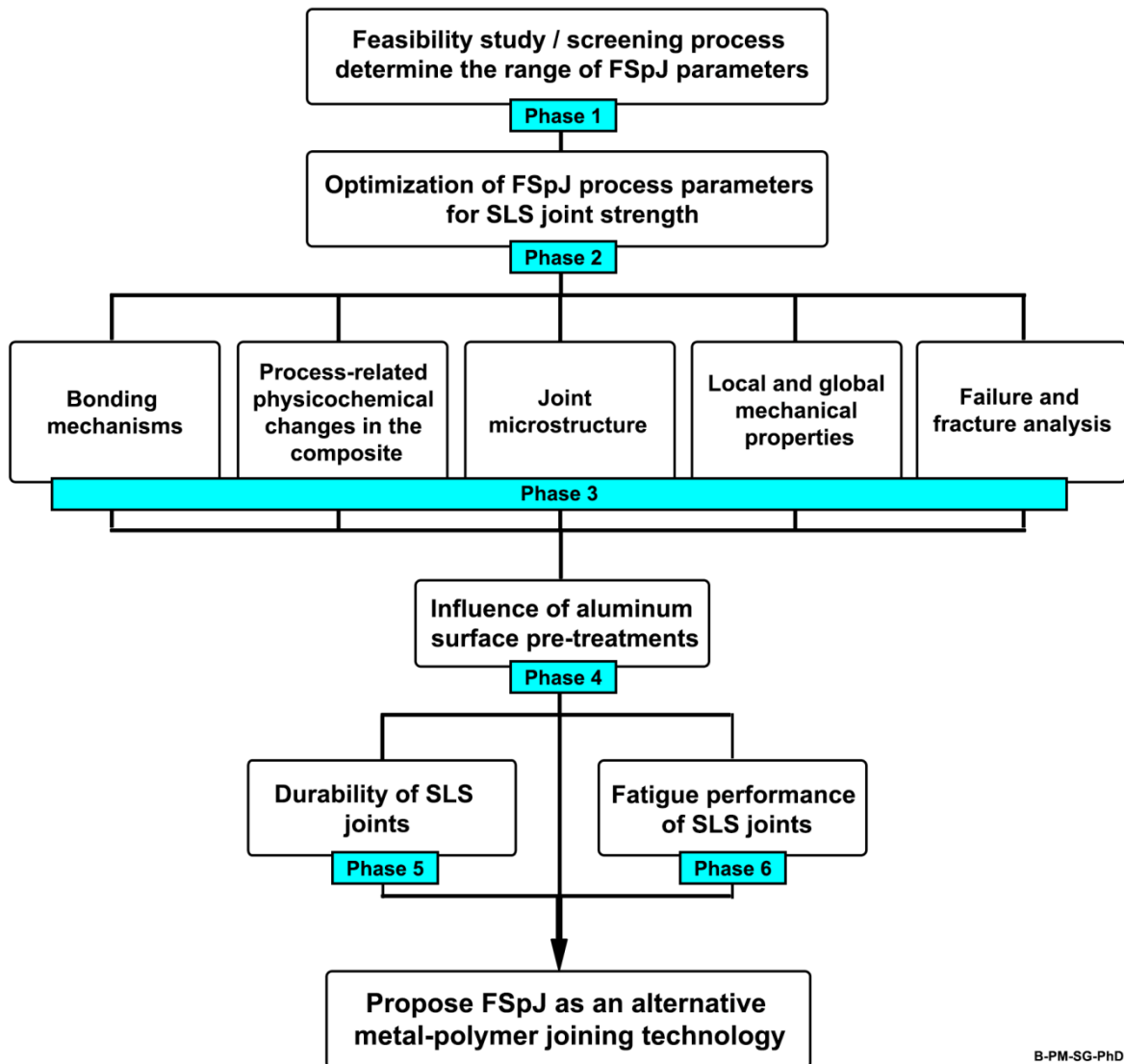


Figure 5.1 Schematic illustration of the experimental approach of this PhD project.

---

# Chapter 6. Materials, Equipment, and Methods

## 6.1 Base materials

### 6.1.1 AA2024-T3 rolled sheets

Rolled sheets of aluminum alloy AA2024-T3 with a thickness of 2 mm (supplied by Constellium, France) were used as the metallic partner for FSpJ throughout this work. This alloy is mainly used in the primary structures of aircraft. AA2024 is an alloy suited to precipitation hardening with Cu and Mg as its main alloying elements. Heat treatment (T3) leads to the formation of strengthening phases such as  $Al_2CuMg$  and  $CuAl_2$ , which give rise to the high strength of this alloy [128]. The alloy exhibits a high strength to weight ratio, good fatigue resistance and damage tolerance, high fracture toughness, as well as good formability [149]. Table 6.1 lists the nominal chemical composition of the AA2024-T3 alloy used in this work, which was determined by chemical analysis. The main mechanical and physical properties of the alloy are also given in Table 6.2.

**Table 6.1 Nominal chemical composition of AA2024-T3 used in this work.**

Element	Si	Fe	Cu	Mn	Mg	Cr	Zn	Ti	Al
Wt%	0.1	0.17	4.55	0.45	1.49	<0.01	0.16	0.021	Bal.

**Table 6.2 Selected mechanical and physical properties of the AA2024-T3 used in this work.**

Tensile strength (direction TL) [MPa]	Yield strength (direction TL) [MPa]	Elongation [%]	Melting onset [°C]	Thermal conductivity [ $Wm^{-1}K^{-1}$ ]	Coefficient of thermal expansion within 20-300°C [ $K^{-1}$ ]
437*	299*	21*	502**	121**	24.7**

\* Experimentally evaluated in this work.

\*\* Data obtained from [149].

Figure 6.1 shows the microstructure of the alloy in longitudinal (L), transverse (T) and surface view with respect to the rolling direction. It is possible to observe more elongated grains in the longitudinal direction in contrast with the equiaxed grains of the transverse direction and surface view. Black spots are visible in the microstructure in all directions. These are secondary hardening particles as a result of the formation of  $Al_2CuMg$  and  $CuAl_2$  phases in AA2024-T3 [139, 140, 143].

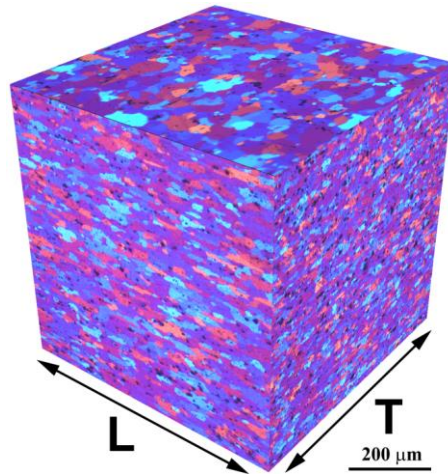


**Figure 6.1** Microstructure of AA2024-T3 in longitudinal (L) and transverse (T) directions according to the alloy rolling direction, as well as the surface view (Barker etched, magnification 50X).

### 6.1.2 CF-PPS

CF-PPS with a 2.17 mm nominal thickness consisting of 5 harness-woven quasi-isotropic laminates (supplied by TenCate, the Netherlands) with 50 vol% fibers (42 wt% fibers) was used as the composite partner for FSpJ. The composite consists of 7 plies of carbon fibers in the following sequence:  $[(0,90)/(\pm 45)]_3/(0,90)$ . CF-PPS is considered a high-performance semi-crystalline thermoplastic composite that is mainly used in primary and secondary aircraft parts, because of its high strength, rigidity, chemical resistance and low water absorption [153-155]. Table 6.3 lists the main mechanical and physical characteristics of the CF-PPS used in this work.

**Table 6.3** Selected mechanical and physical properties of the CF-PPS used in this work.

Tensile strength (warp) [MPa]	In-plane shear strength [MPa]	Glass transition temperature [°C]	Melting temperature [°C]	Thermal conductivity [ $\text{Wm}^{-1}\text{K}^{-1}$ ]	Coefficient of thermal expansion within 23-300°C [ $\text{K}^{-1}$ ]
580*	119**	85*	285*	0.19**	52.2**

\* Experimentally evaluated in this work.

\*\* Data obtained from supplier's datasheet [193].

Figure 6.2 illustrates the microstructure of the composite in the warp direction ( $0^\circ$  oriented fibers). Weft fibers ( $90^\circ$  oriented fibers) and  $\pm 45^\circ$  oriented fibers are visible in between the warp fibers in the figure.

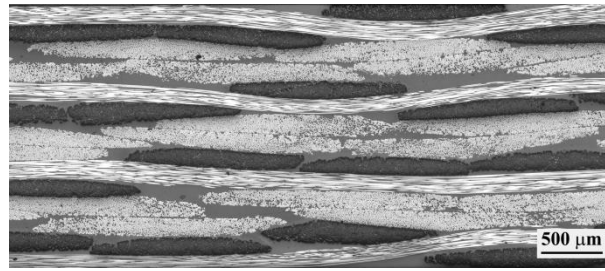


Figure 6.2 Microstructure of CF-PPS in the warp direction, showing fibers in  $0^\circ$ ,  $90^\circ$ , and  $\pm 45^\circ$ .

## 6.2 FSpJ equipment

The equipment used to produce FSp joints was a displacement-controlled machine (RPS100, Harms & Wende GmbH, Germany) at Helmholtz-Zentrum Geesthacht. The machine was originally manufactured for the FSpW of metals such as aluminum and magnesium. One of the advantages of the FSpJ process is that the same FSpW equipment already available in the market can be readily used without the need for any modifications. The equipment consists of a welding head, in which the FSpJ tool is assembled, and a pneumatic piston that applies the joining pressure against the FSpJ tool. The design of the RPS100 equipment is such that the welding head is fixed and the pneumatic piston applies the joining pressure from below. The piston moves up and down vertically to apply and release the joining pressure. A welding table is used to place the joining parts or a sample holder on. A switch cabinet is attached to the equipment as the main electrical unit to control the rotation and movement of the FSpJ tool parts. Figure 6.3 depicts various features of the RPS100 FSpW/J equipment.

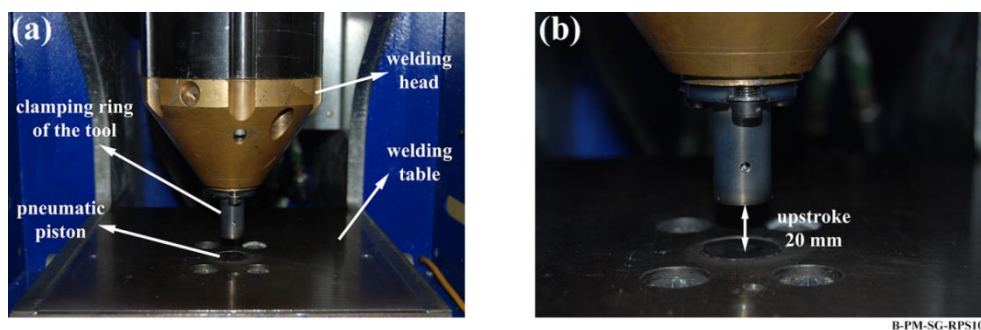


Figure 6.3 (a) A photo of the RPS100 welding head, the assembled tool, welding table, the pneumatic piston, and (b) a magnified image of the welding head and table showing the limited upstroke in the equipment.

The machine is capable of applying the tool's rotational speed in the range 500-3300 rpm. In addition, the upstroke (in the z-axis) of 20 mm provides a limited space to join thick specimens. The specimen can be cooled down after the joining process by blowing a pressurized air stream and the airflow can be controlled. Although the equipment is supplied with sensors that make it possible to control and evaluate the FSpJ tool position and rotational speed during the process, it is not capable of giving additional information on the joining force and applied torque, which is a limitation of the equipment RPS100. Newer releases of the joining equipment are available with force and torque monitoring systems.

---

## 6.3 Methods

### 6.3.1 Joining procedure

Prior to the joining process, the composite parts were cleaned in an acetone ultrasonic bath for 3 minutes and dried in air. The aluminum parts were wiped with acetone to remove loose surface contaminations. In addition, some of the aluminum specimens were pre-treated with a variety of procedures. These are explained in detail in Section 6.3.8. After cleaning the specimen, the aluminum part was placed above the composite in an overlap configuration against the sample holder. The joining parts were clamped together during and after the joining cycle, to ensure an intimate contact and to avoid separation of the parts during the cooling phase due to the differing coefficients of thermal expansion of the selected materials. The configuration of the FSpJ tool, joining parts, sample holder, and the clamping part was illustrated in Figure 4.2 (Page 26). Joining parameters (RS, PD, JT, JP) were set in the control unit of the RPS100 and then the joining process was started manually. At the end of the joining process, an experimental consolidation time (intentionally extended to times above the minimum time required for polymer consolidation, to ensure the complete absence of differential contraction) of one minute was selected for the joining conditions. During the consolidation time pressurized air (flow rate: 22.9 l/min) was blown continuously over the joint. Finally, the joint was removed from the clamping system for further analysis.

### 6.3.2 Temperature measurement

Temperature development during the FSpJ process was monitored by thermometry and infrared (IR) thermography. Chromium-nickel type K thermocouples (TC) (with a diameter of 0.7 mm) were used for thermometry, to measure the local temperature in the aluminum part as well as at the interface. Holes of 0.8 mm were drilled at the required positions to set up the thermocouples. A data acquisition system connected to the thermocouples was used to collect the measured data at the rate of 50 Hz. Figure 6.4 schematically shows the position of the three thermocouples used in this work.

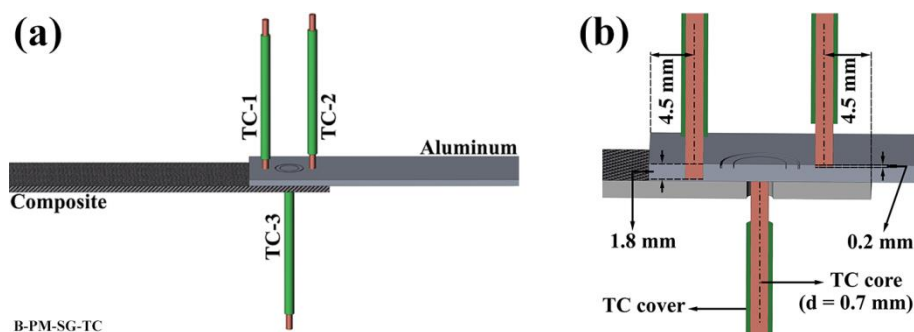


**Figure 6.4 Schematic presentation of the position of thermocouples to measure the local temperature of the aluminum (TC-1 and TC-2) and interface (TC-3); (a) 3-D view, and (b) magnified cross-section showing the exact position of each thermocouple.**

TC-1 and TC-2 were placed at 1.8 mm and 0.2 mm respective depths in the aluminum part, 4.5 mm away from the overlap edges (i.e. 0.5 mm away from the clamping ring's outer diameter). These thermocouples were used to measure the local temperature of the aluminum close to the interface

(TC-1) and surface (TC-2) to be able to later interpret aluminum microstructural changes at different positions due to temperature variation. The third thermocouple was placed within the CF-PPS in the interface with the aluminum at the center of the spot. As the center of the spot is believed to experience the highest temperatures during the joining process, TC-3 gives the highest possible temperature achieved by the PPS molten layer.

Since the thermocouples are only capable of measuring the temperature locally and not over a wider area, an infrared thermographic camera (VarioTHERM, Jenoptik, Germany) was also used to monitor temperature changes on the surface of the aluminum during the joining cycle. The monitoring process was carried out in the range of 150 to 700°C with a resolution of  $256 \times 256$  pixels at 50 Hz. Figure 6.5 (a) illustrates the position of the infrared camera in relation to the joining parts. The camera was inclined approximately  $15^\circ$  both in x and z directions to be able to capture the temperature on the aluminum surface through the whole bonding area. Moreover, Figure 6.5 (b) illustrates the measurement set up and the position where the temperature was captured on the surface of the aluminum. This figure also shows a snapshot of a thermograph in which the measurement area is indicated. The peak temperature in the selected area was reported as the process temperature. Prior to capturing the temperature, the aluminum parts were painted with black paint to reduce any measurement errors as a result of the light reflection.

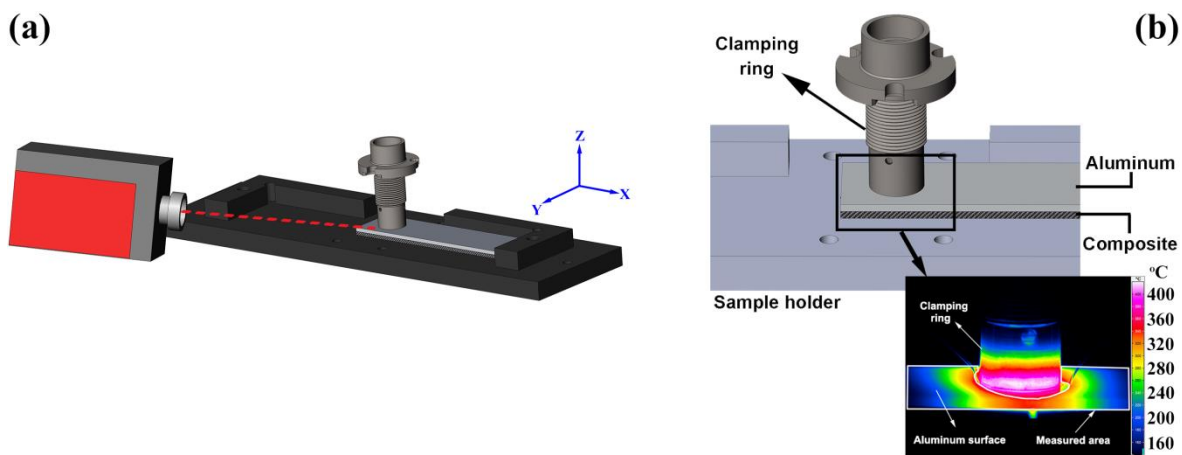


**Figure 6.5** Schematic illustration of temperature measurement by IR-thermography; (a) showing the position of the IR-camera, and (b) an example of a snapshot from the peak temperature on the aluminum surface during FSpJ. The area used to measure the temperature is indicated in the snapshot.

### 6.3.3 Microstructural analysis

To analyze the microstructure of the base materials and joints as well as the fracture surfaces of the joints after mechanical testing, light optical microscopy (LOM) and scanning electron microscopy (SEM) were employed. LOM (DM IR microscope, Leica, Germany) was used mainly to characterize the microstructure of the base materials. In addition, the cross-section of the joints at the center of the spot joint was analyzed by LOM, to reveal the joint's microstructure. Standard materialography procedures were followed to prepare the samples for LOM. The joints were cut in the middle of the spot and embedded in cold resin. The embedded specimens were ground and polished following standard procedures to obtain a smooth surface suitable for LOM. Similar procedures were followed to prepare the base materials for analysis. In order to reveal the

---

microstructure of the aluminum in the base material and joints, electrochemical etching (30 V, 120 s, room temperature) in Barker solution (200 ml water and 5 ml fluoroboric acid) was carried out.

In order to characterize features of the aluminum surface after various surface pre-treatments, and to analyze the joint fracture surfaces SEM (Quanta<sup>TM</sup> FEG 650 equipment) was used. In the case of aluminum surface analysis, a voltage of 10 kV, spot size of 3 and a working distance of 10 mm were used. For fracture surfaces, a voltage of 5 kV, spot size of 3 and a working distance of 15 mm were set. Before analyzing non-conductive samples (e.g., all the fracture surfaces) their surfaces were gold sputtered using a Q150R ES equipment (Quorum Technologies Ltd., England) for 30 s with a current of 65 mA. A very thin layer of gold (a few nm in thickness) makes the samples conductive and facilitates their imaging without hiding any small features of their surfaces.

Besides LOM and SEM, laser scanning confocal microscopy (LSCM) (VK-9700, Keyence, Japan) was used as a non-contact method to analyze the roughness of the aluminum surfaces after various surface pre-treatments. For this purpose a 20X magnifying lens was set. Average surface roughness parameters were calculated from 5 different samples; six regions were selected on each sample to measure the surface roughness. The average of these 30 measurements (6 areas on 5 samples) was taken as the surface roughness of each specimen. Two parameters were selected to analyze the surface roughness of the specimens;  $R_a$  (arithmetic mean value), which shows the mean deviation from the mean line, and  $R_z$  (highest peak to lowest valley distance). Figure 6.6 illustrates  $R_a$  and  $R_z$ .

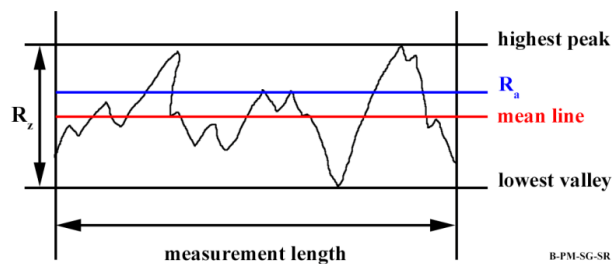


**Figure 6.6 Schematic illustration of the surface roughness features and parameters.**

## **6.3.4 Chemical composition**

### **6.3.4.1 Energy dispersive X-ray spectroscopy (EDS)**

EDS coupled with SEM was carried out to obtain chemical information from the bulk of the specimens for the base materials and the fracture surface of the joints. To obtain and analyze the EDS spectra an EDAX TEAM<sup>TM</sup> software V4.0.2 was used. Both spot and area analysis were used to characterize small features and larger areas respectively. All EDS spectra were taken with a voltage of 10 kV, spot size of 3, at working distance of 10 mm. For the non-conductive specimens gold sputtering was performed prior to EDS experiments. For those specimens a gold peak is thereby always present in the respective spectra.

### **6.3.4.2 X-ray photoelectron spectroscopy (XPS)**

XPS was carried out using a Kratos DLD Ultra Spectrometer with an Al-K $\alpha$  X-ray source (monochromator) operated at 225 W. For the survey spectra a pass-energy (PE) of 160 eV was

---

used, while for the region scans PE was 40 eV. The spectra of clean surfaces (contamination from environment removed) were calibrated to 284.8 eV binding energy of the C1s signal. For all the samples a charge neutralization was necessary. The processing and mathematical treatment were carried out using CasaXPS V.2.3.16 software. For deconvolution of the region files, background subtraction was performed before calculation. Smoothing of the data in region files was carried out for low signal-to-noise ratios. Depth profiling was carried out using argon sputtering with a beam energy of 3.8 keV and a current density of 120  $\mu\text{A}/\text{cm}^2$ . The etching rate was calibrated to 10 nm/min using  $\text{Ta}_2\text{O}_5$ .

### 6.3.5 Thermal analysis (DSC and TGA)

Thermal analysis of the composite part in the FSp joints was carried out in order to evaluate the local physicochemical changes in the composite as a result of the FSpJ process. The composite base material was also characterized as a reference for comparison with the composite in the joints. Differential scanning calorimetry (DSC) and thermogravimetry (TG) were performed using Netsch DSC 200 F3 Maia® and TG 209 F3 Tarsus® equipment respectively. DSC was mainly used to analyze crystallinity alteration of the PPS and its melting behavior due to the FSpJ process. Moreover, the decomposition and thermal degradation of PPS was analyzed by the TG experiments.

In this work, PPS was extracted from the consolidated molten layer on the aluminum side of the fractured joint with the aid of a scalpel. Figure 6.7 shows the position of the PPS extracted for the thermal analysis. In addition, PPS from the composite was also extracted from pieces of the base material.

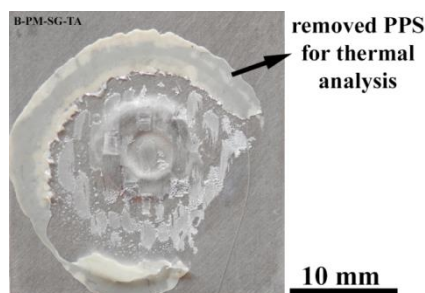


**Figure 6.7 Consolidated PPS layer that remained attached to the aluminum after mechanical testing was removed and used for thermal analysis.**

For DSC analysis, a mass of 10 mg of extracted PPS was placed in aluminum crucibles. Heating and cooling rates of 10 K/min were selected in the temperature range of 25-330°C to obtain the DSC curve. Inert nitrogen gas was used as the purge gas throughout the experiment with a flow rate of 250 ml/min.

For the TG experiments, a mass of 10 mg of the extracted PPS was placed in aluminum oxide crucibles. A heating rate of 20 K/min was selected in the temperature range of 25-800°C for obtaining the PPS mass change over temperature. Inert nitrogen gas with a flow rate of 250 ml/min was used as the purge gas to investigate the thermal decomposition of the PPS.

Both DSC and TG were calibrated before the experiments. In addition, ASTM standards D3418-08 [194] and E1131-08 [195] were followed for DSC and TG experiments respectively.

---

## 6.3.6 Local mechanical properties

### 6.3.6.1 Microhardness

A microhardness investigation was carried out on the aluminum from the cross-section of the joints, prepared similar to the LOM specimens, to analyze the local mechanical properties of the aluminum in the joints. The measurements were performed using Vickers Zwick/Roell indenter equipment and followed the ASTM E384-992e1 standard [196]. A microhardness map was obtained from one half of the specimen (due to the symmetry in the FSp joint) by applying an indentation load of 200 g for 10 s. The distance between the indents was 300  $\mu\text{m}$ .

### 6.3.6.2 Nanoindentation

When it came to the composite, the presence of pores and voids in the consolidated molten PPS particularly close to the interface with the aluminum in addition to a relatively high volume fraction of fibers made it almost impossible to employ microhardness. The area of the indenter was relatively large, which in most of the cases partially touched fibers or pores, leading to inaccurate values of the hardness. For this reason nanoindentation was selected to evaluate the local mechanical properties of the composite in the joints.

The nanoindentation experiments were carried out using a Nano indenter® XP (Agilent Technologies, USA) with a load capacity of 10 N. For the experiments a Berkovich diamond indenter was employed. A maximum indentation depth ( $h_{\text{max}}$ ) of 1  $\mu\text{m}$  was fixed and the maximum indentation load ( $P_{\text{max}}$ ) corresponding to the maximum indentation depth was recorded. The continuous stiffness measurement (CSM) method was used to monitor the stiffness while the indenter was being driven into the specimen. Both hardness and stiffness of the PPS matrix were then calculated and reported as the results of the nanoindentation experiments.

Nanoindentation was performed on the polished cross-section of the joints from the center of the spot joints and prepared according to the standard materialography procedures briefly explained in Section 6.3.3. Figure 6.8 illustrates the position of the indentations in the joints. The indents were positioned in the consolidated PPS molten layer, close to the interface with the aluminum. Note that the indents are sketched larger than to scale for better visibility. Between seven to ten indents were distributed in the consolidated molten layer in the middle of the joint. In the CF-PPS base material, the indents were positioned in the PPS matrix, far from the carbon fibers at different positions.

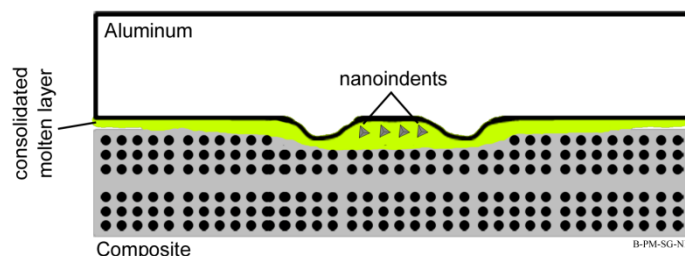


**Figure 6.8 Schematic illustration of the position of nanoindentations in the consolidated PPS molten layer in the joints.**

---

### 6.3.7 Global mechanical properties

#### 6.3.7.1 Single lap shear (SLS) testing

SLS testing was carried out as the main method to analyze mechanical performance of the joints throughout this work. The SLS joint geometry is widely used in the literature by researchers to study joint mechanical performance, due to its geometrical simplicity. The SLS strength of the joints was evaluated according to the ASTM D3163-01 standard [197] using a universal testing machine (Zwick Roell model 1478) with a load capacity of 100 kN. The traverse test speed was 1.27 mm/min and the tests were performed at room temperature. Three to five replicates were used to obtain the average ultimate lap shear force (ULSF) of the joints. The ULSF obtained is the peak force that a joint can bear before final failure. Aluminum and composite specimens with dimensions of  $100 \times 25.4 \text{ mm}^2$  were machined for joining and subsequent single-lap shear testing. The overlap area of the joints was  $25.4 \times 25.4 \text{ mm}^2$ . For mechanical testing, a free distance of 150 mm between the grips was used. Figure 6.9 shows the SLS geometry of the joints and its dimensions used in this work.

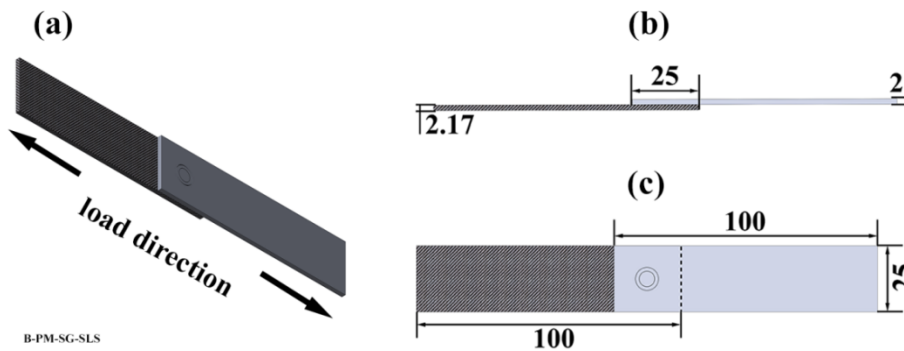


**Figure 6.9 (a) Schematic illustration of the SLS joint geometry; the respective dimensions used in this work from (b) side-view and (c) top-view. All dimensions are in mm.**

#### 6.3.7.2 Cross-tensile (CT) testing

CT joint geometry was also used in this work to evaluate the mechanical performance of FSp joints following the guidelines in the DIN EN ISO 14272 standard [198]. Similar to SLS testing, a universal testing machine (Zwick Roell model 1478) with a load capacity of 100 kN was used to evaluate the mechanical performance of the CT joints. The traverse test speed was 2 mm/min and the tests were performed at room temperature. Three replicates were used to obtain the average ultimate CT force of the joints. The dimensions of the aluminum and composite specimens were  $150 \times 50 \text{ mm}^2$  with an overlap of  $50 \times 50 \text{ mm}^2$ . During CT testing, the aluminum was fixed and the load was applied to the composite part of the joint. Figure 6.10 illustrates the CT geometry of the joints and the dimensions used in this work.

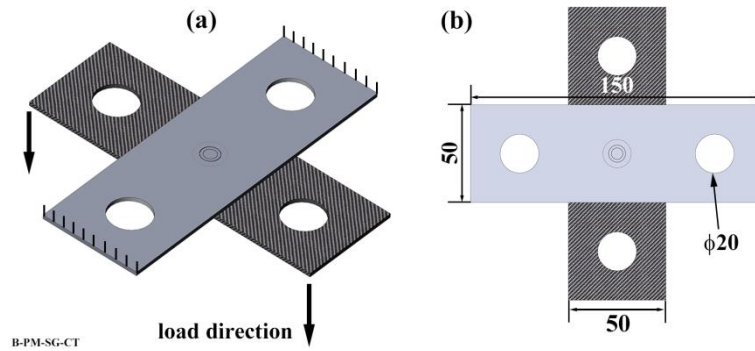


**Figure 6.10 (a) Schematic illustration of the CT joint geometry and (b) top-view of the joint design with the respective dimensions used. All dimensions are in mm.**

### 6.3.7.3 Fatigue experiments

Fatigue experiments of the FSp joints were performed using SLS joint geometry. The experiments were carried out under constant amplitude at a frequency of 5 Hz using load-controlled servo-hydraulic equipment with a load capacity of 25 kN. A tension-tension load ratio (minimum to maximum applied cyclic load) of  $R=0.1$  was selected to perform the experiments. All the experiments were carried out at room temperature. Different load levels (maximum applied cyclic load) were selected to obtain fatigue lives between approximately  $10^3$  and  $10^6$  cycles. A minimum of two specimens for each load level were tested. To align the SLS joints, end tabs with dimensions of  $40 \times 25 \text{ mm}^2$  were machined and attached to the specimens. Two rivets were used to fix the joint in the grips of the testing machine. For this purpose, a hole was drilled in each side of the joint at a distance of 27 mm from the edge. A free length of 95 mm was used during the fatigue experiments. Figure 6.11 displays the geometry of the joints and its dimensions for fatigue testing used in this work.

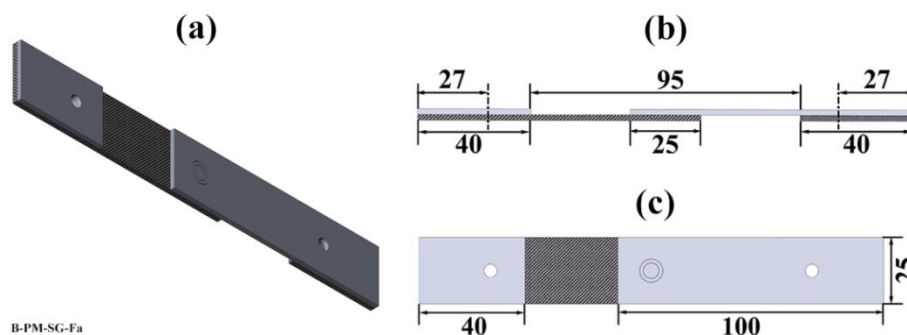


**Figure 6.11 (a) Schematic illustration of the geometry of the fatigue specimen; the respective dimensions used in this work from (b) side-view and (c) top-view. All dimensions are in mm.**

The joints that survived one million fatigue cycles without failure (called run-out specimens) were subsequently tested under quasi-static conditions as explained in Section 6.3.7.1. The results are reported as the residual strength of the joints after one million cycles of fatigue.

### 6.3.8 Aluminum surface pre-treatments

To investigate the influence of aluminum surface morphology and chemistry, various surface pre-treatments were performed on the aluminum prior to the joining process. The term surface pre-treatment is used throughout this thesis, because the treatments were performed prior to the FSpJ process. The aluminum specimens were machined according to the SLS and CT configurations described above, followed by the surface pre-treatment procedures. Table 6.4 lists the various surface pre-treatments carried out in this work. Details of each surface pre-treatment are explained following this table.

**Table 6.4 Various aluminum surface pre-treatments performed in this work.**

Category	Surface pre-treatment	Symbol
As-received	(untreated)	AR
Mechanical	Mechanical Grinding	MG
	Sandblasting	SB
Chemical	Acid Pickling (Etching)	AP
	Conversion Coating	CC
Mechanical & Chemical	Sandblasting + Acid Pickling	SB+AP
	Sandblasting + Conversion Coating	SB+CC
electrochemical	Sulfuric Acid Anodizing	SAA
	Phosphoric Acid Anodizing	PAA
	Phosphoric Acid Anodizing + Primer	PPA-P

a) As-received (AR)

The AR aluminum samples, cut into the required dimensions, were slightly wiped with acetone to remove any loose contaminations. These samples were used as a base reference for comparison with the surface pre-treatments. Acetone wiping was performed prior to all other surface pre-treatments as well.

b) Mechanical Grinding (MG)

Some of the samples were mechanically ground manually using sand paper P1200. The specimens were ground in four directions: parallel (0°) to the rolling direction of the aluminum, followed by 90°, +45° and -45°. After grinding the specimens were blown by pressurized air and placed into an ultrasonic acetone bath for three minutes to remove any residues from the sand paper.

c) Sandblasting (SB)

SB was also carried out manually on a number of the specimens. Several trials were performed to find the optimum SB conditions. Corundum (Al<sub>2</sub>O<sub>3</sub>) with a particle size in the range of 100-150 μm was used as the medium of treatment. The pressure of blasting was set at 6 bar and the duration of

---

SB at 10 s. The distance between the blasting nozzle and the specimens was 25 cm and the angle to the specimens with respect to the nozzle was 45°. Table 6.5 lists the chemical composition of the corundum used in this work.

**Table 6.5 Chemical composition of the corundum used in this work [199].**

Element	Al <sub>2</sub> O <sub>3</sub>	Na <sub>2</sub> O	Fe <sub>2</sub> O <sub>3</sub>	SiO <sub>2</sub>	Rest
Weight%	99.70	0.20	0.02	0.02	0.06

d) Acid Pickling (AP)

AP was performed using a highly concentrated (65%) nitric acid (HNO<sub>3</sub>) solution. The specimens were dipped into the concentrated HNO<sub>3</sub> solution for 15 minutes. Afterwards the samples were rinsed under tap water and dried.

e) Conversion Coating (CC)

For CC pre-treatment, Alodine® 4850 (kindly provided by Henkel AG & Co., Germany) was used as the chemical solution. The solution is chromium-free, contains primarily hexafluorozirconate (HFZ) [200], which produces a colorless conversion layer. The concentrated solution was diluted according to the recommendations of the producer: 10 ml of the solution was added to 500 ml distilled water while stirring. The pH of the solution was controlled during the treatment to be stable at 4. The aluminum specimens were then immersed into the diluted solution for 60 s at room temperature. After this immersion time, the samples were rinsed thoroughly under tap water and dried.

f) Sandblasting + Acid Pickling (SB+AP)

A combination of SB and AP was also carried out to investigate the combined effect of both processes. The samples were first given SB as explained in (c) followed by AP as briefly introduced in (d).

g) Sandblasting + Conversion Coating (SB+CC)

Similar to SB+AP, the samples were sandblasted as in (c) followed by Alodine® CC as explained in (e).

h) Electrochemical pre-treatments

The electrochemical pre-treatments (SAA, PAA, and PAA-P) were kindly provided by Embraer Co., Brazil. Specimens were prepared following the internal procedures used by Embraer to treat specimens for adhesive bonding.

Apart from the electrochemical, all the other pre-treatments, including CC, were carried out under lab conditions at Helmholtz-Zentrum Geesthacht.

---

### 6.3.9 Durability of the joints (accelerated aging)

Similar to the other joining techniques, particularly adhesive bonding, it is important to understand the long term behavior and durability of joints. Since in many cases it is not possible to evaluate the joints under real conditions, by waiting for a very long period of time (several years), simulation of the behavior of joints under artificial conditions is generally accepted. Such conditions are chosen to be much more aggressive than real applications, but for a shorter time. The results of such artificially accelerated testing are used to predict and understand the long term behavior of joints and materials in real conditions. In order to investigate the behavior of the FSp joints under harsh environments, the SLS FSp joints of the selected aluminum surface pre-treatments were placed in an artificial aging chamber (VCL 0003, Vötsch Industrietechnik, Germany) for 28 days. The temperature of the chamber was set at 71°C with 100% relative humidity following the recommendations given in the ASTM D3762 standard [201]. From the conditions given in the ASTM standard, the one selected for this work was the most severe environment. The humidity of the chamber during the test was constantly controlled and adjusted by pumping water into the chamber. After 28 days, the specimens were removed from the chamber and visually inspected for any possible changes. Shortly thereafter the SLS joints were mechanically tested following the same procedure explained in Section 6.3.7.1. The residual strength of the joints was then calculated by dividing the SLS strength of the joint after aging over the SLS strength of the joint before aging.

---

## Results and Discussion

The results obtained from this PhD work and their respective discussions are divided into four chapters in order to provide a logical structure and further facilitate understanding of the discussions. Chapter 7 is devoted to the further development of FSpJ process. The influence of various surface pre-treatments of aluminum on the mechanical performance of the joints is discussed in Chapter 8. The physical and chemical alterations of the aluminum surface after pre-treatments are considered in order to discuss the mechanical performance of the joints. Chapter 9 deals with the accelerated aging behavior of the joints at high relative humidity and moderate temperature. Finally, Chapter 10 covers the performance of the FSp joints under dynamic loading and fatigue resistance of the joints.

---

## Chapter 7. Development of the FSpJ Process

### 7.1 Process optimization for detailed joint characterization

Complex processes like welding and joining involve a large number of parameters that interact with each other. Statistical analysis by design of experiment (DoE) techniques is a helpful tool to understand the influence of process parameters and how their interactions affect the desired response(s). Recently, many researchers in the area of welding and joining have been using various DoE techniques coupled with analysis of variance (ANOVA) to depict the effects of process parameters on the behavior of the selected joints. These statistical tools and models are also used frequently to optimize the joining process based on one or more response(s).

A part of the current PhD work was dedicated to investigating the influence of the FSpJ process parameters and their interactions on the bonding area and mechanical performance of the joints were the chosen responses. For this purpose, single lap shear geometry was used, because of its simplicity and adequacy to the joint's design. Full factorial DoE and ANOVA were used to assess the lap shear strength as well as formation of the bonding area by alteration of process parameters. The details of this part of investigations is beyond the scope of the current thesis and was previously published as a separate manuscript [176].

Briefly, we showed that RS is the most important parameter affecting the strength of the joints. The reason for this is that a higher RS value increases heat input to the joints and therefore a larger bonding area is achieved [84]. A trend was observed that the larger the bonding area is, the higher the strength would be, because the contact area is larger and thus adhesion forces between the aluminum and composite are greater. JP was shown to be the second most important parameter influencing the joint's strength. Higher JP drives more of the molten PPS into the pores and crevices on the surface of pre-treated aluminum and so increases micro-mechanical interlocking between the joining parts. It was found that PD also contributes to the strength of the joints, because it controls the shape and extent of the nub and therefore the amount of molten PPS entrapped inside the nub. Larger PD increases macro-mechanical interlocking by the entrapment of a larger volume of PPS in the nub and so higher strength is obtained. Investigation of the JT has shown that its influence is insignificant for strength in the selected range of process parameters. However, elevated JT keeps the viscosity of the PPS low, whereby the applied JP facilitates the flow of the molten polymer and results in generation of excessive flash material outside the joining area. This leads to reduction in the strength obtained, because the flash material does not contribute towards bonding between the joining parts. Finally, an interaction between RS and JP had a significant influence on the strength. This was explained as due to higher RS reducing the viscosity of the molten PPS, which requires a higher JP to keep the molten PPS in intimate contact with the aluminum, thereby enhancing pore filling, wetting and achieving optimal micro-mechanical interlocking.

Resulting from the statistical analysis, a set of joining parameters (RS: 2900 rpm, PD: 0.8 mm, JT: 4 s, JP: 0.3 MPa) was achieved that optimized the strength of the single overlap FSp joints. Moreover, we showed that lower heat input reduces the amount of defects in the joints. Another set of parameters (RS: 1900 rpm, PD: 0.8 mm, JT: 4 s, JP: 0.2 MPa) was achieved with the highest lap shear strength over area fraction of the pores.

In this chapter the terms high heat input (HHI) and low heat input (LHI) joining condition are frequently used, which refer respectively to the first and second set of parameters mentioned above. The HHI and LHI joining conditions are summarized in Table 7.1. Note that sandblasting was applied as the aluminum surface pre-treatment in all joints produced.

**Table 7.1 LHI and HHI joining conditions used in this work.**

Joining condition	Symbol	Rotational speed [rpm]	Plunge depth [mm]	Joining time [s]	Joining pressure [MPa]
High heat input	HHI	2900	0.8	4	0.3
Low heat input	LHI	1900	0.8	4	0.2

## 7.2 Temperature development

Temperature development is of utmost importance since it gives information about temperature-dependent phenomena taking place in the course of the joining process such as metallurgical changes in the aluminum, possible degradation of the composite, formation of defects, etc. As explained in Section 6.3.2 (Page 43) IR-thermography was the main method used to measure the temperature on the surface of the aluminum. For the HHI and LHI joining conditions (Table 7.1), three thermocouples, whose positions are illustrated in Figure 6.4 (Page 43), were also used to validate the measurements by the IR-thermography and to be able to measure the temperature at the interface.

Figure 7.1 shows an example of the typical temperature development over time for both LHI and HHI joining conditions measured by IR-thermography and thermometry. The curves related to the IR-thermography measurements illustrate the changes in peak temperature on the surface of the aluminum over time. It can be observed from the figure that the highest measured temperature by IR-thermography is close to the measurement obtained by TC-1 with a maximum deviation of 15°C. The difference in the measurements may be explained by the fact that thermocouples measure the temperature locally at the contact position between the aluminum and the tip of the thermocouple. However, IR-thermography measures the temperature on the surface of the aluminum from an area of approximately 25x25 mm<sup>2</sup>. With IR-thermography the temperature beside the clamping ring on the surface of the aluminum was obtained. The peak temperature obtained inside (thermocouples) and on the surface of the aluminum (IR-thermography) alters from 345°C to 399°C and from 385°C to 437°C, for the LHI and HHI joining conditions respectively. The lowest and highest temperatures are approximately 69% and 87% of the aluminum incipient melting temperature of 502°C [149] respectively. It was reported [152] that a temperature of approximately 400°C lies in the range of dynamic recrystallization of AA2024 for friction-based joining processes. So, metallurgical transformations such as recrystallization of the grains are expected in the aluminum in the vicinity of the tool, which will be explained in Section 7.4. The whole range of temperature development measured by IR-thermography with other joining conditions is reported in [176] that showed it varies between 345°C and 474°C.

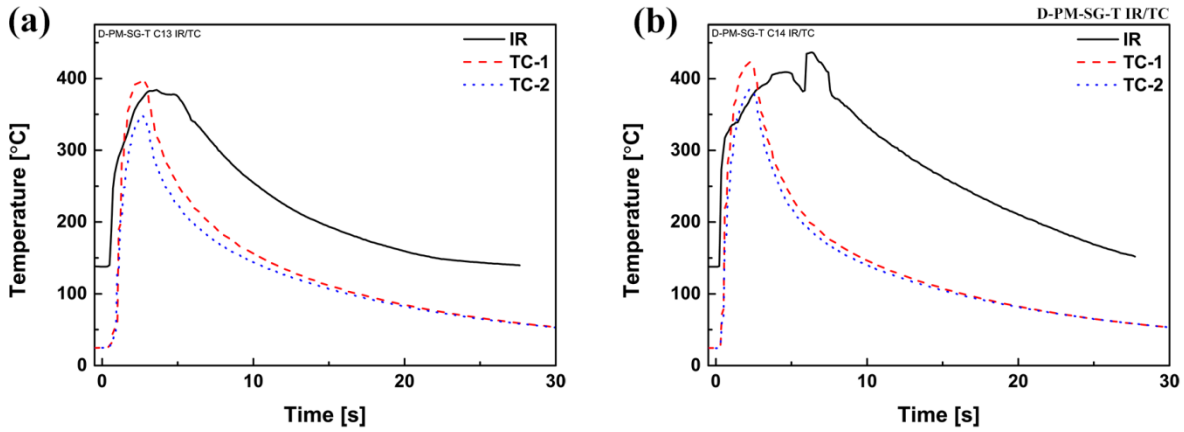


**Figure 7.1** Process temperature evolution measured on the aluminum part by IR-thermography (IR) and by thermocouples (TC) for the (a) LHI joint, and (b) HHI joint.

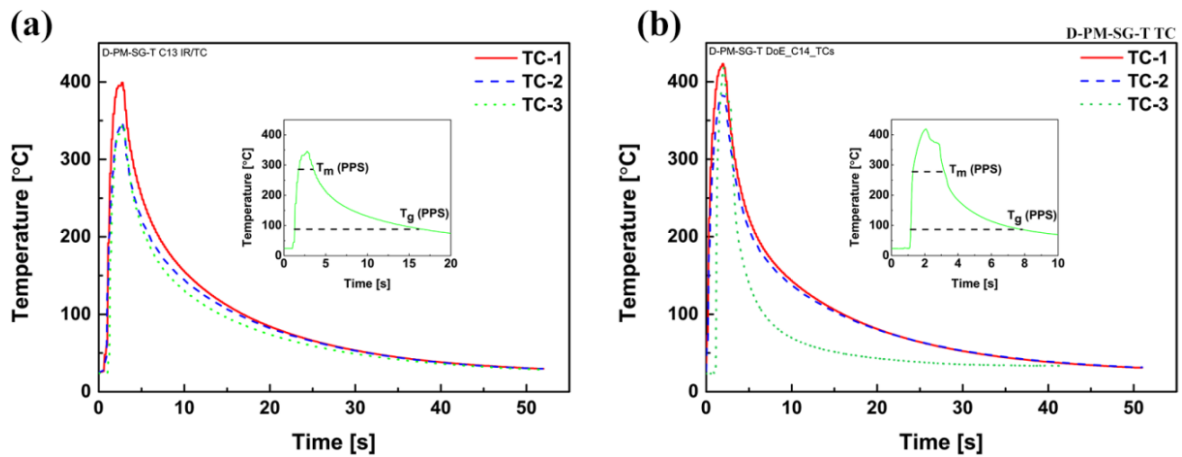
In addition to temperature measurement of the aluminum part, the thermocouple TC-3 was also used to measure the temperature of the molten PPS layer at the interface between the aluminum and CF-PPS (refer to Figure 6.4, Page 43 for the positions of the thermocouples). Since the temperature of the molten PPS at the interface below the tool is expected to be higher than the rest of the interface, the temperature measured by TC-3 can be used to explain any physicochemical changes or possible degradation on the PPS.

Figure 7.2 depicts the temperature measurements over time from all three thermocouples for both LHI and HHI joining conditions. The peak temperature obtained by TC-3 at the interface was 345°C and 418°C for the LHI and HHI joining conditions respectively. In addition to the peak temperature, the heating and cooling rates between  $T_g$  (90°C) and  $T_m$  of the PPS were also calculated linearly through the following equations:

$$\text{heating rate (HR)} = \frac{T_m - T_g}{t_m - t_{g1}} \quad (7.1)$$

$$\text{cooling rate (CR)} = \frac{T_m - T_g}{t_{g2} - t_m} \quad (7.2)$$

where  $T_m$  and  $T_g$  are the melting point and glass transition temperatures of the PPS respectively,  $t_m$  is the time taken to reach the melting temperature and  $t_{g1}$  and  $t_{g2}$  are the time taken until the glass transition temperature is achieved during heating and cooling respectively.



**Figure 7.2** Process temperature evolution measured by thermocouples (TC) in the aluminum (TC-1 and TC-2) and at the aluminum-composite interface (TC-3) for the (a) the LHI joint, and (b) the HHI joint. Inset charts relate to the TC-3.

The measured peak temperatures, as well as the calculated heating and cooling rates are shown in Table 7.2 and Table 7.3 respectively, for both LHI and HHI joining conditions. The heating rate is very fast, both inside the aluminum and at the interface, with the latter giving the highest rate due to the higher heat development experienced. High average values for heating rates are expected due to the very low thermal conductivity of PPS ( $0.19 \text{ Wm}^{-1}\text{K}^{-1}$ ) that leads to a reduction in heat dissipation to the surroundings. Therefore, the temperature rises very fast as the heat is conducted from aluminum to composite. The measured cooling rate showed a moderate decrease in temperature ( $63^\circ\text{C/s}$  against  $19^\circ\text{C/s}$  for the TC-3 thermocouple), which is again attributed to the low thermal conductivity of PPS. In contrast to the heating phase, during cooling phase the low thermal conductivity does not allow rapid heat dissipation to the environment.

**Table 7.2** Average peak temperatures by IR-thermography and the thermocouples (TC) for the LHI and HHI joining conditions.

Joining condition	Symbol	TC-1 [°C]	TC-2 [°C]	TC-3 [°C]	IR-thermography [°C]
High heat input	HHI	423±2	385±6	418±7	437±6
Low heat input	LHI	399±1	348±1	345±1	384±8

**Table 7.3** Average heating and cooling rates inside the aluminum (TC-1 and TC-2) and at the aluminum-composite interface (TC-3) using thermocouples for the LHI and HHI joining conditions.

	HHI		LHI	
	HR [°C/s]	CR [°C/s]	HR [°C/s]	CR [°C/s]
TC-1	206±1.2	21±0.2	199±0.3	19±0.5
TC-2	190±0.3	19±0.7	178±0.4	17±0.3
TC-3	355±0.2	63±1	205±0.3	19±0.7

The inset graph in Figure 7.2 illustrate a section of the temperature-time graphs related to the TC-3 where the temperature increases to the melting point of PPS and decreases to below its  $T_g$ . It can be observed from the graph insets that it takes a very short time for the interface temperature to exceed the melting point of the PPS (280°C) and reach a peak temperature that then decreases below  $T_m$  again. The same observation can be made for the time that the interface temperature is above the  $T_g$  of the PPS. Since both  $T_g$  and  $T_m$  are critical temperatures for thermoplastics, calculating the time that the joint's interface temperature is above them will facilitate the discussions in the next sections. Table 7.4 lists the total time that the joint's interface (molten PPS layer) temperature is above  $T_g$  and  $T_m$  of the PPS.

**Table 7.4 The total time fraction that the composite at the interface remained above  $T_g$  and  $T_m$  of the PPS, obtained from the TC-3.**

Joining condition	Symbol	Total time above $T_g$ [s]	Total time above $T_m$ [s]
High heat input	HHI	6	1.9
Low heat input	LHI	14	1.9

### 7.3 Process-related physicochemical changes in the CF-PPS

Thermal effects in polymers and composites, such as alteration of the amount of crystallinity, morphology of crystals, and the extent of thermal degradation are temperature dependent. In high temperature processes, such as welding and joining, an understanding of the physicochemical changes induced by the process is crucial, since local and global mechanical properties of the material depend on its physicochemical state. For this reason, both TG and DSC analytical techniques were used to study the physicochemical properties of the affected zone in CF-PPS as a result of the FSpJ process.

Figure 7.3 shows the TG curves for CF-PPS as base material (BM) prior to the joining process, as well as for LHI and HHI joining conditions between 30°C and 800°C. The onset temperature of decomposition was obtained and resulted in  $511.7 \pm 4.5^\circ\text{C}$  for BM,  $512.4 \pm 2.8^\circ\text{C}$  for LHI, and  $514.5 \pm 0.5^\circ\text{C}$  for the HHI joining condition. The results obtained for the BM are in agreement with those reported in the literature for the onset decomposition of PPS [159, 168, 170, 171, 202]. As illustrated in Figure 7.3 and reported in [176] the range of process peak temperatures achieved in this work was between 345°C and 474°C. The peak temperature for the selected LHI and HHI joining conditions measured at the interface by TC-3 was 345°C and 418°C respectively, as shown in Table 7.2. The peak temperatures for both conditions are far below the onset decomposition temperature of CF-PPS. Thus, extensive thermal degradation of the PPS, such as decomposition, main chain scission, or carbonization as a result of the process is not expected. In addition, it is reported that increasing the heating rate in the TG experiments shifts the onset degradation to higher temperatures, for instance, for PMMA [203] and PA 66 [204]. This is probably due to a delay in the beginning of chain motion. At a high heating rate, the chains do not have enough time to react to the high temperatures. Since the heating rate in FSpJ is much faster than the 20°C/min used in the TG experiments, it is believed that the actual onset decomposition temperature would have been far more than the temperatures obtained, if the TG scanning had been done using this

---

process heating rates. This further supports the assumption that extensive thermal degradation (decomposition) does not occur with the studied process parameter range and base materials. Changes in molecular weight, indicating thermal degradation (both by chain scission or cross-linking) may take place. However, this was not the focus of this work, particularly considering that the process did not lead to decomposition (excessive thermal degradation).

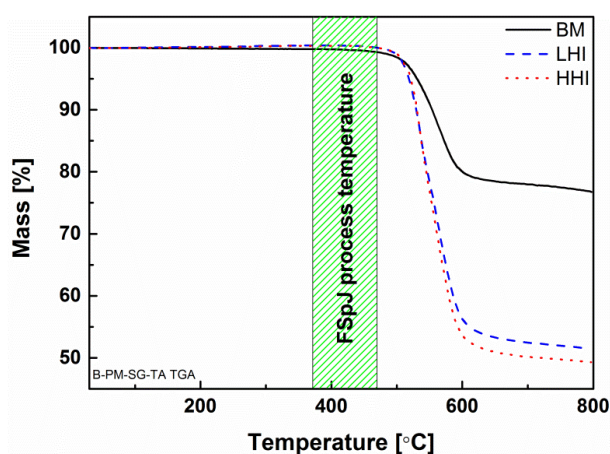


**Figure 7.3 TG analysis of the PPS in the BM, LHI and HHI in nitrogen showing the mass change between 30°C and 800°C. The green area shows the window of the FSpJ process temperature in this work.**

In addition to the TG curve, a derivative thermogravimetry (DTG) curve helps to indicate the degradation stages and the temperature at which the rate of decomposition is maximum. Figure 7.4 depicts a part of the TG curves (in green) in the range of 400-700°C along with the respective DTG curves (in blue) for BM, LHI and HHI conditions. It is obvious from the DTG curve that weight loss and thermal degradation for the CF-PPS occurs at one stage with its maximum rate at about 566°C. This result agrees with the literature for instance the studies by Bo *et al.* [171] and Day *et al.* [169]. In contrast to the BM, both joining conditions showed a two-step degradation obtained by DTG curves. The peaks at above 560°C are close to the single peak from the BM, suggesting the same degradation mechanisms as CF-PPS such as pyrolysis or main chain scission. The appearance of another peak at 534.6°C for the joints may be attributed to slight cross-linking of the PPS molten layer. It was reported that intermolecular branching, similar to cross-linking in PPS, may occur at temperatures above 300°C in air [205]. Therefore, slight cross-linking in the consolidated molten PPS layer may take place during the FSpJ process. The cross-linked part of the PPS may then start to degrade at a separate stage, leading to the formation of a new peak in the DTG curves.

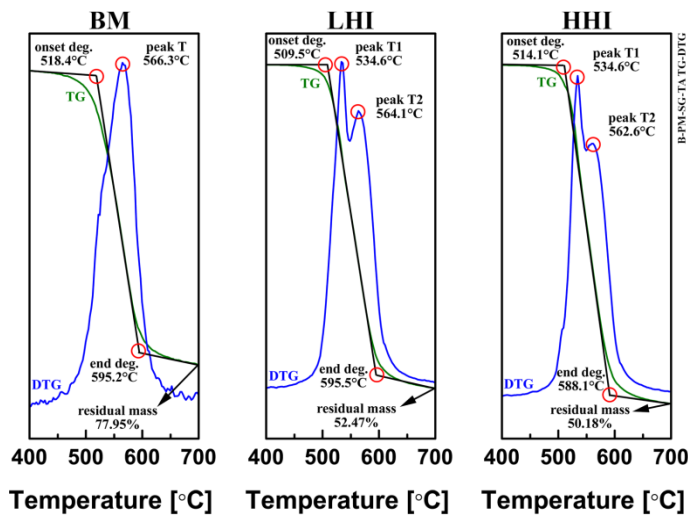


Figure 7.4 TG-DTG curves for the BM, LHI and HHI conditions in the range of 400°C to 700°C. the BM showed one-step degradation, whereas LHI and HHI joint showed two-step degradation as indicated by the two peaks in the DTG curve.

DSC analysis was also used to study the crystallization and melting behavior of the molten PPS from the joints in comparison with the CF-PPS in the BM. Figure 7.5 illustrates an example of the first heating curves for the BM, LHI, and HHI joining conditions using a heating rate of 10°C/min, in the range of interest. The first heating curve is especially important in this work to investigate the influence of the process on the thermal behavior of the joints. All the obtained results from the DSC analysis are listed in Table 7.5.

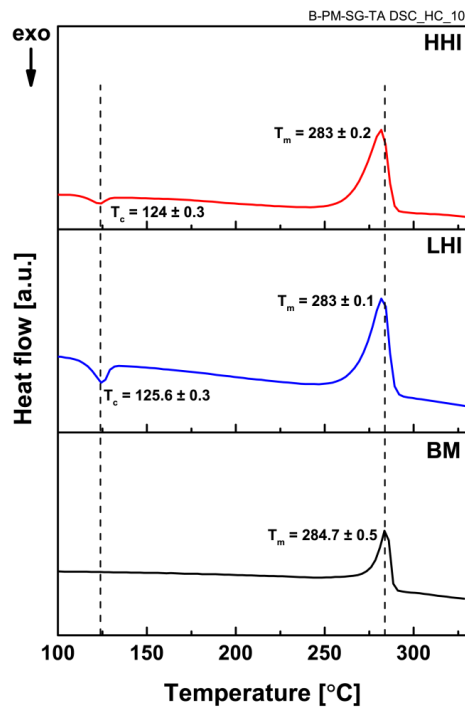


Figure 7.5 Example of DSC curves for the BM, LHI and HHI samples in the range of interest using a heating rate of 10°C/min in nitrogen.

**Table 7.5** The main parameters obtained from DSC analysis.  $T_c$ : crystallization temperature,  $\Delta H_c$ : enthalpy of crystallization,  $T_m$ : melting temperature,  $\Delta H_m$ : enthalpy of melting, FWHH: full-width at half-height.

Joining condition	$T_c$ [°C]	$\Delta H_c$ [J/g]	$T_m$ [°C]	$\Delta H_m$ [J/g]	% Crystallinity	FWHH [°C]
BM	-	-	284.7±0.1	44.7±2.3	30±1.5	7.5±0.2
LHI	125.6±0.3	-7±0.9	283±0.5	35.5±2.8	22±2.8	13.3±0.7
HHI	124±0.3	-1.1±0.9	283±0.2	37±0.5	24±0.3	13.1±0.4

Figure 7.5 compares the DSC curves of the BM and the joining conditions. It is apparent from this figure that the joints show an exothermic peak which is not present in the BM. The exothermic peak appeared at  $125.6 \pm 0.3^\circ\text{C}$  and  $124 \pm 0.3^\circ\text{C}$  for the LHI and HHI joining conditions respectively (Figure 7.5). The exothermic peak is believed to be related to the cold crystallization temperature of the PPS which is reported in the range of  $120^\circ\text{C}$  to  $126.5^\circ\text{C}$  [153, 165, 166]. Such a peak was not detected for the BM since it was in its full crystallinity state. However, the PPS in the joints experienced a fast cooling rate and resulted in lower crystallinity than the BM, leading to the recrystallization of the amorphous part during the DSC heating scan.

The amount of the crystalline phase was also determined for the PPS from the BM and from joints. Equation (7.3) was used to measure the crystallinity as described below:

$$X_c = \frac{\Delta H_m + \Delta H_c}{\Delta H_m^\circ} \quad (7.3)$$

where  $X_c$  is the crystalline fraction,  $\Delta H_m$  is the enthalpy of melting for a partially crystallized sample,  $\Delta H_c$  is the enthalpy of the crystallization, and  $\Delta H_m^\circ$  is the enthalpy of melting for a 100% crystalline sample [153].  $\Delta H_m$  and  $\Delta H_c$  can be determined from the area under the melting and crystallization peaks in the DSC scan. The values reported on  $\Delta H_m^\circ$  in the literature for PPS range from 50 J/g to 150.4 J/g [153]. The wide difference in these values is due to the fact that it is impossible to synthesize a 100% crystalline sample of PPS. Therefore, researchers used different methods of estimating  $\Delta H_m^\circ$  which led to different results. The value of 150.4 J/g was obtained and reported by the TenCate company [153, 166] and so was used as the basis for calculations in this work, because TenCate was the supplier of the CF-PPS. Furthermore, choice of a value for  $\Delta H_m^\circ$  was not critical in this work, because the main objective of this study was to compare the crystallinity of the BM and the joints. According to the measurements, the crystallinity of the CF-PPS was  $30 \pm 1.5\%$ , whereas it was  $22 \pm 2.8\%$  and  $24 \pm 0.3\%$  for the LHI and HHI conditions. In case of the BM, since it contains 42 wt% carbon fibers, a correction factor of 0.42 was used in calculating the heat of fusion [166]. However, this is not the case for the joints, since the removed PPS layer did not contain a large amount of carbon fibers. Due to the very fast cooling rate in FSpJ (Table 7.3) it was expected that the joints would show a completely amorphous structure. Contrary to such expectations, both LHI and HHI joints showed a relatively high degree of crystallinity as discussed above. There are several possible explanations for the high crystallinity obtained from the joints. Nohara *et al.* [164] recently demonstrated that PPS heated up to  $330^\circ\text{C}$  with a heating rate of

---

10°C/min still showed some remnant crystals, which can act as nuclei for recrystallization during the cooling phase. It is believed that remnant crystals are also present in PPS during the FSpJ process, particularly due the fact that the PPS is exposed only about 2 s above its melting temperature (Table 7.4) as a result of very rapid heating and cooling rates. It seems that there is not enough time for all the crystals to melt during the heating phase. In addition to residual crystallites, carbon fibers [153] and small amounts of cross-linking [167] may act as nucleation sites for the subsequent crystallization during the cooling phase. For example, Deporter and Baird [174] investigated the crystallinity of CF-PPS (66 wt% unidirectional fibers) under different cooling rates. The sample was heated to 310°C and kept there for 10 min followed by quenching with a cooling rate of 68°C/s (which is faster than cooling rates in FSpJ). They demonstrated that the sample contained 7% crystallinity after quenching. Cross-linking may also contribute to the increase in crystallinity during recrystallization, as branching points can act as nucleation sites [206].

As can be seen in Figure 7.5, besides the exothermic peaks both BM and the joints showed one endothermic peak related to melting of the crystalline part of the PPS. The melting temperature of the BM was measured as  $284.7 \pm 0.5^\circ\text{C}$ . This result is in accordance with other studies [153, 159, 163, 164] that show the melting temperature of PPS in the range 280°C to 295°C depending on the size and amount of crystals. The melting temperature of PPS obtained from LHI and HHI joints was  $283 \pm 0.1^\circ\text{C}$  and  $283 \pm 0.2^\circ\text{C}$  respectively. Since the melting temperature of the PPS in the joints slightly decreased compared to the BM, it could support the idea of a slight cross-linking taking place in the joints. It is reported [173] that cross-linking may reduce the melting temperature in thermoplastics such as PA 6 and PPS. In addition to the melting temperature, enthalpy of melting was measured from the area under the melting peak. The results are listed in Table 7.5 and show a reduction in  $\Delta H_m$  from BM ( $44.7 \pm 2.3 \text{ J/g}$ ) to the joints (LHI:  $35.5 \pm 2.8 \text{ J/g}$  and HHI:  $37 \pm 0.5 \text{ J/g}$ ). As a lower number of crystals require less energy to be melted, the joints demonstrated a smaller enthalpy of melting as a result of their reduced crystallinity. Moreover, cross-linking reduces the enthalpy of melting [173], which could be another reason for the reduction in  $\Delta H_m$  in the joints. Furthermore, Full-Width at Half-Height (FWHH) can be used as an indication of crystal size distribution. A narrow peak is an indication of a more homogeneous crystal size, as is the case in the BM. However, the FWHH of the joints is much larger compared to the BM. This might be an indication of crystal growth in the joints. It is reported that crystal growth in polymers may occur above their glass transition temperature and below melting point [207-209]. It is believed that during the heating phase in FSpJ some of the crystals may grow, resulting in a larger lamella structure. This may result in a broader melting peak, with smaller crystallites from BM and larger ones from process-related thermal processing. However, it is important to bear in mind the possible bias to such arguments as a result of the fast heating rate during the FSpJ process. Therefore, further analysis is required to confirm whether crystal growth actually occurs.

As a summary for this section: no extensive thermal degradation of the PPS during FSpJ was detected, although it is believed that slight cross-linking may occur during the process. The consolidated molten PPS in the joints showed a relatively high level of crystallinity (only 6-8% less than the BM), which is explained by the fact that all the crystals were not melted during the very brief thermal cycles in FSpJ. In addition, carbon fibers and points of branching, as a result of slight cross-linking, may act as nucleation sites for recrystallization during cooling. Finally, broader melting peaks of the joints compared to the BM may be an indication of crystal growth during the heating phase in the FSpJ process.

---

## 7.4 Microstructural zones

Microstructural zones form in an FSp joint as a result of the interaction of the tool with the metal, generating frictional heat and a local rise of temperature, and the amount of the heat conducted from the metal to the composite. Generally, the microstructural zones can be divided into four areas: metal stir zone (MSZ), metal thermo-mechanically affected zone (MTMAZ), metal heat affected zone (MHAZ), and polymer heat affected zone (PHAZ).

The microstructural zones on the aluminum are very similar to those reported for FSpW of AA2024 [152] and AA6181 [210]. The microstructural zones in FSpJ are shown in Figure 7.6 for the HHI joining condition, in which Figure 7.6 (a) shows an overview of the microstructure, and Figure 7.6 (b-f) illustrates the detailed microstructure of each zone. Figure 7.6 (b) & (c) compare the microstructure of the base material (BM) and MTMAZ respectively. The microstructure of the AA2024 in the MTMAZ is influenced by the relatively high temperature attained during the process as well as severe deformation [152, 210]. This zone forms in a volume close to the plunging sleeve where the aluminum grains are affected by the high strain rate as a result of the tool's rotational speed as well as axial movement [152, 210, 211]. The microstructure in this zone is thus characterized by elongated grains that are rotated approximately 45 degrees compared with unaffected grains. One can see that the grains in MTMAZ are elongated and rotated from top-left to bottom-right (Figure 7.6 (c)) compared to the AA2024-T3 BM (Figure 7.6 (b)). The induced grain deformation in this zone may contribute to the strain hardening effect [210]. However, since the temperature and strain rate are relatively high in MTMAZ, some dynamic recovery may also occur, which reduces the strain hardening effect [212, 213]. In addition, due to the relatively high temperature achieved in this area, coarsening of the strengthening particles may also take place [214]. Therefore, the local mechanical strength of the aluminum in the MTMAZ is affected by these competing phenomena (strain hardening, dynamic recovery, and precipitation coarsening).

MSZ lies in the center of the spot that undergoes the highest strain rate as a result of the aluminum being stirred by the tool [210, 215]. The highest frictional heat generation and attained temperature is also expected in this zone [210, 215]. Dynamic recrystallization (DRX) is one of the main mechanisms taking place in the MSZ in FSpW of aluminum, which leads to an equiaxed, refined grain structure [152, 210]. DRX occurs in many metallic materials above  $0.6 T_m$  under high stress or high deformation rates [212, 213]. The temperature measured by IR-thermography on the surface of the aluminum resulted in  $384^\circ\text{C}$  and  $437^\circ\text{C}$  for LHI and HHI conditions respectively, as can be seen in Table 7.2. These temperatures correspond to 0.76 and 0.87 of the incipient melting temperature of AA2024 [149]. Since these temperatures are obtained on the surface of the aluminum in the vicinity of the tool, the temperature in the MSZ is probably a little higher than these values. Such high temperatures in combination with a high strain rate as a result of the tool's rotational speed results in a very fine grain structure in the MSZ. Figure 7.6 (d) shows the boundary between MSZ and MTMAZ, and Figure 7.6 (e) illustrates the MSZ with very fine grain structure. In addition to grain refinement, solubilization of the strengthening particles in the course of the joining cycle is expected in the MSZ as a result of the high temperature. Re-precipitation of these particles during the cooling phase is believed to increase the local strength of the MSZ [210].

MHAZ is the third zone formed during the FSpJ process between the BM and MTMAZ. In this region the aluminum is not affected mechanically and the temperature is not as high as in the MSZ and MTMAZ. The moderate temperatures achieved in MHAZ may lead to the recovery

phenomenon and coarsening of the strengthening particles [210]. Although such metallurgical phenomena may have occurred, no differences in grain structure could be observed between the MHAZ and BM by optical microscopy. Figure 7.6 (f) illustrates the boundary between MTMAZ (left part of the figure) and MHAZ (right part of the figure).

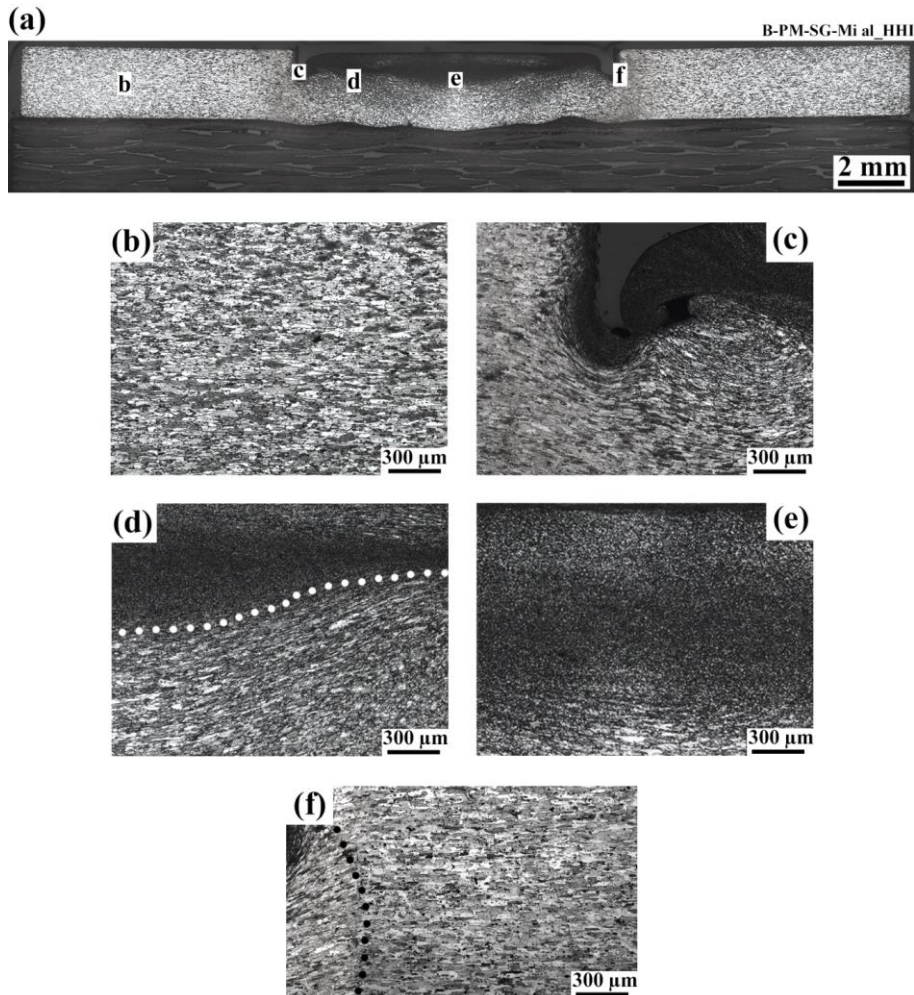


**Figure 7.6** Microstructural zones that form in the aluminum. (a) General overview of the joints microstructure, (b) microstructure in the BM, (c) MTMAZ showing elongated grains rotated compared to the BM grains, (d) boundary between MTMAZ and MSZ, (e) MSZ showing very fine DRX grains, and (f) boundary between MTMAZ and MHAZ.

In addition to the microstructural zones in the aluminum a PHAZ was detected in the CF-PPS, as illustrated in Figure 7.7, which compares LHI and HHI joints. The yellow dashed lines in the figure show the boundary between the PHAZ and the CF-PPS base material. It can be seen from the figure that the HHI joint (b) had an extended PHAZ compared to the LHI joint (a). The width (w) and depth (d) of the PHAZ showed an increase of 21% and 44% from LHI to HHI. Table 7.6 lists the values of w and d for both LHI and HHI joining conditions, along with the obtained average temperature at the interface.

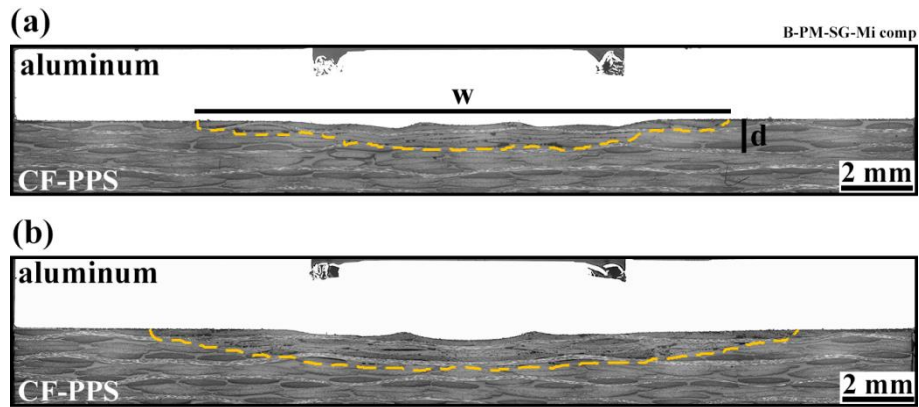


**Figure 7.7** Microstructure of the (a) LHI and (b) HHI joints. Yellow dashed lines indicate the boundary between PHAZ and BM. The PHAZ in the HHI joint shows an extended width ( $w$ ) and depth ( $d$ ) into the composite compared to the LHI joint.

The conducted heat from aluminum is mainly accumulated at the interface, as a result of very low thermal conductivity of PPS, which led to melting of a thin layer of PPS close to the interface. However, due to the high thermal conductivity of the carbon fibers, the heat is dissipated to some extent inside the thickness of the composite, which results in an increase in the depth of the PHAZ.

**Table 7.6** Average width ( $w$ ) and depth ( $d$ ) of the PHAZ, and the obtained average temperature at the interface in LHI and HHI joining conditions.

Joining condition	$w$ [mm]	$d$ [mm]	Average temperature at the interface (TC-3) [°C]
LHI	$14.6 \pm 0.2$	$0.9 \pm 0.06$	345
HHI	$17.7 \pm 0.12$	$1.3 \pm 0.08$	418

The temperature in the PHAZ is higher than the  $T_g$  of CF-PPS as well as being above  $T_m$  in the vicinity of the interface, as mentioned above. Some of the molten PPS matrix is squeezed out of the nub area as explained in Chapter 4. In addition, the viscosity of the molten polymer is reduced, which leads to the entrapment of air pockets in the slowly flowing PPS. As the cooling rate is very fast, these entrapped air pockets cannot escape from the PPS and remain as volumetric flaws in the joint. Since extensive thermal degradation is absent, there is a strong indication that the main type of flaw identified in the PHAZ close to the interface with the aluminum is due to pores and voids. The formation of voids giving rise to defects as a result of air entrapment is also detected in resistance welding [186] and laser welding [216] of thermoplastics. However, the temperature through the thickness of the composite reduces to below  $T_m$ . During the cooling phase, debonding between the PPS matrix and carbon fibers is expected as a result of large differences between the coefficients of thermal expansion of the PPS and fibers. For more details on the formation of defects in the PHAZ, refer to Section 4.3 and Figure 4.12.

In addition to defects, the growth of the spherulitic crystals may also occur in the PHAZ since the temperature is above  $T_g$ . However, investigation into the spherulitic structure and crystal growth was not in the scope of this work.

---

## 7.5 Local mechanical properties

Local mechanical properties in FSpJ are divided into aluminum properties and CF-PPS properties. Microhardness was used to evaluate the local mechanical properties of the AA2024, following the procedure explained in Section 6.3.6.1. For properties of the composite, nanoindentation was used to evaluate the local mechanical properties as explained in Section 6.3.6.2. This section is also divided into two parts; first the local mechanical properties of aluminum are discussed, followed by the results and discussion of the CF-PPS.

### 7.5.1 AA2024-T3

Figure 7.8 compares microhardness maps of the aluminum part of (a) LHI and (b) HHI joints. Due to microstructural symmetry around the center of the spot in FSpJ, only half of the sample was needed to generate the microhardness map. In the x-axis, 0 mm corresponds to the edge of the sample, whereas 12.5 mm is the exact center of the spot. In the y-axis, 0 mm shows the top surface of the aluminum, approaching the interface with the CF-PPS at 2 mm.

From the microhardness maps presented in Figure 7.8 one observes four distinct zones, numbered in Figure 7.8 (b). The BM (Zone 1) with an average hardness of 135 HV starts from the edge of the sample. The BM ends at a distance of approximately 7 mm from the edge for the LHI joint, and ends at approximately 6 mm for the HHI joint. Inhomogeneous distribution of the microhardness map in this zone may be attributed to the distribution of the strengthening particles. In positions where the indenter touches or is very close to the particles, a higher value of hardness was obtained.

The MSZ (Zone 2) with higher hardness compared to the BM is obvious as the upper portion of the aluminum part inside the spot area, with an average hardness of 151 HV. The high hardness in the MSZ is related to the very fine DRX grains as well as re-precipitation of strengthening particles as explained in the previous section.

The area below the MSZ approaching the interface is a mixture of MTMAZ (Zone 3) and MHAZ with an average value of 139 HV. As explained earlier, there are three competing mechanisms taking place in the MTMAZ. From the microhardness results, it seems that strain hardening has a larger influence than dynamic recovery or precipitation coarsening, since the average hardness is higher than the BM.

Finally, the MHAZ (Zone 4) with a much lower hardness of 123 HV is visible between the BM and the beginning of the spot area. Recovery and coarsening of the strengthening particles are the primary mechanisms, leading to a reduction of hardness in the MHAZ.

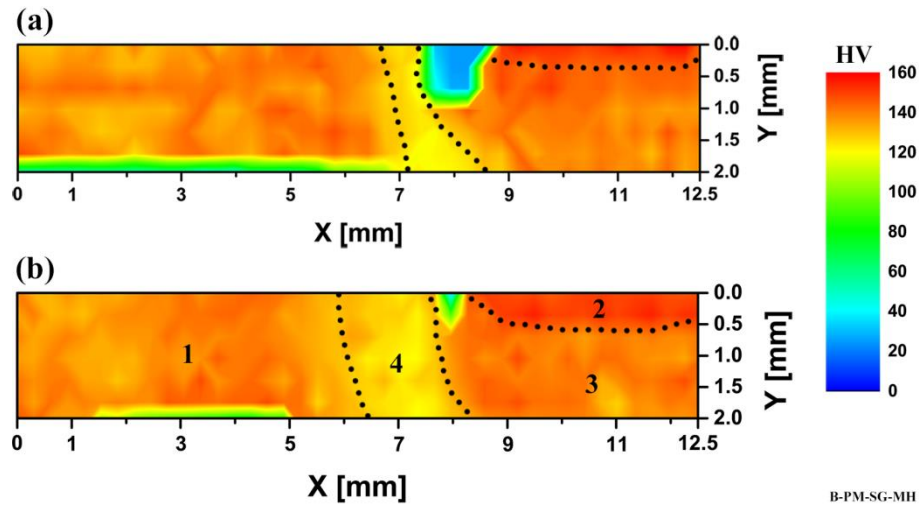


**Figure 7.8** Microhardness maps of the AA2024-T3 from the edge of the specimen ( $x=0$  mm) to the middle of the spot ( $x=12.5$  mm) in the (a) LHI and (b) HHI joining conditions. The observed zones are indicated in (b).

A comparison between the microhardness maps of the LHI (Figure 7.8 (a)) and HHI (Figure 7.8 (b)) joints showed an extended MHAZ in the HHI condition. This was expected, because due to the relatively high thermal conductivity of the aluminum ( $121 \text{ Wm}^{-1}\text{K}^{-1}$ ) a larger amount of heat is dissipated over a larger area. So a temperature increase in an extended area is expected, which leads to a larger MHAZ.

It is worth mentioning that the areas in the figure with very low hardness on top of the aluminum surface and close to the interface result from indents very close to the embedding resin and PPS respectively.

### 7.5.2 CF-PPS

Nowadays, the use of nanoindentation for the mechanical evaluation of composites and nanocomposites is well established [217]. In this technique, a force-displacement curve is traditionally plotted during loading and unloading. Hardness and quasi-static elastic modulus are obtained from the unloading part of the curve, as explained by Oliver and Pharr [218]. Figure 7.9 presents an example of the load-displacement curve of the PPS matrix in the composite's base material, which represents typical behavior reported for nanoindentation. The graph is comprised of a loading and an unloading curve.  $P_{\text{max}}$  in the graph corresponds to the peak indentation load,  $h_{\text{max}}$  is related to the maximum indentation depth, and  $h_f$  shows the final displacement after release of the elastic portion.

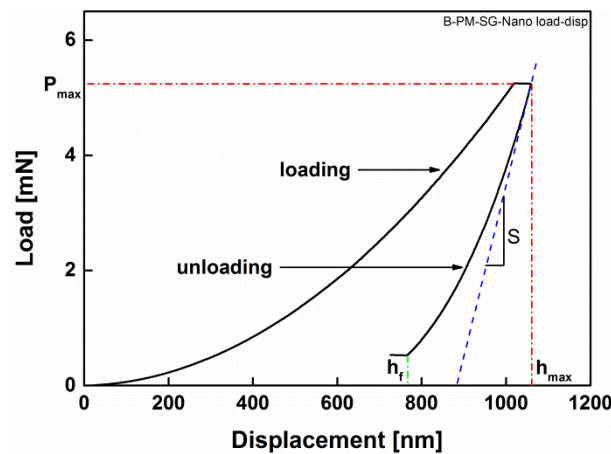


**Figure 7.9** An example of the load-displacement curve obtained through nanoindentation in the CF-PPS base material.  $S$ : stiffness obtained from the unloading curve,  $P_{\max}$ : maximum load achieved in the experiment,  $h_{\max}$ : maximum indentation displacement, and  $h_f$ : final displacement after release of the elastic deformation (Adapted from [218]).

Oliver and Pharr [218] discussed the method to obtain the hardness and stiffness of a material from the unloading curve. In this method, stiffness ( $S$ ) is calculated from a linear fit to the unloading curve as illustrated in Figure 7.9. Hardness is then obtained by dividing  $P_{\max}$  by the projected area of the indenter impression. However, measuring the hardness and stiffness by such a method is limited to the material's giving an elastic or elastic-plastic response [217, 219]. Since polymer materials possess time-dependent deformation behavior, the slope of the unloading curve usually does not represent linear elastic recovery [219] and so may not give the accurate measurements. A more advanced technique of continuous stiffness measurement (CSM) was introduced for materials with time-dependent properties [217-221]. In this technique, a sinusoidal force is superimposed on a quasi-static load during the loading segment [217, 219]. Employing the CSM technique allows dynamic evaluation of the properties as a function of the indentation depth, among other possibilities [217]. Since the goal of this section is not to present a comprehensive overview on the nanoindentation technique, for more information refer to [217-219].

Figure 7.10 illustrates an example of the dynamic indentation modulus and hardness (obtained by CSM technique) of the PPS obtained as a function of displacement into the surface for the BM and for LHI and HHI joints (for the positions of the indents refer to the description in Section 6.3.6.2, Page 47). Oscillation in the modulus curves (Figure 7.10 (a)) is obvious and might be attributed to the surface roughness of the samples. Despite the presence of such oscillation, the average value of the modulus between contact depths of 200 nm to approximately 800 nm is almost constant for all specimens tested. Moreover, the hardness curves in Figure 7.10 (b) show a small decrease in the range 200 nm to 1000 nm of contact depth. This behavior probably occurs as a result of an inaccurate calculation of the contact area. Some of the phenomena that lead to an inaccurate measurement of the contact area are sink-in, pile-up and surface roughness [222]. Surface roughness could be the primary cause of a slightly inaccurate measurement in this work, resulting from the polishing procedure prior to the nanoindentation experiment.

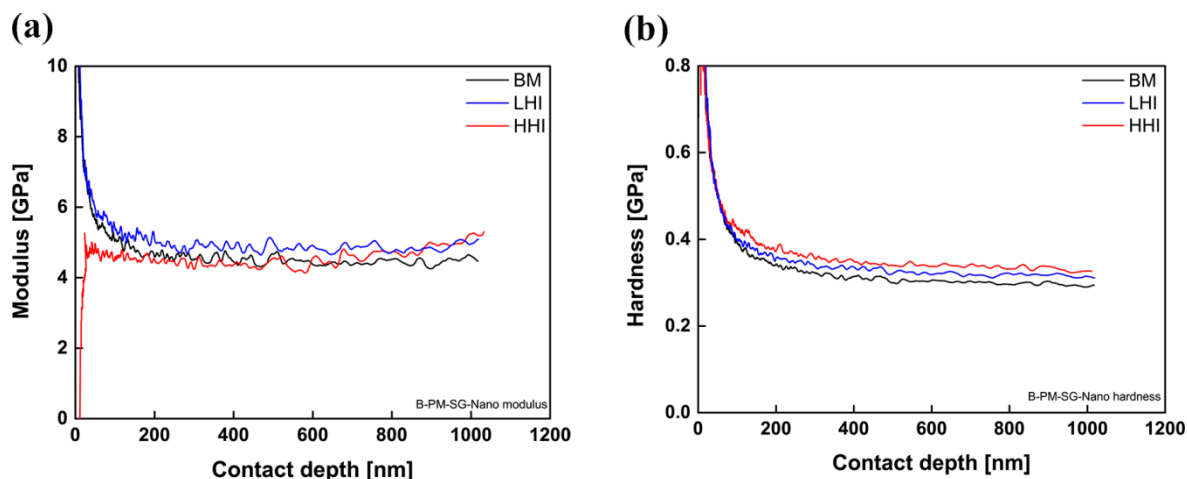


**Figure 7.10** Example of the dynamic indentation (a) modulus and (b) hardness of the PPS as a function of the displacement into the surface for the BM, LHI, and HHI specimens.

The average values of modulus and hardness of the PPS matrix for the BM, LHI, and HHI joints were measured both from the unloading curve according to the Oliver and Pharr method, and from the CSM curves. Since the aim of this section is a qualitative analysis to compare the behavior of the PPS in BM and the joints, there is no difference in using either the Oliver and Pharr method or CSM technique. A summary of the measured data from the unloading segment of the load-displacement curves (Oliver and Pharr method) are listed in Table 7.7 and graphically illustrated in Figure 7.11.

**Table 7.7** Average and standard deviation of indentation modulus and hardness of the PPS obtained from the unloading section of the load-displacement curves.

Joining condition	Modulus [GPa]	Hardness [GPa]
BM	4.7±0.1	0.26±0.005
LHI	5.1±0.47	0.27±0.035
HHI	5.3±0.7	0.28±0.03

The results demonstrated a slight increase in the average of both modulus and hardness of the joints compared to the BM. The HHI specimen demonstrated the highest modulus and hardness. Since the crystallinity of the joints is lower than in the BM (Table 7.5), there must be another phenomenon responsible for the observed increase in the local mechanical properties. Ovsik *et al.* [223] reported an increase in nanoindentation modulus and hardness of Polyamide 12 (PA12) as a result of increased cross-linking. As explained in Section 7.3 cross-linking may occur in PPS during FSpJ, which might be responsible for the higher values of modulus and hardness of the joints compared to the BM. Cross-linking increases the chain entanglement and branching points, and consequently more load is required to overcome the cross-linked structure [40]. The results of nanoindentation along with the presented results of DSC and TGA support the idea of a slight cross-linking taking place in PPS during FSpJ process. Furthermore, no extensive thermal degradation of the PPS is

---

expected, because the local mechanical properties obtained from nanoindentation would otherwise be reduced compared to the BM.

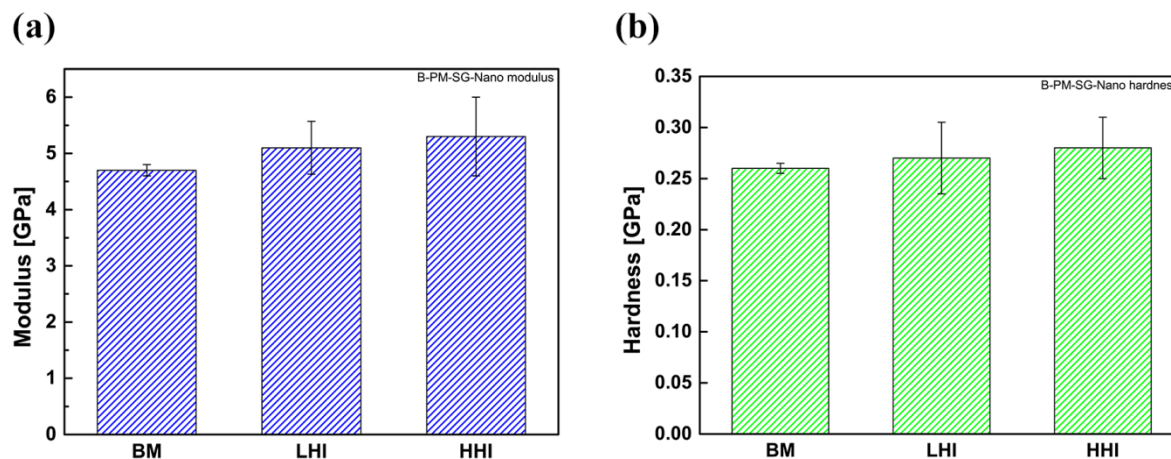


Figure 7.11 Comparison of the indentation (a) modulus and (b) hardness of the PPS from the BM, LHI, and HHI specimens.

## 7.6 Bonding zones, failure, and fracture analysis

### 7.6.1 Bonding zones

With joining technologies gaining an understanding of the bonding mechanisms is crucial for subsequent evaluation of failure mechanisms. As discussed earlier in Chapter 4, two primary bonding mechanisms are present in FSpJ between the metal and composite parts; mechanical interlocking and adhesion forces. It is worth noting that in some of the literature, mechanical interlocking is described as a category under adhesion forces. However, in this work mechanical interlocking mechanisms are differentiated from adhesion forces for simplicity of the discussion.

A simple model was proposed to discuss the bonding zones and failure mechanisms in FSpJ [84]. As illustrated in Figure 7.12 (a), three zones can be identified in the fracture surface of an FSp joint. The first zone corresponds to the area in which the mechanically deformed nub is present and the process temperature was high enough in the region to produce a thin molten polymer layer. This zone is called Plastically Deformed Zone (PDZ). The PDZ is believed to be the strongest part of the joint, as there is intimate contact between the PPS matrix and the carbon fibers with the plasticized aluminum volume. Most of the failure mechanisms, such as cohesive failure inside the PPS and partial fiber breakage, occur in this region. The outer region is the zone in which the flowing molten polymer is consolidated in a few seconds as a result of the very fast cooling rates. This zone is called Adhesion Zone (AZ). There is also a Transition Zone (TZ) identified next to the internal border of the consolidated layer. Due to the low viscosity of the flowing molten polymer during the joining process, air bubbles remain entrapped in this layer. These three zones are not homogeneously distributed around the nub as shown in Figure 7.12 (b), which may be an indication of inhomogeneous heat distribution in the aluminum.

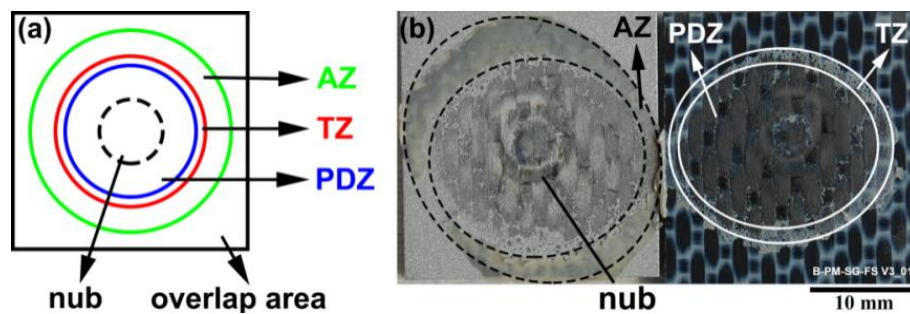


**Figure 7.12 (a) Schematic fracture surface of an FSp joint and (b) real fracture surface of an AA2024-T3 / CF-PPS FSp joint, indicating three bonding zones; plastically deformed zone (PDZ), transition zone (TZ), and adhesion zone (AZ).**

Mechanical interlocking in FSpJ is divided into “macro-mechanical interlocking” and “micro-mechanical interlocking”. Macro-mechanical interlocking is only the result of nub insertion into the composite inside the PDZ. By contrast, micro-mechanical interlocking occurs throughout the bonding area in all three zones. The PPS molten layer flows into porosities and asperities on the surface of the aluminum, creating micro-mechanical interlocking. Another sub-category of mechanical interlocking is fiber entrapment by the aluminum. Some of the carbon fibers become embedded in the aluminum inside the PDZ, by which further micro-mechanical interlocking is achieved. Figure 7.13 (a) and (b) illustrate the cross-section of a joint examined by LSCM showing the micro-mechanical interlocking phenomenon by aluminum pore and crevice filling by the molten PPS, and fiber entrapment in the PDZ. High magnification SEM imaging (Figure 7.13 (c)) shows that in some cases a layer of PPS flows between the carbon fibers and the aluminum. Although direct contact between the aluminum and carbon fibers may improve mechanical performance of the joints by improved micro-mechanical interlocking, it could nonetheless prove detrimental to its corrosion behavior when exposed to a corrosive environment. Therefore, the presence of such a layer may in fact inhibit or reduce the rate of corrosion. Adhesion forces act in the whole bonding area between the molten PPS and aluminum. The main characteristics of the adhesion forces in FSpJ will be thoroughly discussed in the next chapter.

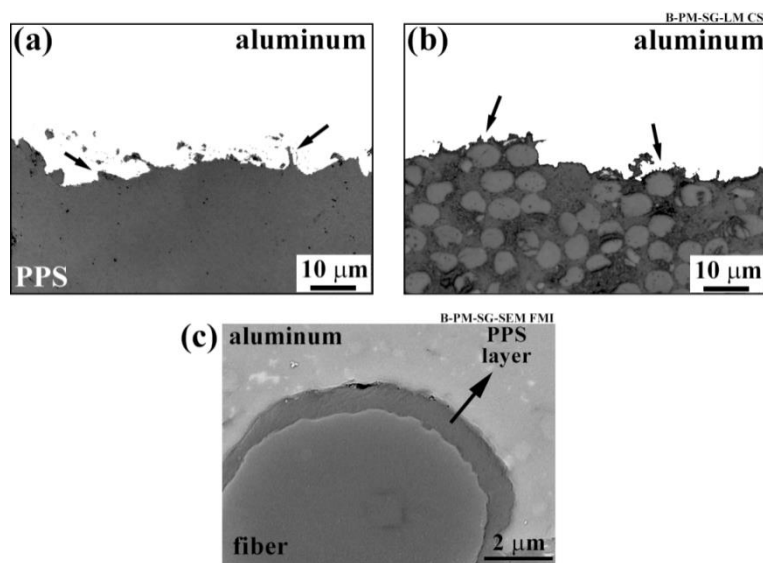


**Figure 7.13** Cross-section of an AA2024-T3 / CF-PPS FSp joint in the PDZ examined by LSCM showing micro-mechanical interlocking through (a) aluminum pore/crevice filling by the molten PPS in a resin-rich area and (b) fiber entrapment. (c) High magnification SEM image showing a thin layer of the PPS between aluminum and carbon fibers.

To summarize, metal-polymer bonding mechanisms in the PDZ consist of macro-mechanical interlocking (as a result of nub insertion), micro-mechanical interlocking (due to metal pore-filling by the molten polymer and fiber entrapment by the metal), and adhesion forces. The mechanisms of bonding in AZ are mainly adhesion forces with micro-mechanical interlocking as a result of aluminum pore-filling by the molten PPS. Similar bonding mechanisms as for the AZ exist in the TZ, although a reduction in bonding forces is expected here as a result of voids at the interface.

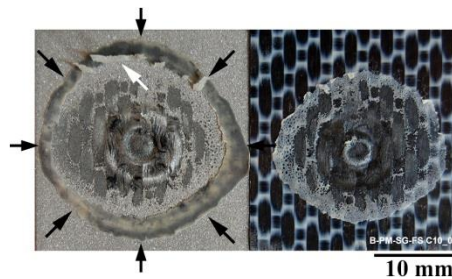
## 7.6.2 Failure analysis

Failure of the FSp joint was analyzed by SLS testing as explained in Section 6.3.7.1. SLS geometry is widely used in the literature, due to its simplicity to evaluate mechanical performance [224] and further develop joining technologies. Although SLS geometry is simple to produce and test a joint it leads to a complex, mixed-mode loading scenario in the specimens [225]. Shear loading (Mode II) in combination with out-of-plane, normal forces (Mode I), as a result of the well-known secondary bending effect [225, 226], are the main loading types with SLS testing [225]. Due to the presence of load eccentricity in the SLS joint, a bending moment and a transverse load is generated as a result of the secondary bending to reduce the eccentricity [29, 30]. The bending of the joining parts and generation of transverse load leads to the formation of out-of-plane, normal stresses known as peeling stress [30]. Peeling stresses increase the stress concentration, especially at the ends of the overlap, which reduces the mechanical performance of the joint. The influence of secondary bending and the resultant peeling stresses have been widely studied for SLS adhesively bonded [30, 225, 227, 228] and mechanically fastened joints [226, 229].

Figure 7.14 illustrates the fracture surface of a joint after lap shear testing that is typical for FSpJ. It is clear from the figure that the FSp joints fail in shear mode through a mixed adhesive-cohesive failure, which was also observed in other combinations of joining parts [20, 179]. According to discussions about the bonding mechanisms, the failure explanation in FSpJ was proposed [84] as

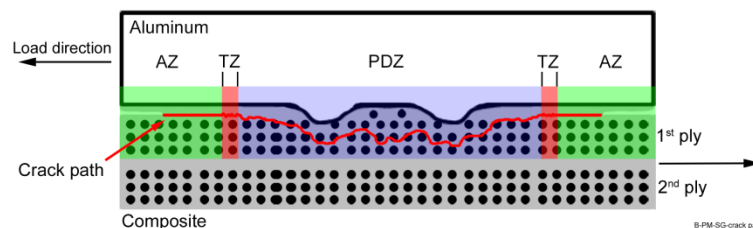
follows. Cracks initiate at the periphery of the AZ (indicated by black arrows in the figure) and radially propagate along the interface between this layer and either the aluminum or composite surface in a plane parallel to the applied loading direction. Should the cracks reach the beginning of the TZ, their path can shift from the interface into CF-PPS. However, the crack's path may switch between the interface and inside CF-PPS depending on the amount and distribution of voids in this zone, representing stochastic crack propagation. The cracks further propagate in the PDZ within a volume close to the metallic nub, in the first ply of the CF-PPS. Two primary cracking zones can be delineated during failure of an FSp joint: crack initiation and propagation zones. The cracking zones can be correlated to the bonding zones as follows: crack initiation zone covers the AZ, whereas crack propagation zone can be divided into two regions. The first crack propagation zone takes place in the TZ and the second zone involves crack propagation in the PDZ. Such crack initiation and propagation behavior lead to a pure adhesive failure in the AZ, also known as interfacial failure [230]. However, cohesive failure was also observed in the PDZ, in which a large amount of polymer matrix and carbon fibers remain attached to the aluminum surface. TZ shows a mixed adhesive-cohesive failure with the adhesive failure being more pronounced.

It is also possible to observe in Figure 7.14 that a part of the AZ (indicated by a white arrow) has failed by tearing perpendicular to the loading plane. This might be an indication of the influence of secondary bending taking place close to the edge of the bonding area, which indeed reduces the lap shear strength of the joints.



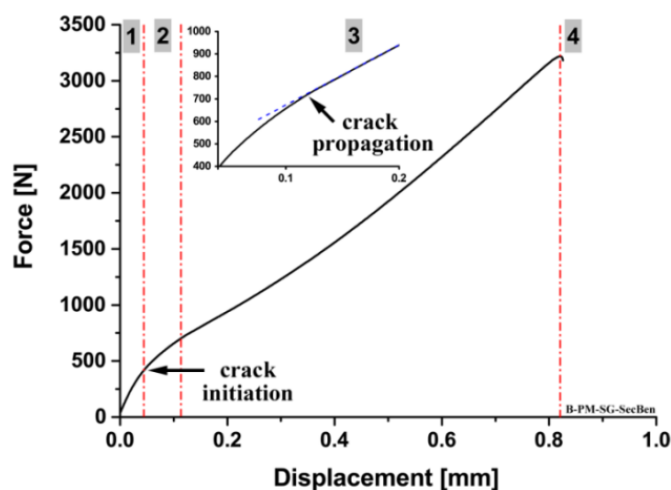
**Figure 7.14 Fracture surface of an AA2024-T3 / CF-PPS FSp joint (produced by the LHI condition) showing the initiation of radial cracks in the external periphery of the AZ. The white arrow indicates the influence of secondary bending on the tearing fracture of the PPS in the AZ.**

Figure 7.15 summarizes the crack propagation behavior of spot joints failing by shear. For simplicity, only unidirectional fibers in the first two plies of the composite are sketched in this figure.



**Figure 7.15 Schematic illustration of the proposed crack propagation mechanism in friction spot joints under shear loading [84].**

To further evaluate the mechanical behavior of the joints, based on the failure mechanisms, one can analyze the load-displacement curve obtained from lap shear testing of a joint. Figure 7.16 depicts a typical load-displacement curve for an FSp joint. It is obvious from the figure that FSp joints show a linear elastic behavior with limited failure displacement. The load-displacement curve can be divided into four zones. Zone 1 shows a linear elastic behavior with a high stiffness. This zone is relatively short and finishes when the cracks start to appear at the periphery of the AZ. Zone 2 corresponds to the propagation of the radial cracks until they reach the TZ, and the AZ has completely failed. This zone shows a reduced stiffness compared with Zone 1 as a result of crack propagation and loss of the AZ. Zone 3 illustrates a return to a quasi-linear elastic behavior with a slightly reduced stiffness compared to Zone 2 (see graph inset depicted in Figure 7.16). The beginning of the crack propagation in the TZ is the start of the third zone. The crack propagation in the TZ, PDZ and finally the area under the nub forms the third zone. The behavior of the joint in this zone is influenced by the secondary bending phenomenon. Similar behavior is reported by Olmedo *et al.* [226], where the stiffness of a bolted composite-composite single lap joint is highly influenced by the secondary bending phenomenon in different failure zones. Formation of peeling stresses as a result of the secondary bending in FSpJ leads to high stress concentration in the inner periphery of the AZ. The third zone ends when the load reaches the ultimate lap shear strength of the joint. Finally, Zone 4 corresponds to the final catastrophic failure of the joint in a short fraction of a second.



**Figure 7.16** An example of the typical load (force) - displacement curve in FSpJ under shear loading divided into four regions. The graph inset shows a section of the curve related to the beginning of the crack propagation.

In order to further understand the characteristics of the FSp joint under lap shear loading, the behavior of the joint was simulated [231] in Abaqus software. A snapshot of the simulation result is presented in Figure 7.17. This figure presents a cross-section of the joint to enable evaluation inside the overlap. As can be seen in the figure, the simulation result confirmed the occurrence of secondary bending at the ends of the joint, where both the aluminum and the composite are deflected to reduce load eccentricity. Deformation in the aluminum is expected to be higher due to its lower elastic modulus compared to CF-PPS, which leads to the formation of higher stress concentrations as can be seen in the simulation result. Large stresses form between the nub and the AZ inside the overlap area. Premature failure of the joint may happen as a result of such stress concentration in a region near to the metallic nub.

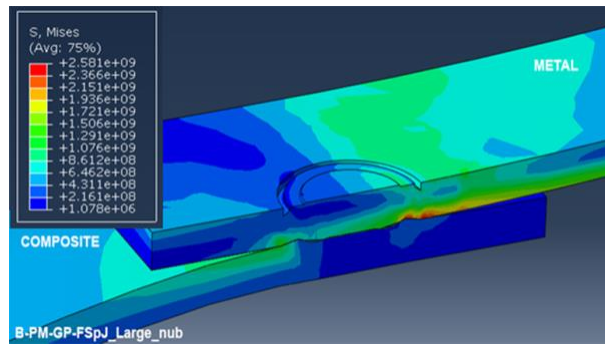


**Figure 7.17** A cross-section snapshot of the AA2024-T3 / CF-PPS FSp joint simulated by finite elements analysis. A region of high stress concentration inside the overlap area between the nub and the edge of the joint is visible [231].

### 7.6.3 Fracture analysis

This part deals with examination of fracture micro-mechanisms in the FSpJ by post-failure SEM analysis. The initiation and propagation zones explained previously can be related to three fracture zones based on roughness features: a very smooth area known as the mirror zone, a quasi-smooth (mist) zone, and a rough zone as explained by Kytopoulos *et al.* [232]. This correlation will be explained in the following text.

Figure 7.18 illustrates an overview of the AZ-TZ boundary both on the aluminum and composite surfaces. As explained in the previous section, cracks initiate at the external periphery of the AZ and propagate into the TZ. As can be observed from Figure 7.18 (a) the AZ (on the aluminum surface) illustrates a very smooth, featureless area known as the mirror zone [232]. The AZ fails and detaches from the TZ by tearing, as shown by the arrows in the figure. Such a tearing failure is similar to those reported in [233] for ductile failure of thermoplastics. The tearing failure is characterized by a smooth area close to the failure site without any noticeable deformed structure (such as fibrils). The AZ on the composite side is depicted in Figure 7.18 (b) where the crack initiation sites are indicated by arrows. The cracks propagate between the consolidated molten PPS layer and the composite, thus no traces of the consolidated layer can be detected on the composite. Note that the color difference in Figure 7.18 (b) between AZ and the CF-PPS surface is due to a manual contrast change, to enable the distinguishing of the AZ.

Stochastic crack propagation can be seen in the TZ where some of the PPS matrix remains attached to the aluminum in the form of individual islands (indicated by arrows in Figure 7.18 (c)). The fracture analysis of the TZ on the composite side (Figure 7.18 (d)) illustrates two primary features: elongated fibrous-like features as in [233] (indicated by the white arrow), and a vein-type feature (indicated by the black arrow), as also reported by Tanniru *et al.* [234]. Figure 7.18 (e) shows a higher magnification of the elongated fibrils (from the elongated fibrous-like region in Figure 7.18 (d)) that indicate a ductile fracture. However, a high magnification of the vein-type features is given in Figure 7.18 (f) and as is apparent in this figure, within the large vein-type features the surface is very smooth, which resembles a brittle fracture. Furthermore, on the edges of both features, tearing of the PPS is clearly visible. Therefore, the TZ shows a quasi-smooth (mist) area [232] with a mixed brittle-ductile fracture.

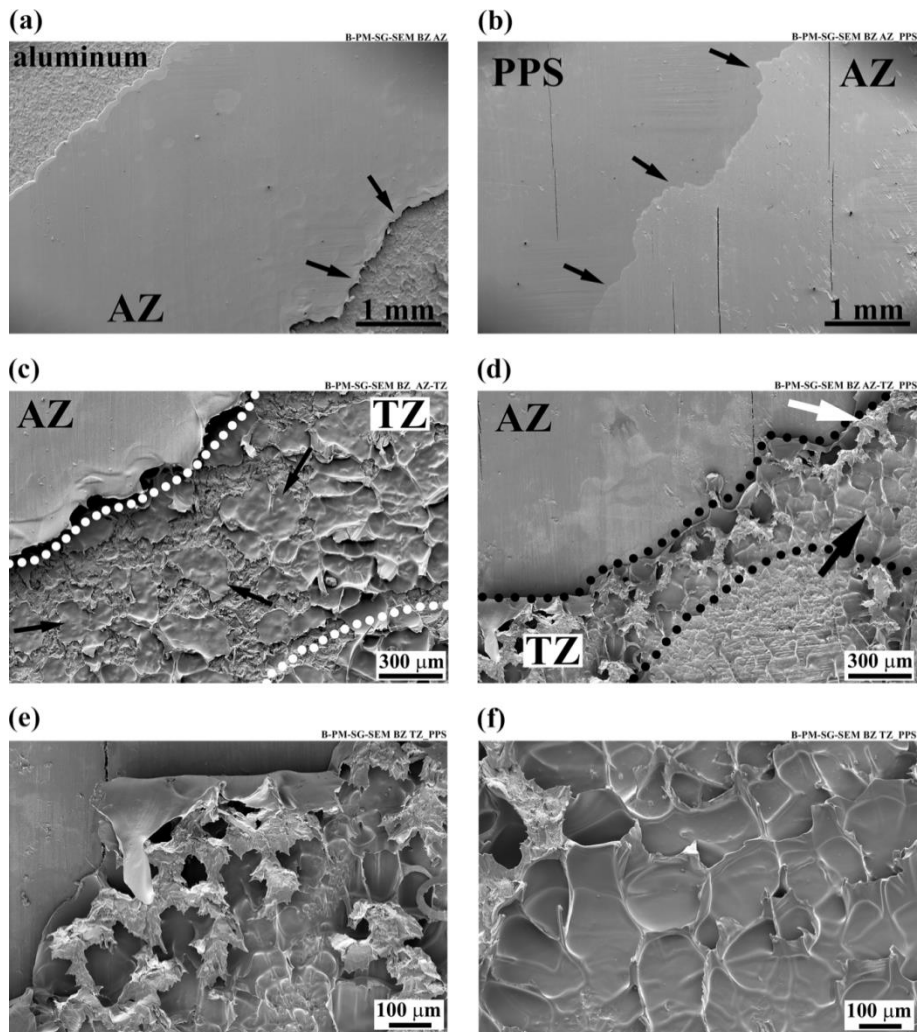
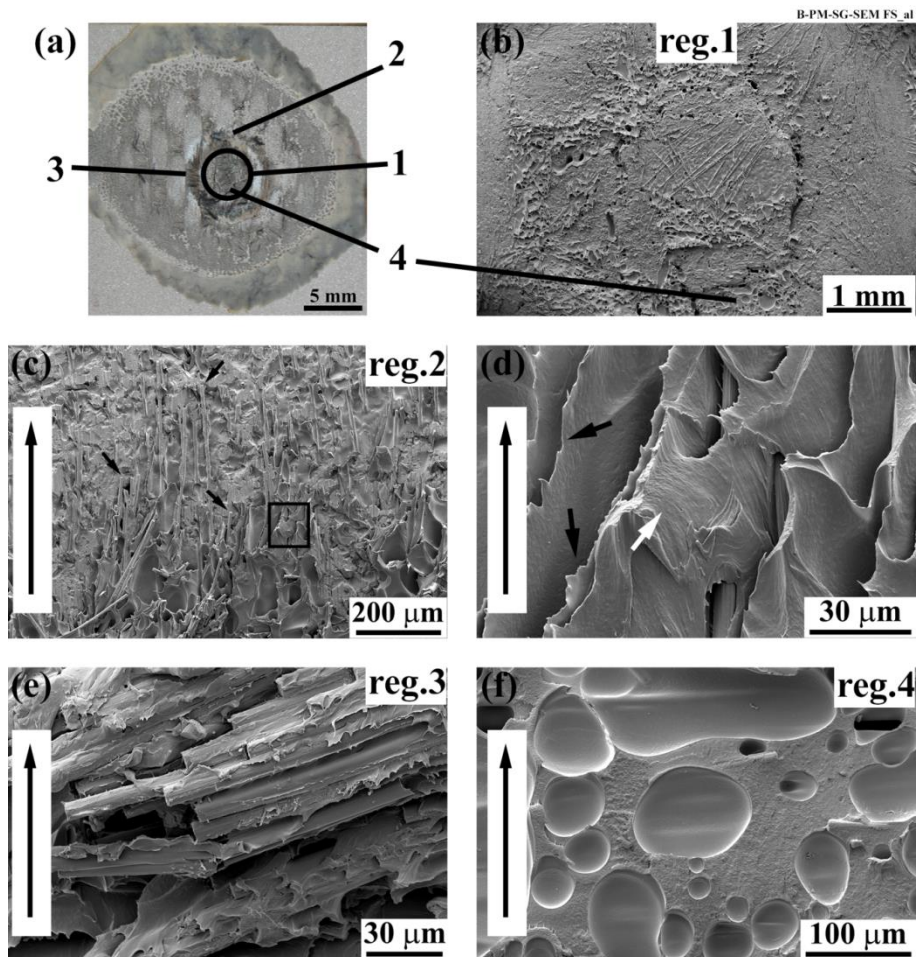


Figure 7.18 SEM fracture surface examination of the AA2024-T3 / CF-PPS FSp joint (an example of a HHI joint); (a) AZ on the aluminum, (b) AZ on the composite, (c) AZ-TZ boundary on the aluminum showing pieces of the PPS remaining attached as individual islands inside the TZ, (d) AZ-TZ boundary on the composite showing fibrous-like (indicated by the white arrow) and vein-type (indicated by the black arrow) features in the TZ, (e) magnified image of the fibrous-like features, implying a ductile fracture, and (f) magnified image of the vein-type features showing a smooth area inside, implying a brittle fracture. Note that in these figures the path of the radial cracks follow from top-left to bottom-right of the images.

---

Turning now to the fracture mechanisms in the PDZ as the main crack propagation zone, Figure 7.19 displays the main features on the aluminum side. The SEM image of the nub area (as indicated by the circle in Figure 7.19 (a)) is depicted in Figure 7.19 (b). It is visible from this figure that the whole surface of the aluminum is covered completely by the PPS. A fraction of the carbon fibers is also apparent, especially on the center of the spot. This is a clear indication that the cracks propagate inside the first ply of the CF-PPS, as illustrated in Figure 7.15. Fiber pull-out is another fracture micro-mechanism that was observed in the FSp joint. Figure 7.19 (c) shows carbon fibers (indicated by the black arrows) that were pulled-out from the composite and remain attached to the aluminum surface. These fibers come from the warp direction in the composite, which were probably entrapped by the aluminum at the interface. Fiber-pull out is a well-known fracture mechanism in composites, which dissipates energy through fiber breakage and friction between the extracted fiber and matrix [113]. Fiber pull-out as a result of micro-mechanical interlocking was also reported by Balle *et al.* [57] in the ultrasonic welding of aluminum-CFRP. In addition to the pulled-out fibers, some of the PPS matrix was also detected on the aluminum. Figure 7.19 (d) magnifies a piece of the PPS matrix that remained on the aluminum as indicated by the rectangle in Figure 7.19 (c). Tearing of the PPS is one of the primary fracture micro-mechanisms apparent in the figure (also indicated by the black arrows). However, as indicated by the white arrow, a feature that resembles a drawing of the fibrils can also be seen, suggesting plastic deformation of the PPS. It seems that the PPS matrix is plastically deformed under complex combined shear and peeling stresses. As soon as the generated stresses exceed the local strength of the PPS, it fails through tearing. In addition to the warp fibers, fibers in the weft direction also contribute in the failure mechanisms. Figure 7.19 (e) displays pieces of the weft fibers that are broken and remain attached to the aluminum. Since the weft fibers are perpendicular to the loading direction, when the local stresses exceed the transverse strength of the carbon fibers, fracture of the fibers occurs, leading to detachment of the fibers from the PPS matrix. Finally, as shown in Figure 7.19 (f) areas with a very smooth, brittle fracture with micro-voids in the attached PPS material can be seen, especially inside the nub (Region 1). Since the micro-voids may act as stress concentration sites, micro-flaws originate from such voids. In areas where the density of the voids is high, coalescence of such micro-flaws leads to a very fast fracture in a brittle manner with a smooth appearance. The voids in this figure are believed to be formed during the FSpJ process as a result of air entrapment in the low viscosity PPS molten layer as discussed in Chapter 4, Section 4.3.



**Figure 7.19 SEM fracture surface examination on the AA2024-T3 side from four regions indicated in (a), (b) general overview in the center of the spot showing PPS matrix and carbon fibers remain attached to the aluminum, (c) Pulled-out warp carbon fibers and some of the PPS matrix attached to the aluminum due to the micro-mechanical interlocking phenomenon, (d) high magnification image of the PPS matrix from (c) illustrating plastic deformation of the PPS (indicated by the white arrow) and tearing (indicated by black arrows), (e) some of the weft carbon fibers remain attached to the aluminum, while most of the fibers are partially covered by the PPS matrix, and (f) high magnification of a region with high concentration of voids; showing a very smooth, brittle fracture in the vicinity of the voids. Direction of the applied load is indicated by the arrows in (c), (d), (e), and (f).**

---

The main features of the composite fracture surface in the PDZ were examined in five regions as indicated in Figure 7.20 (a). The SEM images of these regions are illustrated in Figure 7.20 and continue in Figure 7.21. Figure 7.20 (b) reveals an overview of the spot area in which parts of the carbon fibers are shown to be slightly distorted, as indicated by arrows. Distortion of the fibers probably occurs during the joining process, due to the fact that the viscosity of the PPS is largely reduced and the molten PPS squeezed out of the region. As one of the roles of the matrix in composites is to tightly hold the fibers together, an outward flow of molten PPS results in less matrix material around the carbon fibers, which can lead to slight distortion and rearrangement of the fibers.

The zone containing warp fibers (Figure 7.20 (c)) shows a very rough surface involving large PPS fibrils elongated in the loading direction (the loading direction is shown with an arrow). The lengths of the fibrils were measured and they demonstrated a range between tens of microns to approximately 100  $\mu\text{m}$ . In polymer composites a fibrous fracture with fibrils more than 10  $\mu\text{m}$  in length implies ductile fracture [233]. Therefore, ductile fracture is the main feature in this area. In addition, tearing is shown to be the primary fracture micro-mechanism in this zone, which follows after the occurrence of a large plastic deformation of the PPS matrix. Tearing at the end of the fibril plastic deformation is shown in the high magnification image in Figure 7.20 (d). As discussed earlier, fiber pull-out is another fracture mechanism detected in the FSpJ as some of the warp fibers remain attached to the aluminum after the joint failure. The fiber pull-out mechanism can also be seen on the composite side as illustrated in Figure 7.21 (a). The white arrow in the figure shows a region (valley) where a fiber was pulled-out from the PPS matrix.

However, the area of the composite containing weft fibers shows mainly fractured fibers (Figure 7.20 (e)). The weft fibers, which are aligned perpendicular to the loading direction, break when the local stress exceeds their transverse strength. A high magnification image of the broken weft fibers is depicted in Figure 7.20 (f). Some pieces of the fibers are bent in the direction of the applied load prior to their failure. The broken fibers remain attached to the aluminum as displayed in Figure 7.19 (e). Details of the fracture mechanism that takes place in the weft fibers are shown in Figure 7.21 (b). As indicated by the black arrows in this figure, micro-voids are generated at the fiber-matrix interface. Such micro-voids act as the origin of micro-cracks. The coalescence of such micro-cracks forms a larger crack that will propagate either along the fiber-matrix interface or into the fiber. In cases of strong adhesion between carbon fibers and the PPS matrix, the transverse strength of the fibers is overcome as a result of high local stresses and so the crack propagates into the fiber, resulting in fiber fracture as shown in Figure 7.20 (f). However, if fiber-matrix adhesion is reduced (for instance by process-induced softening of the PPS matrix because of the high temperatures involved), the crack propagates at the fiber-matrix interface, leading to debonding and PPS matrix fracture by final tearing, as illustrated in Figure 7.21 (b). The crack propagation path is clearly apparent in the figure, as also indicated by the smaller white arrows (top of the figure). One can also see large plastic deformation of the PPS matrix and the tearing fracture along the fiber-matrix interface. The latter is indicated by larger white arrows (at the bottom) in the figure.

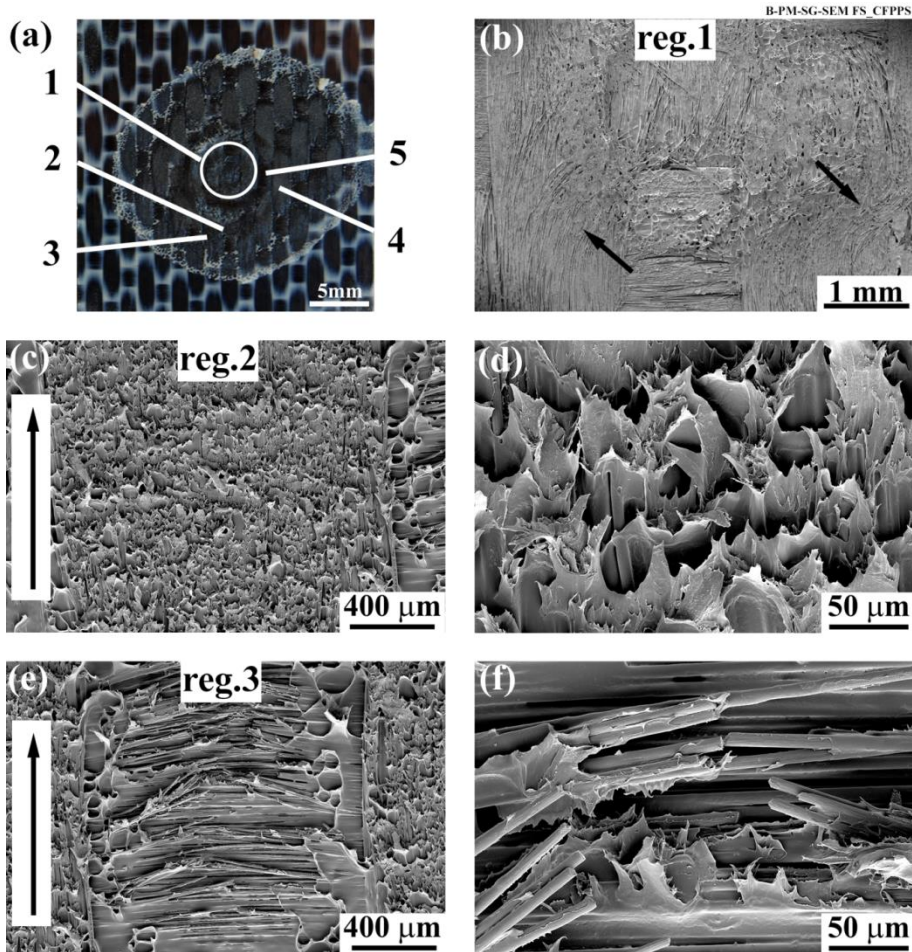


Figure 7.20 SEM fracture surface examination on the CF-PPS side from the regions indicated in (a), (b) general overview in the center of the spot, where slight distortions of the fibers are indicated by the arrows, (c) elongated fibrils in an area containing warp fibers resembling a ductile fracture, (d) high magnification of the fibrils in (c) where the tearing fracture at the ends of the fibrils is apparent, (e) broken weft fibers, and (f) high magnification of the broken weft fibers where slight rotation of the fibers in the direction of the applied load is visible. Direction of the applied load is indicated by the arrows in (c) and (e).

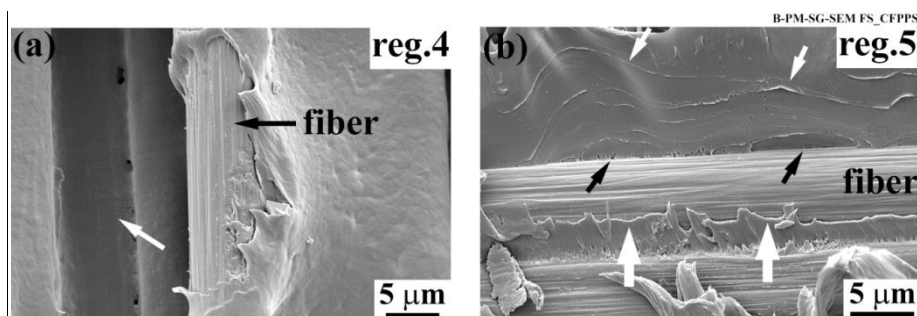


Figure 7.21 (a) High magnification image of the warp fibers region in which the white arrow indicates an impression of a pulled-out fiber, (b) high magnification image of the fiber-matrix debonding in a weft fiber as a result of weakened fiber-matrix adhesion. Black arrows indicate some micro-voids acting as crack initiation, smaller white arrows (top) show crack propagation path and larger white arrows (bottom) illustrate a tearing fracture along the fiber-matrix interface.

---

All in all, the SEM images reveal a three-dimensional rough surface in the PDZ on the composite side that resembles the rough area in the crack propagation zone as discussed by Kytopoulos *et al.* [232].

To summarize the fracture micro-mechanisms: The adhesion zone (AZ) is characterized by a very smooth, featureless area known as a mirror zone. PPS did not show any deformation in the AZ resembling a brittle fracture. The transition zone (TZ) showed a mixture of an elongated fibrous-like region and a smooth veined-type area. Therefore, TZ is characterized by a quasi-smooth (mist) area and a mixture of ductile and brittle fractures. Finally, the plastically-deformed zone (PDZ) showed a mixture of various fracture micro-mechanisms. Some of the warp fibers from CF-PPS were broken and pulled-out of the matrix. In addition, pieces of the weft fibers were broken and remained attached to the aluminum. The PPS matrix showed elongated fibrils in the direction of the applied load. The fibrils had a length of between tens of microns to approximately 100 microns, implying a ductile fracture. Fiber-matrix debonding was also detected in this zone. All in all, the failure micro-mechanisms in an FSp joint showed a mixture of ductile and brittle fractures.

---

## Chapter 8. Influence of the Aluminum Surface Pre-treatments on the FSp Joints

In this chapter, the influence of the selected aluminum surface pre-treatments mentioned in Section 6.3.8 (Table 6.4) on the mechanical performance of the FSp joints will be discussed. The term pre-treatment is used because these were treatments applied to the aluminum surface prior to the joining process. To explain the mechanical performance of pre-treated AA2024-T3 / CF-PPS FSp joints, the effects of pre-treatment on the surface features of the aluminum are first addressed. To compare the performance of the selected aluminum surface pre-treatments, an optimized set of joining parameters obtained from the process optimization study was used (refer to Section 7.1). The joining parameters selected were: RS (2900 rpm), PD (0.8 mm), JT (4 s), and JP (0.3 MPa). As only one set of joining parameters was used, the formation of the nub was similar in all cases and hence the macro-mechanical interlocking was too. So in this chapter the influence of the aluminum surface pre-treatments on the adhesion forces and micro-mechanical interlocking will be explained. It is worth mentioning that surface pre-treatment of the composite also underwent preliminary investigation. For this purpose, plasma pre-treatment was used for some of the composite specimens. However, the SLS strength of the joints using plasma pre-treated composite did not result in any appreciable difference in strength over the as-received composite samples (Appendix A.6). This was probably due to the melting of the surface PPS matrix during the joining process, leading to the elimination of any pre-treatment influence. Therefore, the main focus of this part of the work was put on the surface pre-treatment of the aluminum specimens.

### 8.1 Aluminum surface analysis

Mechanical interlocking and adhesion forces are the primary bonding mechanisms found in FSpJ. So any alteration on the surface of the aluminum (surface morphology and chemistry) will influence the bonding mechanisms and hence the strength of the FSp joints. Accordingly, it is of utmost importance to examine and understand the aluminum surface modifications as a result of the surface pre-treatments.

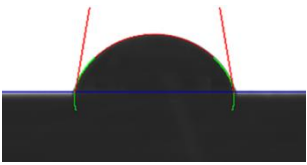
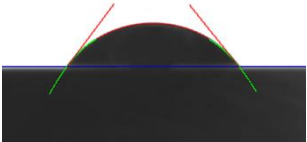
#### 8.1.1 Wettability

It is well-known from the principles of adhesive bonding that the surface energy of the substrate must be greater than or equal to the adhesive to achieve a complete wetting, good adhesion, and so increased mechanical performance [32, 72, 73]. It is believed that in FSpJ increasing the surface energy of the joining parts will increase the wettability of the surface for the molten PPS. One way to increase the surface energy is by performing a surface pre-treatment [32, 74].

Water contact angle measurement was used to evaluate the wettability of the aluminum surface after the pre-treatments. Table 8.1 summarizes the results obtained from static contact angle measurements. One can observe from this table that all the surface pre-treatments used decreased the water contact angle compared to the as-received (AR) specimens. Among all the pre-treatments tested, chemical and electrochemical pre-treatments proved more efficient than mechanical pre-treatments. A reduction in the water contact angle can be attributed primarily to the removal of the

contaminations and the natural aluminum oxide ( $\text{Al}_2\text{O}_3$ ) from the aluminum surface. To improve the adhesion between the molten PPS and the aluminum, obtaining a surface with less contamination plays an important role. High surface energy as a result of reduced contamination enhances the adhesion forces between the PPS and the aluminum.

**Table 8.1 Water contact angle measurements and an example of the water droplet on the AA2024-T3 surface after various pre-treatments.**

Surface pre-treatment	Contact angle [degrees]	Example of the water droplet on the surface
AR	79±2	 A photograph showing a water droplet on a smooth, untreated aluminum surface (AR). The droplet is nearly spherical, indicating high surface energy and low wettability. Red and green lines are drawn tangent to the droplet's edges to measure the contact angle.
MG	50±2	 A photograph showing a water droplet on a surface treated with mechanical grinding (MG). The droplet is more spread out than on the AR surface, indicating improved wettability. Red and green lines are drawn tangent to the droplet's edges to measure the contact angle.
SB	35±2	 A photograph showing a water droplet on a surface treated with sandblasting (SB). The droplet is significantly more spread out, indicating further improved wettability. Red and green lines are drawn tangent to the droplet's edges to measure the contact angle.
Chemical and electrochemical pre-treatments, as well as mechanical + chemical pre-treatments	< 5	No image could be obtained as a result of very low contact angle and instability of the water droplet

In addition to the cleaning effect of the surface pre-treatments used in this work, the positive effects of increased surface roughness was observed, particularly resulting from mechanical pre-treatments. As Wenzel argues [80], increased effective surface area due to the generation of macro-rough and micro-rough asperities improves the wettability of the aluminum surface. Sandblasting proved an effective pre-treatment, producing a very macro-rough surface, which indeed led to an effectively large surface area on the aluminum and so improved wettability. Even simple manual mechanical grinding (MG) reduced the contact angle by approximately  $30^\circ$  compared to the AR samples, as a result of larger effective surface area. Chemical and electrochemical pre-treatments resulted in a surface with highly micro-rough asperities, which reduced the contact angle enormously, to below  $5^\circ$ . Aspects of aluminum surface morphology will be further discussed in the next sub-section.

Physicochemical alteration of the surface is another issue that should be taken into account. Surface energy is also changed as a result of modifications to the surface composition. Even mechanical pre-treatments, such as sandblasting, may alter the surface energy as a result of varying the chemical composition (depending on the medium used for the pre-treatment), as reported for example in [77].

---

In summary: removal of surface contaminations, generation of macro-rough and micro-rough asperities, and alteration of the surface chemical composition led to enhancement of the surface energy and improved wettability of the surface of the AA2024-T3.

### **8.1.2 Surface topography and morphology**

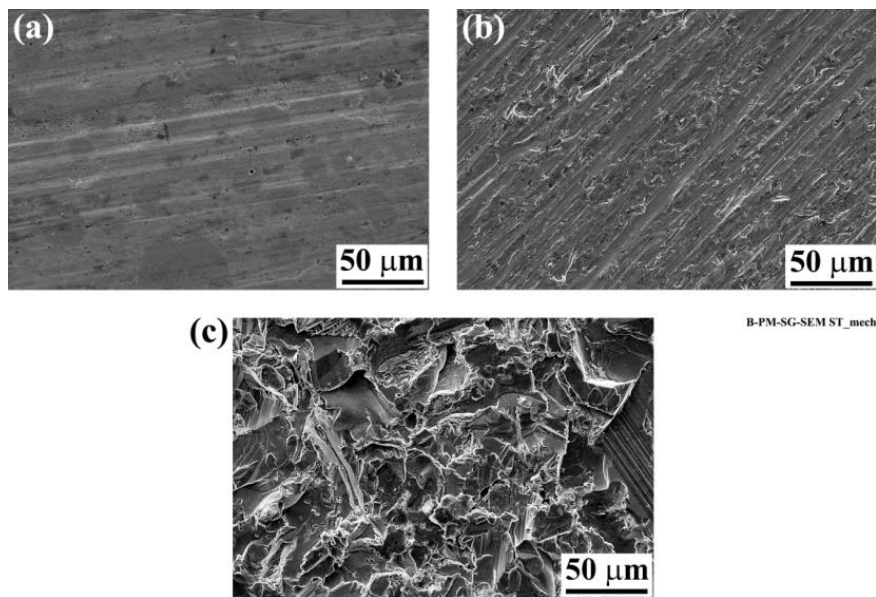
Obtaining a rough surface, to a certain extent, was one of the primary motivations to employ various surface pre-treatments. In particular, the aim was to achieve a macro-rough surface as a result of mechanical pre-treatments and a micro-rough surface through the application of the chemical and electrochemical pre-treatments. Table 8.2 lists the average surface roughness parameters ( $R_a$  and  $R_z$ ) of the AA2024-T3 after applying each surface pre-treatment. It is apparent from the table that both MG and SB successfully increased the aluminum surface roughness compared to the AR state, and the increase was much more using SB. Obviously excessive surface roughness is detrimental to the mechanical performance, because larger asperities can act as barriers to the molten polymer flow and hence reduce the bonding area. Despite this, such a negative effect was not detected in this work. SB generated a macro-porous aluminum surface that effectively increased the micro-mechanical interlocking. In particular, very large  $R_z$  shows the ability of the SB specimens to accommodate a large amount of molten PPS. Chemical pre-treatments did not show any influence on the  $R_a$ , although they did increase  $R_z$  and that can slightly contribute to an increase in mechanical interlocking. It is interesting that CC pre-treatment produced the same surface roughness as AP pre-treatment, but much faster (1 min as opposed to 15 min of pre-treatment respectively). This may be related to the effectiveness of the fluoride ions in the CC solution in rapidly attacking the aluminum surface [87]. A combination of mechanical (SB) and chemical pre-treatments also resulted in a large surface roughness. However, the values of  $R_a$  and  $R_z$  were reduced, compared to the stand alone SB. This is in fact due to partial removal of surface ridges by the chemical etching.

Electrochemical pre-treatments produced similar surface roughness to chemical pre-treatments. It should be noted that in cases of chemical and electrochemical pre-treatments a very fine microporous oxide layer is expected to be formed. It seems that in such cases the effectiveness of surface roughness analysis is questionable.

**Table 8.2 Average surface roughness parameters of the AA2024-T3 after various surface pre-treatments obtained by non-contact LSCM.**

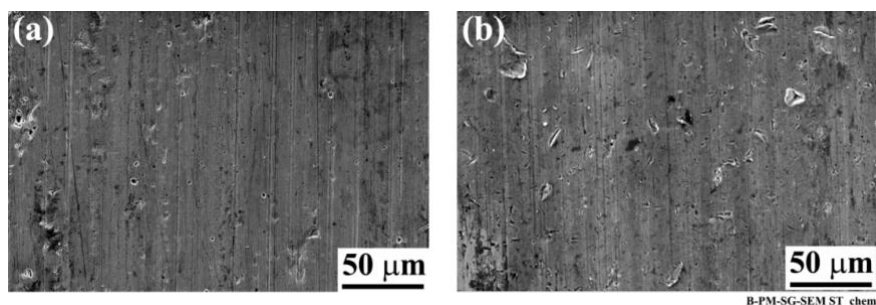
Category	Surface pre-treatment	R <sub>a</sub> [μm]	R <sub>z</sub> [μm]
	AR	0.4	16.9
Mechanical	MG	0.7	30.1
	SB	5.2	100.1
Chemical	AP	0.4	32.8
	CC	0.4	32.7
Mechanical & Chemical	SB+AP	3.9	69.4
	SB+CC	3.9	75.8
Electrochemical	SAA	0.8	38.2
	PAA	0.6	38.8
	PAA-P	1.1	21

SEM was used to examine the morphology of the oxide layer on the aluminum surface. As can be observed in Figure 8.1 (a), the AR specimens showed a smooth, featureless surface. Only some rolling lines are visible on the surface. The smoothness of their surfaces was confirmed by the results of surface roughness analysis presented above in Table 8.2. Unlike the AR specimens, the mechanically ground samples had slightly rough, parallel lines from the final stages of manual grinding in one direction (see Section 6.3.8 for MG procedure), as shown in Figure 8.1 (b). The generated groove-like features and some other irregularities on the surface led to a slightly higher surface roughness, as shown in Table 8.2. However, markedly more modification by mechanical pre-treatment was identified on the SB surfaces. As illustrated in Figure 8.1 (c), with SB a very rough surface with different irregular shapes was obtained. The molten PPS layer can readily penetrate into porosities and crevices leading to a strong micro-mechanical interlocking effect. As explained in Section 3.2.1 (Figure 3.7), the shape and angle of surface asperities play an important role in mechanical interlocking between polymer and substrate, which in turn influences the mechanical performance of a joint. It is believed that as SB generated asperities with various shapes and angles it can effectively increase micro-mechanical interlocking, both under shear and normal loading. Furthermore, the larger effective surface area obtained by SB increases the contact between PPS and the aluminum, leading to the promotion of adhesion forces across an extended area.



**Figure 8.1 SEM images of the AA2024-T3 surface from (a) AR, and after (b) MG and (c) SB pre-treatments.**

The surface features of the chemically pre-treated aluminum are shown in Figure 8.2. Both AP and CC pre-treatments led to surfaces very similar to the AR surface. No specific features could be identified apart from some slight scratches and localized etch pits. The rolling lines were also retained to some extent after both pre-treatments. Chemical conversion treatments, for example Ti/Zr, usually lead to the formation of a uniform layer consisting of spherical particles [87, 90]. In the current work we did not detect such a layer on the surface of the CC pre-treated aluminum. This could be due to differing chemical compositions of CC solutions and to the duration of the treatment being shorter in this study. An investigation of the changes in the CC pre-treatment procedure is beyond the scope of this work. The influence of parameters such as duration of pre-treatment, concentration of solution, etc. on the formation and morphology of the CC layer was not considered.



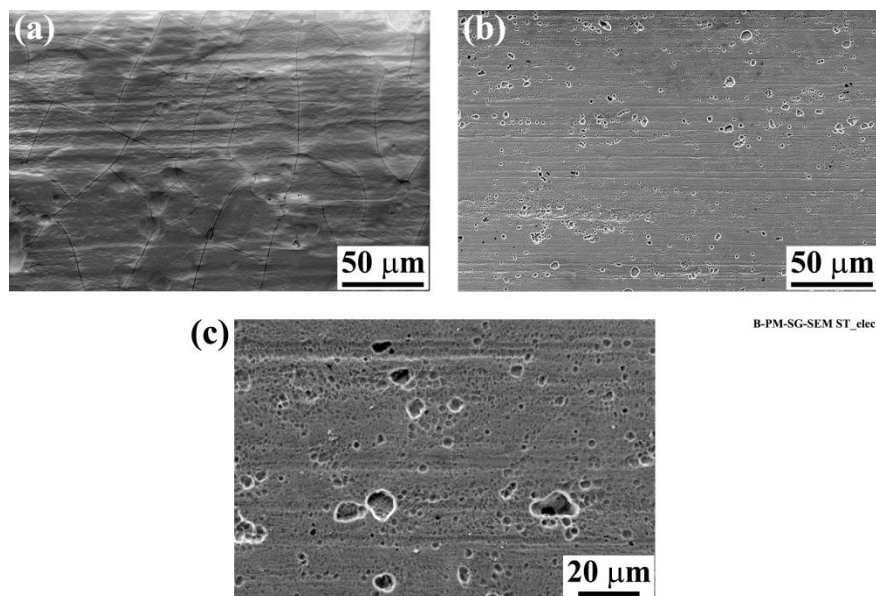
**Figure 8.2 SEM images of the AA2024-T3 surface after (a) AP and (b) CC pre-treatments.**

Figure 8.3 illustrates the aluminum surface features after electrochemical pre-treatments. The SAA pre-treated surface (Figure 8.3 (a)) demonstrated a combination of aspects. Firstly, the surface showed an incomplete coverage, which most probably occurs at the grain boundaries. Such a structure was observed by Lunder *et al.* [93] in the chromate conversion coating of AA6060, and a similar feature was also found by Critchlow *et al.* [75] in the chromic acid anodizing of AA2024-T3 clad. Secondly, very few scalloped features could be identified, similar to [75, 93]. In addition, a

---

few shallow rolling lines were still observed on the surface. The presence of these features can increase the micro-mechanical interlocking between the molten PPS and the oxide layer, leading to an increase in the strength of the joints. At low magnification (Figure 8.3 (b)) the PAA pre-treated specimens showed a porous surface with relatively small generated pores. A higher magnification image of the surface (Figure 8.3 (c)) revealed a very porous oxide layer, similar to those reported in the literature [94, 96, 235, 236]. A few larger pores were also detected on the surface. Such very fine porous structure promotes the micro-mechanical interlocking phenomenon and is believed to increase the strength of the joint. It was reported [96] that such a fine porous structure is responsible for achieving strong joints in adhesive bonding as well. It is however important to mention that, in contrast to the adhesive bonding, for FSpJ a very fine porous structure may not prove so beneficial. Due to the fact that PPS is in a molten or softened state only for a few seconds, there may not be enough time for it to complete the pore penetration and result in effective micro-mechanical interlocking. This aspect of completing the pore filling is especially important for achieving a durable joint, as discussed by Digby and Packham [69]. The durability aspects of FSpJ will be discussed in the next chapter.

Figure 8.4 shows a low magnification SEM image of the surface of the aluminum after PAA pre-treatment and the subsequent application of primer. The surface illustrated has a very dense and compact structure with very small and elongated whisker-like particles deposited homogeneously on the surface. These particles were examined by means of EDS, which showed the presence of strontium oxide and chromium oxide. The chemical composition of the aluminum surface will be discussed next. As mentioned in the literature review (Section 3.3.4), a primer can adjust the surface energy of aluminum and dissolve some organic contaminations on the surface [103]. Such characteristics improve the wettability, as demonstrated by a very low contact angle of less than  $5^\circ$ , as shown in Table 8.1.



**Figure 8.3 SEM images of the AA2024-T3 surface after (a) SAA and (b) PAA pre-treatments, and (c) high magnification image of the PPA pre-treated surface.**

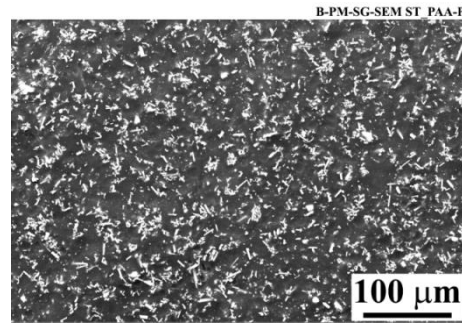


**Figure 8.4 SEM image of the AA2024-T3 surface after PAA-P pre-treatment.**

### **8.1.3 Surface chemical composition**

In addition to the topography and morphology of the surface, which affect micro-mechanical interlocking, alteration of the chemical composition as a result of surface pre-treatments influences the adhesion forces between the PPS and AA2024-T3. Therefore, the surface chemical composition of the aluminum was also investigated, using EDS and XPS.

Figure 8.5 illustrates the EDS spectra of the aluminum surface in the AR condition and after the various surface pre-treatments. As examples here, the spectrum of only one surface pre-treatment sample in each category is shown in this figure, but the average surface chemical compositions of all the surface pre-treated specimens is tabulated in Table 8.3. The spectra selected were for those specimens with highest mechanical performance in each category (see Section 8.2). It is clearly visible that apart from the PAA-P specimens the amount of surface carbon is reduced by all other surface pre-treatments, compared to the AR condition. This is one of the reasons why the wettability of the aluminum surface was increased and the water contact angle reduced (see Table 8.1). Organic contaminations may adhere to the aluminum due to the aluminum sheet processing or during the machining of the coupon specimens. Such contaminations are not easily eliminated by a simple wiping procedure (in AR condition) and often require a stronger surface cleaning. In addition, the PAA-P specimens showed a high amount of carbon on the surface, confirming the presence of a thick layer of the primer.

In all surface pre-treated specimens, the amount of Cu and Mg was also reduced, compared to the AR samples. This is probably due to the removal of secondary particles by mechanical pre-treatment or dissolution of the particles by chemical and electrochemical pre-treatments. In the PAA-P specimens, no Cu or Mg could be detected due to the deposition of the primer layer. The variation of Al and O was slightly different as a result of surface pre-treatments. It seems that to some extent MG removed the aluminum's natural oxide leading to a higher amount of Al and lower amount of O. By contrast, SB, AP, and CC did not change the composition drastically. It is believed that the oxide layer generated by these surface pre-treatments was not extended or thickened, compared to the AR condition. Similar behavior was also reported in [237] for mechanical and chemical surface pre-treatments of AA2024.

However, SAA and PAA pre-treatments showed a high amount of O, implying the formation of a thicker oxide layer on the aluminum surface after the anodizing process. Comparing the amount of O and Al for SAA (O: 49.9%; Al: 38.3%) and for PAA (O: 14.9%; Al: 76.9%) pre-treatments suggests that the oxide layer formed after SAA pre-treatment was much thicker than the PAA one.

---

This agrees with the results published in the literature [99]. Nevertheless, another reason for the high amount of O in the SAA specimen could be attributed to absorbed water. As explained in Section 3.3.3 (Page 18), the SAA pre-treated aluminum is highly susceptible to water absorption [99, 100]. A small amount of sulfur was also detected on the surface of the SAA pre-treated samples due to the anodizing solution, which contained sulfuric acid, and this could be related to the formation of aluminum sulfate [100]. A low concentration of P could also be detected on the surface of the PAA pre-treated aluminum. Phosphorous is reported to form an  $\text{AlPO}_4$  monolayer on the top surface of aluminum [98, 238, 239].

Moreover, the PAA-P specimens showed a very low amount of Al in the spectra obtained. This is due to a thick layer of deposited primer; which masked detection of the bulk aluminum. In addition, a relatively high O content was detected for the PAA-P pre-treated surfaces. The epoxy-based primer contains O in its structure, which is one source of this oxygen. Chromium oxide and strontium oxide are also normally used in the primer layer as corrosion inhibitors [112], which are further sources of oxygen. The presence of Cr and Sr were also confirmed by the EDS analysis as can be seen in Figure 8.5 (e) and Table 8.3. Chromium oxide and strontium oxide were identified on the PAA-P pre-treated surfaces as whisker-like particles as illustrated in Figure 8.4.

The EDS analysis provided useful information on pre-treatment alterations of the chemical composition of the aluminum surface. Such changes in chemical composition and an oxide layer generated on the surface influence the adhesion between the aluminum and PPS and hence the mechanical performance of the joints. However, in some surface pre-treatments, particularly CC, a more fundamental composition alteration was expected, because of the hexafluorozirconate (HFZ) basis of the alodine solution used in this work [200]. As the information depth by EDS was large, chemical information for just the top surface could not be obtained. Therefore, for selected surface pre-treatments an XPS analysis was also performed, to better understand the chemical composition modifications of the aluminum surface.

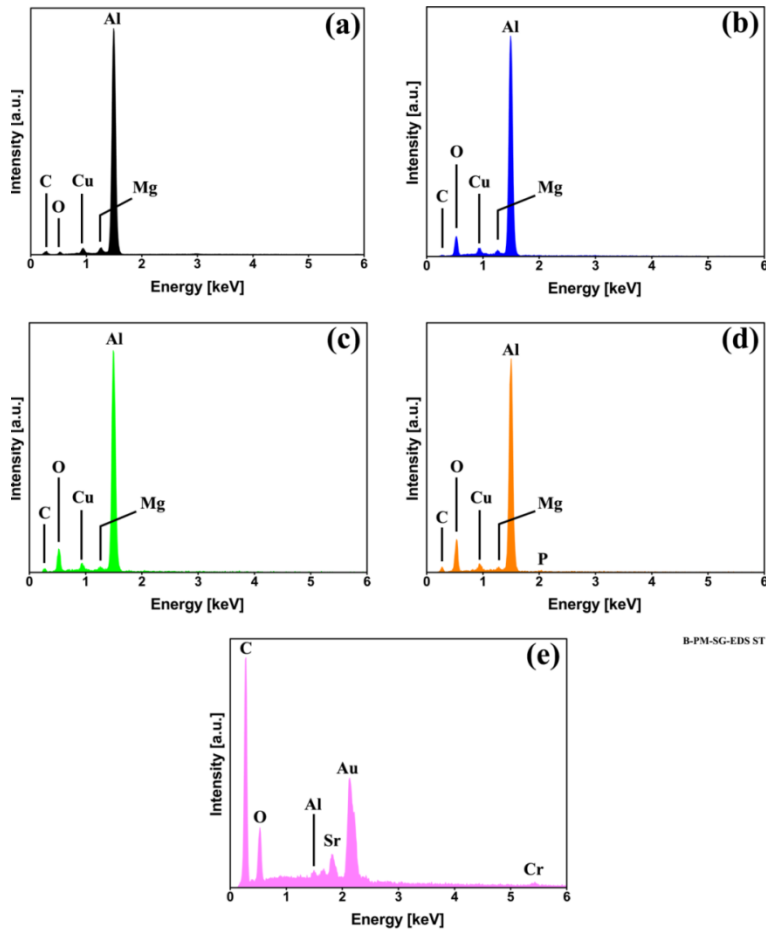
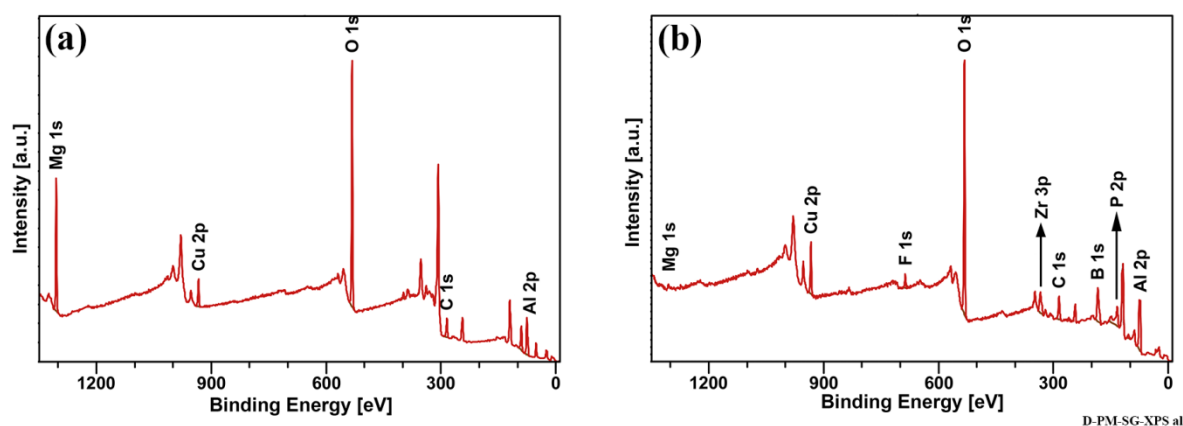


Figure 8.5 Example of selected spectra from the EDS analysis of the AA2024-T3 surface; from (a) AR, (b) SB, (c) CC, (d) PAA, and (e) PAA-P.

Table 8.3 Average chemical composition (in wt%) of the AA2024-T3 surface after different surface pre-treatments by EDS analysis.

Surface pre-treatment	Al	O	C	Cu	Mg	P	S	Cr	Sr
AR	78.4	6.0	6.5	4.9	4.2	-	-	-	-
MG	92.3	1.3	0.4	3.8	2.2	-	-	-	-
SB	87.3	6.8	1.2	3.1	1.6	-	-	-	-
AP	85.5	4.9	3.8	4.1	1.7	-	-	-	-
CC	88.1	5.1	1.5	3.9	1.4	-	-	-	-
SAA	38.3	49.9	2.4	3.1	0.4	-	5.9	-	-
PAA	76.9	14.9	2.0	3.0	1.5	1.7	-	-	-
PAA-P	0.2	17.8	76.0	-	-	-	-	2.5	3.5

Figure 8.6 illustrates the XPS spectra on the aluminum surface in the (a) AR condition and (b) after CC pre-treatment. For the AR specimen XPS shows similar elements obtained by EDS analysis. However, for the CC pre-treated specimen, unlike the EDS analysis, XPS reveals more elements on the aluminum surface than expected. F, Zr, B, and P are the main elements detected by XPS in addition to those in the AA2024-T3 itself. The presence of all these elements from the bulk of the aluminum as well as those from the CC process in the XPS spectrum suggests that the coated layer generated on the surface is very thin, probably only a few nanometers in thickness. It is discussed in [87] that hexafluorozirconate (HFZ) may not remove the natural aluminum oxide layer, but leads to the formation of a layer containing Al-Zr-O-F complex with low interfacial tension. The presence of this layer is thought to increase the activation and wettability of the aluminum surface [87]. Increased wettability and hydrophilicity of the surface was also confirmed in this work, as illustrated in Table 8.1. The main reaction products of the HFZ solution with the aluminum surface were reported to be zirconium oxide and aluminum fluoride [240, 241]. The activation of the surface and presence of new elements are believed to increase the possibility of chemical bond formation between the molten PPS and the CC layer on the aluminum surface during the joining process. As XPS analysis of the other surface pre-treatments did not reveal any different elements on the aluminum surface than those obtained by EDS analysis, their XPS spectra are not shown here, but can be found in Appendix A.7.



**Figure 8.6 XPS analysis of the AA2024-T3 surface; (a) AR and (b) CC.**

To summarize: all the surface pre-treatments altered the surface morphology and / or surface chemistry. Although mechanical pre-treatments, especially SB, drastically increased the surface roughness, no noticeable changes in chemical composition could be detected. In particular, AP and CC led to a clean surface with a low amount of contaminations, but the surface roughness did not alter significantly. Unlike AP, which did not reveal any changes in the chemical composition of the surface, CC led to the formation of an Al-Zr-O-F layer, which may contribute to the formation of chemical bonds with PPS during the joining cycle. Combinations of mechanical and chemical pre-treatments, particularly SB+CC, changed both surface morphology and chemistry, which in turn increases the activation of several bonding mechanisms between the aluminum and PPS. Electrochemical pre-treatments, especially PAA, led to a highly porous oxide layer with very small diameter pores. Slight changes in chemical composition were also identified by addition of P to the surface. Both PAA and SAA surfaces showed a high amount of oxygen, which could indicate a thick oxide layer formed on the surface of aluminum. Finally, PAA-P specimens had a very compact primer layer, which did not prominently alter the surface roughness. Nevertheless, a very

thick carbon-based epoxy primer layer was formed with whisker-like particles of chromium and strontium oxides as corrosion inhibitors. The carbon-based epoxy layer is also expected to form chemical bonds with the PPS during the FSpJ process.

## 8.2 Mechanical performance of the joints

This section deals with the mechanical performance of the FSp joints and its relation to changes on the aluminum surface. The main mechanical testing used in this work was SLS testing. In addition, CT joint geometry was examined for selected surface pre-treatments to evaluate the joint behavior and the influence of surface pre-treatments under mode I loading.

Figure 8.7 shows the strength (ULSF) of the SLS FSp joint with the various surface pre-treatments. All surface pre-treatments increased the SLS strength of the joint to some extent, compared to the AR specimen (strength  $878 \pm 89$  N). Such an increase is particularly pronounced in the case of the PAA-P pre-treatment. Both MG (strength  $2474 \pm 294$  N) and SB (strength  $2252 \pm 212$  N) specimens showed an increase of more than 150% compared to the AR specimen. As explained previously, both mechanical pre-treatments increased the surface roughness, by introducing parallel grooves in the case of MG or asperities and irregularities with SB. Although SB gave a much rougher surface than MG, their similar mechanical performance, in terms of SLS strength, suggests that the groove-like features produced by MG were sufficient to generate micro-mechanical interlocking between the molten PPS and aluminum under shear loading. As the final grinding direction was  $\pm 45^\circ$  to the loading direction, efficient interlocking was achieved.

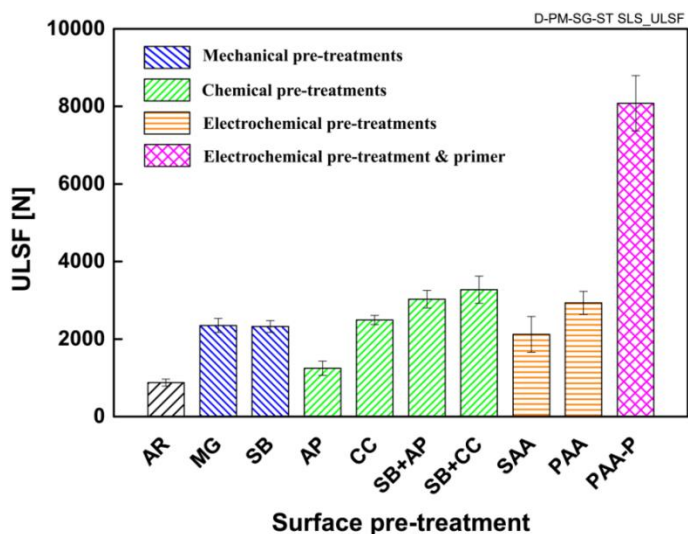


**Figure 8.7 Mechanical strength of SLS FSp joints after aluminum surface pre-treatments.**

AP had the lowest increase in strength ( $1246 \pm 186$  N) of approximately 42%. Since AP does not change the chemistry of the surface, such an increase in strength can be attributed to a slight increase in surface roughness, and so a small increase in micro-mechanical interlocking. Improved micro-mechanical interlocking was particularly achieved due to efficient wetting of the aluminum by the molten PPS, as explained in the previous section. CC had a similar surface topography to AP (see Table 8.2), but the increase in strength ( $2493 \pm 118$  N) was over 180%, compared with the AR specimen. In addition to improved wettability, similar to the AP pre-treatment, CC altered the

---

chemical composition markedly. The formation of strong chemical bonds is thought to be the main cause of such an increase in the strength of the CC pre-treated specimen. The formation and nature of bonds during FSpJ will be explained briefly in the next section. A combination of SB with AP and CC further increased the strength of the joint ( $3028 \pm 228$  N and  $3276 \pm 352$  N respectively) which was expected. Both micro-mechanical interlocking and the formation of chemical bonds (in case of the SB+CC pre-treatment) in addition to improved wettability are the main reasons for such improvement.

Electrochemical pre-treatments also positively influenced the strength of the joints, but PAA performed better than SAA ( $2932 \pm 298$  N and  $2120 \pm 464$  N respectively). Both pre-treatments did not change the surface chemistry noticeably and the formation of chemical bonds by new elements was not expected. As discussed earlier, the SAA pre-treatment led to the formation of a very small number scalloped features and incomplete coverage at the grain boundaries was also identified (see Figure 8.3 (a)). The penetration of the molten PPS into these features is believed to increase micro-mechanical interlocking. In the case of the PAA pre-treatment, the generation of a highly porous oxide layer also improved the micro-mechanical interlocking. Although the pores were very fine after PAA pre-treatment and the PPS was only a few seconds in the molten state, sufficient pore filling was achieved to improve the micro-mechanical interlocking and increase the strength of the joint under quasi-static loading. The lower strength of SAA pre-treated specimens compared to their PAA counterparts might be related to the hydrated state of the aluminum oxide layer after SAA pre-treatment as discussed earlier.

Finally, the PAA-P specimen had the highest average strength of  $8081 \pm 716$  N, which is approximately 10 times the AR condition. This prominent increase in strength is believed to result from the formation of primary carbon-carbon chemical bonds between the primer layer and the molten PPS. As surface roughness was not altered markedly after PAA-P pre-treatment, the cause of this strength increase must be mainly due to the promotion of adhesion forces by the formation of chemical bonding. Kinloch *et al.* [242] observed in adhesive bonding of aluminum joints that the primer forms an interphase with the underlying oxide layer. Such an interphase between the oxide layer and the adhesive decreases the local stress concentration between the high-modulus oxide layer and low-modulus adhesive [242]. A similar interphase with intermediate modulus may be formed during the FSpJ process, between the aluminum oxide and molten PPS, leading to better crack resistance and hence improved joint strength.

To understand the effectiveness of surface pre-treatments and joint behavior under mode I tensile loading (which might be important for certain engineering applications), CT geometry was selected. Figure 8.8 shows the CT strength (achieved ultimate CT force) of the FSp joint for selected pre-treatments. One observes that the strength of the joint under tensile loading is much lower than under shear loading. Comparison of surface pre-treatments reveals that among the mechanical pre-treatments, SB outperformed MG (strength  $507 \pm 101$  N and  $253 \pm 16$  N respectively). Although the groove-like features in the MG specimen were efficient enough to increase micro-mechanical interlocking under shear loading, they have a reduced performance under tensile loading. However, the irregularities of the SB specimen were sufficient to generate more suitable micro-mechanical interlocking. The stand-alone CC exhibited a similar strength to the SB specimen ( $497 \pm 80$  N), which shows that micro-mechanical interlocking, as a result of SB, and adhesion forces, due to chemical bonding in the CC specimen, exert similar influences on the mode-I strength of the joint. This behavior was also observed with SLS geometry, as depicted in Figure 8.7. Analogous to the

behavior of SLS geometry, the SB+CC specimen showed slightly higher cross-tensile strength ( $585 \pm 76$  N) than stand-alone SB and CC due to the combined effects of micro-mechanical interlocking and chemical bonding.

The PAA specimen had an average cross-tensile strength of  $888 \pm 41$  N and that is approximately 77% higher than SB or CC pre-treatments. This is probably due to the shape and angle of the fine pores formed on the aluminum surface after PAA pre-treatment, which also improve the micro-mechanical interlocking under tensile loading. In order to confirm this hypothesis, advanced analysis is required, such as by transmission electron microscopy (TEM) of the joint cross-section, which was beyond the scope of this work. Similar to the SLS results, PAA-P achieved the highest cross-tensile strength ( $1078 \pm 58$  N) among the surface pre-treatments tested, due to the strong primary bonds between the primer layer and PPS.

In summary: CT strength of the FSp joint was approximately 10-30% of the respective SLS strength for the various surface pre-treatments. Cross-tensile testing has not been used frequently in the literature to evaluate the mechanical performance of metal-polymer joints. From the scarce results in the literature, for example, Seidlitz *et al.* [243] recently reported on the cross-tensile strength of steel / GFRP riveted joints, and CT forces between approximately 500 N and 1200 N were reported in their work. Therefore, the CT strength of the FSp joints obtained in this work give comparable results with those reported in [243].

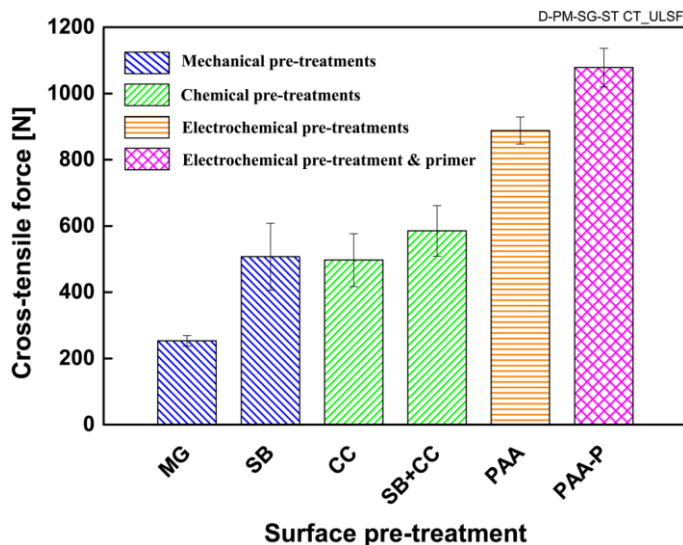
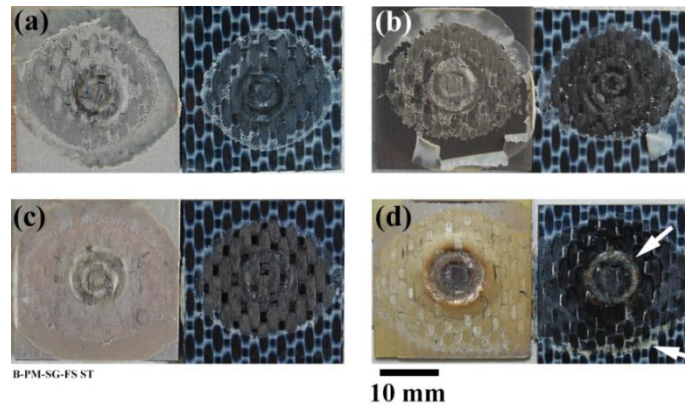


Figure 8.8 Cross-tensile strength of the FSp joint for the selected surface pre-treatments.

### 8.3 Failure and fracture surface analysis

In this section, the fracture surfaces from the selected pre-treatment categories are analyzed for the SLS joint geometry. Due to similarities in the failure mechanisms, from each category the best surface pre-treatment, based on SLS strength, was selected for the analysis. Figure 8.9 illustrates the fracture surface of the SB, CC, PAA, and PAA-P pre-treated specimens. Generally, all the fracture surfaces have similar macro features. As explained earlier in Section 7.6 and in [84] the pre-treated joints also failed under shear mode and frequently in the composite as illustrated in Figure 7.15. For SB, CC, and PAA specimens no aluminum residues could be identified on the

composite side (neither visually nor through SEM examination), but some of the PPS and carbon fibers remained attached to the aluminum after mechanical testing. Therefore, the crack propagation scenario explained in Figure 7.15 remains valid for this set of surface pre-treatments. However, in the fracture surfaces of the PAA-P specimens (Figure 8.9 (d)) yellowish features could be detected on the composite surface, as indicated by the white arrows. These features are believed to be primer material removed from the pre-treated aluminum surface. As a result of the strong bonds generated between the primer and PPS, the crack frequently alters its propagation path between within the primer and the molten PPS layer.



**Figure 8.9** Fracture surfaces of the SLS joints; (a) SB, (b) CC, (c) PAA, and (d) PAA-P. White arrows in (d) indicate primer remaining attached to the CF-PPS.

To further evaluate the yellowish features on the composite, SEM and EDS analysis were employed. Figure 8.10 shows the SEM images from the composite side in Figure 8.9 (d) close to the edge of the composite indicated by the lower white arrow. Two parts were detected on the composite with different features to those observed previously in Section 7.6. A high-magnification SEM image of the white rectangle in Figure 8.10 (a) is shown in Figure 8.10 (b). Strong bonding between the primer layer and the underlying PPS could be identified, because no detachment of the two layers was detected in the SEM images. Moreover, the PPS below the primer layer shows elongated features approximately perpendicular to the loading plane. This could be an indication of out-of-plane forces as a result of the secondary bending effect, particularly near to the edges of the overlap area.

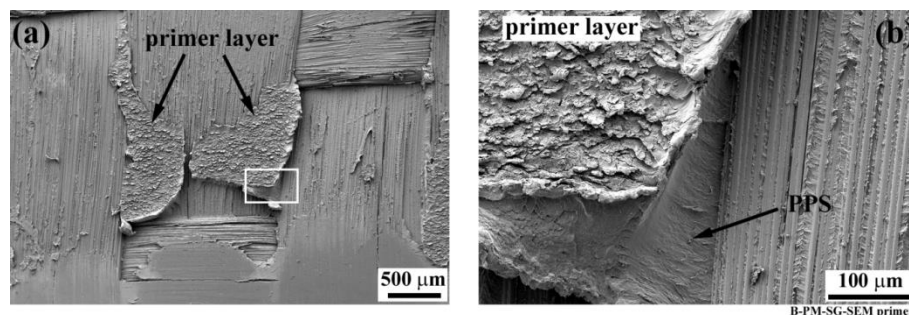


**Figure 8.10** SEM imaging of the fracture surface of the CF-PPS; (a) primer residues remain attached to the composite, and (b) a high magnification image of the white rectangle in (a).

To further confirm that such layers are in fact removed primer, EDS analysis was performed at a high magnification as shown in Figure 8.11 (a). Two spots were selected for the analysis as shown in this figure. The EDS spectra of both spots are also illustrated in Figure 8.11. The spectrum of Spot 1, (Figure 8.11 (b)), contains several elements in which carbon has the highest concentration with 70 wt%. Although the carbon can be related both to the primer and PPS, the presence of O (11 wt%), Sr (7 wt%), and Cr (6 wt%) reveal that this spot refers to the primer that contains chromium and strontium oxides. Furthermore, a small amount of Al (2 wt%) was also identified in this spectrum, which suggests that the failure in some regions might have occurred in the underlying aluminum oxide. This is an indication of very strong bonding between the primer and the aluminum oxide. A small amount of S (4 wt%) was also detected, which is due to failure of the composite part (PPS matrix). By contrast, the spectrum of Spot 2 reveals only 3 elements; C (62 wt%), S (34 wt%), and Cr (4 wt%). This indicates that this spot relates to a PPS-rich area. EDS analysis of the CF-PPS showed a carbon content of approximately 55 wt% and sulfur 45 wt%. Therefore, the higher C ratio in Spot 2 suggests that the primer is another source of the carbon in this position. In addition, the small amount of Cr in Spot 2 also originated from the whisker-like particles in the primer.

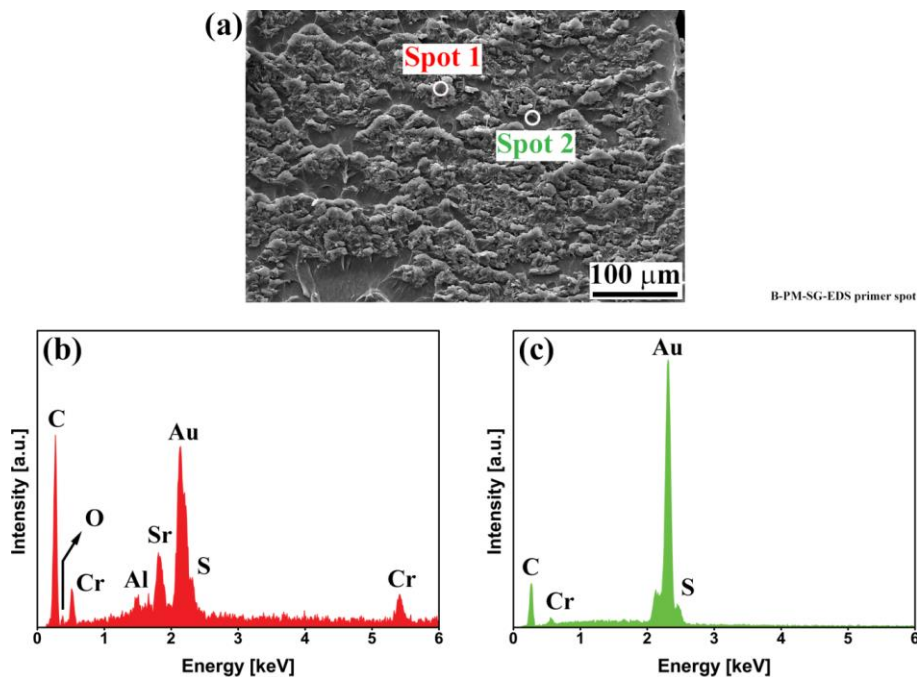


**Figure 8.11 (a) SEM image of the primer layer remained attached to the composite, (b) EDS spectrum of Spot 1 in (a), and (c) EDS spectrum of Spot 2 in (a).**

To summarize: In all surface pre-treated specimens except PAA-P, the failure in the PDZ takes place inside the composite, because a layer of the PPS could be identified on the aluminum side. However, for the PAA-P specimens the failure occurs both in the PPS and the primer, where the crack alters its path frequently between the two. In some places, the crack may further propagate into the aluminum oxide beneath the primer layer.

---

## 8.4 Interfacial bonding mechanisms

To better understand the bonding mechanisms at the interface between AA2024-T3 and CF-PPS during the FSpJ process, the fracture surfaces were analyzed with XPS, because it provides information on the nature of the chemical bonds at the very top surface (5 nm maximum). As described in the previous section, except for the PAA-P pre-treated specimens, the failure in FSp joints takes place primarily inside the PPS (in the PDZ), and some of the PPS layer remains attached to the aluminum after fracture. For this reason, XPS analysis of the fracture surfaces was performed on several areas of the consolidated polymer inside the PDZ on the aluminum side of the failed specimens.

No significant differences in the resulting spectra from various areas were identified. The XPS spectra were obtained from fracture surfaces after argon etching for 1800 s to remove any possible environmental contamination (e.g., CO<sub>2</sub>) and the majority of the adhered PPS layer to obtain information from just the interface. Such spectra were compared to the spectrum of the same position before argon etching. From each surface pre-treatment category, the best specimen in terms of mechanical performance was selected for XPS analysis of the bonding mechanisms. However, for the SB specimen, no changes in the spectrum before and after etching could be identified. This is due to the fact that the PPS layer on the aluminum was so thick it could not be completely removed by an etching process of 1800 s. For the PAA-P specimens, because both the PPS and primer are mainly carbon-based, no conclusive information could be obtained from the preliminary XPS investigation. Therefore, the description in this section is primarily related to the CC and PAA pre-treated samples.

Figure 8.12 illustrates the high-resolution XPS spectra (C 1s and Al 2p regions) obtained for CC and PAA before and after etching for 1800 s. As can be seen from the C 1s region of the CC specimen (Figure 8.12 (a)) a peak at approximately 284.5 eV binding energy is present both before and after etching. This can be attributed to the C bonds from the PPS layer. A binding energy of 284.5 eV corresponding to the C 1s spectrum of PPS was reported to be related to carbon atoms in phenyl rings [244]. It is worth noting that a peak related to adventitious carbon contamination has a slightly higher bonding energy in the spectrum (284.8 eV or even 285.2 eV) [245-247], but there may be an overlap between such a peak and the peak from the PPS, particularly before etching. After 1800 s two small peaks appeared in the C 1s spectrum, one at about 282.1 eV and the other at approximately 289 eV. The first peak position is similar to the C-Zr compound reported in [248, 249]. However, because of the very low signal-to-noise ratio, further evaluation of the Zr region for confirmation of a Zr-C bond formation was not possible.

The new peak at 289 eV is believed to appear as a result of C-Al covalent bond formed at the interface. The C-Al bond formation may be further analyzed from the Al 2p region in Figure 8.12 (b). Both spectra show a peak at 72.8 eV that has been reported as the peak of metallic aluminum [250, 251]. Before etching a peak at approximately 75.8 eV can be identified, corresponding to Al-O bonds and probably from the aluminum oxide layer. Marcus *et al.* [252] reported the formation of an Al-O chemical bond in an aluminum-polymer system at 75.5 eV, very close to the one identified in this work. After etching this peak became broader, which is believed to be due to the Al-C bond formation at the interface, overlapping with the existed Al-O peak. A combination of both C 1s and Al 2p spectra of the CC pre-treated specimen confirms the formation of the covalent Al-C chemical bond at the interface.

A similar behavior could be observed for the PAA specimen. In the C 1s region (Figure 8.12 (c)) a new peak appeared at approximately 289 eV after 1800 s of etching, similar to the CC pre-treated specimen. This peak might also result from Al-C chemical bond formation at the interface. The formation of an Al-C bond in the PAA specimen can likewise be further confirmed from the Al 2p region shown in Figure 8.12 (d). The spectrum after 1800 s of argon etching clearly shows a peak at approximately 75.1 eV, which is also very close to the Al-C chemical bond reported in [250, 251]. This can also support the formation of Al-C chemical bond for the CC specimen. The formation of chemical bonds at the metal-polymer interface was also reported for a Ti-Teflon laser joint, where Ti-C was the primary chemical bond formed at the interface [253, 254].

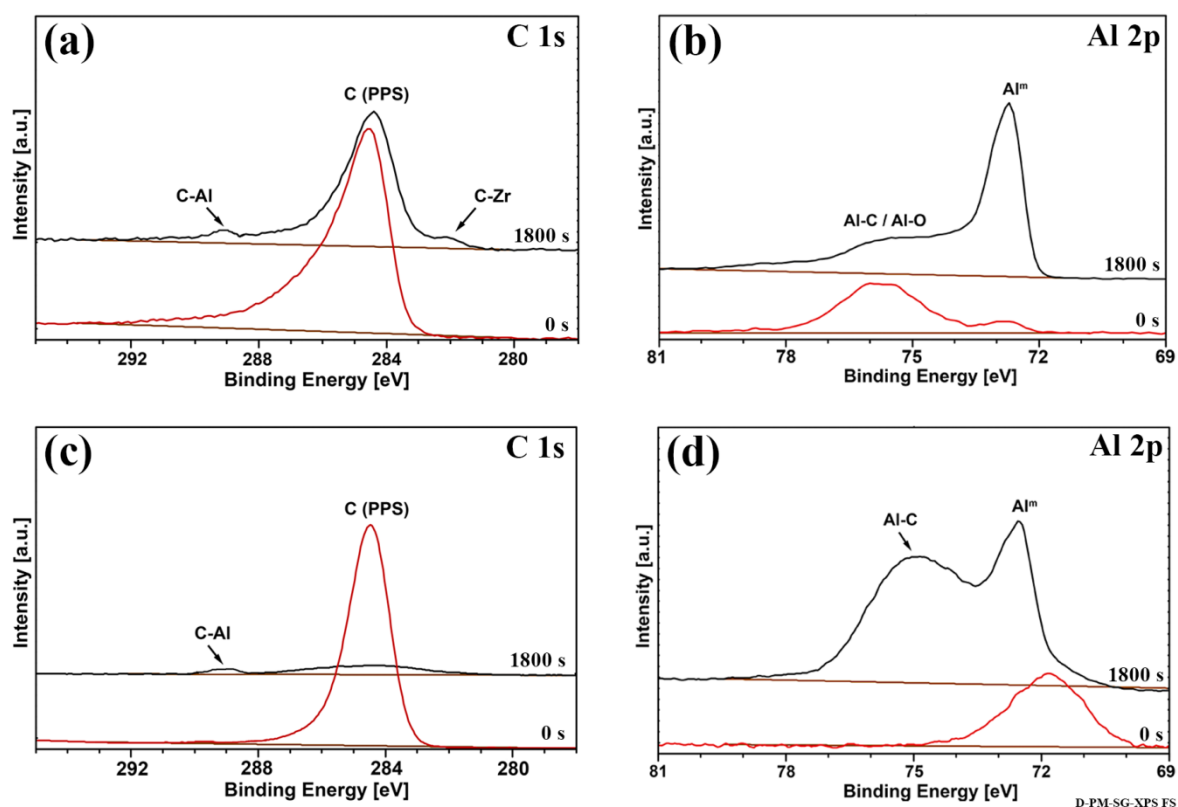


**Figure 8.12 High-resolution XPS region spectra before (red) and after (black) etching for 1800 s for (a) and (b) CC pre-treatment, (c) and (d) PAA pre-treatment.**

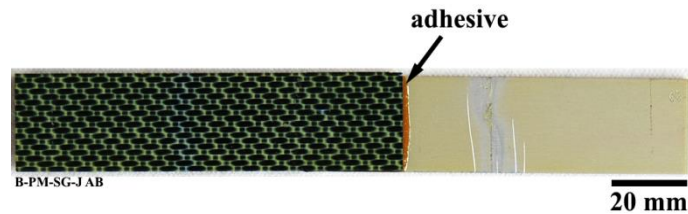
To summarize: XPS analysis of the fracture surfaces of CC and PAA specimens revealed that FSPJ leads to the formation of primary chemical bonds between the aluminum alloy elements and carbon from the molten PPS layer. Covalent Al-C is believed to be the primary chemical bond at the interface. In the case of the CC specimen where other elements are present on the surface of the aluminum, further chemical bonds were formed. Formation of a Zr-C covalent bond could be identified in this work. The SB specimen did not provide any information, probably due to the thick PPS layer that remained attached to the aluminum and was not completely removed by argon etching. Furthermore, strong primary carbon-carbon bonds are believed to form at the interface of the primed aluminum and PPS in the PAA-P specimen. Although, similar to the SB specimens, no information could be obtained from XPS analysis of the PAA-P specimens, but such bond formation is expected to cause very high mechanical strength of the joints. Although, this argument

---

is speculative, it is certainly easily conceivable since both joining surfaces (the primed aluminum and CF-PPS surfaces) are carbon based.

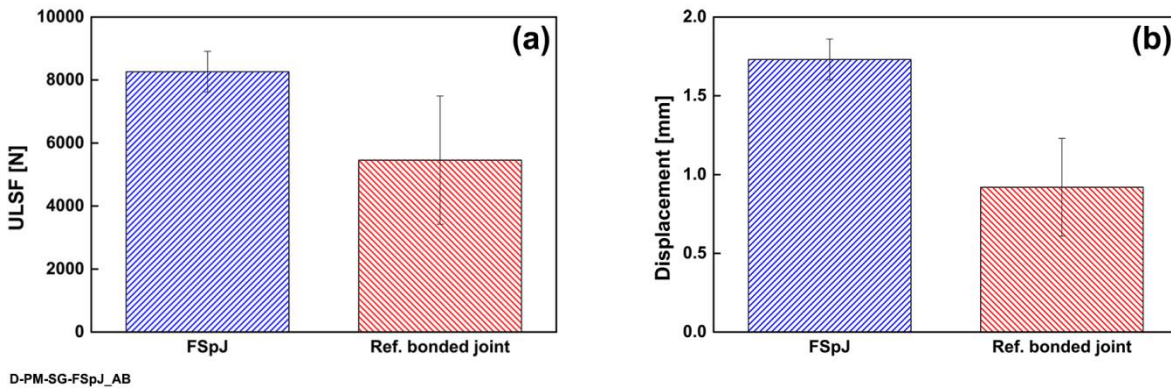
## 8.5 Comparison between the mechanical performance of FSp and state-of-the-art adhesively bonded joints

To assess the mechanical performance of the FSp joints compared to the state-of-the-art metal-composite joining technologies, reference adhesively bonded joints were produced in accordance with the Embraer standards using the same materials used in this work. In order to provide a direct comparison, five reference single lap shear joints with similar configuration to FSp joints (bonding area of 25x25 mm<sup>2</sup>) were assembled using structural adhesive. Furthermore, because PAA-P is the standard surface pre-treatment in the aircraft industry, it was also selected for the reference adhesively bonded joints. However, for adhesive bonding, the composite was also pre-treated using PAA-P. This was done in accordance with internal Embraer procedures due to the difficulties of bonding thermoplastic composites because of their low surface tension. It is well known that thermoplastics require physical or chemical surface modification to produce acceptable adhesively bonded joints [36]. All the reference bonded joints were prepared at the Embraer (Brazil) facilities. Figure 8.13 shows an example of the top view of the aluminum-composite bonded joint.



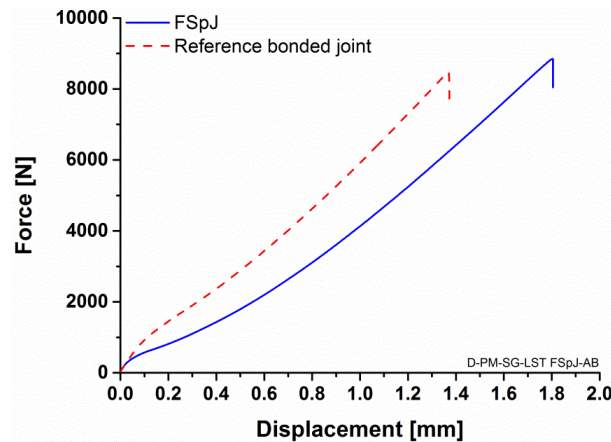
**Figure 8.13 View from above of an adhesively bonded joint between AA2024-T3 and CF-PPS pre-treated by the PAA-P procedure.**

The reference bonded joints were mechanically tested under lap shear loading similar to FSp joints and following the procedures explained in Section 6.3.7.1. Figure 8.14 shows the comparison between the lap shear strength and displacement at the peak load of FSp and reference bonded joints. FSp joints displayed an average ultimate lap shear force (ULSF) of  $8264 \pm 645$  N, whereas the reference bonded joints showed an average ULSF of  $5459 \pm 2036$  N. Moreover, the FSp joints reached an average displacement of  $1.73 \pm 0.13$  mm, whereas the average maximum displacement reached by the reference bonded joints was  $0.92 \pm 0.31$ . Therefore, FSp joints showed an increase of 51% in lap shear strength and 88% in displacement compared to the state-of-the-art adhesive bonded joints.



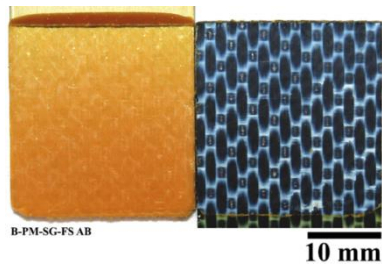
**Figure 8.14 Comparison of the (a) lap shear strength and (b) displacement at the peak load of the FSp joints and reference bonded joints.**

Figure 8.15 compares an example of the load-displacement curve of the FSp joint with reference bonded joint under shear loading. Both joints showed a linear elastic behavior prior to final catastrophic failure. As can be seen in Figure 8.14 and Figure 8.15, the displacement of the bonded joints was also limited, because the adhesive used for bonding was a low-ductility high-strength adhesive.



**Figure 8.15 Load (force)-displacement curves of the FSp joint and reference bonded joint under shear loading.**

In contrast to FSp joints that showed a mixed adhesive-cohesive failure (Section 7.6.2), all the reference bonded joints failed 100% adhesively, as depicted in Figure 8.16 (for comparison purposes see fracture of PAA-P specimens in Figure 8.9). Although, the composite surface was pre-treated prior to bonding, it seems that a suitable adhesion was not produced between the adhesive and composite.



**Figure 8.16 Fracture surface of the reference bonded joint indicating 100% adhesive failure.**

In addition to the better mechanical performance of FSp joints in direct comparison with adhesively bonded joints, an important characteristic of the FSpJ process is its ability to produce lighter structures, because no additional material such as adhesive is used to join the parts together. In this work, the weight reduction using FSpJ was approximately  $3.4 \pm 0.5\%$  compared to the reference adhesive bonding. The average weight of the FSp joints was  $22.6 \pm 0.14$  g, whereas the reference adhesively bonded joints weighed  $23.37 \pm 0.08$  g. Finally, it should also be remembered that the joining time is much faster for FSpJ (4 s in this work) compared to the adhesive bonding.

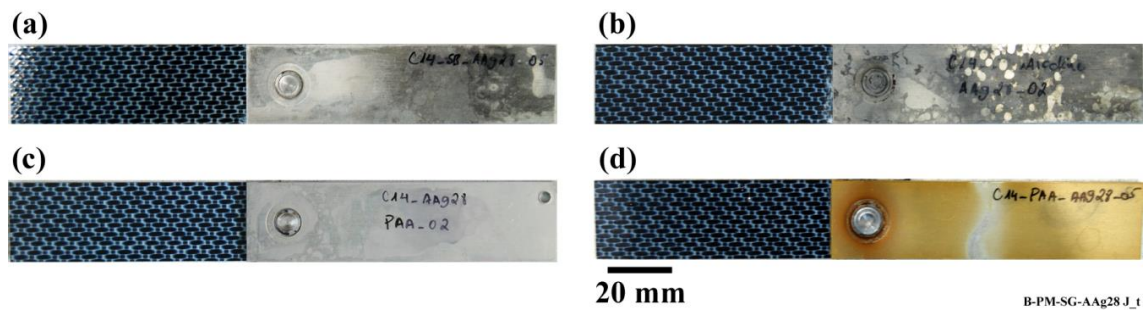
---

## Chapter 9. Durability of FSp Joints

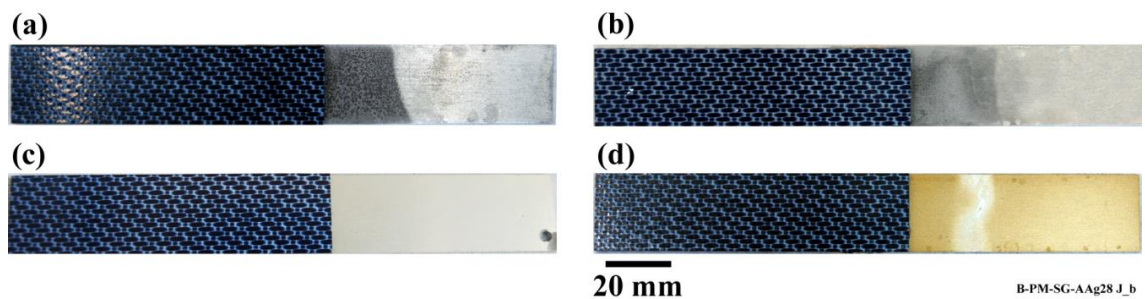
This chapter deals with the durability of SLS FSp joints and their behavior under harsh accelerated aging conditions. Four surface pre-treatments were selected to perform the aging experiments; these were sandblasting (SB), stand-alone conversion coating (CC), phosphoric acid anodizing (PAA), and PAA with subsequent application of primer (PAA-P). Further, the optimized set of joining parameters (RS: 2900 rpm, PD: 0.8 mm, JT: 4 s, and JP: 0.3 MPa) was selected to FSp join the single lap shear AA2024-T3 and CF-PPS specimens. Although SB+CC gave a slightly higher lap shear strength than stand-alone CC in dry conditions, the CC specimen was selected for the aging experiments, in order to understand the behavior of chemical pre-treatment under harsh environments.

### 9.1 Surface features and chemical composition

First of all, the joints were visually inspected as soon as they were taken out of the aging chamber. Figure 9.1 shows the top view of the SLS FSp joints after 28 days of the aging experiment, and Figure 9.2 the bottom view of the same joints. Noticeable changes could be seen in the SB and CC pre-treated specimens on the aluminum part. Dark regions were identified both on the top and bottom surfaces of the SB and CC pre-treated aluminum. Aluminum oxide formed on the surface of the SB and CC pre-treated specimens interacts with the humidity in the aging chamber, which leads to the formation of weak aluminum hydroxide layer. It is well known that an aluminum surface undergoes hydration in the presence of a high level of humidity or when immersed in water [238]. Despite PAA and PAA-P samples having slight water stains on the aluminum, no notable changes could be identified. PAA pre-treatment is known to produce an oxide layer that is more corrosion resistant than CC [255]. This could be the reason that the PAA pre-treated specimen did not exhibit any noticeable surface changes after 28 days of aging. Moreover, phosphate ions in the  $\text{AlPO}_4$  monolayer that is formed on the aluminum surface after PAA pre-treatment reduce the hydration rate of the aluminum as reported in [98, 242]. On the PAA-P specimen, the primer is a thick, corrosion resistant layer [256-258] that inhibits interaction of the underlying aluminum oxide with humidity. That is why no visual changes could be observed on the PAA-P sample. Finally, the composite parts did not show any visual changes after 28 days of aging. This was expected, because PPS is a highly moisture-resistant polymer [153].

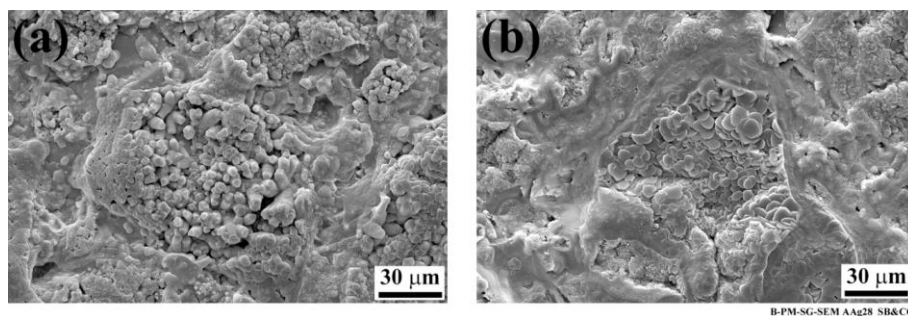


**Figure 9.1** Top view of the SLS FSp joints after 28 days of aging; (a) SB, (b) CC, (c) PAA, and (d) PAA-P.



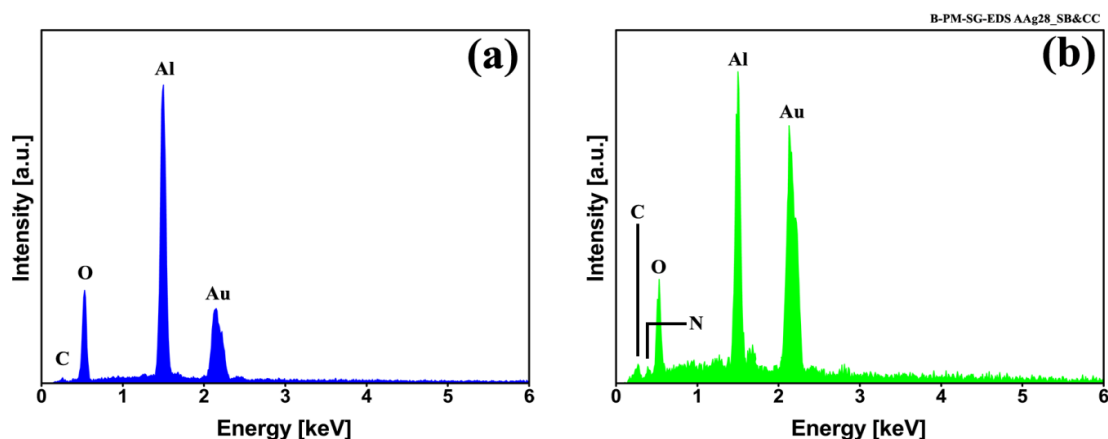
**Figure 9.2** Bottom view of the SLS FSp joints after 28 days of aging; (a) SB, (b) CC, (c) PAA, and (d) PAA-P.

To further analyze the aluminum surfaces, high-magnification SEM images were taken from the affected areas on the specimens. Both SB and CC specimens showed compact areas consisting of the very fine nodular and flake-like structures that are related to the weak aluminum hydroxide formation (Figure 9.3).



**Figure 9.3** High-magnification SEM images of the aluminum affected areas after 28 days of aging; (a) SB and (b) CC specimens showing nodular, flake-like structures.

EDS spectra of the dark areas on the SB and CC specimens are shown in Figure 9.4. The spectra reveal that Al and O are the main elements present in these areas. A small amount of carbon was also detected on both specimens, which may be related to contamination in the aging environment. An even smaller amount of N was identified on the CC specimen, also from the humid environment in the aging chamber. In contrast to the as-pre-treated specimens, other AA2024-T3 alloying elements, such as Cu and Mg, were not detected on the aged aluminum surfaces. Such an alteration of elements on the aged surfaces confirms the formation of an aluminum hydroxide layer on the SB and CC pre-treated specimens.



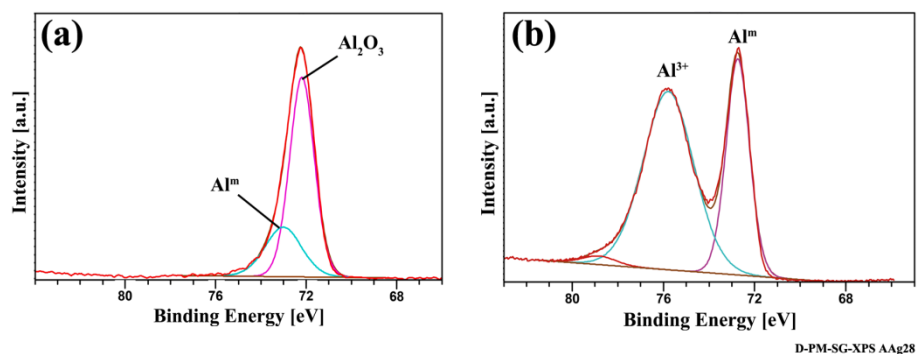
**Figure 9.4** EDS analysis of the aluminum affected areas on (a) SB and (b) CC specimens.

Table 9.1 shows the average chemical composition of the aluminum in the affected areas for the SB and CC pre-treated specimens. The results showed an enormous increase in oxygen compared to the specimens before aging (see Table 8.3). In both cases the oxygen content increased by more than 5 times after accelerated aging. This increase in oxygen was reported due to the conversion of aluminum oxide to hydroxide [96]. The aluminum content in the CC specimen was higher than that for the SB specimen, which may be attributed to a thinner hydroxide layer formed on the CC specimen. This would cause the aluminum from the bulk of the specimen to contribute in the EDS analysis.

**Table 9.1** Average chemical composition (in wt%) of the SB and CC pre-treated AA2024-T3 surface after 28 days of accelerated aging through EDS analysis.

Surface pre-treatment	Al	O	C	N
SB	45.7	43.2	11.1	-
CC	63.3	32.4	0.8	3.5

Furthermore, XPS analysis can further confirm conversion of the oxide layer to aluminum hydroxide. Figure 9.5 shows a high-resolution Al 2p region of the SB specimen (a) before and (b) after accelerated aging. The aluminum before aging (Figure 9.5 (a)) revealed two peaks at approximately 72 eV and 72.8 eV that are related to aluminum oxide [249, 259, 260] and metallic aluminum [249, 261, 262] respectively. After aging, the peak at 72.8 eV (related to the metallic aluminum) was still detectable, but the peak at 72 eV disappeared and a new peak at approximately 76 eV was identified. The appearance of this peak might be due to the aluminum hydroxide formation [260]. It was reported that aluminum oxyhydroxide (AlOOH) is the most common form of aluminum hydroxide generated on the aluminum surface in the presence of humidity and at a temperature range of 25-100°C [87, 263-265]. However, it has also been suggested that after further aging, hydration of the AlOOH leads to the formation of Al(OH)<sub>3</sub> [75]. Regardless of the type of aluminum hydroxide present, the hydration of aluminum oxide was confirmed through XPS analysis.



**Figure 9.5** High-resolution Al 2p XPS region spectra of SB specimen (a) before aging and (b) after aging.

In contrast to the SB and CC specimens, the PAA and PAA-P samples did not show any noticeable changes on the aluminum surface after aging, as shown in Figure 9.1 and Figure 9.2. High-magnification SEM images of the aluminum surface, illustrated in Figure 9.6, appear very similar to the ones before aging. The PAA specimen (Figure 9.6 (a)) showed an open porous structure with some coalesced pores, similar to its surface before aging. The compact structure of the PAA-P specimen was also retained with the whisker-like particles of chromium and strontium oxides, as shown in Figure 9.6 (b).

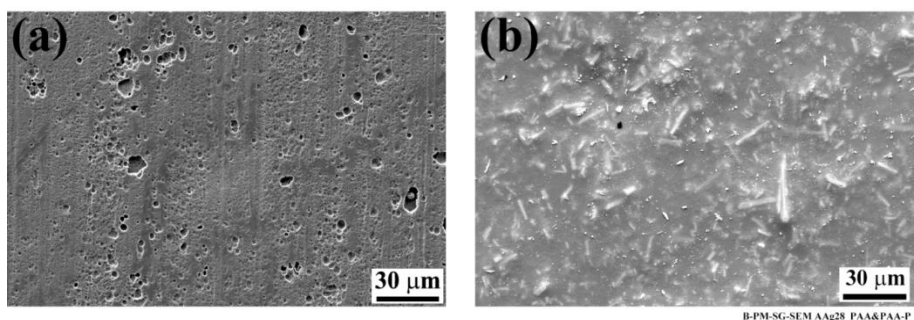


**Figure 9.6** High-magnification SEM images of the aluminum side of the joint after 28 days of aging; (a) PAA and (b) PAA-P specimens.

As with the SB and CC specimens, an EDS analysis was performed on PAA and PAA-P specimens as shown in Figure 9.7. In addition to Al, O, and C, in contrast with SB and CC specimens, Cu and Mg were identified on the surface of the PAA specimen. The spectrum is very similar to that before aging, as depicted in Figure 8.5 (d), but with the exception of P that was not detected after aging. Table 9.2 lists the elemental composition of PAA and PAA-P pre-treated aluminum surfaces after aging. A comparison of these results with the chemical composition of the PAA specimen before accelerated aging (Table 8.3), reveals that the only major alteration of the surface is a reduction in aluminum concentration by about 7 wt% and an increase in carbon content by approximately 10 wt%. The increase in carbon content could be attributed to contamination from the aging chamber. Such an increase in carbon content as a new layer on the aluminum surface would slightly reduce the aluminum content captured by EDS analysis. Furthermore, it was suggested that the hydration of the PAA pre-treated aluminum surface starts with a slow dissolution of the  $\text{AlPO}_4$  layer, followed by the conversion of the aluminum oxide to aluminum hydroxide [98, 238, 239]. The absence of the P in the EDS analysis may be correlated with the early stages of the hydration process.

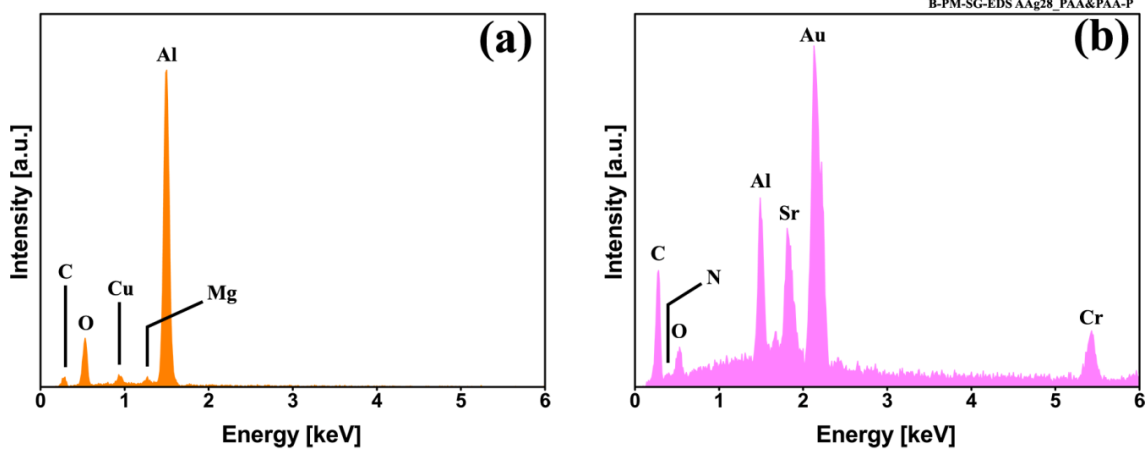


**Figure 9.7** EDS analysis of the aluminum side of the joints from (a) PAA and (b) PAA-P specimens after aging.

The behavior of the PAA-P specimen was slightly different to the PAA sample. The EDS spectrum of the PAA-P pre-treated aluminum after aging (Figure 9.7 (b)) is very similar to the one before aging (Figure 8.5 (e)) with the addition of an N peak. However, quantification of the elements as listed in Table 9.2 reveals that the carbon content was reduced by 15 wt%, whereas the aluminum content showed an increase of approximately 8 wt%. This clearly indicates a thickness reduction of the carbon-based primer layer leading to reduced carbon content. Moreover, the aluminum beneath the primer layer could be detected in a higher concentration due to reduced primer thickness. In addition, a 10 wt% reduction of the oxygen content after aging was also identified. Since there were various sources of oxygen, the aluminum oxide, primer, chromium and strontium oxides, a partial removal of the primer layer appears to have more influence on the reduction of oxygen content. Finally, both Cr and Sr showed an increase in content of approximately 7 wt% and 10 wt% respectively after aging. This is probably due to partial removal of the carbon contained in the primer layer (as a result of its interaction with humidity), leading to an exposure of chromium and strontium oxides. Therefore, a higher concentration of the whisker-like oxides could be observed (see Table 8.3 and Table 9.2 for comparison of the Cr and Sr contents before and after aging).

**Table 9.2** Average chemical composition (in wt%) of the PAA and PAA-P pre-treated AA2024-T3 surface after 28 days of accelerated aging through EDS analysis.

Surface pre-treatment	Al	O	C	Cu	Mg	N	Cr	Sr
PAA	69.3	14.9	11.8	2.6	1.4	-	-	-
PAA-P	8.0	7.6	51.0	-	-	10.0	9.3	14.1

To summarize: SB and CC specimens showed the formation of a new hydroxide layer on the aluminum side of the joints outside the overlap area after 28 days of aging. The PAA specimen did not reveal any notable changes on the aluminum surface. Furthermore, the PAA-P specimen had a reduced thickness of primer, as confirmed by EDS analysis.

---

## 9.2 Mechanical performance of the SLS joints

The joints were mechanically tested to evaluate their lap shear strength shortly after removal of the joints from the aging chamber (within an hour). The obtained lap shear strength of the SLS joints were divided by their initial strength before aging and the results were reported as the residual strength of the joints, as illustrated in Figure 9.8. The SB, CC, and PAA-P specimens had only a small reduction in strength, but the PAA specimen was approximately 42% reduced, compared to their initial strength. Such results are in agreement with those reported in the literature for adhesively bonded aluminum joints, for example in [266].

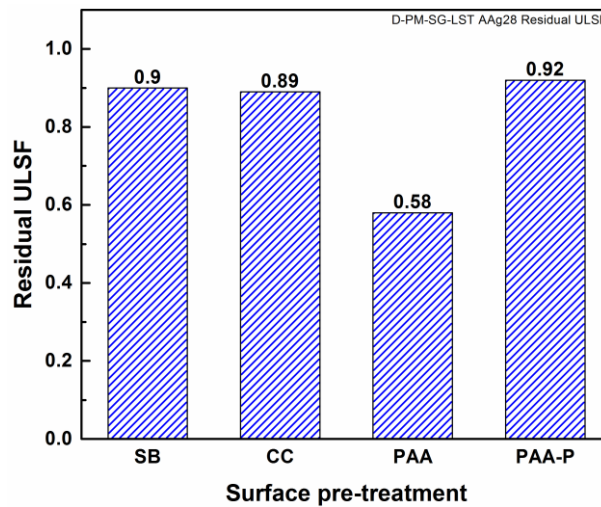


**Figure 9.8 Residual strength of the SLS FSp joints after 28 days of accelerated aging.**

It is believed that both the morphology and chemical composition of the aluminum surface play important roles in the durability of FSp joints. The SB pre-treatment generated large pores and crevices on the surface of the aluminum that could be filled completely by the molten PPS throughout the bonding area. Since molten PPS wet and fill such crevices, moisture cannot penetrate easily or fast into the interface between the aluminum and PPS, which in turn reduces the degradation kinetic of the joints. Further, the chemical bonding between the aluminum and PPS, in the cases of CC and PPA-P pre-treatments (as discussed in Chapter 8) reduce the moisture path into the joints. In all three cases, the moisture diffusion was not completely inhibited, but diffusion kinetic was significantly reduced. This is the reason for the small reductions in strength, compared to the initial strength of the joints.

By contrast, it seems that the moisture could penetrate easier and much faster with the PAA pre-treated joint, leading to aluminum-PPS interface degradation and hence a reduction in mechanical performance. In the PAA pre-treated specimen, diffusion into the interface may be related to the morphology of the oxide layer formed and the extent of pore filling by the PPS. A model with four possible situations for aluminum oxide pore filling by PPS is proposed here, as illustrated in Figure 9.9. The four possible pore filling cases can be summarized as follows:

- 
1. Complete wetting and pore filling
  2. Complete wetting, incomplete pore filling
  3. Partial wetting, incomplete pore filling
  4. No wetting or pore filling

As soon as the PPS in contact with the aluminum starts to soften and melt during the FSpJ process, its viscosity reduces, which leads to penetration of the softened or molten PPS into the aluminum oxide porous structure. As the PPS is in the molten state only for a few seconds (as shown in Table 7.4) its viscosity starts to increase rapidly and that in turn reduces the flow of the PPS. While the PPS is still in the molten state, some of the aluminum oxide pores will become completely filled with PPS and simultaneously the pore walls are completely wetted (Case 1). However, because the viscosity of the PPS increases rapidly, some of the pores will remain incompletely filled by PPS and the pore walls may be completely (Case 2) or partially (Case 3) wetted to the depth penetrated. Finally, there could be some pores that are not filled by the PPS and so no wetting can be expected with these (Case 4). Since the pores are very small and the PPS only sufficiently fluid for a short time, it is believed that Cases 2, 3 and 4 occur more frequently than Case 1.

Although such incomplete pore filling could still result in adequate micro-mechanical interlocking and acceptable initial strength, it is detrimental to the durability of the joints. According to the proposed model, while the joint is in contact with a humid atmosphere diffusion of the humidity into the interface depends on the pore filling situation. In Case 1 and Case 2, where the wetting between pore walls and the PPS is complete, the humidity diffusion is expected to be sluggish. By contrast, in Case 3 and particularly in Case 4 the humidity can penetrate much faster into the pores and into the interface of the aluminum-PPS. This leads to degradation of the interface and hence the mechanical strength of the joint. Kinloch *et al.* [242] suggested that in adhesively bonded aluminum, interfacial micro-voids in PAA pre-treated aluminum allow the penetration of the water (or humidity) into the interface between aluminum and adhesive. The penetration of water was reported to be detrimental to the durability of the adhesive joint. Moreover, Digby and Packham [69] stated that in adhesive bonding, obtaining durable joints depends on penetration of the adhesive into the aluminum oxide pores. Such penetration was considered to be dependent on several factors such as pore dimensions, adhesive viscosity, and the viscosity characteristic of the adhesive at working temperature. Incomplete pore filling was reported to be the main reason for reduced durability of the joints for specific surface pre-treatments such as PAA [69].

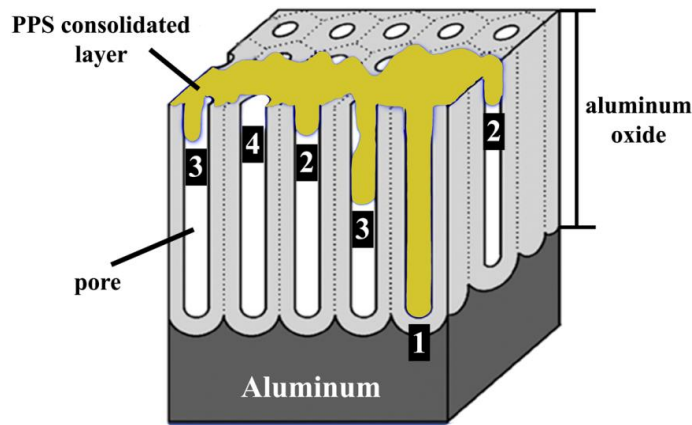


**Figure 9.9 Schematic illustration of aluminum oxide after PAA pre-treatment, adapted from [95], and the proposed model of pore filling by the PPS. (1) complete wetting and pore filling, (2) complete wetting, incomplete pore filling, (3) partial wetting and incomplete pore filling, and (4) no wetting and no pore filling.**

Therefore, it is believed that complete wetting and pore filling as well as strong chemical bonds are important aspects in achieving durable FSp joints. SB resulted in pores and crevices large enough to be completely filled and wetted by the molten PPS during the FSpJ process, suitable for a durable joint. By contrast, the small pores of the PAA pre-treated specimen did not allow complete pore filling and wetting of the oxide layer by PPS, leading to a less durable joint. Both CC and PAA-P specimens provided strong chemical bonds between the aluminum and PPS, which gave these joints high durability.

### 9.3 Failure and fracture surface analysis

Figure 9.10 shows the fracture surface of the four pre-treated joints after 28 days of accelerated aging. As explained in Section 9.1, the SB (Figure 9.10 (a)) and CC (Figure 9.10 (b)) pre-treated specimens had a dark aluminum hydroxide layer on the aluminum surface. This hydroxide layer is even formed very close to the consolidated molten PPS (the AZ) on the aluminum, particularly in the SB specimen, as indicated by the black arrows in the figure. However, in none of the joints could any indication of aluminum hydroxide formation inside the bonding area be detected. It is believed that in FSpJ, strong micro-mechanical interlocking and/or adhesion forces between the aluminum and consolidated molten PPS (AZ) significantly reduce moisture diffusion into the PDZ, which is the strongest part of the joint. Therefore, the rate of the interface deterioration is reduced, as was observed from the residual strength of the joints as shown in Figure 9.8. Although, the PAA specimen did not show any significant changes on the fracture surface (Figure 9.10 (c)), humidity diffusion is expected to take place faster than with the other surface pre-treatments, as explained in the previous section. To confirm this hypothesis a more detailed analysis is required, for example by TEM and EDS / TEM. The PAA-P specimen also showed very similar features to the specimen before aging, such as the primer remaining attached to the composite, as indicated by the white arrows in Figure 9.10 (d). However, some very small features could be observed on the composite side of the fracture surfaces, usually outside the AZ, as indicated, as an example, on the SB specimen by the white arrow in Figure 9.10 (a). These features will be further explained next by SEM imaging.

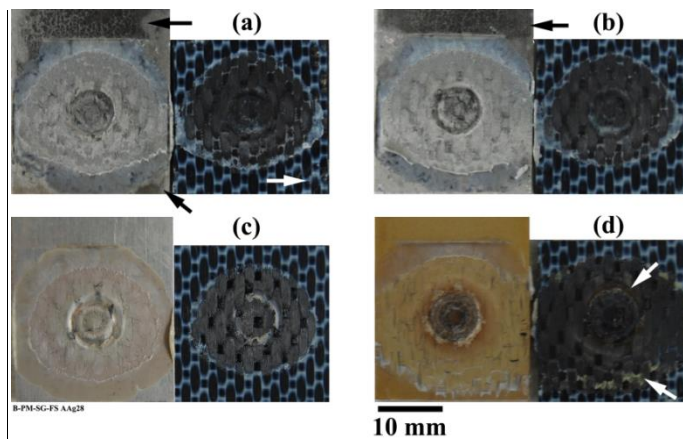


**Figure 9.10** Fracture surfaces of the SLS joints after 28 days accelerated aging; (a) SB, (b) CC, (c) PAA, and (d) PAA-P. Black arrows in (a) and (b) indicate the aluminum hydroxide formation. The white arrow in (a) indicates small features outside the AZ. White arrows in (d) indicate the primer remaining attached to the CF-PPS.

Since the features of the fracture surfaces for all the pre-treatments were similar, only the SEM images of the SB specimen are shown here as an example.

Figure 9.11 (a) shows the fracture surface of the SB specimen on the aluminum side of the joint. The image illustrates the AZ with a very smooth surface at the top of the image followed by the TZ. The TZ shows typical features explained in Chapter 7, where PPS remains attached to the aluminum as individual islands. Figure 9.11 (b) is a high-magnification image of the exposed SB aluminum indicated by the white rectangle in Figure 9.11 (a) inside the TZ. No alteration of the aluminum surface could be identified by this high-magnification image compared to the SB surface before aging (see Figure 8.1 (c)). This confirms that neither did moisture penetrate inside the bonding area nor did it convert aluminum oxide to aluminum hydroxide. The same observation can be seen for the rest of the surface pre-treatments as well.

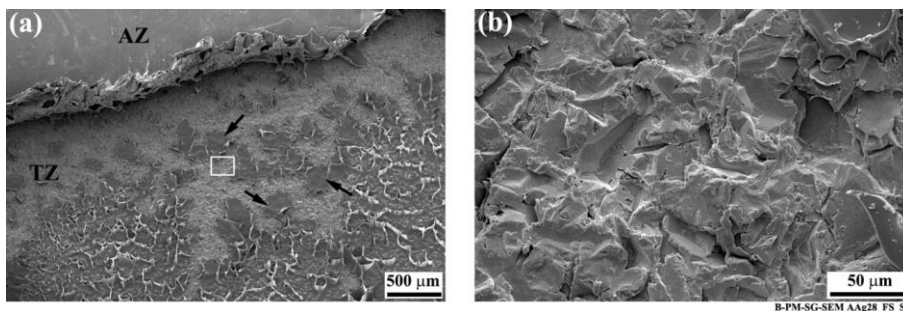


**Figure 9.11** SEM image of the fracture surface of the SB specimen on the aluminum side after 28 days of accelerated aging. (a) Low-magnification image of the AZ-TZ area and (b) high-magnification image of the white rectangle indicated in (a).

As illustrated in Figure 9.10, small features could also be observed on the composite side of the fracture surfaces outside the AZ. Figure 9.12 shows as an example such features on the CF-PPS of the SB specimen indicated by the white arrow in Figure 9.10 (a). Although the low-magnification image (Figure 9.12 (a)) did not reveal any specific features, high-magnification images (Figure 9.12 (b) and (c)) show flake-like features and agglomerates of small particles. As this area on the CF-PPS corresponds to the aluminum hydroxide on the aluminum side of the joints, it is believed that

these particles are the hydroxide layer removed from the aluminum and remaining attached to the composite. Despite the fact these particles are outside the bonding area, they remained attached to the composite. This may be attributed to the weak nature of the hydroxide layer and that was easily detached from the underlying aluminum oxide as a result of frictional forces between the aluminum and composite during the lap shear testing of the joint.

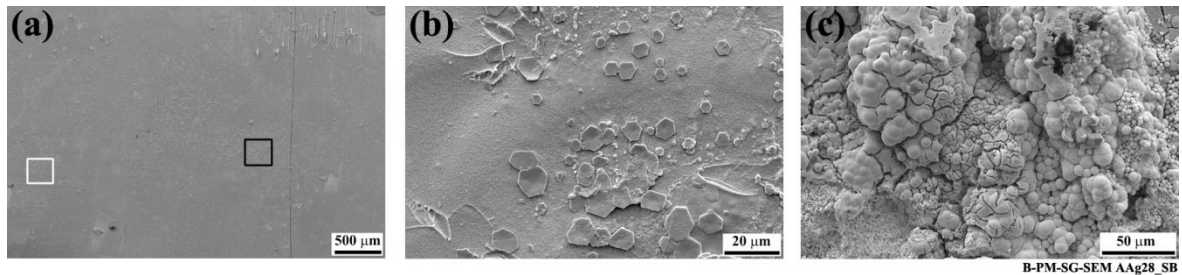


**Figure 9.12** SEM image of the fracture surface of the SB specimen on the composite side after 28 days of accelerated aging. (a) Low-magnification image from the area indicated by the white arrow in Figure 9.10 (a); (b) high-magnification image from the black rectangle indicated in (a), and (c) high-magnification image from the white rectangle indicated in (a).

EDS analysis further confirmed that both the flake-like structures and the agglomerates of particles contain Al, Cu, Mg, and O, as illustrated in Figure 9.13. The average chemical composition of both features is listed in Table 9.3. In both cases the presence of aluminum and a high amount of oxygen, compared to the as-pre-treated specimen, indicates that these particles are aluminum hydroxide, similar to the explanation in Section 9.1. Sulfur from the underlying PPS could be detected in the case of the flake-like structures, which is an indication of the thinness of the flakes. However, because the agglomerates are larger in thickness, no sulfur from the PPS was detected in the respective EDS spectrum.

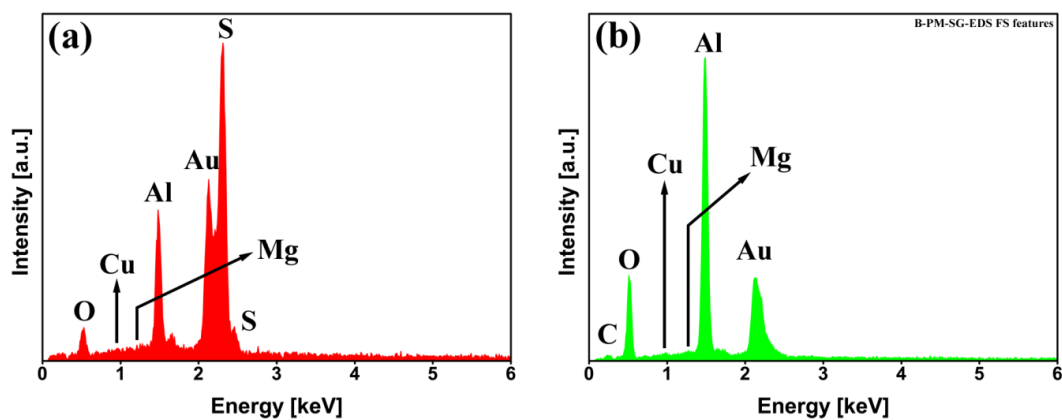


**Figure 9.13** EDS analysis of the (a) flake-like features and (b) agglomerates in Figure 9.12.

---

**Table 9.3 Average chemical composition (in wt%) of the flake-like features and agglomerates on the CF-PPS through EDS analysis.**

Features	Al	O	C	Cu	Mg	S
Flake-like	42.4	32.1	-	0.5	0.5	24.5
Agglomerates	38.5	42.1	18.3	0.8	0.3	-

To summarize: It can be concluded that moisture could lead to the formation of aluminum hydroxide in SB and CC specimens, because the generated oxide was not durable, whereas PAA and PAA-P specimens did not show noticeable changes to the aluminum surface. However, diffusion of the moisture into the bonding area was very sluggish for the SB, CC, and PAA-P specimens, as indicated by the SEM images and their high residual lap shear strength. Although the PAA specimen did not reveal any notable changes through visual observation and SEM images, it showed considerable decrease in mechanical performance. This was attributed to the penetration of moisture into the interface of the aluminum and composite by only partially filling with PPS the fine porous structure of the aluminum oxide.

---

## Chapter 10. Fatigue Behavior of the FSp Joints

This chapter describes the fatigue performance of the SLS FSp joints based on the S-N curve life analysis, under constant amplitude loading. Similar to the previous chapter, four surface pre-treatments were selected to carry out the fatigue experiments; these were sandblasting (SB), sandblasting with subsequent conversion coating (SB+CC), phosphoric acid anodizing (PAA), and PAA with subsequent application of the primer (PAA-P). Although unlike for the aging experiments, the SB+CC specimen was selected to perform fatigue analysis, because it had the highest quasi-static strength among the chemical and mechanical+chemical pre-treatments. In addition, the optimized set of joining parameters (RS: 2900 rpm, PD: 0.8 mm, JT: 4 s, and JP: 0.3 MPa) was selected to FSp join the single lap shear AA2024-T3 / CF-PPS specimens.

In this work, three fitting procedures were chosen to obtain S-N curves; firstly the exponential model, also known as the semi-log or Lin-Log, secondly the power law model, also referred to as the Log-Log model in the literature, and finally the wear-out model based on the Sendeckyj approach. These models are briefly described in Appendix A.11.

In this chapter, the results obtained from fatigue loading and the analysis of S-N curves will be presented. The previously mentioned models were employed to obtain S-N curves. Moreover, the fracture surface of the joints under fatigue loading will be briefly discussed. It is worth mentioning that all the results in this chapter are presented as load-life (F-N) graphs. However, the term S-N curve (strength-life) is used, due to its widespread usage in the literature.

### 10.1 Fatigue life analysis of the FSp joints

This section describes the results obtained from the fatigue experiments of the FSp joints using four selected surface pre-treatments and the life analysis based on the selected models.

#### 10.1.1 Application of the models

First of all, the replication of the fatigue samples was examined according to the described procedure in [122] and Equation (A.1). The replication analysis showed a variation of 57% to 73%, which corresponds to allowable in the design according to the ASTM standard. Since the replication is higher than that required for the research and development phase [122], one is assured that the obtained S-N curves are sufficiently reliable as a basis to better understand the behavior of the FSp joints under fatigue loading.

The S-N curves derived using the examined models and the selected surface pre-treatments are illustrated in Figure 10.1. In addition to the fatigue data (indicated by the open circles) and the derived S-N curves, the quasi-static strength of the joints (indicated by solid triangles) is also plotted for comparison. Further, Table A.2 (Appendix A.11) lists the parameters obtained for the selected models. Note that for the wear-out model 50% reliability was used, which is usual for composite materials [120]. The detailed results of the fatigue data of all surface pre-treated samples are also listed in Appendix A.11).

A major assumption in the wear-out model is that the failure mode of the fatigue specimens should be similar to the quasi-static samples and that no competing failure modes are presented [118]. This assumption is valid in the case of the FSp joints, as will be illustrated later in this chapter (Section 10.2).

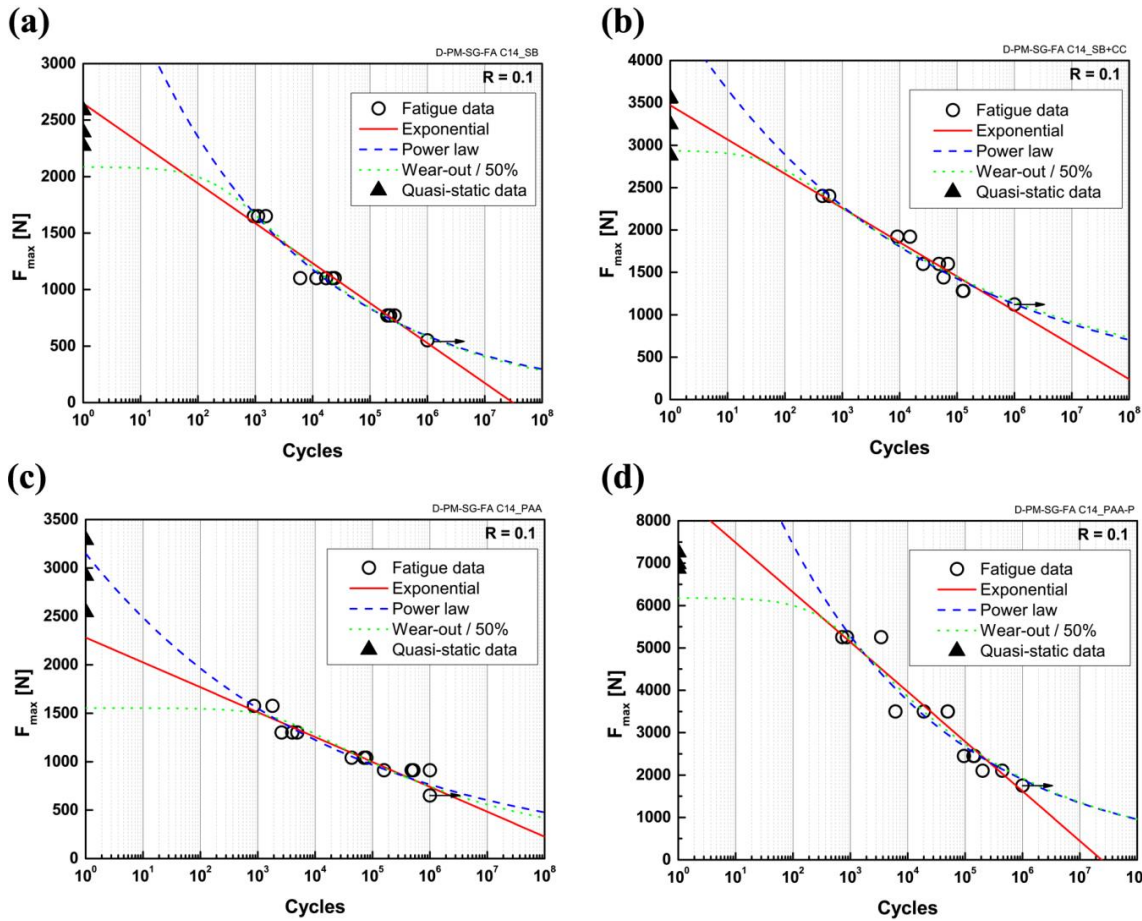


**Figure 10.1** Derived S-N curves based on exponential, power law, and wear-out models for the (a) SB, (b) SB+CC, (c) PAA, and (d) PAA-P specimens.

In all cases, the behavior of the three models is similar across the range of the experiments ( $10^3$ - $10^6$  cycles), and all the models are capable of fitting the fatigue data. One can also observe that the wear-out model exhibits a similar trend to the power law, except in the low cycle fatigue (LCF) range. This was expected, because the wear-out model also obeys a power law except that parameter  $C$  controls the shape of the curve in the LCF range leading to deviation from the power law model. In the range of very high cycle fatigue (HCF) above  $10^6$  cycles the exponential model seems to be a very conservative approach, because it predicts a limited fatigue life under load zero. The same behavior for the exponential model was reported for adhesively bonded CFRP joints [120]. The power law and the wear-out models tend to follow the experimental data in this range. However, in the LCF regime below  $10^3$  cycles for SB and SB+CC specimens, the exponential model could more appropriately predict the fatigue life, whereas at one cycle the predicted results are in the range of the quasi-static strength of the joints. Nevertheless, comparison between fatigue strength (at one cycle) and the quasi-static strength should be treated with care, since the strain rate during both testing could be different and may influence the obtained strength [118]. The wear-out

model gave the lowest predicted strength at LCF, followed by the exponential model and power law in all surface pre-treated joints. The power law model predicted very high strength for the SB, SB+CC, and PAA-P specimens (even higher than their respective quasi-static strength), whereas it could still predict the strength appropriately for the PAA specimens. Finally, the wear-out model predicted the strength of the joints in the LCF regime close to the quasi-static strength for the SB, SB+CC, and PAA-P samples, but it appeared to be very conservative for the PAA specimens.

To summarize: For all surface pre-treatments, all the models fitted well in the experimental range. The exponential model showed to be very conservative in the HCF range, whereas the power law and wear-out models followed the trend of the experimental data. In the LCF regime, the wear-out model gave the best although it was slightly conservative for the SB, SB+CC, and PAA-P specimens. The trend of the S-N curves for the PAA specimens are similar to the other surface pre-treatments, however the models showed a more conservative approach, especially for the wear-out model, where the predicted strength is much lower than the quasi-static strength.

All the models were also validated using relevant statistical analysis to evaluate the fitting procedure. The results of validation are presented in Appendix A.11.

As all the models showed an effective fitting in the experimental range, the exponential model was selected to compare the fatigue behavior of the pre-treated specimens. The comparison is shown in Figure 10.2. It is possible to observe that PAA-P specimens exhibited a much better fatigue performance compared to the rest of the pre-treatments. This was expected, because the quasi-static strength of the PAA-P joints was higher, as discussed in Chapter 8. The other three surface pre-treatments showed a similar fatigue performance, but the SB+CC specimens performed slightly better than PAA and SB specimens. This also accords with their quasi-static strength, where SB+CC showed a higher strength than PAA and SB specimens.

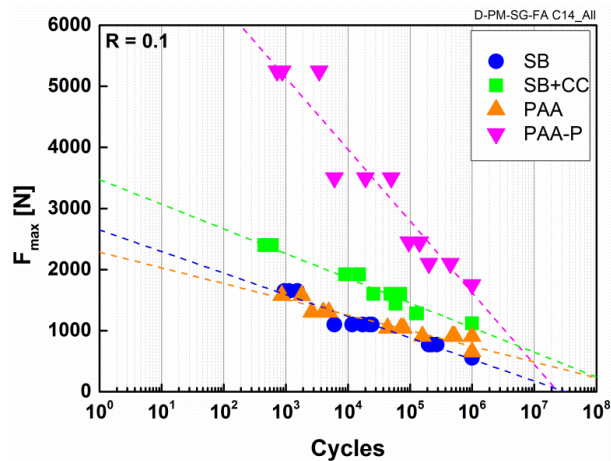


**Figure 10.2 S-N curves of the various surface pre-treatment specimens based on the exponential model.**

One can also observe that the fatigue performance of the pre-treated specimens in the LCF regime ( $10^3$  cycles) was very similar to their quasi-static strength, being much higher for the PAA-P. By contrast, in the HCF range ( $10^6$  cycles) the fatigue performance of the PAA-P specimens tended to approach the other surface pre-treatments, although it remains better than the other specimens, as shown in Figure 10.2. It is known that SLS geometry has very poor resistance to shear loading due to the secondary bending effect [267, 268]. It is also reported that during fatigue testing peel

stresses are generated at the edges of the joints during each cycle [267, 268]. As the applied fatigue loads were higher for the PAA-P specimens, it is believed that higher peel stresses were generated in these joints, particularly in the HCF regime. Such peel stresses reduce the fatigue performance of SLS joints. Moreover, it is well known from the principles of adhesive bonding that shear stresses are maximized (peak shear stresses) at the edges of the joint. Generally, higher applied external loads and shear modulus of the adhesive increases the peak shear stresses at the edges [28-30, 227]. Due to the similarities between FSpJ and adhesive bonding, analogous conclusions may be drawn. Since the PAA-P specimens led to much stronger joints, compared to other surface pre-treatments, and the applied fatigue loads were also higher, it would be expected that the generated shear stresses at the edge of the joint are also higher. Increased peel stresses and peak shear stresses in the PAA-P specimens resulted in a steeper slope of the S-N curve.

Furthermore, the fatigue performance of the PAA specimens was slightly better than the SB specimens in the HCF range. This may be attributed to the influence of surface roughness on stress concentration and fatigue life reduction. It was reported by Shahzad *et al.* [269] that high surface roughness reduced the fatigue life of the aluminum alloy 7010 single material, especially in the HCF regime. With FSpJ it is believed that aluminum surface's asperities and ridges due to the SB pre-treatment acted as stress concentration points, which in turn facilitated crack nucleation, leading to the reduction of fatigue life, particularly in the HCF. However, for the PAA specimens, due to the lower surface roughness, the slope of the S-N curve was less steep. The same trend as for SB specimens can be seen for the SB+CC specimens, but the slightly higher fatigue strength in the HCF range compared with the PAA specimens can be related to the presence of chemical bonding in addition to mechanical interlocking, as discussed in Chapter 8. Nevertheless, and similar to the above discussions, generated peel and maximum shear stresses were generally smaller for SB, SB+CC, and PAA specimens when compared with the PAA-P samples, leading to less steep S-N curves.

Table 10.1 shows the fatigue strength of the FSp joints using different pre-treatments at  $10^5$  cycles of fatigue life.  $10^5$  cycles is usually used in the aircraft industry as a reference to compare the fatigue performance of different designs [270]. The results show that the models predict quite similar strengths for each surface pre-treatment. Furthermore, the PAA-P specimens gave the highest fatigue strength as a result of the very strong chemical bonds formed at the interface, as described previously in Chapter 8. The SB+CC specimens ranked second in fatigue performance followed by the PAA and SB specimens.

**Table 10.1 Fatigue strength (N) of various specimens based on the three models at  $10^5$  cycles.**

Surface pre-treatment	Exponential	Power law	Wear-out	Ranking fatigue strength
SB	846	851	838	4
SB+CC	1381	1387	1445	2
PAA	1003	1000	990	3
PAA-P	2644	2589	2730	1

---

### 10.1.2 Residual strength

The specimens that survived one million cycles of fatigue loading were subsequently tested under lap shear testing to obtain their residual strength. Figure 10.3 illustrates the comparison between initial quasi-static and residual strength of the joints after one million cycles. Surprisingly, SB and PAA-P specimens showed an average residual strength slightly higher than the initial lap shear strength by 15% and 7% respectively. For the SB+CC and PAA specimens the residual strengths were lower compared to the initial strengths by 10% and 22% respectively. However, since the standard deviation in all surface pre-treatments neither the increases in strength for SB and PAA-P specimens nor the decreases for SB+CC and PAA specimens are conclusive. It is known that damage accumulation reduces the residual strength of composite joints [268]. So it is believed that no damage is generated and accumulated in the FSp joints for the selected loading conditions even after one million cycles. Although it was mentioned earlier that peel stresses could be generated during the fatigue loading, which would lead to damage accumulation, it may be concluded that the induced peel stresses are negligible under these loading conditions. The fatigue shear loads were also quite low, whereby damage is not induced and accumulated. The fatigue loads under which the samples survived one million cycles correspond to 25% of the initial lap shear strength for SB, PAA, and PAA-P specimens and 35% for the SB+CC samples.

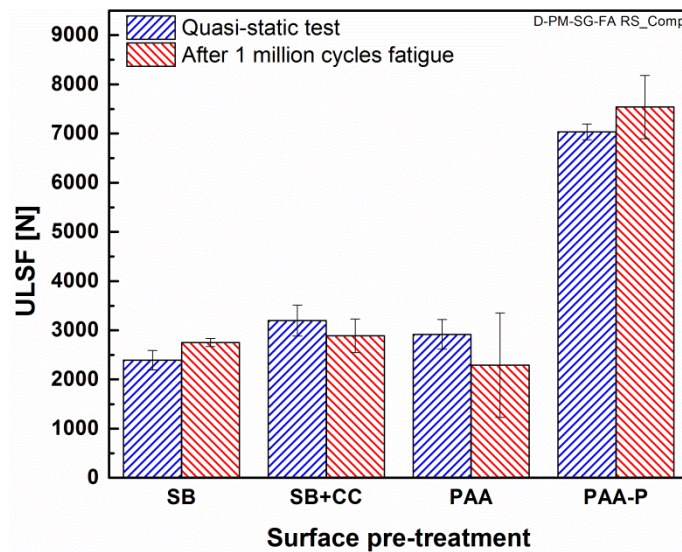


**Figure 10.3** Quasi-static strength of the FSp joints for the surface pre-treatments after  $10^6$  cycles of fatigue loading compared with the respective initial quasi-static strength.

### 10.2 Fatigue failure behavior

As described in Chapter 7, the primary failure mode of an FSp joint under quasi-static loading is shear through the composite. Figure 10.4 illustrates the failure behavior of the joints in the high cycle fatigue regime for the four pre-treated specimens. It can be observed that the fatigued failure mode is similar to quasi-static failure. All the joints failed in shear mode through the composite under all fatigue load levels and for all surface pre-treatments. In addition, AZ and PDZ are clearly visible in the fracture surfaces, revealing the same features as the joints that failed under quasi-static loading. Radial cracks initiate in the outer periphery of the AZ and propagate towards the

PDZ and the center of the joint. For the PAA-P specimen a piece of the primer layer was removed and remained attached to the composite, again similar to the quasi-static failure. The crack path switched frequently between inside the PPS molten layer and the primer.

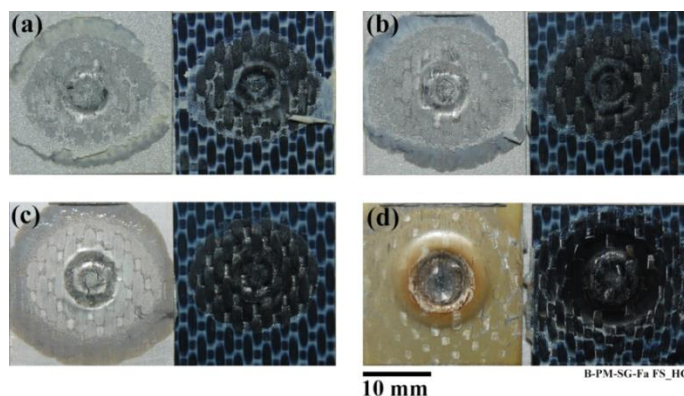


**Figure 10.4** Fracture surfaces of the HC fatigue specimens; (a) SB – 606,281 cycles to failure, (b) SB+CC – 129,406 cycles to failure, (c) PAA – 482,136 cycles to failure, and (d) PAA-P – 442,673 cycles to failure.

Figure 10.5 shows the SEM examination of the fracture surface of an SB specimen on the PPS side. Similar micro-mechanisms to quasi-static failure samples could also be detected. Elongated matrix fibrils in the warp direction along the loading direction (Figure 10.5 (a)) are an indication of ductile fracture, whereas fiber breakage and fiber-matrix debonding were the main failure micro-mechanisms in the weft direction (Figure 10.5 (b)). In both warp and weft directions, the fibrils had a length of between about 10  $\mu\text{m}$  and 100  $\mu\text{m}$ . At high magnification two types of fatigue striations could be observed; first, debonding from the fibers in the elongated PPS matrix in the weft direction (Figure 10.5 (c)), and second, in the resin-rich area between the fibers (Figure 10.5 (d)). As explained by von Bestenbostel and Friedrich [271] striations are step-like structures that can be detected using a suitable contrast origin in the SEM. Since striations are generated out of the fracture plane, a tilt angle is usually also required to identify them [271]. In the FSp joints, striations could be observed at various positions in the weft direction, but the generation of fatigue striations could not be confirmed in the warp direction.

Similar fatigue striations to those illustrated in Figure 10.5 (c) were also observed in resistance-welded thermoplastic composites [268]. The authors concluded that the striations were generated due to peel stresses perpendicular to the loading direction. The cause of this type of fatigue striation in this work appears similar, due to local out-of-plane stresses generated along the fiber-matrix interface (weft direction). It is believed that in the weft direction the cracks propagate out-of-plane, perpendicular to the fiber-matrix interface, producing fatigue striations in the PPS. Even so the final failure occurs due to the tearing of the PPS matrix. In the final stages, the torn matrix becomes elongated in the loading direction. The second type of striation shown in Figure 10.5 (d) is very similar to those reported in [271] in resin pockets, which are typical defects in the composites. Since there is a change in the local stiffness between the fibers and the surrounding resin, such resin pockets act as crack initiation sites during fatigue loading [271]. In FSpJ, micro-voids have a similar effect to the resin pockets, acting as initiation sites for fatigue cracks. Therefore, two types of striation could be identified as micro-mechanisms in fatigue failure of an FSp joint.

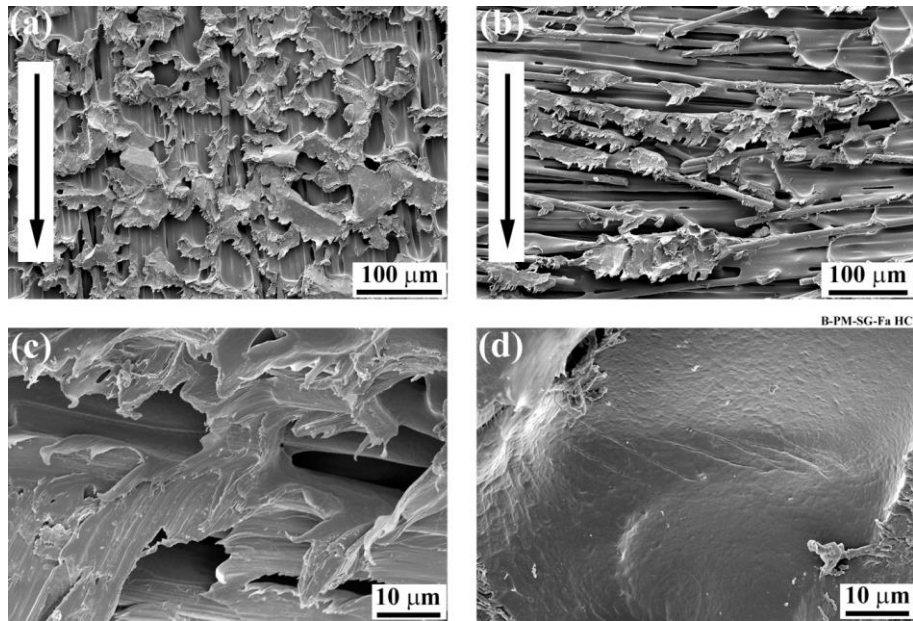


**Figure 10.5** Failure micro-mechanisms of a high cycle fatigue SB specimen from the composite side; (a) warp fibers orientation, (b) weft fibers orientation, (c) fatigue striations in the PPS matrix debonding from the fibers, and (d) striations in the PPS matrix in a resin-rich area. Black arrows in (a) and (b) indicate the loading direction; (c) and (d) were taken at a tilt angle of 45°.

---

# Chapter 11. Summary of the Results and Conclusions

This PhD work was conducted to explore the FSpJ technique for joining metal and composites, its fundamentals, the bonding mechanisms generated during the process as well as the failure mechanisms. Moreover, the work was aimed at establishing a relationship between the process parameters (heat input), microstructure and mechanical performance of the joints. The study has further sought to understand the influence of various metal surface pre-treatments on the metal-composite bonding mechanisms and mechanical performance. Understanding the durability under accelerated aging conditions and fatigue performance of the FSp joints was also an aim of this work. In accordance with the goals of the work, the following main observations and conclusions were drawn from the results obtained:

## Development of the FSpJ process

In all welding-based metal-composite joining techniques, which includes FSpJ, heat input plays an important role. It influences the joint's microstructure, physicochemical alterations in the composite part, the local and global mechanical properties, as well as the failure mechanisms of the joint. This work has demonstrated that the process temperature (due to heat input) can be controlled by changing the process parameters. Extensive thermal degradation of the PPS matrix in the composite was avoided due to appropriate selection of the process parameters. However, some slight intermolecular branching, similar to cross-linking, was observed in the PPS. Nevertheless, the crystallinity of the PPS was approximately 70-80% retained, due to the fact that the heating and cooling rates were very rapid. The original PPS crystals were not completely melted during the joining cycle, these also acted as nucleation sites for new crystals. The microstructure and local mechanical properties of the joining parts were also influenced by the process. Of particular interest were the changes in the composite, since joint failure more often took place inside the composite at the interface with the aluminum. In the composite, a PHAZ containing volumetric flaws, such as voids and fiber-matrix debonding, was observed. As no extensive thermal degradation of PPS was detected, the formation of voids was attributed to entrapped air in the molten PPS. Large differences in the shrinkage behavior of PPS and carbon fibers led to the debonding phenomenon. Investigation of the local mechanical properties of the PPS molten layer by nanoindentation revealed that both hardness and modulus were slightly higher than PPS in the BM. Since the crystallinity of the joints was lower than the BM, such an increase was attributed to slight cross-linking (intermolecular branching) of the PPS. Chain entanglement and branching points increase the required force to overcome a cross-linked structure. To explore the bonding mechanisms in FSpJ, the bonding area was divided into three zones. PDZ was the inner zone, where the primary bonding mechanisms were: macro-mechanical interlocking due to nub insertion into the composite, micro-mechanical interlocking between aluminum surface irregularities and molten PPS, and fiber entrapment. The outer zone (AZ) was the region within which the flowing molten polymer was consolidated. A transition zone (TZ) was also identified between the PDZ and AZ, which was characterized by a high amount of air bubbles remaining entrapped in this layer. Micro-mechanical interlocking was the main bonding mechanism in the AZ and TZ. Adhesion forces between the aluminum and PPS are believed to exist in all bonding zones. Failure analysis of an SLS FSp joint showed that the joint failed in shear mode through a mixed adhesive-cohesive failure, frequently

---

inside the composite. Moreover, fractography analysis of the joints with SEM revealed a mixed brittle-ductile fracture with failure micro-mechanisms including tearing of the PPS matrix, elongated PPS fibrils, warp-fiber pull-out, and weft-fiber fracture.

#### Influence of aluminum surface pre-treatments

All aluminum surface pre-treatments carried out in this work resulted in the enhancement of joint strength to some extent, when compared to the AR specimens. This was attributed to changes in the topography and chemical state of the aluminum surface, as well as to the cleaning effect of certain pre-treatments. Improvements in the bonding mechanisms were directly influenced by physicochemical changes on the surface of aluminum. From all surface pre-treatments, the PAA-P pre-treated specimens showed the highest mechanical strength. This was expected, because the carbon-based primer layer forms a strong, primary C-C chemical bonding with the molten PPS layer. PAA electrochemical pre-treatment led to a highly porous oxide layer that increased micro-mechanical interlocking between the molten PPS and the oxide layer. In addition, XPS analysis revealed the formation of an Al-C chemical bond at the interface. CC caused the formation of an Al-Zr-O-F layer, which contributed to chemical bonding with PPS during the joining process. Al-C and Zr-C were identified as the chemical bonds by XPS analysis. Mechanical pre-treatments, especially SB, produced a very rough aluminum surface with various shapes of pores and crevices. Therefore, micro-mechanical interlocking was the main bonding mechanism augmented by mechanical pre-treatments. It was shown in this work that both enhanced micro-mechanical interlocking and chemical bond formation improve the quasi-static strength of the FSp joints. However, the nature of the chemical bonds is substantially important for the joint strength. C-C bonds formed in the PAA-P pre-treated joints are much stronger than Al-C or Zr-C bonds in other pre-treated samples. Additionally, failure and fracture surface analysis of various surface pre-treated SLS joints showed that all the joints failed in shear inside the first layer of CF-PPS. However, in the PAA-P samples, a layer of the primer remained attached to the PPS. Therefore, in PAA-P specimens the failure occurred both in PPS and the primer, because the crack alters its path frequently between PPS and the primer. In some positions, the crack propagated further into the aluminum oxide beneath the primer layer, as confirmed by EDS analysis.

#### Durability of FSp joints

An accelerated aging experiment was carried out on four selected surface pre-treatments: SB, CC, PAA, and PAA-P. The surface of the aluminum, outside the bonding area, after 28 days of aging showed a dark layer on the SB and CC specimens. This dark layer was determined to be  $\text{Al}(\text{OH})_3$  aluminum hydroxide, as confirmed by EDS and XPS analysis. In contrast with SB and CC specimens, PAA and PAA-P samples did not have any noticeable changes on the aluminum surface. Although SB and CC specimens showed the formation of a weak aluminum hydroxide layer, the residual strength of these joints was approximately 90% of the initial dry quasi-static strength. This was comparable with the residual strength of the PAA-P pre-treated joint, which was 92% of the initial dry quasi-static strength of the respective joint. The high residual strength of the SB, CC, and PAA-P pre-treated joints was ascribed to the low level of moisture diffusion in the bonding area. Moisture diffusion was significantly decelerated due to the favorable wetting of the aluminum surface by the molten PPS. In contrast, PAA pre-treated joints resulted in a residual strength of approximately 58% after accelerated aging. This may be explained as due to the partial wetting and pores filling of the aluminum oxide layer by the molten PPS. A very fine structure of

---

the pores, high viscosity of the PPS and a very fast cooling rate are the main causes of the partial wetting. Such partial wetting allows moisture diffusion, degrading the aluminum-PPS interface and hence the strength of the joint. Further in-depth interface analysis, for example by TEM, is required to confirm this explanation.

#### Fatigue behavior of the joints

Fatigue life analysis of the selected surface pre-treated joints under tension-tension ( $R=0.1$ ) loading was examined. Three statistical models were employed to fit the fatigue data and showed a similar behavior in the experimental range for all pre-treatments. However, the models deviated in HCF and LCF regimes. An exponential model was very conservative in HCF, showing a strength of zero in a limited number of cycles. Power law and wear-out models had similar behavior, displaying a fatigue limit at HCF. In the LCF regime, wear-out was illustrated as a suitable model for SB, SB+CC, and PAA-P pre-treated joints, because it predicted approximately the quasi-static strength of the respective joints in one cycle. The exponential model also showed good predictability for SB and SB+CC samples, but it overestimated the fatigue strength for the PAA-P specimens. For all of the pre-treatments used, power law proved unreliable. However, for PAA pre-treated joints, power law gave the best prediction at LCF, followed by the exponential model. In fact, the wear-out model was very conservative. Apart from with PAA samples, the wear-out model showed to be a reliable method for the fitting procedure. Finally, the joints that survived one million cycles did not show any considerable reduction in their quasi-static strength. This was a clear indication that damage was not accumulated in the joints after one million cycles at the respective load level. Therefore, such a load level can be used as the joint fatigue endurance limit.

The results achieved by this PhD and the proposed mechanisms and descriptions have provided a better understanding of the principles of the FSpJ technique. In addition, the influence of process parameters (heat input) on the microstructure and physicochemical behavior of the joints has been established and correlated with the mechanical performance of the joints. The primary metal-composite bonding mechanisms (mechanical interlocking and adhesion forces) as well as the failure and fracture mechanisms have been discussed in detail. It was also demonstrated that a suitable surface pre-treatment has a major influence, not only on the initial quasi-static strength, but also on the durability and cyclic strength of the joints. This was achieved through understanding the influence of surface pre-treatments on the bonding mechanisms in FSpJ. Therefore, this work has been successful in fulfilling its defined objectives.

Apart from scientific examination of the process, it clearly demonstrated that FSpJ is an interesting and alternative joining technology for metal-composite multi-material structures, with particular potential for application in the transport industries. Although this work was performed on AA2024-T3 and CF-PPS, the main principles of the technique remain valid for other combinations of lightweight metal alloys and thermoplastic polymers or composites.

---

## Chapter 12. Recommendations for Future Work

Although many aspects of the FSpJ technique were studied in this PhD work, some topics remain open to be addressed by future investigation. The following recommendations are suggested for future work:

Investigation of the crashworthiness and damage tolerance of FSp joints would provide valuable information on the performance and design of the joints for industrial applications. Impact resistance, creep behavior, and corrosion properties are all important subjects to be investigated. In addition, analysis of the static and fatigue behavior of multi-spot high-load and low-load transfer specimens would advance knowledge on the mechanical properties of FSp joints.

Simulation and modeling of heat development during the process and mechanical behavior of the joints would reduce the cost and effort of experimentation. Moreover, computer-based simulations can be used to increase knowledge of fracture analysis and the failure behavior of joints.

As the principles and fundamentals of the FSpJ process are now well understood at coupon level through this work, an important next step would be to up-scale the process. It is important to understand the behavior of the process on multi-spot sub-component specimens. The interaction of individual spots with each other, in terms of heat development and transfer, and the generation of residual stresses are important aspects for further study. An investigation of the mechanical performance of multiple joints on the sub-component level would complement understanding of the process by up-scaling.

---

## References

1. J. Zhang, *et al.*, Hybrid composite laminates reinforced with glass/carbon woven fabrics for lightweight load bearing structures. *Mats & Des*, 2012. **36**: p. 75-80.
2. P.K. Mallick, Joining for lightweight vehicles, in *Materials, design and manufacturing for lightweight vehicles*, P.K. Mallick, Editor. 2010, Woodhead Publishing Ltd.: Cambridge. p. 275-308.
3. T. Dursun and C. Soutis, Recent developments in advanced aircraft aluminium alloys. *Mats & Des*, 2014. **56**: p. 862-71.
4. Y. Li and J. Lu, Lightweight structure design for wind energy by integrating nanostructured materials. *Mats & Des*, 2014. **57**: p. 689-96.
5. G. Sedlacek and H. Trumpf, *Innovative developments for bridges using FRP composites*. 2007, Cambridge: Woodhead Publishing Ltd.
6. G. Marsh, Composites and Metals – A Marriage of Convenience? *Reinforced Plastics*, 2014. **58**: p. 38-42.
7. S.T. Peters, *Handbook of composites*. 2nd ed. 1998, London: Chapman & Hall.
8. N.N. Airbus A350 XWB. [cited 5<sup>th</sup> January 2015]; Available from: [www.a350xwb.com](http://www.a350xwb.com).
9. N.N. Boeing 787 from the ground up. [cited 5<sup>th</sup> January 2015]; Available from: [www.boeing.com](http://www.boeing.com).
10. J. Sloan. The making of the BMW i3. 2014 [cited 3<sup>rd</sup> January 2015]; Available from: <http://www.compositesworld.com>.
11. N. Drake, *Thermoplastics and Thermoplastic Composites in the Automotive Industry 1997-2000*. 1998, Rapra Industry Analysis Report Series.
12. N.N., *Plastics and Polymer Composites Technology Roadmap for Automotive Markets*. 2014, American Chemistry Council.
13. R. Yancey, Carbon fiber composites: Into the automotive mainstream?, in *High-Performance Composites*. 2013. p. 7.
14. V. Srivastava and R. Srivastava, Advances in Automotive Polymer Applications and Recycling. *Int. J. Innov. Res. Sci., Eng. & Technol.*, 2013. **2**(3): p. 744-6.
15. N.N. Mercedes-Benz Forschungsfahrzeug F 125! [cited 25<sup>th</sup> January 2015]; Available from: [www.daimler.com](http://www.daimler.com).
16. S.T. Amancio-Filho and J.F. dos Santos, Joining of Polymers and Polymer-Metal Hybrid structures: Recent Developments and Trends. *Poly. Eng. Sci.*, 2009. **49**(8): p. 1461-76.
17. A.J. Kinloch and G.K.A.Kodokian, *The adhesive bonding of thermoplastic composites*. 1989, Imperial College of Science, Technology and Medicine: London, England.
18. S.T. Amancio-Filho and J.F. dos Santos, Method for joining metal and plastic workpieces. 2012, European Patent No. EP2329905B1.

- 
19. C. Schiling and J.F. dos Santos, Method and device for linking at least two adjoining work pieces by friction welding. 2005, International Patent Publication WO/2001/036144.
  20. S.T. Amancio-Filho, *et al.*, On the feasibility of friction spot joining in magnesium/fiber-reinforced polymer composite hybrid structures. *Mater. Sci. Eng. A*, 2011. **528**: p. 3841-8.
  21. J.V. Esteves, *et al.*, Friction spot joining of aluminum AA6181-T4 and carbon fiber-reinforced poly(phenylene sulfide): Effects of process parameters on the microstructure and mechanical strength. *Materials and Design*, 2014. **66 (Part B)**: p. 437-45.
  22. R.D. Adams, J. Comyn, and W.C. Wake, *Structural Adhesive Joints in Engineering*. Second ed. 1997, London: Chapman & Hall.
  23. D.A. Dillard, ed. *Advances in structural adhesive bonding*. 2010, Woodhead Publishing Ltd.: Cambridge.
  24. A. Higgins, Adhesive bonding of aircraft structures. *Int. J. Adhes. Adhes.*, 2000. **20**: p. 367-76.
  25. B. Klein, *Leichtbau-Konstruktion*. 8. ed. 2009, Wiesbaden: Vieweg+Teubner.
  26. J.-H. Kweon, *et al.*, Failure of carbon composite-to-aluminum joints with combined mechanical fastening and adhesive bonding. *Comp. Struc.*, 2006. **75**: p. 192-8.
  27. ASTM D5573 - 99, Standard practice for classifying failure modes in fiber-reinforced-plastic (FRP) joints. ASTM International, 2005.
  28. O. Volkersen, Die Nietkraftverteilung in zugbeanspruchten Nietverbindungen mit konstanten Laschenquerschnitten. *Luftfahrtforschung*, 1938. **15**: p. 41-7.
  29. M. Goland and E. Reissner, The Stresses in Cemented Joints. *J. Appl. Mech.*, 1944. **11**: p. A17-A27.
  30. L.F.M. da Silva, *et al.*, Analytical models of adhesively bonded joints - Part I: Literature survey. *Int. J. Adhes. Adhes.*, 2009. **29**: p. 319-30.
  31. J.D. Minford, *Handbook of Aluminum Bonding Technology and Data*. 1993, New York: Marcel Dekker.
  32. A. Baldan, Review Adhesively-bonded joints and repairs in metallic alloys, polymers and composite materials: Adhesives, adhesion theories and surface pretreatment. *J. Mater. Sci.*, 2004. **39**: p. 1-49.
  33. G. Habenicht, *Applied Adhesive Bonding, A Practical Guide for Flawless Results*. 2009, Weinheim: Wiley-VCH Verlag.
  34. J. Rotheiser, *Joining of Plastics - Handbook for Designers and Engineers*. 1999, Munich: Carl Hanser.
  35. R.W. Messler, Trends in key joining technologies for the twenty-first century. *Assembly Automation*, 2000. **20(2)**: p. 118-128.
  36. R.W. Messler Jr., *Joining of Materials and Structures: From Pragmatic Process to Enabling Technology*. 2004, Burlington, MA: Elsevier.

- 
37. E. Patterson, D. Backman, and G. Cloud, eds. *Composite Materials and Joining Technologies for Composites, Volume 7: Proceedings of the 2012 Annual Conference on Experimental and Applied Mechanics*. 2013, Springer.
  38. S.T. Amancio-Filho, A. Abibe, and J.F. dos Santos, *Joining: Mechanical Fastening of Polymers, Composites, and Polymer-Metal Hybrid Structures*, in *Wiley Encyclopedia of Composites*, L. Nicolais and A. Borzacchiello, Editors. 2012, John Wiley & Sons.
  39. S.T. Amancio-Filho, M. Beyer, and J.F. dos Santos, US 7.575.149 B2: Method for connecting a metallic bolt to a plastic piece. 2009: US Patent.
  40. S.T. Amancio Filho, *Friction Riveting: development and analysis of a new joining technique for polymer-metal multi-materials structures*. 2007, PhD thesis, Hamburg University of Technology: Hamburg.
  41. L. Blaga, *et al.*, Friction Riveting of glass–fibre-reinforced polyetherimide composite and titanium grade 2 hybrid joints. *Mater Des*, 2013. **50**: p. 825-9.
  42. S.T. Amancio-Filho and J.F. dos Santos. Fricriveting: A new technique for joining thermoplastics to lightweight alloys. in *Annual Conference of the Society of Plastics Engineers, ANTEC 2008*. 2008. Milwaukee.
  43. J. Altmeyer, J.F. dos Santos, and S.T. Amancio-Filho, Effect of the friction riveting process parameters on the joint formation and performance of Ti alloy/short-fibre reinforced polyether ether ketone joints. *Mater Des*, 2014. **60**: p. 164-76.
  44. C.F. Rodrigues, *et al.*, FricRiveting of aluminum 2024-T351 and polycarbonate: Temperature evolution, microstructure and mechanical performance. *J Mater Proc Technol*, 2014. **214**: p. 2029-39.
  45. S.T. Amancio-Filho and J.F. dos Santos. FricRiveting: A New Joining Technique for Thermoplastics-Lightweight Alloy Structures. in *Materials Science and Technology (MS&T) 2008*. 2008. Pittsburgh, Pennsylvania.
  46. N.Z. Borba, *et al.*, Friction Riveting of Pultruded Thermoset Glass Fiber Reinforced Polyester Composite and Ti6Al4V Hybrid Joints. in *Annual Conference of the Society of Plastics Engineers, ANTEC 2014*. 2014. Las Vegas, CA.
  47. S.T. Amancio-Filho, J.F. dos Santos, and M. Beyer, US 7,780,432 B2: Method and Device for Connecting a Plastic Workpiece to a Further Workpiece. 2010: US Patent.
  48. A.B. Abibe, *et al.*, Mechanical and failure behaviour of hybrid polymer–metal staked joints. *Mater Des*, 2013. **46**: p. 338-47.
  49. A.B. Abibe, *et al.*, Development and Analysis of a New Joining Method for Polymer-Metal Hybrid Structures. *J. Thermoplast. Compos. Mater.*, 2011. **24**: p. 233-49.
  50. A.B. Abibe, *et al.*, Processing and Analysis of a New Joining Method for Polymer-Metal Hybrid Structures. in *Proceedings of the Polymer Processing Society 26th Annual Meeting*. 2010. Banff, Canada.
  51. A.B. Abibe, *et al.*, A method for joining a plastic workpiece to a further workpiece. 2014, European Patent Application: 14182938.2 - 1706.

- 
52. S.T. Amancio-Filho, A.B. Abibe, and J.F. dos Santos, Welding and Joining of Composites and Composite-metal Structures by Frictional Heating, in 19. Nationalen SAMPE Deutschland Symposium. 2013: Hamburg.
  53. P. Mitschang, R. Velthuis, and M. Didi, Induction Spot Welding of Metal/CFRPC Hybrid Joints. *Adv. Eng. Mater.*, 2013.
  54. P. Mitschang, *et al.*, Induction Heated Joining of Aluminum and Carbon Fiber Reinforced Nylon 66. *J. Thermoplast. Compos. Mater.*, 2009. **22**: p. 767-801.
  55. F. Balle and D. Eifler, Statistical test planning for ultrasonic welding of dissimilar materials using the example of aluminum-carbon fiber reinforced polymers (CFRP) joints. *Mat.-wiss. u. Werkstofftech.*, 2012. **43**(4): p. 286-92.
  56. F. Balle, G. Wagner, and D. Eifler, Ultrasonic Metal Welding of Aluminium Sheets to Carbon Reinforced Thermoplastic Composites. *Adv. Eng. Mat.*, 2009. **11**(1-2): p. 35-9.
  57. F. Balle, G. Wagner, and D. Eifler, Ultrasonic spot welding of aluminum sheet/carbon fiber reinforced polymer – joints. *Mat.-wiss. u. Werkstofftech.*, 2007. **38**(11): p. 934-8.
  58. F. Balle, G. Wagner, and D. Eifler. Combined Process of Ultrasonic Welding and Precipitation Hardening of Aluminium Alloy 2024/Carbon Fibre Reinforced Composites Structures. in *Proceedings of the 12th International Conference on Aluminium Alloys*. 2010. Yokohama, Japan: The Japan Institute of Light Metals.
  59. J.P. Bergmann and M. Stambke, Potential of laser-manufactured polymer-metal hybrid joints. *Physics Procedia*, 2012. **39**: p. 84-91.
  60. K.W. Jung, *et al.*, Laser direct joining of carbon fiber reinforced plastic to zinc-coated steel. *Mater Des*, 2013. **47**: p. 179-88.
  61. S. Katayama and Y. Kawahito, Laser direct joining of metal and plastic. *Scripta Materialia*, 2008. **59**: p. 1247-50.
  62. X. Tan, *et al.*, Characteristics and formation mechanism of porosities in CFRP during laser joining of CFRP and steel. *Composites: Part B*, 2015. **70**: p. 35-43.
  63. A. Baldan, Adhesion phenomena in bonded joints. *Int. J. Adhes. Adhes.*, 2012. **38**: p. 95-116.
  64. F. Awaja, *et al.*, Adhesion of polymers. *Prog. Polym. Sci.*, 2009. **34**(9): p. 948-68.
  65. S. Yang, L. Gu, and R.F. Gibson, Nondestructive detection of weak joints in adhesively bonded composite structures. *Comp. Struc.*, 2001. **51**(1): p. 63-71.
  66. A.J. Kinloch, Review; The science of adhesion *J. Mater. Sci.*, 1980. **15**(9): p. 2141-66.
  67. E. Maeva, *et al.*, Acoustical methods for the investigation of adhesively bonded structures: A review. *Canad. J. Phys.*, 2004. **82**(12): p. 981-1025.
  68. M.C. van der Leeden and G. Frens, Surface Properties of Plastic Materials in Relation to Their Adhering Performance. *Adv. Eng. Mat.*, 2002. **4**(5): p. 280-9.
  69. R.P. Digby and D.E. Packham, Pretreatment of aluminium: topography, surface chemistry and adhesive bond durability. *Int. J. Adhes. Adhes.*, 1995. **15**: p. 61-71.

- 
70. D.E. Packham, The Adhesion of Polymers to Metals: The Role of Surface Topography, in Adhesion Aspects of Polymeric Coatings, K.L. Mittal, Editor. 1983, Plenum Press: New York, p. 19-44.
  71. L.H. Sharpe and H. Schonhorn, Surface Energetics, Adhesion, and Adhesive Joints, in Contact Angle, Wettability, and Adhesion, Advances in Chemistry Series, F.M. Fowkes, Editor. 1964, American Chemical Society. p. 189-201.
  72. C. Creton, Materials Science of Pressure-Sensitive Adhesives, in Materials Science and Technology, H.E.H. Meijer, Editor. 1997, Wiley-VCH Verlag: Weinheim. p. 707-41.
  73. T.G. Gutowski, The Mechanics of Composite Deformation During the Manufacturing Process, in First Conference of Composite Materials. 1986, American Society for Composites: Dayton, OH.
  74. P. Molitor and T. Young, Adhesives bonding of a titanium alloy to a glass fibre reinforced composite material. *Int. J. Adhes. Adhes.*, 2002. **22**(2): p. 101-7.
  75. G.W. Critchlow, *et al.*, Strategies for the replacement of chromic acid anodising for the structural bonding of aluminium alloys. *Int. J. Adhes. Adhes.*, 2006. **26**: p. 419-53.
  76. G.W. Critchlow and D.M. Brewis, Review of surface pretreatments for aluminium alloys. *Int. J. Adhes. Adhes.*, 1996. **16**: p. 255-275.
  77. A.F. Harris and A. Beevers, The effects of grit-blasting on surface properties for adhesion. *Int. J. Adhes. Adhes.*, 1999. **19**: p. 445-52.
  78. C. Huh and S.G. Mason, Effects of surface roughness on wetting (theoretical). *J. Colloid. Interf. Sci.*, 1977. **60**(1): p. 11-38.
  79. F.G. Yost, J.R. Micheal, and E.T. Eisenmann, Extensive wetting due to roughness. *Acta Metall. Mater.*, 1995. **43**(1): p. 299-305.
  80. R.N. Wenzel, Resistance of solid surfaces to wetting by water. *Ind. Eng. Chem.*, 1936. **28**(8): p. 988-94.
  81. A. Carre and J. Schultz, Polymer-Aluminium Adhesion. I. The Surface Energy of Aluminium in Relation to its Surface Treatment. *J. Adh.*, 1983. **15**(2): p. 151-61.
  82. F. Balle, Ultraschallschweißen von Metall / C-Faser\_Kunststoff (CFK) - Verbunden. 2009, PhD thesis, University of Kaiserslautern: Kaiserslautern.
  83. M. Shahid and S.A. Hashim, Effect of surface roughness on the strength of cleavage joints. *Int. J. Adhes. Adhes.*, 2002. **22**: p. 235-44.
  84. S.M. Goushegir, J.F. dos Santos, and S.T. Amancio-Filho, Friction Spot Joining of aluminum AA2024/carbon-fiber reinforced poly(phenylene sulfide) composite single lap joints: Microstructure and mechanical performance. *Mater. Des.*, 2014. **54**: p. 196-206.
  85. N. Liu, W. Li, and J. Du, Study on the structure and corrosion resistance of chromatic Ti-Zr based conversion layer on 6063 aluminum magnesium alloy. *Surf. Technol.*, 2010. **39**(5): p. 45-7.
  86. X. Jin and J.D. Scantlebury, An investigation of paint adhesion to chromate conversion coating on aluminum alloys. *Mater. Prot.*, 1992. **25**(4): p. 4-9.

- 
87. D. Chidambaram, C.R. Clayton, and G.P. Halada, The role of hexafluorozirconate in the formation of chromate conversion coatings on aluminum alloys. *Electrochimica Acta*, 2006. **51**: p. 2862-71.
  88. M. Takai and M. Takaya, Influence of Conversion Coating on Magnesium and Aluminum Alloys by Adhesion Method. *Mater. Trans.*, 2008. **49**(5): p. 1065-70.
  89. N. Fin, *et al.*, Oxide Treatments of Al 2024 for Adhesive Bonding - Surface Characterization. *Appl. Surf. Sci.*, 1987. **28**: p. 11-33.
  90. S. Yu, *et al.*, Composition and Performance of Nanostructured Zirconium Titanium Conversion Coating on Aluminum-Magnesium Alloys. *J. Nanomaterials*, 2013. **2013**.
  91. J.H. Nordlien, *et al.*, Formation of a zirconium-titanium based conversion layer on AA 6060 aluminium. *Surf. Coat. Technol.*, 2002. **153**(1): p. 72-8.
  92. Z. Chen, *et al.*, Preparation & Microscopic Characterization of Non-Chrome Chemical Conversion Film in Aluminum Surface. *Adv. Mater. Phys. Chem.*, 2013. **3**: p. 7-9.
  93. O. Lunder, *et al.*, Formation and characterisation of a chromate conversion coating on AA6060 aluminium. *Corr. Sci.*, 2005. **47**: p. 1604-24.
  94. F. Le Coz, L. Arurault, and L. Datas, Chemical analysis of a single basic cell of porous anodic aluminium oxide templates. *Mater. Charac.*, 2010. **61**: p. 283-88.
  95. G.D. Sulka, Highly Ordered Anodic Porous Alumina Formation by Self-Organized Anodizing, in *Nanostructured Materials in Electrochemistry*, A. Eftekhari, Editor. 2008, Wiley-VCH Verlag: Weinheim. p. 8.
  96. J.D. Venables, Review Adhesion and durability of metal-polymer bonds. *J. Mater. Sci.*, 1984. **19**: p. 2431-53.
  97. J. Sykes, *et al.*, Anodic film formation on high strength aluminium alloy FVS0812. *J. Mater. Sci.*, 1997. **32**(18): p. 4909-16.
  98. G.D. Davis, *et al.*, Application of surface behaviour diagrams to the study of hydration of phosphoric acid-anodized aluminium. *J. Mater. Sci.*, 1982. **17**(6): p. 1807-18.
  99. B.B. Johnsen, *et al.*, The effect of pre-bond moisture on epoxy-bonded sulphuric acid anodised aluminium. *Int. J. Adhes. Adhes.*, 2004. **24**: p. 183-91.
  100. P.G. Sheasby, R. Pinner, and S. Wernick, eds. *The surface treatment and finishing of aluminium and its alloys*, Volume 1. 2001, ASM International: Materials Park, OH.
  101. B.B. Johnsen, F. Lapique, and A. Bjorgum, The durability of bonded aluminium joints: a comparison of AC and DC anodising pretreatments. *Int. J. Adhes. Adhes.*, 2004. **24**(2): p. 153-61.
  102. W. John and B. Ibber. Chromate-free conversion coatings for aluminum magnesium alloy. in *Proceedings of the AESF Annual Technical Conference*. 2002.
  103. E.M. Petrie, Primers and Adhesion Promoters, in *Handbook of Adhesives and Sealants*. 2006, McGraw Hill. p. 253-78.
  104. J. Comyn, *Adhesion science*. 1997, Cambridge: Royal Society of Chemistry.

- 
105. C. Bolger, Acid Base Interactions Between Oxide Surfaces and Polar Organic Compounds, in Adhesion Aspects of Polymeric Coatings, K.L. Mittal, Editor. 1983, Plenum Press: New York. p. 19-44.
  106. C. Kerr, N.C. Macdonald, and S. Orman, Effect of certain hostile environments on adhesive joints. *J. Appl. Chem.*, 1967. **17**(3): p. 62-5.
  107. F.M. Fowkes, Donor-Acceptor Interactions at Interfaces. *J. Adh.*, 1972. **4**(2): p. 155-9.
  108. G.D. Davis, Durability of Adhesive Joints, in Handbook of Adhesive Technology, Revised and Expanded, A. Pizzi and K.L. Mittal, Editors. 2003, Marcel Dekker: New York. p. 273-92.
  109. G.D. Davis and D.K. Shaffer, in Handbook of Adhesive Technology, A. Pizzi and K.L. Mittal, Editors. 1994, Marcel Dekker: New York. p. 113.
  110. A. Bjorgum, *et al.*, Anodising as pre-treatment for structural bonding. *Int. J. Adhes. Adhes.*, 2003. **23**: p. 401-12.
  111. A.J. Kinloch, L.S. Welch, and H.E. Bishop, The Locus of Environmental Crack Growth in Bonded Aluminium Alloy Joints. *J. Adh.*, 1984. **16**(3): p. 165-77.
  112. D.J. Bland, A.J. Kinloch, and J.F. Watts, The Role of the Surface Pretreatment in the Durability of Aluminium-Alloy Structural Adhesive Joints: Mechanisms of Failure. *J. Adh.*, 2013. **89**(5): p. 369-97.
  113. K.K. Chawla, Composite Materials: Science and Engineering. Third ed. 2012, New York: Springer.
  114. R. Srinivasan and L.H. Hihara, Corrosion Protection of Interfaces between Aluminum and Mechanically-Coupled Polymer Matrix Composites (PMCs), in 224th ECS Meeting, The Electrochemical Society. 2013: San Francisco - California.
  115. G. Habenicht, Kleben: Grundlagen, Technologie, Anwendungen. Second ed. 1990, Berlin: Springer.
  116. M.M.A. Wahab, Fatigue in Adhesively Bonded Joints: A Review. *ISRN Materials Science*, 2012. **2012**.
  117. W. Weibull, Fatigue testing and the analysis of results. 1961, Oxford: Pergamon Press.
  118. A.P. Vassilopoulos and T. Keller, Fatigue of Fiber-reinforced Composites. *Engineering Materials and Processes*. 2011, London: Springer-Verlag.
  119. D.F. Sims and V.H. Brogdon, Fatigue behavior of composites under different loading modes, in ASTM STP 636, K.L. Reifsnider and K.N. Lauraitis, Editors. 1977, American society for testing and materials: Philadelphia. p. 185-205.
  120. R.S. Khabbaz, Fatigue Life Prediction of Adhesively-Bonded Fiber-Reinforced Polymer Structural Joints under Spectrum Loading Patterns. 2012, PhD thesis, Ecole Polytechnique Federale de Lausanne: Lausanne.
  121. J.A. Epaarachchi and P.D. Clausen, An empirical model for fatigue behavior prediction of glass fibre-reinforced plastic composites for various stress ratios and test frequencies. *Comp. Part A*, 2003. **34**(4): p. 313-26.

- 
122. ASTM E739 - 10, Standard Practice for Statistical Analysis of Linear or Linearized Stress-Life (S-N) and Strain-Life ( $\epsilon$ -N) Fatigue Data. ASTM International, 2010.
  123. G.P. Sendeckyj, Fitting Models to Composite Materials Fatigue Data, in Test Methods and Design Allowables for Fibrous Composites, ASTM STP 734, C.C. Chamis, Editor. 1981, American Society for Testing and Materials. p. 245-60.
  124. J.M. Whitney, Fatigue characterization of composite materials, in Fatigue in fibrous composite materials, K.N. Lauraitis, Editor. 1981, ASTM STP 723, American society for testing and materials: Philadelphia. p. 133-51.
  125. A.M. Pereira, *et al.*, Study on the fatigue strength of AA 6082-T6 adhesive lap joints. Int. J. Adhes. Adhes., 2009. **29**(6): p. 633-8.
  126. W.-S. Kim and J.-J. Lee, Adhesion strength and fatigue life improvement of co-cured composite/metal lap joints by silane-based interphase formation. J. Adh. Sci. Technol., 2007. **21**(2): p. 125-40.
  127. F. Balle, *et al.*, Damage Monitoring of Ultrasonically Welded Aluminum/CFRP-Joints by Electrical Resistance Measurements. Procedia Eng., 2011. **10**: p. 433-8.
  128. Z. Huda, N.S. Taib, and T. Zaharinie, Characterization of 2024-T3: An aerospace aluminum alloy. Mats Chem Phys, 2009. **113**: p. 515-7.
  129. J-P. Immarigeon, *et al.*, Lightweight materials for aircraft applications. Mater. Charac., 1995. **35**(1): p. 41-67.
  130. A. Heinz, *et al.*, Recent development in aluminium alloys for aerospace applications. Mater. Sci. Eng. A, 2000. **280**(1): p. 102-7.
  131. I.J. Polmear, Wrought aluminium alloys, in Light Alloys, From Traditional Alloys to Nanocrystals. 2005, Butterworth-Heinemann: Oxford. p. 97-204.
  132. C. Vargel, Corrosion of Aluminium. 2004, Amsterdam: Elsevier.
  133. J.R. Davis, ed. Corrosion of Aluminum and Aluminum Alloys. 1999, ASM International: Materials Park, OH.
  134. J.R. Galvele and S.M. De Micheli, Mechanism of intergranular corrosion of Al-Cu alloys. Corr. Sci., 1970. **10**: p. 795-807.
  135. V. Guillaumin and G. Mankowski, Localized corrosion of 2024-T351 aluminium alloy in chloride media. Corr. Sci., 1998. **41**(3): p. 421-38.
  136. W. Qafsaoui, G. Mankowski, and F. Dabosi, The pitting corrosion of pure and low alloyed copper in chloride-containing borate buffered solutions. Corr. Sci., 1993. **34**(1): p. 17-25.
  137. Z. Szklarska-Smialowska, Insight into the pitting corrosion behaviour of aluminium alloys. Corr. Sci., 1992. **33**(8): p. 1193-1202.
  138. L.F. Mondolfo, Aluminium alloys structure and properties. 1976, London: Butterworths.
  139. R.K.W. Marceau, *et al.*, Evolution of solute clustering in Al-Cu-Mg alloys during secondary ageing. Acta Materialia, 2010. **58**: p. 1795-1805.
  140. S. Abis, *et al.*, Early ageing mechanisms in a high-copper AlCuMg alloy. Scripta Materialia, 2001. **45**(6): p. 685-91.

- 
141. M. Karlik and B. Jouffrey, High resolution electron microscope study of Guinier-Preston (GPI) zones in aluminium alloys. *Acta Materialia*, 1997. **45**: p. 3251-63.
  142. C.R. Hutchinson and S.P. Ringer, Precipitation processes in Al-Cu-Mg alloys microalloyed with Si. *Metall. Mater. Trans. A*, 2000. **31A**: p. 2721-33.
  143. S.P. Ringer, *et al.*, Precipitation processes during the early stages of ageing in Al-Cu-Mg alloys. *Appl. Surf. Sci.*, 1996. **94**: p. 253-60.
  144. A.E. Hughes, *et al.*, Sheet AA2024-T3: A new investigation of microstructure and composition. *Surf. Interf. Anal.*, 2010. **42**(4): p. 334-8.
  145. H.C. Shih, N.J. Ho, and J.C. Huang, Precipitation behaviours in Al-Cu-Mg and Aluminium 2024 alloys. *Metall. Mater. Trans. A*, 1996. **27**: p. 2479-94.
  146. M.W. Mahoney, Mechanical Properties of Friction Stir Welded Aluminum Alloys, in *Friction Stir Welding and Processing*, R.S. Mishra and M.W. Mahoney, Editors. 2007, ASM International: Materials Park, OH. p. 71-110.
  147. G. Mathers, *The welding of aluminium and its alloys*. 2002, Cornwall, England: Woodhead Publishing, CRC Press.
  148. C. Genevois, A. Deschamps, and P. Vacher, Comparative study on local and global mechanical properties of 2024 T351, 2024 T6 and 5251 O friction stir welds. *Mater. Sci. Eng. A*, 2006. **415**: p. 162-70.
  149. J.R. Davis, ed. *ASM International: Handbook of Aluminium & Aluminium Alloys*. 3rd ed. 1996: Ohio.
  150. P. Cavaliere, *et al.*, Mechanical and microstructural behaviour of 2024–7075 aluminium alloy sheets joined by friction stir welding. *Int. J. Machine Tools Manuf.*, 2006. **46**(6): p. 588-94.
  151. P. Sadeesh, *et al.*, Studies on Friction Stir Welding of AA 2024 and AA 6061 Dissimilar Metals. *Procedia Eng.*, 2014. **75**: p. 145-9.
  152. S.T. Amancio-Filho, *et al.*, Preliminary Investigation of the Microstructure and Mechanical Behaviour of 2024 Aluminium Alloy Friction Spot Welds. *Materials Transactions*, 2011. **52**(5): p. 985-91.
  153. J.E. Spruiell and C.J. Janke, *A Review of the Measurement and Development of Crystallinity and Its Relation to Properties in Neat Poly(Phenylene Sulfide) and Its Fiber Reinforced Composites*. 2004, Oak Ridge National Laboratory: USA.
  154. N.N., Thermoplastic composites for aerospace, in *The IAPD magazine*. April/May 2010.
  155. W. Maruszczak. Advanced composite polymer for the automotive market; long fiber reinforced linear polyphenylene sulfide (PPS). in *SPE ACCE conference*. 2007. Michigan, USA.
  156. J.K. Fink, *High Performance Polymers*. 2014, MA, USA: Elsevier.
  157. C. Friedel and J.M. Crafts, Sur une nouvelle méthode générale de syn-thèse des combinaisons aromatiques (deuxième mémoire). *Ann. Chim. Phy.*, 1888. **6**(14): p. 433-72.

- 
158. J. Geibel and J. Leland, Polymers Containing Sulfur, Poly(Phenylene Sulfide), in Kirk-Othmer Encyclopedia of Chemical Technology, J.I. Kroschwitz and A. Seidel, Editors. 2000, John Wiley and Sons.
  159. L.C. Lopez and G.L. Wilkes, Poly(p-Phenylene Sulfide)—An Overview of an Important Engineering Thermoplastic. *J. Macromolecular Sci., Part C: Polymer Reviews*, 1989. **29**(1): p. 83-151.
  160. J.T. Edmonds and H.W. Hill, U.S. Patent 3,354,129. 1967: USA.
  161. W.D. Callister Jr. and D.G. Rethwisch, *Fundamentals of Materials Science and Engineering: An Integrated Approach*. Fourth ed. 2012, New York: John Wiley & Sons.
  162. R. Zhang, *et al.*, Row nucleation phenomenon of Poly(phenylene sulfide) under shear condition. *Mater. Lett.*, 2008. **62**: p. 1414-7.
  163. H.W. Hill Jr. and D.G. Brady, in *High Performance Polymers and Composites*, J.I. Kroschwitz, Editor. 1991, John Wiley & Sons: New York. p. 551.
  164. L.B. Nohara, *et al.*, Study of Crystallization Behavior of Poly(Phenylene Sulfide). *Polímeros: Ciência e Tecnologia*, 2006. **16**(2): p. 104-10.
  165. M.P. Sepe. The Effects of Mold Temperature on the Creep Performance of PET Polyester and PPS below the Glass Transition Temperature. in *50th Annual Technical Conference - Society of Plastics Engineers*. 1992. Detroit, Michigan.
  166. N.N., CETEX® - PPS Guide Lines. 2003, Ten Cate Advanced Composites: Nijverdal, Netherlands.
  167. S. Lee, *et al.*, Effect of Curing Poly(p-Phenylene Sulfide) on Thermal Properties and Crystalline Morphologies. *Advances in Chem. Eng. Sci.*, 2013. **3**: p. 145-9.
  168. C.C.M. Ma, *et al.*, Thermal and Rheological Properties of Poly(Phenylene Sulfide) and Poly(Ether Etherketone) Resins and Composites. *Poly Comp*, 1987. **8**(4): p. 256-64.
  169. M. Day and D.R. Budgell, Kinetics of the thermal degradation of poly(phenylene sulfide). *Thermochimica Acta*, 1992. **203**: p. 465-74.
  170. L.H. Perng, Thermal decomposition characteristics of poly(phenylene sulfide) by stepwise Py-GC/MS and TG/MS techniques. *Poly. Deg. Stab.*, 2000. **69**: p. 323-32.
  171. Y. Bo, *et al.*, Kinetics of the Thermal Degradation of Hyperbranched Poly(phenylene Sulfide). *J. Appl. Poly. Sci.*, 2009. **111**: p. 1900-4.
  172. A.B. Port and R.H. Still, Synthesis and Characterization of Poly(Arylene Sulphides) - Part 4. Curing and Degradation Studies. *Poly Degradation Stability*, 1980. **2**: p. 1-22.
  173. G.W. Ehrenstein, G. Riedel, and P. Trawiel, *Thermal Analysis of Plastics Theory and Practice*. 2004, Germany: Carl Hanser Verlag.
  174. J. Deporter and D.G. Baird, The effects of thermal history on the structure/property relationship in polyphenylenesulfide/carbon fiber composites. *Poly. Comp.*, 1993. **14**(3): p. 201-13.

- 
175. B. Vieille, J. Aucher, and L. Taleb, Carbon Fiber Fabric Reinforced PPS Laminates: Influence of Temperature on Mechanical Properties and Behavior. *Advances in Poly. Tech.*, 2011. **30**(2): p. 80-95.
176. S.M. Goushegir, J.F. dos Santos, and S.T. Amancio-Filho, Influence of process parameters on mechanical performance of AA2024/CF-PPS friction spot joints. *Mater. Des.*, 2015. **83**: p. 431-442.
177. S.T. Amancio-Filho, *et al.*, Preliminary Investigation of the Microstructure and Mechanical Behaviour of 2024 Aluminium Alloy Friction Spot Welds. *Materials Transactions*, 2010. **52**(5): p. 985-91.
178. U. Suhuddin, *et al.*, A review on microstructural and mechanical properties of friction spot welds in Al-based similar and dissimilar joints. in *1st International Joint Symposium on Joining and Welding*. 2013. Osaka, Japan.
179. J.V. Esteves, *et al.*, Friction spot joining of aluminum 6181-T4 and carbon fiber reinforced poly(phenylene sulfide), in *70th Annual Technical Conference of the Society of Plastics Engineers 2012, ANTEC 2012*. 2012: Orlando, FL. p. 1698-1704.
180. L. Ye, *et al.*, De-consolidation and re-consolidation in CF/PPS thermoplastic matrix composites. *Composites: Part A*, 2005. **36**: p. 915-22.
181. S.T. Amancio-Filho, *et al.*, Thermal degradation of polyetherimide joined by friction riveting (FricRiveting). Part I: influence of rotation speed. *poly Degradation Stability*, 2008. **93**: p. 1529-38.
182. F. Yusof, *et al.*, Effect of anodizing on pulsed Nd:YAG laser joining of polyethylene terephthalate (PET) and aluminium alloy (A5052). *Mats & Des*, 2012. **37**: p. 410-5.
183. K.W. Jung, *et al.*, Laser direct joining of carbon fiber reinforced plastic to zinc-coated steel. *Mater. Des.*, 2013. **47**: p. 179-88.
184. S. Arai, Y. Kawahito, and S. Katayama, Effect of surface modification on laser direct joining of cyclic olefin polymer and stainless steel. *Mater. Des.*, 2014. **59**: p. 448-53.
185. C. Ageorges and L. Ye, *Fusion Bonding of Polymer Composites; From Basic Mechanisms to Process Optimization*, ed. B. Derby. 2002, London, Great Britain: Springer.
186. C. Ageorges, L. Ye, and M. Hou, Experimental investigation of the resistance welding of thermoplastic-matrix composites. Part II: optimum processing window and mechanical performance. *Compos. Sci. Tech.*, 2000. **60**: p. 1191-1202.
187. P.P. Parlevliet, H.E.N. Bersee, and A. Beukers, Residual stresses in thermoplastic composites—A study of the literature—Part I: Formation of residual stresses. *Composites: Part A*, 2006. **37**: p. 1847-57.
188. N.M. Andre, *et al.*, On the Microstructure and Mechanical Performance of Friction Spot Joining with Additional Film Interlayer. in *Annual Conference of the Society of Plastics Engineers, ANTEC 2014*. 2014. Las Vegas, CA.
189. G.G. Maksimovich, *et al.*, Effect of temperature on the strength of aluminum alloy base composites reinforced with networks. Translated from *Fiziko-Khimicheskaya Mekhanika Materialov*, 1975. **11**(2): p. 57-60.

- 
190. R.R. Cervay, Temperature Effect on the Mechanical Properties of Aluminum Alloy 2124-T851. 1975, University of Dayton Research Institute.
  191. S. Gudmundsson, General Aviation Aircraft Design: Applied Methods and Procedures. 2013, MA, USA: Butterworth-Heinemann.
  192. A. Skorupa and M. Skorupa, Riveted Lap Joints in Aircraft Fuselage: Design, Analysis and Properties. 2012, London, UK: Springer.
  193. N.N., CETEX® PPS, Technical datasheets, Tencate Advanced Composites. 2009: Netherlands.
  194. ASTM D3418 - 08, Standard Test Method for Transition Temperatures and Enthalpies of Fusion and Crystallization of Polymers by Differential Scanning Calorimetry. ASTM International, 2008.
  195. ASTM E1131 - 08, Standard Test Method for Compositional Analysis by Thermogravimetry. ASTM International, 2008.
  196. ASTM E384-99e1, Standard Test Method for Microindentation hardness of Material. ASTM International, 2005.
  197. ASTM D3163 - 01, Standard Test Method for Determining Strength of Adhesively Bonded Rigid Plastic Lap-Shear Joints in Shear by Tension Loading. ASTM International, 2008.
  198. DIN EN ISO 14272, Specimen dimensions and procedure for cross tension testing resistance spot and embossed projection welds. DIN, 2002.
  199. N.N., Technical datasheet Corundum, WIWOX GmbH Surface Systems. 2009.
  200. N.N., Alodine 4850 Sicherheitsdatenblatt gemäß Verordnung (EG) Nr. 1907/2006. Henkel Co., 2014.
  201. ASTM D3762 - 03, Standard Test Method for Adhesive-Bonded Surface Durability of Aluminum (Wedge Test). ASTM International, 2010.
  202. X.G. Li, *et al.*, High-Resolution Thermogravimetry of Polyphenylene Sulfide Film under Four Atmospheres. *J. App. Poly. Sci.*, 2002. **83**: p. 2053-9.
  203. A. Bauernhuber and T. Markovits, Investigating thermal interactions in the case of laser assisted joining of PMMA plastic and steel. *Physics Procedia*, 2014. **56**: p. 811-7.
  204. R. Velthuis, Induction Welding of Fiber Reinforced Thermoplastic Polymer Composites to Metal. 2007, PhD thesis, Vol. 75, IVW, Kaiserslautern.
  205. C. Gros, *et al.*, A study of mechanisms of Poly (PhenyleneSulfide) thermal degradation in air. *Adv. Mater. Res.*, 2010. **112**: p. 9-17.
  206. X.D. Wang, *et al.*, Crystallization Behavior and Crystal Morphology of Linear/Long Chain Branching Polypropylene Blends. *Polymer Journal*, 2008. **40**(5): p. 450-4.
  207. L.A. Utracki and A.M. Jamieson, eds. *Polymer Physics: From Suspensions to Nanocomposites and Beyond*. 2011, John Wiley & Sons: New Jersey, USA. p. 1951.
  208. H.F. Giles Jr., J.R. Wagner Jr., and E.M. Mount, *Extrusion: The Definitive Processing Guide and Handbook*. 2nd ed. 2013, Waltham, USA: William Andrew. p. 118.

- 
209. M. Kutz, ed. Applied Plastics Engineering Handbook: Processing and Materials. 1st ed. 2011, William Andrew: Waltham, USA. p. 263.
  210. T. Rosendo, *et al.*, Mechanical and microstructural investigation of friction spot welded AA6181-T4 aluminium alloy. Mater. Des., 2011. **32**: p. 1094-1100.
  211. R. Hancock, Friction Welding of Aluminum Cuts Energy Costs by 99%. Welding Journal, 2004. **83**(2): p. 40.
  212. R.W. Cahn and P. Haasen, eds. Physical Metallurgy. Fourth ed. 1996, Elsevier: Amsterdam, Netherlands.
  213. D. E. Laughlin and K. Hono, eds. Physical Metallurgy. Fifth ed. Vol. 3. 2014, Elsevier.
  214. C.A.W. Olea, Influence of energy input in friction stir welding on structure evolution and mechanical behaviour of precipitation-hardening in aluminium alloys (AA2024-T351, AA6013-T6 and Al-Mg-Sc). 2008, PhD thesis, University of Bochum: Bochum, Germany.
  215. A. Gerlich, G. Avramovic-Cingara, and T.H. North, Stir zone microstructure and strain rate during Al 7075-T6 friction stir spot welding. Metal Mater. Trans. A, 2006. **37**: p. 2773-86.
  216. N. Amanat, *et al.*, Transmission laser welding of amorphous and semi-crystalline poly-ether-ether-ketone for applications in the medical device industry. Mater. Des., 2010. **31**: p. 4823-30.
  217. A.M. Díez-Pascual, *et al.*, Nanoindentation in polymer nanocomposites. Prog. Mater. Sci., 2015. **67**: p. 1-94.
  218. W.C. Oliver and G.M. Pharr, An improved technique for determining hardness and elastic modulus using load and displacement sensing indentation experiments. Mater. Res., 1992. **7**(6): p. 1564-85.
  219. R.F. Gibson, A review of recent research on nanoindentation of polymer composites and their constituents. Compos. Sci. Tech., 2014. **105**: p. 51-65.
  220. J.B. Pethica and W.C. Oliver, Mechanical properties of nanometer volumes of material: use of the elastic response of small area indentations, in Thin films: Stresses and mechanical properties, J.C. Bravman, *et al.*, Editors. 1989, Mater. Res. Soc.: Pittsburgh. p. 13-23.
  221. W.C. Oliver and J.B. Pethica, Method for continuous determination of the elastic stiffness of contact between two bodies. 1989, U.S. Patent No. 4,848,141.
  222. Z. Chen, Nanoindentation testing of soft polymers: Computation, experiments and parameters identification. 2013, PhD thesis, University of Saarbrücken: Saarbrücken.
  223. M. Ovsik, *et al.*, Nano-Indentation Hardness of PA12 after Cross-linking Due to Beta Radiation. in Recent Advances in Automatic Control, Information and Communications. 2013. Valencia, Spain.
  224. L.F.M. da Silva, *et al.*, Effect of material, geometry, surface treatment and environment on the shear strength of single lap joints. Int. J. Adhes. Adhes., 2009. **29**: p. 621-32.
  225. H.Y. Yeh and D. Tandjung, Mixed Mode Fracture Analysis of the Lap Shear Specimen Test Per ASTM D1002. J. Reinf. Plast. Comp., 2005. **24**: p. 839-53.

- 
226. A. Olmedo, C. Santiuste, and E. Barbero, An analytical model for the secondary bending prediction in single-lap composite bolted-joints. *Comp. Struc.*, 2014. **111**: p. 354-61.
227. L.F.M. da Silva, *et al.*, Analytical models of adhesively bonded joints - Part II: Comparative study. *Int. J. Adhes. Adhes.*, 2009. **29**: p. 331-41.
228. H.K. Lee, S.H. Pyo, and B.R. Kim, On joint strengths, peel stresses and failure modes in adhesively bonded double-strap and supported single-lap GFRP joints. *Comp. Struc.*, 2009. **87**: p. 44-54.
229. J. Ekh, Multi-Fastener Single-lap Joints in Composite Structures. 2006, PhD thesis, Royal Institute of Technology: Stockholm.
230. G. Fessel, *et al.*, Evaluation of different lap-shear joint geometries for automotive applications. *Int. J. Adhes. Adhes.*, 2007. **27**(7): p. 574-83.
231. G. Paz, *et al.*, Numerical Simulation of the Mechanical Behavior of Polymer-Metal Joints, in 21st CBECiMat, Brazilian Congress of Materials Science and Engineering, Congresso Brasileiro de Engenharia e Ciencia dos Materiais. 2014: Cuiaba.
232. V.N. Kytopoulos, *et al.*, A SEM-Fractographic Study of Dynamic Crack Propagation Effects in Particulate Epoxy Systems under Impact Loading Conditions. *J. Reinf. Plast. Comp.*, 2009. **28**: p. 353-77.
233. L. Engel, *et al.*, Rasterelektronenmikroskopische Untersuchungen von Kunststoffschäden. 1978, München: Carl Hanser Verlag.
234. M. Tanniru, Q. Yuan, and R.D.K. Misra, On significant retention of impact strength in clay-reinforced high-density polyethylene (HDPE) nanocomposites. *Polymers*, 2006. **47**: p. 2133-46.
235. J.S. Solomon and D.E. Hanlin, AES and SEM Characterization of Anodized Aluminum Alloy Adherends for Adhesive Bonding Application. *App. Surf. Sci.*, 1980. **4**: p. 307-23.
236. J.A. Treverton, *et al.*, SSIMS, XPS and Microstructural Studies of ac-Phosphoric Acid Anodic Films on Aluminium. *Surf. Interf. Anal.*, 1990. **15**: p. 369-76.
237. S.G. Prolongo and A. Urena, Effect of surface pre-treatment on the adhesive strength of epoxy-aluminium joints. *Int. J. Adhes. Adhes.*, 2009. **29**(1): p. 23-31.
238. D.R. Baer, *et al.*, eds. State-of-the-art Application of Surface and Interface Analysis Methods to Environmental Material Interactions: In Honor of James E. Castle's 65th Year. 2001, The Electrochemical Society: New Jersey.
239. A.J. Kinloch, Adhesion and Adhesives: Science and Technology. First ed. 1987, Cambridge: Springer.
240. J.P. Rocher, J.M. Quenisset, and R. Naslain, Wetting improvement of carbon or silicon carbide by aluminium alloys based on a K<sub>2</sub>ZrF<sub>6</sub> surface treatment: application to composite material casting. *J. Mater. Sci.*, 1989. **24**(8): p. 2697-2703.
241. S. Schamm, *et al.*, The K<sub>2</sub>ZrF<sub>6</sub> wetting process: Effect of surface chemistry on the ability of a SiC-Fiber preform to be impregnated by aluminum. *Metall. Trans. A*, 1991. **22**(9): p. 2133-9.
-

- 
242. A.J. Kinloch, M.S.G. Little, and J.F. Watts, The Role of the Interphase in the Environmental Failure of Adhesive Joints. *Acta Materialia*, 2000. **48**: p. 4543-53.
243. H. Seidlitz, L. Ulke-Winter, and L. Kroll, New Joining Technology for Optimized Metal/Composite Assemblies. *J. Eng.*, 2014. **2014**.
244. H. Shimizu, Y. Tanabe, and H. Kanetsuna, X-Ray Photoelectron Spectroscopy of Electron Acceptor Doped Poly(p-phenylene sulfide). *Polymer Journal*, 1986. **18**(4): p. 367-70.
245. S. Evans, Correction for the Effects of Adventitious Carbon Overlayers in Quantitative XPS Analysis. *Surf. Interf. Anal.*, 1997. **25**: p. 924-30.
246. R.J. Bird and P. Swift, Energy calibration in electron spectroscopy and the re-determination of some reference electron binding energies. *J. Electron Spectros. Relat. Phenom.*, 1980. **21**(3): p. 227-40.
247. V.I. Nefedov, *et al.*, A comparison of different spectrometers and charge corrections used in X-ray photoelectron spectroscopy. *J. Electron Spectros. Relat. Phenom.*, 1977. **10**(2): p. 121-4.
248. R. Kaufmann, *et al.*, XPS studies of the thermal behaviour of passivated Zircaloy-4 surfaces. *Surf. Interf. Anal.*, 1988. **11**(10): p. 502-9.
249. N.N., NIST X-ray Photoelectron Spectroscopy Database, Version 4.1. 2012, National Institute of Standards and Technology, Gaithersburg.
250. K.P. So, *et al.*, Improving the wettability of aluminum on carbon nanotubes. *Acta Materialia*, 2011. **59**: p. 3313-20.
251. K.P. So, *et al.*, Electroplating formation of Al-C covalent bonds on multiwalled carbon nanotubes. *Synthetic Metals*, 2011. **161**: p. 208-12.
252. P. Marcus, *et al.*, An In Situ XPS Study of the Formation of Aluminium-Polymer Interfaces. *J. Surf. Interf. Anal.*, 1992. **19**: p. 127-32.
253. G.L. Georgiev, *et al.*, Chemical bond formation during laser bonding of Teflon FEP and titanium. *Appl. Surf. Sci.*, 2009. **255**: p. 7078-83.
254. D.G. Georgiev, *et al.*, An XPS study of laser-fabricated polyimide/titanium interfaces. *Appl. Surf. Sci.*, 2004. **236**: p. 71-6.
255. A.D. Juhl. Anodizing for Aerospace. 2010 [cited 20<sup>th</sup> December 2014]; Available from: <http://www.metalfinishing.com>.
256. A.A. Baker and R.J. Chester, Minimum surface treatments for adhesively bonded repairs. *Int. J. Adhes. Adhes.*, 1992. **12**(2): p. 73-8.
257. A.N. Rider and D.R. Arnott, Boiling water and silane pre-treatment of aluminium alloys for durable adhesive bonding. *Int. J. Adhes. Adhes.*, 2000. **20**(3): p. 209-20.
258. A. Rider and P. Chalkley, The Effect of FM-73 Cure Temperature on the Durability of Bonded Joints Employing BR127 Primer. 2000, Aeronautical and Maritime Research Laboratory: Melbourne.
259. N.H. Turner and A.M. Single, Determination of peak positions and areas from wide-scan XPS spectra. *Surf. Interf. Anal.*, 1990. **15**(3): p. 215-22.

- 
260. M. Kono, Studies of Metal-Polymer Interfaces. 2000, PhD thesis, University of British Columbia: Vancouver.
261. R. Hauert, *et al.*, XPS investigation of the a-C:H/Al interface. Surf. Sci. Lett., 1993. **292**: p. A605-A606.
262. T.J. Sarapatka, Palladium-induced charge transports with palladium/alumina/aluminum interface formation. J. Phys. Chem., 1993. **97**(43): p. 11274-7.
263. A. Stralin and T. Hjertberg, Influence of surface composition on initial hydration of aluminium in boiling water. Appl. Surf. Sci., 1994. **74**(3): p. 263-75.
264. M.R. Alexander, G.E. Thompson, and G. Beamson, Characterization of the oxide/hydroxide surface of aluminium using x-ray photoelectron spectroscopy: a procedure for curve fitting the O 1s core level. Surf. Interf. Anal., 2000. **29**(7): p. 468-77.
265. R.S. Alwitt, The Growth of Hydrous Oxide Films on Aluminum. J. Electrochem. Soc., 1974. **121**(10): p. 1322-8.
266. R.I. Butt and J.L. Cotter, The Effect of High Humidity on the Dynamic Mechanical Properties and Thermal Transition of an Epoxy-Polyamide Adhesive. J. Adh., 1976. **8**(11): p. 11-9.
267. M. Quaresimin and M. Ricotta, Fatigue behaviour and damage evolution of single lap bonded joints in composite material. Comp. Sci. Technol., 2006. **66**: p. 176-87.
268. M. Dube, *et al.*, Fatigue performance characterisation of resistance-welded thermoplastic composites. Comp. Sci. Technol., 2008. **68**: p. 1759-65.
269. M. Shahzad, *et al.*, Effect of sealed anodic film on fatigue performance of 2214-T6 aluminum alloy. Surf. Coat. Technol., 2012. **206**: p. 2733-9.
270. H.J. Schmidt and B. Schmidt, Fatigue & Damage Tolerance and Composite Training. 2012, Helmholtz-Zentrum Geesthacht: Geesthacht.
271. W. von Bestenbostel and K. Friedrich, The appearance of fatigue striations in the SEM, in 17th International Conference on Composite Materials, ICCM-17. 2009: Edinburgh, UK.
272. P.-C. Lin, J. Pan, and T. Pan, Failure modes and fatigue life estimations of spot friction welds in lap-shear specimens of aluminum 6111-T4 sheets. Part 1: Welds made by a concave tool. Int. J. Fatigue, 2008. **30**: p. 74-89.
273. D.J. Sheskin, Handbook of Parametric and Nonparametric Statistical Procedures, Appendix: Table A4. Third ed. 2003, Florida: Chapman&Hall / CRC.



---

# List of Figures

Figure 1.1 Materials breakdown in Airbus A350XWB. Adapted from [8] with permission. ....	1
Figure 1.2 Mercedes-Benz F125 research vehicle concept. Adapted from [15].....	2
Figure 3.1 Joining techniques for metal-polymer multi-materials [16].....	6
Figure 3.2 Schematic illustration of (a) adhesive bonding of a metal-composite SLS joint, (b) adhesive, (c) cohesive, (d) mixed mode, (e) fiber-tear, and (f) stock-break failure types. ....	8
Figure 3.3 Schematic illustration of the FricRiveting process; (a) positioning of the joining parts, (b) rivet approaching the polymer part, (c) forging of rivet into the polymer, and (d) joint consolidation. Adapted from [41]. ....	10
Figure 3.4 Process steps of (a) E-ICJ (adapted from [48]) and (b) F-ICJ (adapted from [52]). ....	11
Figure 3.5 Schematic illustration of the induction welding process steps. Adapted from [53]. ....	12
Figure 3.6 Schematic illustration of the ultrasonic welding equipment. Adapted from [58]. ....	13
Figure 3.7 Schematic illustration of various types of metal surface irregularities in contact with a molten polymer. Adapted from [68]. ....	15
Figure 3.8 Wetting of a metal surface by the molten polymer; (a) efficient wetting, and (b) poor wetting. Adapted from [63]. ....	16
Figure 3.9 Schematic illustration of the oxide layer structure on aluminum after anodizing pre-treatment. Adapted from [95]. ....	18
Figure 3.10 Schematic illustration of the PPS main structure. ....	23
Figure 3.11 Spherulitic crystal structure of PPS. Adapted from [162]. ....	24
Figure 4.1 Illustration of the FSpJ tool; (a) consisting of three parts (dimensions in mm), (b) tool parts coaxially mounted together, and (c) cross-section of the tool in the middle plane. ....	26
Figure 4.2 Configuration of the joining parts and the FSpJ tool before the process starts. ....	26
Figure 4.3 Schematic representation of the FSpJ process steps; (1) the sleeve plunging plasticizes the metal, (2) spot refilling, and (3) joint consolidation. Adapted from [20]. ....	27
Figure 4.4 Top view of a sound metal-composite FSp joint. ....	27
Figure 4.5 Example of a variation-monitoring diagram showing the FSpJ process phases in the sleeve plunge variant. ....	28
Figure 4.6 Schematic illustration of the spot area showing the impression of the tool parts on the top surface of the metal; (a) top view and (b) 3D view. ....	28
Figure 4.7 Example of a cross-section of an FSp joint in the middle of the spot. The rectangle indicates the nub, and the red circles show the gap formation below the plunging sleeve. (rotational speed: 2900 rpm, plunge depth: 0.8 mm, joining time: 4 s, joining pressure: 0.3 MPa). ....	29

---

Figure 4.8 Schematic illustration of the cross-section of the middle of the spot area. A nub reservoir is formed that accommodates the molten polymer. The composite partner is omitted for better visualization.....	29
Figure 4.9 Comparison of the nub shape in case of (a) a continuous fiber-reinforced composite, and (b) a short fiber-reinforced composite. (rotational speed: 1900 rpm, plunge depth: 0.5 mm, joining time: 4 s, joining pressure: 0.2 MPa).....	29
Figure 4.10 Comparison of the gap formed on the surface of the metal with a plunge depth of (a) 0.8 mm, and (b) 0.5 mm. Other joining parameters were rotational speed: 2900 rpm, joining time: 4 s, and joining pressure: 0.3 MPa. The dashed lines display the mid-plane between metal and composite before the joining process. The arrows in (b) indicate the two bumps helping the keyhole filling. ....	30
Figure 4.11 (a) Illustration of the adhesion forces as one of the primary bonding mechanisms in FSpJ, and (b) an example of the fracture surface of an FSp joint tested by lap shear. ....	31
Figure 4.12 De-consolidation defects in the composite with FSpJ, showing (a) voids in the consolidated molten layer, and (b) fiber-matrix debonding. ....	34
Figure 4.13 Illustration of a broken stir zone (BSZ) that occurs in the metal part; (a) top view of the metal part, and (b) cross-section of the joint in (a) at the center of the spot. (rotational speed: 2900 rpm, plunge depth: 0.8 mm, joining time: 8 s, joining pressure: 0.3 MPa). ....	34
Figure 4.14 Mechanism of the BSZ formation; (a) excessive sleeve plunge, (b) initiation of micro-cracks in the metal, (c) propagation of the crack, and (d) formation of the BSZ. ....	35
Figure 4.15 Schematic illustration of potential FSpJ applications; (a) in the aircraft structure, to join (b) a metal skin to a composite skin, and (c) a metal stringer to the composite skin. ....	37
Figure 5.1 Schematic illustration of the experimental approach of this PhD project. ....	39
Figure 6.1 Microstructure of AA2024-T3 in longitudinal (L) and transverse (T) directions according to the alloy rolling direction, as well as the surface view (Barker etched, magnification 50X).....	41
Figure 6.2 Microstructure of CF-PPS in the warp direction, showing fibers in 0°, 90°, and ±45°. ..	42
Figure 6.3 (a) A photo of the RPS100 welding head, the assembled tool, welding table, the pneumatic piston, and (b) a magnified image of the welding head and table showing the limited upstroke in the equipment. ....	42
Figure 6.4 Schematic presentation of the position of thermocouples to measure the local temperature of the aluminum (TC-1 and TC-2) and interface (TC-3); (a) 3-D view, and (b) magnified cross-section showing the exact position of each thermocouple. ....	43
Figure 6.5 Schematic illustration of temperature measurement by IR-thermography; (a) showing the position of the IR-camera, and (b) an example of a snapshot from the peak temperature on the aluminum surface during FSpJ. The area used to measure the temperature is indicated in the snapshot. ....	44
Figure 6.6 Schematic illustration of the surface roughness features and parameters. ....	45
Figure 6.7 Consolidated PPS layer that remained attached to the aluminum after mechanical testing was removed and used for thermal analysis. ....	46

---

---

Figure 6.8 Schematic illustration of the position of nanoindenters in the consolidated PPS molten layer in the joints. ....	47
Figure 6.9 (a) Schematic illustration of the SLS joint geometry; the respective dimensions used in this work from (b) side-view and (c) top-view. All dimensions are in mm.....	48
Figure 6.10 (a) Schematic illustration of the CT joint geometry and (b) top-view of the joint design with the respective dimensions used. All dimensions are in mm. ....	49
Figure 6.11 (a) Schematic illustration of the geometry of the fatigue specimen; the respective dimensions used in this work from (b) side-view and (c) top-view. All dimensions are in mm. ....	49
Figure 7.1 Process temperature evolution measured on the aluminum part by IR-thermography (IR) and by thermocouples (TC) for the (a) LHI joint, and (b) HHI joint.....	56
Figure 7.2 Process temperature evolution measured by thermocouples (TC) in the aluminum (TC-1 and TC-2) and at the aluminum-composite interface (TC-3) for the (a) the LHI joint, and (b) the HHI joint. Inset charts relate to the TC-3. ....	57
Figure 7.3 TG analysis of the PPS in the BM, LHI and HHI in nitrogen showing the mass change between 30°C and 800°C. The green area shows the window of the FSpJ process temperature in this work. ....	59
Figure 7.4 TG-DTG curves for the BM, LHI and HHI conditions in the range of 400°C to 700°C. the BM showed one-step degradation, whereas LHI and HHI joint showed two-step degradation as indicated by the two peaks in the DTG curve.....	60
Figure 7.5 Example of DSC curves for the BM, LHI and HHI samples in the range of interest using a heating rate of 10°C/min in nitrogen. ....	60
Figure 7.6 Microstructural zones that form in the aluminum. (a) General overview of the joints microstructure, (b) microstructure in the BM, (c) MTMAZ showing elongated grains rotated compared to the BM grains, (d) boundary between MTMAZ and MSZ, (e) MSZ showing very fine DRX grains, and (f) boundary between MTMAZ and MHAZ.....	64
Figure 7.7 Microstructure of the (a) LHI and (b) HHI joints. Yellow dashed lines indicate the boundary between PHAZ and BM. The PHAZ in the HHI joint shows an extended width (w) and depth (d) into the composite compared to the LHI joint.....	65
Figure 7.8 Microhardness maps of the AA2024-T3 from the edge of the specimen (x=0 mm) to the middle of the spot (x=12.5 mm) in the (a) LHI and (b) HHI joining conditions. The observed zones are indicated in (b). ....	67
Figure 7.9 An example of the load-displacement curve obtained through nanoindentation in the CF-PPS base material. S: stiffness obtained from the unloading curve, $P_{max}$ : maximum load achieved in the experiment, $h_{max}$ : maximum indentation displacement, and $h_f$ : final displacement after release of the elastic deformation (Adapted from [218]). ....	68
Figure 7.10 Example of the dynamic indentation (a) modulus and (b) hardness of the PPS as a function of the displacement into the surface for the BM, LHI, and HHI specimens. ....	69
Figure 7.11 Comparison of the indentation (a) modulus and (b) hardness of the PPS from the BM, LHI, and HHI specimens. ....	70

---

---

Figure 7.12 (a) Schematic fracture surface of an FSp joint and (b) real fracture surface of an AA2024-T3 / CF-PPS FSp joint, indicating three bonding zones; plastically deformed zone (PDZ), transition zone (TZ), and adhesion zone (AZ). .....	71
Figure 7.13 Cross-section of an AA2024-T3 / CF-PPS FSp joint in the PDZ examined by LSCM showing micro-mechanical interlocking through (a) aluminum pore/crevice filling by the molten PPS in a resin-rich area and (b) fiber entrapment. (c) High magnification SEM image showing a thin layer of the PPS between aluminum and carbon fibers. ....	72
Figure 7.14 Fracture surface of an AA2024-T3 / CF-PPS FSp joint (produced by the LHI condition) showing the initiation of radial cracks in the external periphery of the AZ. The white arrow indicates the influence of secondary bending on the tearing fracture of the PPS in the AZ. ....	73
Figure 7.15 Schematic illustration of the proposed crack propagation mechanism in friction spot joints under shear loading [84]. ....	73
Figure 7.16 An example of the typical load (force) - displacement curve in FSpJ under shear loading divided into four regions. The graph inset shows a section of the curve related to the beginning of the crack propagation. ....	74
Figure 7.17 A cross-section snapshot of the AA2024-T3 / CF-PPS FSp joint simulated by finite elements analysis. A region of high stress concentration inside the overlap area between the nub and the edge of the joint is visible [231]. ....	75
Figure 7.18 SEM fracture surface examination of the AA2024-T3 / CF-PPS FSp joint (an example of a HHI joint); (a) AZ on the aluminum, (b) AZ on the composite, (c) AZ-TZ boundary on the aluminum showing pieces of the PPS remaining attached as individual islands inside the TZ, (d) AZ-TZ boundary on the composite showing fibrous-like (indicated by the white arrow) and vein-type (indicated by the black arrow) features in the TZ, (e) magnified image of the fibrous-like features, implying a ductile fracture, and (f) magnified image of the vein-type features showing a smooth area inside, implying a brittle fracture. Note that in these figures the path of the radial cracks follow from top-left to bottom-right of the images. ....	76
Figure 7.19 SEM fracture surface examination on the AA2024-T3 side from four regions indicated in (a), (b) general overview in the center of the spot showing PPS matrix and carbon fibers remain attached to the aluminum, (c) Pulled-out warp carbon fibers and some of the PPS matrix attached to the aluminum due to the micro-mechanical interlocking phenomenon, (d) high magnification image of the PPS matrix from (c) illustrating plastic deformation of the PPS (indicated by the white arrow) and tearing (indicated by black arrows), (e) some of the weft carbon fibers remain attached to the aluminum, while most of the fibers are partially covered by the PPS matrix, and (f) high magnification of a region with high concentration of voids; showing a very smooth, brittle fracture in the vicinity of the voids. Direction of the applied load is indicated by the arrows in (c), (d), (e), and (f). ....	78
Figure 7.20 SEM fracture surface examination on the CF-PPS side from the regions indicated in (a), (b) general overview in the center of the spot, where slight distortions of the fibers are indicated by the arrows, (c) elongated fibrils in an area containing warp fibers resembling a ductile fracture, (d) high magnification of the fibrils in (c) where the tearing fracture at the ends of the fibrils is apparent, (e) broken weft fibers, and (f) high magnification of the broken weft fibers where slight	

---

rotation of the fibers in the direction of the applied load is visible. Direction of the applied load is indicated by the arrows in (c) and (e). .....	80
Figure 7.21 (a) High magnification image of the warp fibers region in which the white arrow indicates an impression of a pulled-out fiber, (b) high magnification image of the fiber-matrix debonding in a weft fiber as a result of weakened fiber-matrix adhesion. Black arrows indicate some micro-voids acting as crack initiation, smaller white arrows (top) show crack propagation path and larger white arrows (bottom) illustrate a tearing fracture along the fiber-matrix interface.	80
Figure 8.1 SEM images of the AA2024-T3 surface from (a) AR, and after (b) MG and (c) SB pre-treatments.....	86
Figure 8.2 SEM images of the AA2024-T3 surface after (a) AP and (b) CC pre-treatments.....	86
Figure 8.3 SEM images of the AA2024-T3 surface after (a) SAA and (b) PAA pre-treatments, and (c) high magnification image of the PPA pre-treated surface.....	87
Figure 8.4 SEM image of the AA2024-T3 surface after PAA-P pre-treatment. ....	88
Figure 8.5 Example of selected spectra from the EDS analysis of the AA2024-T3 surface; from (a) AR, (b) SB, (c) CC, (d) PAA, and (e) PAA-P. ....	90
Figure 8.6 XPS analysis of the AA2024-T3 surface; (a) AR and (b) CC.....	91
Figure 8.7 Mechanical strength of SLS FSp joints after aluminum surface pre-treatments. ....	92
Figure 8.8 Cross-tensile strength of the FSp joint for the selected surface pre-treatments. ....	94
Figure 8.9 Fracture surfaces of the SLS joints; (a) SB, (b) CC, (c) PAA, and (d) PAA-P. White arrows in (d) indicate primer remaining attached to the CF-PPS. ....	95
Figure 8.10 SEM imaging of the fracture surface of the CF-PPS; (a) primer residues remain attached to the composite, and (b) a high magnification image of the white rectangle in (a). ....	95
Figure 8.11 (a) SEM image of the primer layer remained attached to the composite, (b) EDS spectrum of Spot 1 in (a), and (c) EDS spectrum of Spot 2 in (a). ....	96
Figure 8.12 High-resolution XPS region spectra before (red) and after (black) etching for 1800 s for (a) and (b) CC pre-treatment, (c) and (d) PAA pre-treatment. ....	98
Figure 8.13 View from above of an adhesively bonded joint between AA2024-T3 and CF-PPS pre-treated by the PAA-P procedure. ....	99
Figure 8.14 Comparison of the (a) lap shear strength and (b) displacement at the peak load of the FSp joints and reference bonded joints.....	100
Figure 8.15 Load (force)-displacement curves of the FSp joint and reference bonded joint under shear loading.....	100
Figure 8.16 Fracture surface of the reference bonded joint indicating 100% adhesive failure. ....	101
Figure 9.1 Top view of the SLS FSp joints after 28 days of aging; (a) SB, (b) CC, (c) PAA, and (d) PAA-P.....	103
Figure 9.2 Bottom view of the SLS FSp joints after 28 days of aging; (a) SB, (b) CC, (c) PAA, and (d) PAA-P. ....	103

---

---

Figure 9.3 High-magnification SEM images of the aluminum affected areas after 28 days of aging; (a) SB and (b) CC specimens showing nodular, flake-like structures. ....	103
Figure 9.4 EDS analysis of the aluminum affected areas on (a) SB and (b) CC specimens. ....	104
Figure 9.5 High-resolution Al 2p XPS region spectra of SB specimen (a) before aging and (b) after aging. ....	105
Figure 9.6 High-magnification SEM images of the aluminum side of the joint after 28 days of aging; (a) PAA and (b) PAA-P specimens. ....	105
Figure 9.7 EDS analysis of the aluminum side of the joints from (a) PAA and (b) PAA-P specimens after aging. ....	106
Figure 9.8 Residual strength of the SLS FSp joints after 28 days of accelerated aging. ....	107
Figure 9.9 Schematic illustration of aluminum oxide after PAA pre-treatment, adapted from [95], and the proposed model of pore filling by the PPS. (1) complete wetting and pore filling, (2) complete wetting, incomplete pore filling, (3) partial wetting and incomplete pore filling, and (4) no wetting and no pore filling. ....	109
Figure 9.10 Fracture surfaces of the SLS joints after 28 days accelerated aging; (a) SB, (b) CC, (c) PAA, and (d) PAA-P. Black arrows in (a) and (b) indicate the aluminum hydroxide formation. The white arrow in (a) indicates small features outside the AZ. White arrows in (d) indicate the primer remaining attached to the CF-PPS. ....	110
Figure 9.11 SEM image of the fracture surface of the SB specimen on the aluminum side after 28 days of accelerated aging. (a) Low-magnification image of the AZ-TZ area and (b) high-magnification image of the white rectangle indicated in (a). ....	110
Figure 9.12 SEM image of the fracture surface of the SB specimen on the composite side after 28 days of accelerated aging. (a) Low-magnification image from the area indicated by the white arrow in Figure 9.10 (a); (b) high-magnification image from the black rectangle indicated in (a), and (c) high-magnification image from the white rectangle indicated in (a). ....	111
Figure 9.13 EDS analysis of the (a) flake-like features and (b) agglomerates in Figure 9.12. ....	111
Figure 10.1 Derived S-N curves based on exponential, power law, and wear-out models for the (a) SB, (b) SB+CC, (c) PAA, and (d) PAA-P specimens. ....	114
Figure 10.2 S-N curves of the various surface pre-treatment specimens based on the exponential model. ....	115
Figure 10.3 Quasi-static strength of the FSp joints for the surface pre-treatments after $10^6$ cycles of fatigue loading compared with the respective initial quasi-static strength. ....	117
Figure 10.4 Fracture surfaces of the HC fatigue specimens; (a) SB – 606,281 cycles to failure, (b) SB+CC – 129,406 cycles to failure, (c) PAA – 482,136 cycles to failure, and (d) PAA-P – 442,673 cycles to failure. ....	118
Figure 10.5 Failure micro-mechanisms of a high cycle fatigue SB specimen from the composite side; (a) warp fibers orientation, (b) weft fibers orientation, (c) fatigue striations in the PPS matrix	

---

debonding from the fibers, and (d) striations in the PPS matrix in a resin-rich area. Black arrows in (a) and (b) indicate the loading direction; (c) and (d) were taken at a tilt angle of 45°.....	119
Figure A.1 Comparison of mechanical strength of the SLS FSp joints between sleeve and pin plunge variants.....	X
Figure A.2 Mechanical performance of SLS FSp joints after one repair process compared with the as-joined condition (joining condition C01 from Table A.1). .....	XI
Figure A.3 Temperature development during the FSpJ process measured by (a) thermography, (b) thermometry TC1 and TC2, (c) thermometry TC3 for LHI and HHI joining conditions.....	XII
Figure A.4 Thermal analysis of the CF-PPS from the BM and LHI and HHI joining conditions by (a) DSC and (b) TGA. ....	XIII
Figure A.5 Detailed results of nanoindentation on the PPS molten layer from the BM and LHI and HHI joining conditions, (a) load-displacement curves, (b) modulus vs contact depth from CSM measurement and (c) hardness vs contact depth from CSM measurement. ....	XIV
Figure A.6 Mechanical performance of SLS FSp joints after plasma treatment of the composite compared with the as received condition (joining condition C03 from Table A.1). ....	XV
Figure A.7 XPS spectra of the aluminum surface after (a) SB, (b) PAA and (c) PAA-P pretreatments. (d) Spectrum of the CF-PPS base material. ....	XVI
Figure A.8 Load-displacement curves of SLS FSp joints for (a) AR condition, and after surface aluminum pre-treatments: (b) MG, (c) SB, (d) AP, (e) CC, (f) SB+AP, (g) SB+CC, (h) SAA, (i) PAA and (j) PAA-P. ....	XVII
Figure A.9 Load-displacement curves of CT FSp joints after aluminum surface pre-treatments: (a) MG, (b) SB, (c) CC, (d) SB+CC, (e) PAA and (f) PAA-P.....	XVIII
Figure A.10 Load-displacement curves of the reference SLS adhesively bonded joints. ....	XIX

---

# List of Tables

Table 4.1 Controllable FSpJ process parameters and their respective functions.....	33
Table 6.1 Nominal chemical composition of AA2024-T3 used in this work.....	40
Table 6.2 Selected mechanical and physical properties of the AA2024-T3 used in this work. ....	40
Table 6.3 Selected mechanical and physical properties of the CF-PPS used in this work.....	41
Table 6.4 Various aluminum surface pre-treatments performed in this work.....	50
Table 6.5 Chemical composition of the corundum used in this work [199].....	51
Table 7.1 LHI and HHI joining conditions used in this work. ....	55
Table 7.2 Average peak temperatures by IR-thermography and the thermocouples (TC) for the LHI and HHI joining conditions. ....	57
Table 7.3 Average heating and cooling rates inside the aluminum (TC-1 and TC-2) and at the aluminum-composite interface (TC-3) using thermocouples for the LHI and HHI joining conditions. ....	57
Table 7.4 The total time fraction that the composite at the interface remained above $T_g$ and $T_m$ of the PPS, obtained from the TC-3.....	58
Table 7.5 The main parameters obtained from DSC analysis. $T_c$ : crystallization temperature, $\Delta H_c$ : enthalpy of crystallization, $T_m$ : melting temperature, $\Delta H_m$ : enthalpy of melting, FWHH: full-width at half-height.....	61
Table 7.6 Average width (w) and depth (d) of the PHAZ, and the obtained average temperature at the interface in LHI and HHI joining conditions.....	65
Table 7.7 Average and standard deviation of indentation modulus and hardness of the PPS obtained from the unloading section of the load-displacement curves. ....	69
Table 8.1 Water contact angle measurements and an example of the water droplet on the AA2024-T3 surface after various pre-treatments. ....	83
Table 8.2 Average surface roughness parameters of the AA2024-T3 after various surface pre-treatments obtained by non-contact LSCM.....	85
Table 8.3 Average chemical composition (in wt%) of the AA2024-T3 surface after different surface pre-treatments by EDS analysis.....	90
Table 9.1 Average chemical composition (in wt%) of the SB and CC pre-treated AA2024-T3 surface after 28 days of accelerated aging through EDS analysis.....	104
Table 9.2 Average chemical composition (in wt%) of the PAA and PAA-P pre-treated AA2024-T3 surface after 28 days of accelerated aging through EDS analysis.....	106
Table 9.3 Average chemical composition (in wt%) of the flake-like features and agglomerates on the CF-PPS through EDS analysis. ....	112
Table 10.1 Fatigue strength (N) of various specimens based on the three models at $10^5$ cycles. ...	116

---

Table A.1 Selected joining conditions for comparison between sleeve and pin plunge variants presented in Figure A.1. ....	X
Table A.2 Estimated parameters for the selected models. ....	XXII
Table A.3 Estimated fatigue strength [N] of the selected pre-treated joints based on exponential, power law, and wear-out models after $10^5$ and $10^6$ cycles. ....	XXII
Table A.4 Fatigue strength / ULSF [%] of the selected pre-treated joints based on exponential, power law, and wear-out models after $10^5$ and $10^6$ cycles.xxx.....	XXIII
Table A.5 Calculation of the linearity index for the exponential and power law models. ....	XXIII
Table A.6 Calculated Kruskal-Wallis statistics index and the respective critical value for the wear-out model. ....	XXIV

---

# Appendices

## Appendix A.1

### Mechanical performance of sleeve plunge vs. pin plunge variants

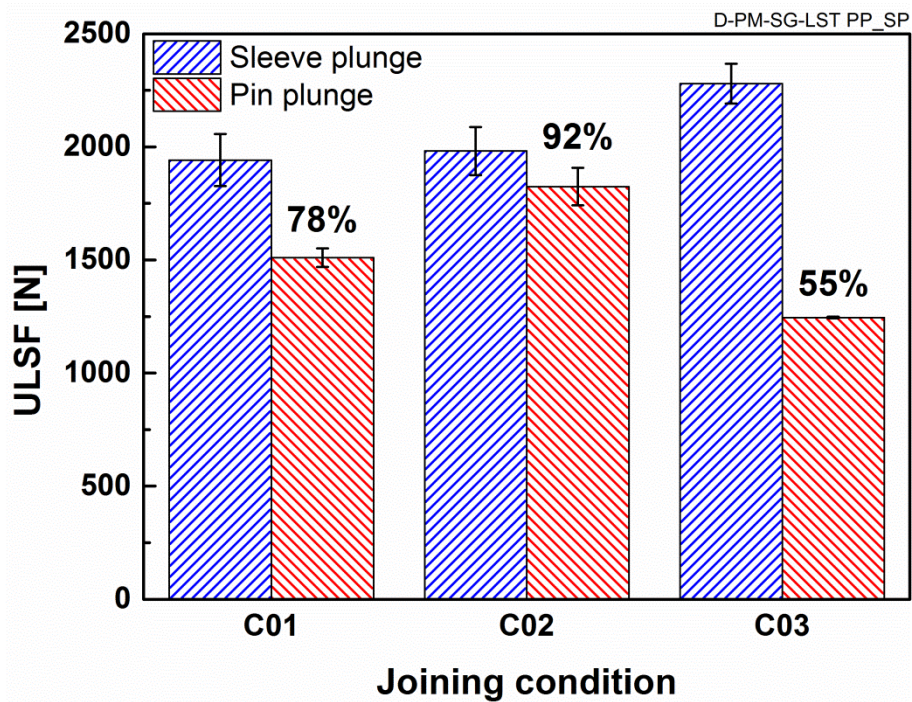


Figure A.1 Comparison of mechanical strength of the SLS FSp joints between sleeve and pin plunge variants.

Table A.1 Selected joining conditions for comparison between sleeve and pin plunge variants presented in Figure A.1.

Joining condition	Symbol	Rotational speed [rpm]	Plunge depth [mm]	Joining time [s]	Joining pressure [MPa]
Condition 1	C01	1900	0.5	4	0.3
Condition 2	C02	1900	0.8	4	0.2
Condition 3	C03	2900	0.8	4	0.3

---

## Appendix A.2

### Mechanical performance of a repaired FSp joint

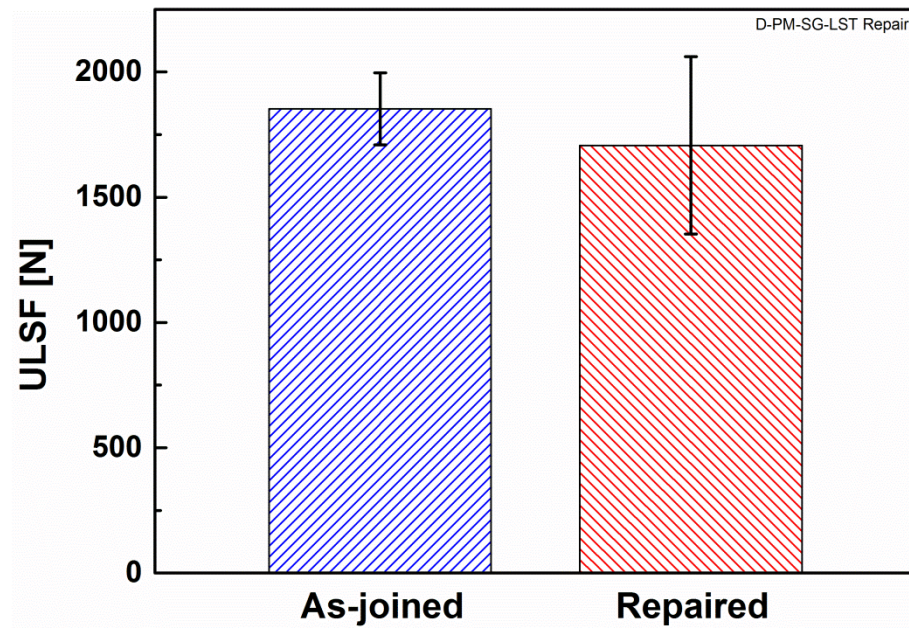


Figure A.2 Mechanical performance of SLS FSp joints after one repair process compared with the as-joined condition (joining condition C01 from Table A.1).

---

# Appendix A.3

## Detailed temperature measurements by thermography and thermometry

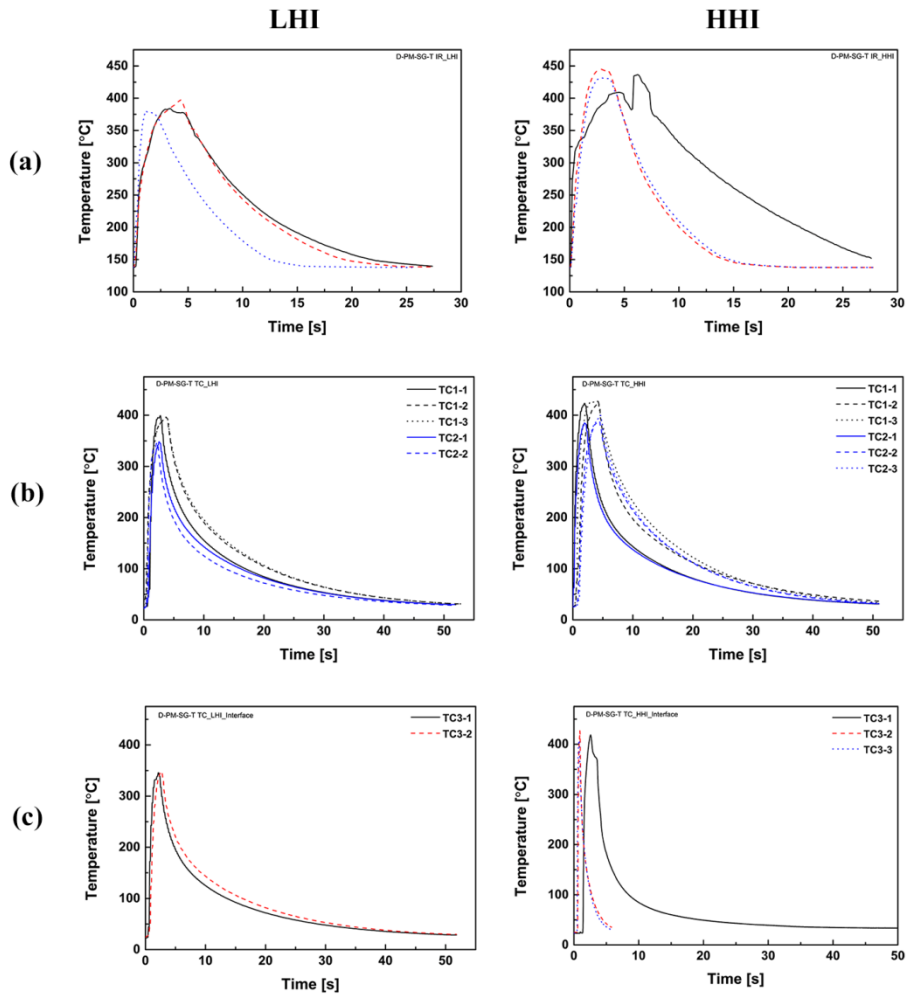


Figure A.3 Temperature development during the FSpJ process measured by (a) thermography, (b) thermometry TC1 and TC2, (c) thermometry TC3 for LHI and HHI joining conditions.

# Appendix A.4

## Detailed thermal analysis of the joints

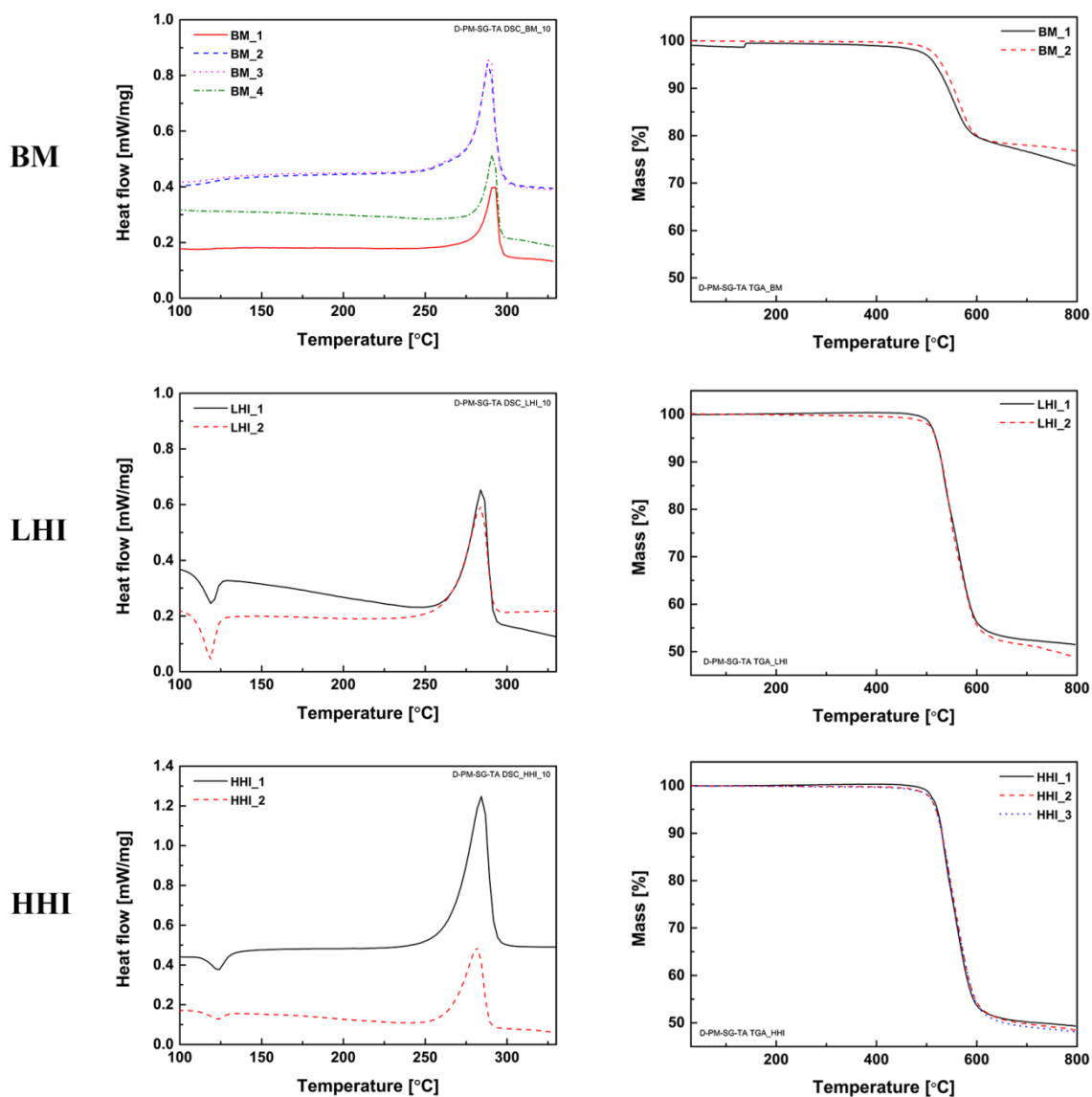
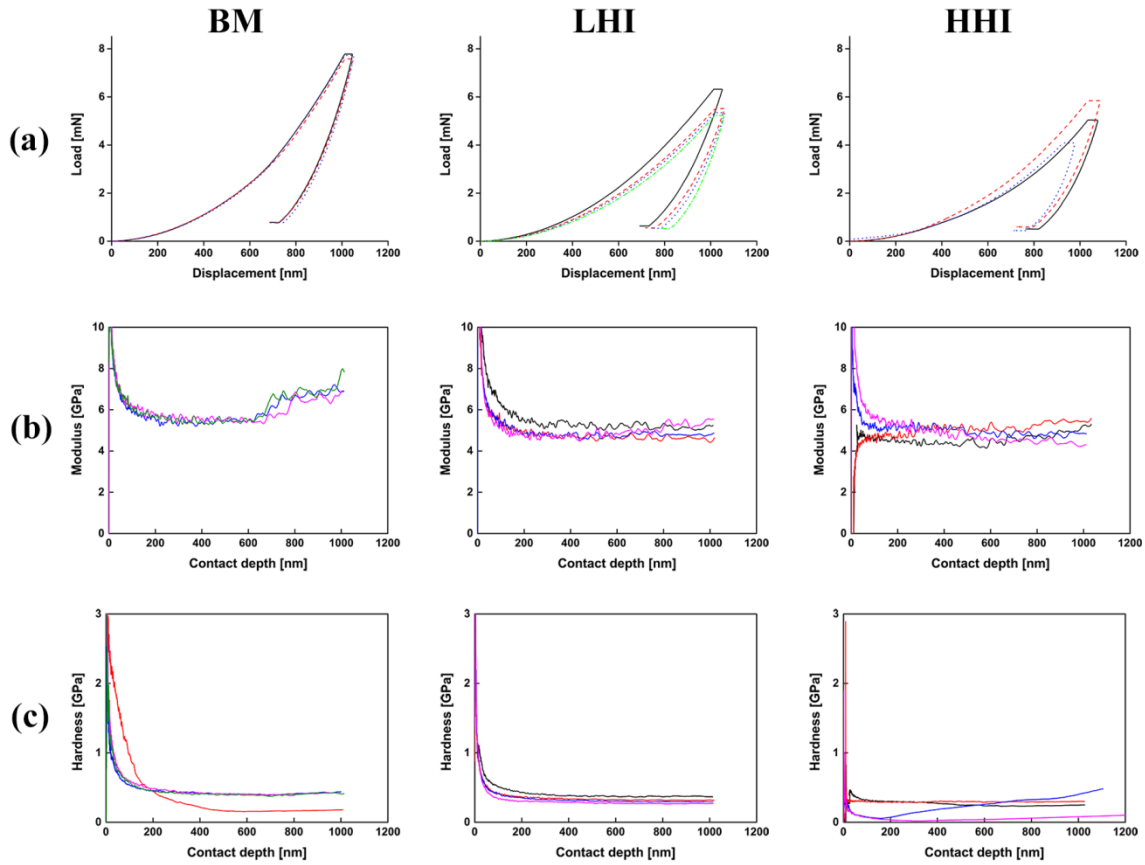


Figure A.4 Thermal analysis of the CF-PPS from the BM and LHI and HHI joining conditions by (a) DSC and (b) TGA.

---

# Appendix A.5

## Detailed nanoindentation experiments



**Figure A.5 Detailed results of nanoindentation on the PPS molten layer from the BM and LHI and HHI joining conditions, (a) load-displacement curves, (b) modulus vs contact depth from CSM measurement and (c) hardness vs contact depth from CSM measurement.**

---

## Appendix A.6

### Mechanical performance of an FSp joint after plasma treatment of the composite

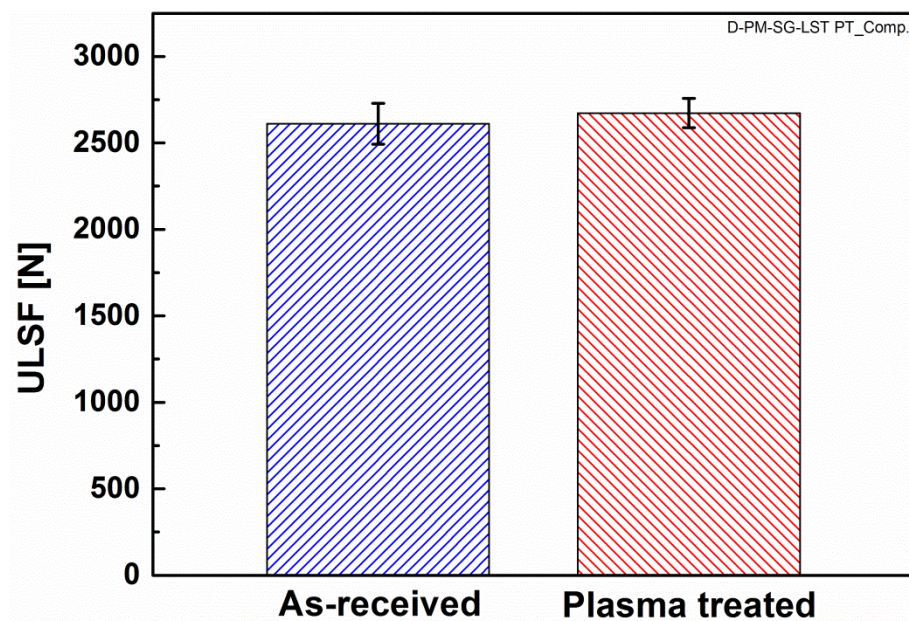


Figure A.6 Mechanical performance of SLS FSp joints after plasma treatment of the composite compared with the as received condition (joining condition C03 from Table A.1).

---

## Appendix A.7

### XPS spectra of the aluminum surface after pre-treatments as well as the composite surface

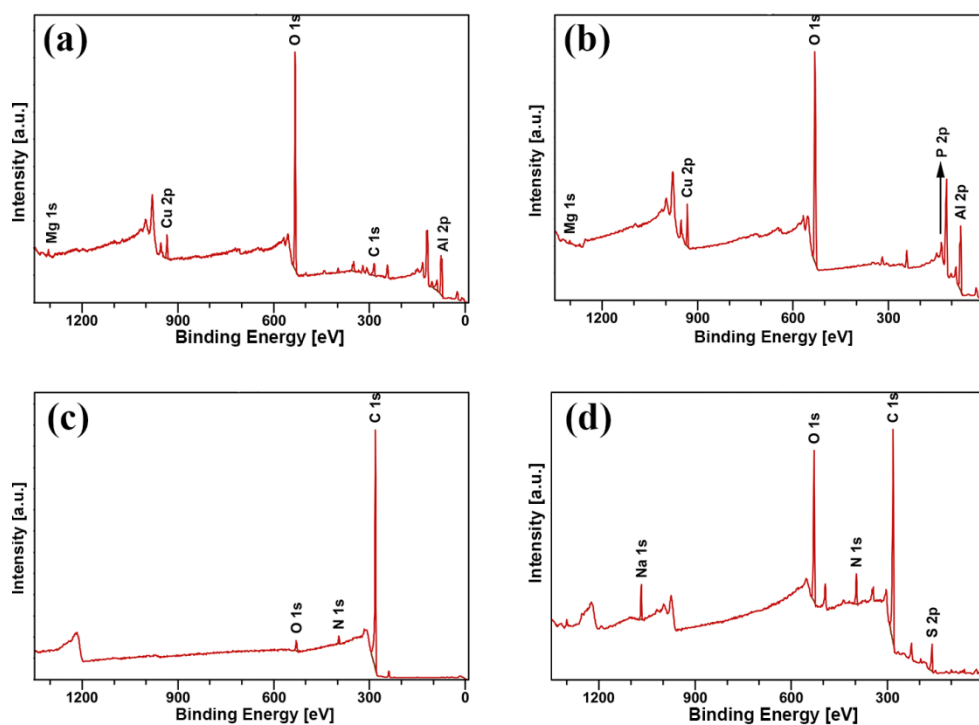


Figure A.7 XPS spectra of the aluminum surface after (a) SB, (b) PAA and (c) PAA-P pretreatments. (d) Spectrum of the CF-PPS base material.

## Appendix A.8

### Detailed load-displacement curves of SLS FSp joints after aluminum surface pre-treatments

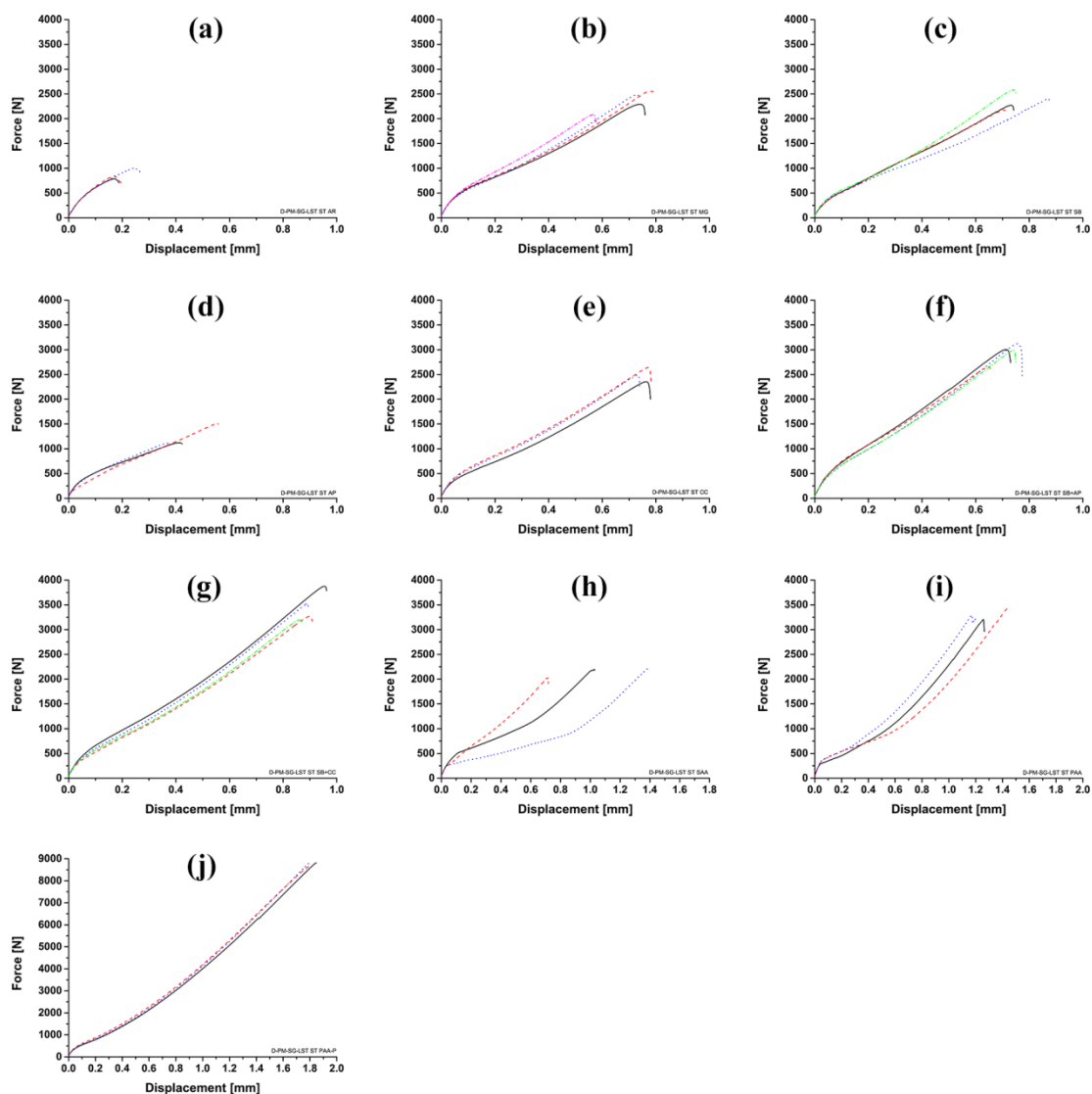


Figure A.8 Load-displacement curves of SLS FSp joints for (a) AR condition, and after surface aluminum pre-treatments: (b) MG, (c) SB, (d) AP, (e) CC, (f) SB+AP, (g) SB+CC, (h) SAA, (i) PAA and (j) PAA-P.

---

## Appendix A.9

### Detailed load-displacement curves of CT FSp joints after aluminum surface pre-treatments

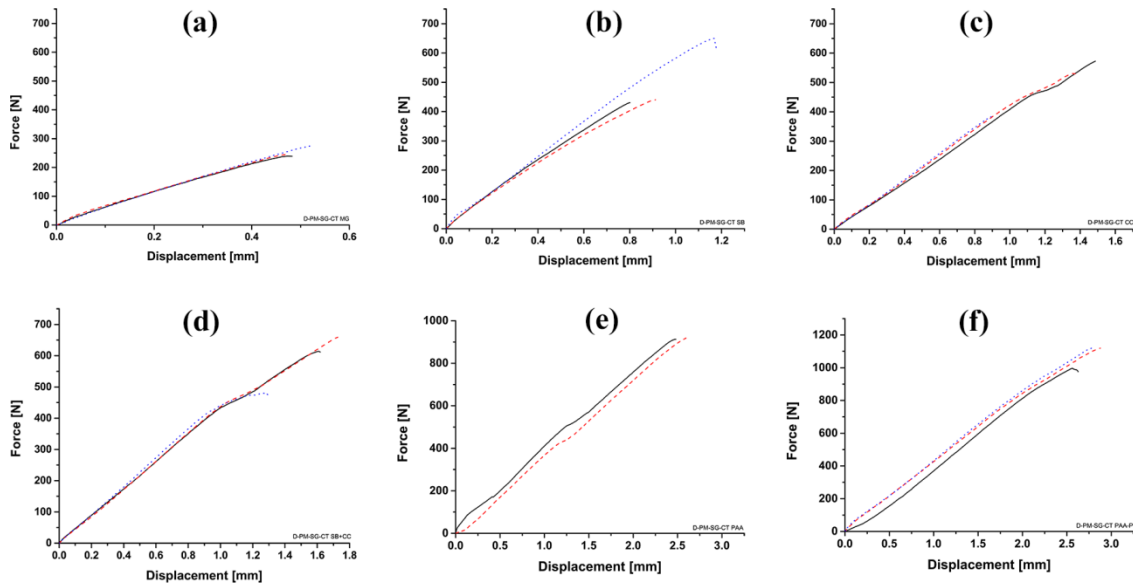


Figure A.9 Load-displacement curves of CT FSp joints after aluminum surface pre-treatments: (a) MG, (b) SB, (c) CC, (d) SB+CC, (e) PAA and (f) PAA-P.

---

## Appendix A.10

### Detailed load-displacement curves of reference adhesively bonded joints

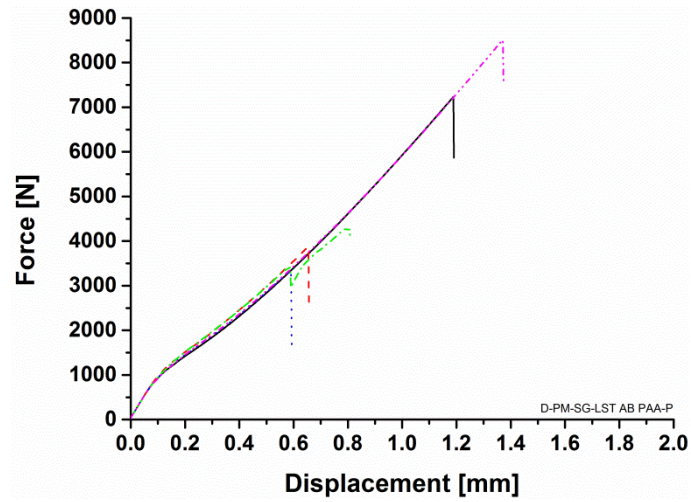


Figure A.10 Load-displacement curves of the reference SLS adhesively bonded joints.

---

# Appendix A.11

## Description of the fatigue fitting models

### Exponential and power law models

Exponential and power law models are the most widely used methods to analyze the fatigue life of overlap joints, for instance in [127, 268, 272]. ASTM standard practice E739-10 [122] explains thoroughly the procedure of fitting the fatigue data using the mentioned models. The following equations are used to define the shape of the S-N curve based on the above ASTM standard:

$$\log(N) = a + bF \quad (\text{A.1})$$

$$\log(N) = c + d\log(F) \quad (\text{A.2})$$

where  $N$  is the fatigue life,  $F$  refers to applied force at a constant amplitude, and  $a, b, c, d$  are the model parameters determined using a linear regression model. Equation (A.1) is employed to fit the exponential model, whereas Equation (A.2) is used for the power law model. A very important consideration for estimating model parameters is that the fatigue life is the dependent parameter, whereas force is an independent parameter. Moreover, in these models a linear relationship between the applied force and the obtained fatigue life is assumed [122]. So the linearity of a model should be analyzed to evaluate the fitting procedure. In addition to the S-N linear relationship, it is assumed that the logarithm of fatigue life ( $N$ ) follows a normal distribution [118, 120, 122]. Finally, it is recommended in ASTM practice that no run-outs are used to estimate the S-N curve. Run-outs are samples that survive a pre-defined number of cycles and testing is stopped before their failure.

The number of samples used to generate an S-N curve and the replication are also two important aspects in the ASTM standard [122]. It is mentioned that a minimum total number of specimens of 6 to 12 are required in the research and development phase, whereas for design purposes and reliability of the data the number of specimens should be increased to 12 to 24. Furthermore, a replication of 33 to 50 percent should be maintained in the research and development, whereas allowable data of 50 to 75 percent is required for the design. Equation (A.3) shows the calculation of replication based on [122]:

$$\%Replication = 100 \left( 1 - \frac{\text{total number of stress levels}}{\text{total number of specimens}} \right) \quad (\text{A.3})$$

### Wear-out model

Although the exponential and power law models have been widely used to fit fatigue data, they do not consider the probabilistic nature of the fatigue properties of composite materials. It is reported that the fatigue life of composite materials indicate high scatter, which forced the development of more complex models to fit the fatigue data and so obtain statistically reliable S-N curves [120].

---

Wear-out or strength degradation models were proposed with various approaches to derive an S-N curve, taking into account the probability of failure under fatigue loading.

Sendeckyj proposed a wear-out model that has a couple of advantages for composite materials [118, 120, 123]. The first advantage, as already mentioned, is consideration of the probabilistic behavior of composite materials under fatigue loading. The second is that run-out specimens can also be used in the analysis to determine the S-N curve.

In the model proposed by Sendekyj, the fatigue strength data are converted to equivalent static strength (ESS) using Equation (A.4):

$$F_e = F_{max} \left[ \left( \frac{F_r}{F_{max}} \right)^{1/S'} + (N - 1)C \right]^{S'} \quad (\text{A.4})$$

where  $F_e$  is the equivalent static force,  $F_{max}$  refers to the maximum applied force,  $F_r$  is the residual strength of the run-out specimens,  $N$  is the fatigue life of each specimen at the applied stress,  $C$  and  $S'$  are the model parameters.  $C$  and  $S'$  control the shape of the S-N curve in the low-cycle fatigue regime as well as the slope of the curve respectively. Note that, in this work the equivalent static force was calculated, however the term ESS is used due to its convention in the literature.

In the wear-out model, in contrast to exponential and power law models, it is assumed that the ESS data follow a two-parameter Weibull distribution. Therefore, a two-parameter Weibull distribution is fitted to the ESS data to obtain the Weibull shape parameter ( $\alpha$ ) and scale parameter ( $\beta$ ). An iterative process needs to be performed based on different values of  $C$  and  $S'$  to obtain the maximum shape parameter of the Weibull distribution ( $\alpha_f$ ). Finally, the S-N curve can be obtained from Equation (A.5) (which is a power equation in nature) for a desired reliability level:

$$F_{max} = \beta \left( -\ln(R(N)) \right)^{1/\alpha_f} \left( (N_f - A)C \right)^{-S'} \quad (\text{A.5})$$

where  $\alpha_f$  and  $\beta$  refer to the maximum shape and scale parameters of the fitted Weibull distribution,  $R(N)$  is the selected reliability value,  $N_f$  is the fatigue life, and  $A$  is calculated as follows:

$$A = -\frac{1 - C}{C} \quad (\text{A.6})$$

A major assumption in this model is that the failure mode of the fatigue specimens should be similar to quasi-static samples, and no competing failure modes are presented.

For more information on fitting procedures using the above mentioned models refer to [122] for the exponential and power law models and to [123] for the wear-out model.

---

## Detailed fatigue data from the S-N curves presented in Chapter 10

**Table A.2** Estimated parameters for the selected models.

Surface pre-treatment	Exponential Equation (A.1)		Power law Equation (A.2)		Wear-out Equation (A.5)			
	a	b	c	d	$\alpha$	$\beta$	C	S
SB	7.16669	-0.00256	25.25512	-6.91255	17.21220	4615.33	0.43191	0.15775
SB+CC	7.90061	-0.00210	31.81210	-8.53354	14.36530	4587.83	0.90861	0.09893
PAA	8.83116	-0.00382	37.1902	-10.72974	6.85346	4210.72	0.65316	0.12544
PAA-P	6.92999	-0.00073	24.9976	-5.85888	7.40972	15653	0.70951	0.15185

**Table A.3** Estimated fatigue strength [N] of the selected pre-treated joints based on exponential, power law, and wear-out models after  $10^5$  and  $10^6$  cycles.

	Exponential (Lin-Log) model		Power law (Log-Log)		Wear-out (Sendeckyj) model	
	$10^5$	$10^6$	$10^5$	$10^6$	$10^5$	$10^6$
SB	846	456	851	610	838	583
SB+CC	1381	905	1387	1059	1445	1151
PAA	1003	741	1000	807	990	744
PAA-P	2644	1274	2589	1748	2730	1926

**Table A.4 Fatigue strength / ULSF [%] of the selected pre-treated joints based on exponential, power law, and wear-out models after  $10^5$  and  $10^6$  cycles.xxx**

	Exponential (Lin-Log) model		Power law (Log-Log)		Wear-out (Sendeckyj) model	
	$10^5$	$10^6$	$10^5$	$10^6$	$10^5$	$10^6$
SB	35	19	36	26	35	24
SB+CC	43	28	43	33	45	36
PAA	34	25	34	28	34	26
PAA-P	38	18	37	25	39	27

## Validation of the models

To validate the models, it was proposed to evaluate the linearity of the exponential and power law models [122], as well as the goodness-of-fit of the wear-out model [123].

A linearity index was calculated for each of the selected surface pre-treatments and the results are listed in Table A.5. These values were compared to the critical linearity index ( $F_p$ ) taken from [122] for a significance level of 5%. The linearity hypothesis is valid in cases where the linearity index is lower than the  $F_p$ . In all cases the linearity is valid, as can be seen in the table, except for the exponential model with the PAA specimens in which the linearity index exceeds the  $F_p$ . The run-outs were not included in the analysis of linearity in accordance with the ASTM standard. It may well be that a slightly higher scattering of the fatigue data in the HCF region (which has a greater impact in the analysis) led to rejection of the linearity hypothesis. Such behavior was also observed in [120].

**Table A.5 Calculation of the linearity index for the exponential and power law models.**

Surface pre-treatment	Exponential		Power law	
	Linearity index	$F_p$	Linearity index	$F_p$
SB	4.46024	5.1174	0.59666	5.1174
SB+CC	3.18467	4.7571	3.33068	4.7571
PAA	6.31900	4.7374	2.89993	4.7374
PAA-P	0.11993	4.4590	0.03010	4.4590

---

An evaluation of the fitting procedure for the wear-out model was performed by an analysis of goodness-of-fit, as described in [123]. Kruskal-Wallis statistics were performed on the ESS data obtained. By Kruskal-Wallis analysis an H value ( $H_{KW}$ ) was calculated and compared to a critical H value ( $H_{cr}$ ) that corresponds to the 5% significance level. The values of  $H_{cr}$  were obtained from [273]. Table A.6 lists the calculated  $H_{KW}$  and obtained  $H_{cr}$ . The degree of freedom (DF) in the table corresponds to the number of selected load levels for each surface pre-treatment. The  $H_{KW}$  was lower than the  $H_{cr}$  for all surface pre-treatments, implying that the fitting procedure of the wear-out model was appropriate. However, for the PAA specimens  $H_{KW}$  was very close to the  $H_{cr}$ , which could indicate a poor fit, as was also observed in Figure 10.1 (Page 114).

**Table A.6 Calculated Kruskal-Wallis statistics index and the respective critical value for the wear-out model.**

Surface pre-treatment	DF	$H_{KW}$	$H_{cr}$
SB	3	5.47	7.81
SB+CC	5	10.28	11.07
PAA	4	9.26	9.49
PAA-P	4	2.16	9.49

---

# List of publications

## Journal papers

- S.M. Goushegir, J.F. dos Santos, S. Amancio-Filho, Failure and fracture micro-mechanisms in metal-composite single lap joints produced by welding-based joining techniques, *J. Composites: Part A*, (accepted for publication), 2015
- S.M. Goushegir, N. Scharnagl, J.F. dos Santos, S. Amancio-Filho, XPS analysis of the interface between AA2024-T3 / CF-PPS friction spot joints, *J. Surface and Interface Analysis*, DOI: 10.1002/sia.5816, 2015
- S.M. Goushegir, J.F. dos Santos, S. Amancio-Filho, Influence of process parameters on mechanical performance and bonding area of AA2024/carbon-fiber reinforced poly(phenylene sulfide) friction spot single lap joints, *J. Materials & Design*, 2015; 83: 431-442
- S.M. Goushegir, J.F. dos Santos, S. Amancio-Filho, Friction spot joining of aluminum AA2024 / CF-PPS composite single lap joints: microstructure and mechanical performance, *J. Materials & Design*, 2014; 54:196-206
- J.V. Esteves, S.M. Goushegir, J.F. dos Santos, L.B. Canto, E. Hage Jr., S. Amancio-Filho, Friction spot joining of aluminum AA6181-T4 and carbon fiber-reinforced poly(phenylene sulfide): Effects of process parameters on the microstructure and mechanical strength, *J. Materials & Design*, 2015; 66 (Part B): 437-445

## Book chapter

- S.M. Goushegir, S. Amancio-Filho, Friction Spot Joining. In: S. Amancio-Filho, J.F. dos Santos, editors. *Joining of Polymer-Metal Hybrid Structures - Principles, Applications and Recent Developments*. Wiley (To be published)

## International conferences

- S.M. Goushegir, N. Scharnagl, J.F. dos Santos, S. Amancio-Filho, XPS analysis of the interface between AA2024-T3 / CF-PPS friction spot joints, *Aluminium Surface Science and Technology (ASST 2015)*, 17-21 May 2015, Madeira, Portugal
- N.M. Andre, S.M. Goushegir, J.F. dos Santos, L.B. Canto, S. Amancio-Filho, On the microstructure and mechanical performance of friction spot joining with additional film interlayer, *Society for Plastics Engineers – ANTEC*, 30 April 2014, Las Vegas, USA
- S.M. Goushegir, J.F. dos Santos, S. Amancio-Filho, Process optimization of friction spot joining for AA2024-T3 / CF-PPS joints through design of experiments and statistical analysis, *66th Annual Assembly of the International Institute of Welding (IIW)*, 12 September 2013, Essen, Germany

- 
- J.V. Esteves, S.M. Goushegir, J.F. dos Santos, L.B. Canto, E. Hage Jr., S. Amancio-Filho, Friction spot joining of aluminum AA6181-T4 and carbon fiber-reinforced poly(phenylene sulfide): Effects of process parameters on microstructure and strength, Euromat 2013, 8-13 September 2013, Sevilla, Spain
  - S.M. Goushegir, J.F. dos Santos, S. Amancio-Filho, Effect of mechanical surface pre-treatment on interlocking phenomenon of AA2024-T3 / CF-PPS friction spot joints, 2nd International Conference on Structural Adhesive Bonding, 4-5 July 2013, Porto, Portugal
  - S.M. Goushegir, J.F. dos Santos, S. Amancio-Filho, Friction spot joining of AA 2024 to carbon reinforced PPS composite; A feasibility study, Materials Science and Engineering (MSE) Conference, 25-27 September 2012, Darmstadt, Germany

## **Award**

- Co-winner of the German High Tech Champions GHTC® Award for Friction Spot Joining of CFRP-Metal Structures, 18 November 2013

---

# Lebenslauf

<b>Name</b>	Goushegir
<b>Vorname</b>	Seyed Mohammad
<b>Geburtsdatum</b>	12.08.1979
<b>Geburtsort, -land</b>	Tehran, Iran
<b>09.1985 – 06.1990</b>	Grundschule in Tehran
<b>09.1990 – 06.1997</b>	Gymnasium in Tehran
<b>09.1997 – 06.2002</b>	Studium an der Shiraz University in Shiraz Abschluss: Bachelor
<b>10.2002 – 07.2004</b>	Zivildienst
<b>08.2004 – 08.2008</b>	Berufstätigkeit bei Iranian Steel Producers Association / Negin Khalij Fars Co.
<b>09.2008 – 11.2010</b>	Studium an der University of Aveiro in Aveiro / Technische Universität Hamburg-Harburg in Hamburg Abschluss: Master
<b>12.2010 – 03.2011</b>	Berufstätigkeit bei Technische Universität Hamburg-Harburg
<b>06.2011 – 10.2015</b>	Berufstätigkeit bei Helmholtz-Zentrum Geesthacht GmbH